Peltier Controlled Growth of Thin Ice Films in the Laboratory and Advancing the Methodology of Cavity Enhanced Laser Induced Fluorescence

WILLIS, OLIVER,RICHARD

Durham University

Peltier Controlled Growth of Thin Ice Films in the Laboratory and Advancing the Methodology of Cavity Enhanced Laser Induced Fluorescence

Author
Oliver WILLIS

Supervisor
Dr. N. Hendrik NAHLER

Co-supervisor
Dr. Eckart WREDE

A thesis submitted for the partial fulfillment of the requirements
for the degree of Doctor of Philosophy

November 2014

ABSTRACT

Cavity enhanced laser induced fluorescence (CELIF) is the first technique to combine cavity ring-down (CRDS) and laser induced fluorescence (LIF) spectroscopies in a single beam experiment. It has been shown previously to extend the dynamic range of CRDS to cover six orders of magnitude in total when observing BPEB concentrations seeded in a pulsed molecular beam. This study has extended CELIF to the most general application where a fluorescer or scatterer fills the length of a pulsed CRD experiment. Under these conditions CELIF is found to produce consistently smaller errors than CRD and is competitive with it but does not extend the dynamic range. Observing acetone fluorescence and nitrogen Rayleigh scattering it has been shown how the CRD signal normalises the LIF signal generated and that the normalisation remains linear during changes to the input powers, pressures and detector gains. Furthermore it has been shown it can be used to measure absolute quantum yields of fluorescence using acetone as an example.

A peltier based set-up for cooling the upper surface of a prism for the growth of thin ice films at temperatures of the troposphere and stratosphere has been constructed. A full temperature range of $225 \rightarrow 303\,\mathrm{K}$ was displayed. Testing showed the optimal conditions of ice growth to be a rapid expansion directed at the surface. Ice films $2.5 \rightarrow 11.8\,\mu\mathrm{m}$ thick have been successfully grown at $225.2 \pm 0.2\,\mathrm{K}$ covering, at maximum, 96 % of a $1\,\mathrm{cm}$ by $3\,\mathrm{cm}$ stainless steel prism surface. During growth a strong migration over time to an area $0.028 \pm 0.002\,\mathrm{cm}^2$ was seen caused by a temperature gradient on the surface, $\Delta T \simeq 5\,\mathrm{K}$ from the centre to the outside of the surface along its short side. To monitor this and ice growth, two methods have been successfully installed and tested. A morphological analysis combined with video monitoring can accurately determine areas within $5\,\%$ and a HeNe laser reflected from the ice is able to monitor surface thicknesses from interference patterns. Together these offer a complete method to characterise an ice film over the duration of an experiment.

CONTENTS

LIST OF ACRONYMS

Acronym	Meaning
ASE	Amplified Stimulated Emission
ATR	Attenuated Total Internal Reflection (Spectroscopy)
BPEB	1,4,Bis-(Phenylethynyl)Benzene
CELIF	Cavity Enhanced Laser Induced Fluoresence
CRDS	Cavity Ring-Down Spectroscopy
EW	Evanescent Wave
EWCRDS	Evanescent Wave Cavity Ring-Down Spectroscopy
FWHM	Full Width Half Maximum
H-Bond	Hydrogen Bond
HF	High Finesse
HR	High Reflectivity
HV	High Vacuum
IR	Infra Red
LIF	Light Induced Fluorescence
LIPF	Light Induced Predissociative Fluorescence
LOD	Limit of Detection
MA	Morphological Analysis
ND	Neutral Density
MS	Multi-Stage
NMR	Nuclear Magnetic Resonance
PID	Proportional-Integral-Derivative
PLIF	Planar Light Induced Fluorescence
PMT	Photo Multiplier Tube
ppb	Parts Per Billion
ppt	Parts Per Trillion
PSC	Polar Stratospheric Cloud
RDT	Ring-Down Time
rds	Rate Determining Step
REMPI	Resonance Enhanced Multi-Photon Ionisation
RP	Rotary Pump
QLL	Quasi Liquid Layer
rtp	Room Temperature and Pressure
SC	Semi-conductor
SNR	Signal to Noise Ratio
SS	Stainless Steel
TC	ThermoCouple
TIR	Total Internal Reflection
TMP	Turbo Molecular Pump
UHV	Ultra High Vacuum
VdW	Van der Waals
VSEPR	Valence Shell Electron Pair Repulsion

Declaration

The material contained within this thesis has not previously been submitted for a degree at Durham University or any other university. The research reported within this thesis has been conducted by the author unless indicated otherwise.

Copyright

ACKNOWLEDGEMENTS

The work presented here occurred only with the support of a large number of people. First I would like to thank my supervisor, Dr. Hendrik Nahler, who offered this opportunity to me some years ago. He has supported this work throughout, lending his experience and knowledge, and helping me to push my own abilities along with the boundaries of science. With him, my co-supervisor, Dr. Eckart Wrede, deserves thanks for the same reasons and for supervising me after Hendrik's move to Heriot-Watt. Together they remain tirelessly enthusiastic, while being approachable and open to discussion. Working in the Laser, Spectroscopy and Dynamics (LS&D) group at Durham has been a pleasure during my time within it. First I would like to thank Scott Sanders for his initial work on CELIF. I would also like to thank the past and current members of LS&D (a list too long to put here) for creating such a productive and enjoyable atmosphere. In particular I thank Scott, Adrian, Daniel and Adam for their coffee, lunch and pub time discussions, both scientific and not, which have made this PhD so enjoyable. A special mention should also be made to Dr. Lianzhong Deng who during his time with LS&D made a lasting impact with his calm and enthusiastic demeanour. Lastly, but certainly not least, I would like to thank Hayley Newton and Tom Adams for their contributions to my work during their fourth year projects.

I would like to thank Durham University and the EPSRC for the funding of my PhD. Durham University has provided a world class establishment to pursue my research interests. I would like to thank all the support staff from the different facilities used during this PhD. However I would like to particularly thank the chemistry mechanical workshop, headed by Neil Holmes. My thesis was primarily a build project that required a lot of demanding and difficult precision work. I am grateful to them for the many hours they spent on this project, in particular for their efforts slotting me in whenever parts needed to be altered or turned around in a short space of time. As well as this the electronics workshop provided a vital service. Although all members contributed, it was Kevlin Appleby's experience and talent that created several key electrical parts of this experiment. His extensive knowledge meant items could be crafted with a very limited input from an inexperienced student and his fast, reliable turn around on items meant that anything related to electrical work need never be a worry. Finally I would like to thank Dr. Jun Jie Wu and Dr. Qian Qian Wang for use of their polishing machine.

This thesis is the culmination of over four years of work but it simply would not have been possible without my friends and family. I would like to thank all my friends who have supported me over these years. I would like to especially thank my mum, dad and sister who have been of immense importance supporting me throughout, particularly during the last year. Finally and most importantly of all I would like to thank, Pip. Without her support, through the highs, the lows, the long hours, through thick and thin, it feels like none of this would even have been possible.

This thesis is dedicated to Pip and all my family.

Thank you for your support and love throughout.

Without it all this would not have been possible.

CHAPTER 1

Experimental Atmospheric Ice Chemistry

1.1 Introduction

There is great scientific interest in the study and understanding of the environment, in particular the atmosphere. It is more than just academic: every living thing on earth has a vested interest. The concept of climate change, of how events on this planet may be affecting the atmosphere, has caused global concern. There are arguments which both support and refute it. Of those which support it, there is further debate as to the extent and severity of the issue. Changes to the atmosphere derive both anthropogenically and naturally. From man they come from industrialisation, particularly through agriculture, transport and utility services such as power generation. From the earth contributions are mainly biological, from the life inhabiting it, and geological, from features such as volcanos. Pollutants added to the atmosphere can be harmless in the correct quantities but left unchecked they can become an issue for both health and the climate. These chemicals are balanced over time by different loss processes. They may be used up in reactions with other chemicals, producing harmless products or even further dangerous ones. They can also disappear permanently and temporarily into sinks on the earth. As time passes it becomes increasingly important to understand the dynamics and the processes taking place in atmosphere. Changes to the atmosphere over time are slow and semi-permanent occurring on a generational scale and longer. Therefore only with continued efforts to understand it can steps be made in enough time to avoid a disaster.[1]

Amongst a multitude of atmospheric processes, there is still a significant proportion of research in a wide variety of fields devoted to the study of ice. Much of this derives from the discovery of the ozone depletion in the Antarctic by Farman *et al.*[2] and the subsequent investigations into its mechanisms[3] and meteorological conditions for its formation.[4] It is this single event which really thrust environmental science into the media spotlight during the end of the last century. Although recently it has been covered less strongly in

popular media, the problems in the ozone layer have not disappeared and there are still regular publications appearing in high impact journals. In recent years, the ozone hole seems to have stabilised, and has even shown some signs of recovery.[5] However overall, given fluctuations from year to year, levels are still as low they have ever been and the size has not changed significantly since 1990 onwards.[6] More interestingly recent data from Manney *et al.*[7] indicates there might be ozone depletion occurring in the Arctic. In recent years, levels are their lowest on record although even these are still significantly higher than those in the Antarctic.

The discovery of the ozone hole has led to a high interest in stratospheric and tropospheric chemistry. Significant levels of active chlorine species were detected and found to play a significant role in the ozone depletion. Further investigation revealed that polar stratospheric clouds (PSCs) were involved catalytically converting chlorine species to active forms involved in ozone destruction. PSCs are composed of water-ice or, more commonly, supercooled aqueous solutions of nitric and sulphuric acid depending on the conditions of their creation. This was one of the first indications of the role of water-ice in atmospheric chemistry. Its role has not been limited to PSCs and chemistry has now been found occurring everywhere in the lower atmosphere where ice is present, from snowpacks at ground level to cirrus cloud particles in the sky. Wherever it is located, it has been shown able to interact with gaseous species and semi-volatile compounds in the atmosphere in different ways, through adsorption on its surface, the promotion of reactive heterogeneous chemistry and incorporation into its bulk. To date, laboratory based studies have tended to deal with colder temperatures, $< 230\,\mathrm{K}$, relating mainly to the stratosphere and beyond. This is in part due to the greater ease creating and dealing with water-ice experimentally in that region and that many spectroscopic techniques perform better, or only, in lower pressure environments.[8–10]

In order to add data to models and studies in the temperature range $210 \rightarrow 273\,\mathrm{K}$ a novel experiment is proposed employing cavity ring-down spectroscopy (CRDS) and a new technique, cavity enhanced laser induced spectroscopy (CELIF), discussed in chapter 3. Both are highly sensitive laser based techniques which can be used in a wide variety of environments such as at atmospherically relevant pressures. The objective of this thesis is in two parts. This first is to further the experimental understanding and development of CELIF discussed in chapter 2 and 3. The second part is to grow ice in an experiment combining CRDS and CELIF across tropospherically and stratospherically relevant temperatures using a novel method based on peltier cooling. A successful implementation would allow the interaction of atmospheric trace volatile organic compounds (VOCs) with water-ice surfaces to be studied. In this chapter the broad areas, underpinning this research, are disassembled into the key topics which complement the objectives that this research is attempting to address.

1.2 Earth's Atmosphere

The atmosphere is broken up into seven spheres which each have a particular temperature and pressure profile; from smallest to highest in altitude these are the troposphere, stratosphere, mesosphere, thermosphere, exosphere and magnetosphere. The seventh is the ionosphere and radially covers a region beginning in the upper part of the mesosphere extending through the exosphere and into the magnetosphere. It is the region in which ions can be produced by photoionisation through the absorption of solar radiation. The boundary between each layer is referred to as the '-pause' of the layer which it sits on. The different spheres are displayed below in figure 1.1 in terms of their temperature and pressure varied with altitude.

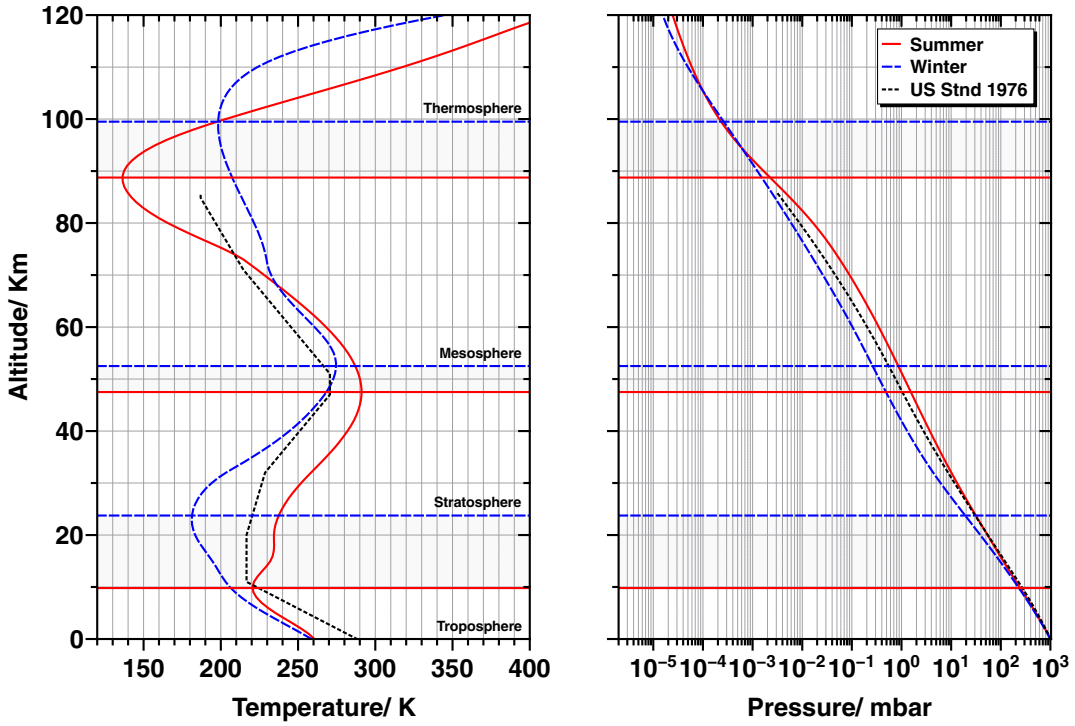

Figure 1.1: Shown above is the variation of temperature and pressure with altitude in the atmosphere. Data is shown for the South Pole in mid-summer, December 15th (red, solid line) and mid-winter, June 15th 2013 (blue, dashed line) using the NRLMSISE-00 empirical model for the atmosphere. Shaded region indicates the range of seasonal difference between the different layers. The US standard model is also shown (black, dotted line)[11] The different "-pauses" are not indicated because they lie at the variable seasonal boundary between each layer.

Far from having a temperature profile that drops consistently with altitude above the earth's surface a more complicated dynamic is observed. Regimes exist where heat gains outweigh losses and the temperature passes through several turning points. The edges of each layer are positioned at these. Their precise location is dependent on longitude and latitude, and is seasonal thus global characterisation of the atmosphere through a single vertical profile is not a straightforward task. Data measurements have been used to put together models ranging from the widely used 1976 US standard model[12] to more

recent in depth studies such as the MSIS empirical models of the atmosphere.[11] In contrast to temperature, pressure constantly decreases with height through over six orders of the magnitude from $\sim$1013 mbar in the troposphere to 10^{-4} mbar by the end of the thermosphere.

The troposphere spans from the surface of the earth to $\sim 10 \rightarrow 20\,\mathrm{km}$ high with large variations depending on the season and latitude at which it is measured. It is found on average at its highest near the equator at $\sim 18\,\mathrm{km}$ and lowest around the poles $\sim 8\,\mathrm{km}$. It is further divided up into the planetary boundary layer, which contains the first $1\,\mathrm{km}$ of altitude, and the free troposphere which contains the rest. Although the troposphere occupies only $\sim 11\,\%$ of the volume in the first three layers,* it contains $\sim 75 \rightarrow 80\,\%$ of the atmosphere by mass and moreover $99\,\%$ of all water. Temperature decreases with height on average about $6.5 \rightarrow 9.5\,\mathrm{K\,km^{-1}}$ depending on the water content, peaking near the surface at $\sim 290\,\mathrm{K}$ on average going down to $190 \rightarrow 210\,\mathrm{K}$ at the tropopause.

Mixing in the atmosphere can be described using the hydrostatic equation. This states for a fluid that the pressure at any height is due to the force per unit area exerted by the weight of the fluid lying above it.

$$\frac{\mathrm{d}\,P(z)}{\mathrm{d}\,z} = -\rho(z)g \tag{1.1}$$

where $P(z)$ (Pa) is the pressure dependent on the height, z (m). ρ is the mass density of air ($\mathrm{Kg\,m^{-3}}$) and g ($\mathrm{m\,s^{-2}}$) is the acceleration due to gravity. By using the ideal gas law we may substitute in for ρ,

$$\begin{aligned} \rho(z) &= \frac{M_{\mathrm{air}} P(z)}{RT(z)} \\ \frac{\mathrm{d}\,P(z)}{\mathrm{d}\,z} &= -\frac{M_{\mathrm{air}} P(z) g}{RT(z)} \end{aligned} \tag{1.2}$$

where M_{air} ($\mathrm{Kg\,mol^{-1}}$) is the average molecular weight of air, R ($\mathrm{J\,K^{-1}\,mol^{-1}}$) is the gas constant and T (K) the temperature. $RT(z)/M_{\mathrm{air}}\,g$ is set to $H(z)$ (m) and called the scale height, the altitude over which atmospheric pressure decreases by a factor of e. Assuming temperature to be very approximately constant† when compared with the pressure drop through the atmosphere, this may be further rewritten by integrating both sides, where

* The remaining layers have less well defined boundaries e.g. the exosphere can theoretically extend to half the distance of the moon, $\sim 190,000\,\mathrm{km}$ † Temperature drops by a factor of 2 but pressure drop by 6 orders of magnitude across the height of the atmosphere

P_0 is the pressure at ground level producing,

$$\int_{P_0}^{P} \frac{\mathrm{d}\, P(z)}{P(z)} = -\int_0^z \frac{M_{\text{air}}\, g}{RT(z)} \mathrm{d}\, z$$
$$\frac{P(z)}{P_o} = \exp\left(\frac{-z}{H}\right) \tag{1.3}$$

So the pressure drop through the atmosphere shows a largely exponential trend. Moreover the scale height, $H(z)$, can be applied to individual molecular species in the atmosphere using their molecular mass, M_{i} and partial pressure P_i. This shows that light molecules have a small scale heights and therefore should tend to congregate at high altitudes of the atmosphere, while heavy molecules should stay at low altitudes. In the troposphere however this is not the case. Since the entirety of the earth's weather system sits inside it comes as no surprise to find that strong vertical mixing characterises the region. This is caused by the cold air in the upper troposphere sitting above warmer air at the surface. Molecules can migrate through its entire height in days during clear skies and minutes in thunderstorms. In fact it is only at heights above the troposphere that the lighter molecules are seen to separate themselves into layers by weight. This strong propensity for mixing lends itself to a wide variety of reactions that are able to take place in the troposphere.

The stratosphere begins where the troposphere ends, at the tropopause $10 \rightarrow 20\,\mathrm{km}$ above the surface of the earth. The temperature profile starts by remaining more or less constant at $210 \rightarrow 215\,\mathrm{K}$ until $20\,\mathrm{km}$ out. Here it begins to rise until $45 \rightarrow 55\,\mathrm{km}$ peaking around $270\,\mathrm{K}$ at the stratopause where another turning point towards cooling is made. The primary reason for this dramatic heating effect is ozone, O_3, which absorbs the UV and visible light emitted from the sun. Pressures in the stratosphere vary from $\sim 200\,\mathrm{mbar}$ near the tropopause to $\sim 1\,\mathrm{mbar}$ at the the stratopause. Above the stratosphere heating processes no longer outweigh cooling processes and temperatures drop again through the mesosphere until another turning point is reached at the start of the thermosphere. Up to beginning of this layer at around $100\,\mathrm{km}$ approximately 99.99997 % of the atmosphere by mass is found. This height is also the position of the Kármán line, named after the Hungarian scientist Theodore von Kármán, representing the point at which aeronautics ends and astronautics begins. The troposphere and the stratosphere are the key layers inside the scope of this thesis as they contain the most water and hence the most ice chemistry. Inside the stratosphere there exists the ozone layer that contains some extremely important reactive processes in which ice plays a significant role.[1,13]

1.3 The Ozone Layer and its Depletion

One of the most significant discoveries made in environmental chemistry is the presence of the ozone layer and subsequently the hole within it. The ozone hole has become the benchmark discovery for the long term detrimental effect mankind can have on the en-

vironment. Ozone was first recorded by Van Marum in 1785 although he was unaware of what exactly it was. 55 years later Schönbein identified it as a product during water electrolysis. Soon afterwards it was quickly identified in the troposphere and by 1881 it was known to have an even stronger presence further above. In 1921, Fabry and Buisson made UV measurements estimating that if stratospheric ozone was brought to surface conditions it would occupy a layer $3\,\mathrm{mm}$ thick.[14,15] This was followed up by Dobson[16] producing a spectrometer for measuring the ozone column. It remains in use today, and operates by studying the relative intensity of spectral line pairs in ozone. By using an attenuator on one of the lines to match their intensities, ozone concentrations are calculated from the resulting relative absorbance through the application of equation 2.1, the Beer-Lambert law.

Ozone is formed from the absorption of UV light by a process which leads to the heating of the stratosphere and the first turning point shown in figure 1.1. In 1930 Chapman[17] developed a mechanism for the photochemical cycling of ozone for which the most updated scheme is laid out in table 1.1. Ozone production begins with the photodissociation of oxygen by the absorption of solar light less than $310\,\mathrm{nm}$. This is the rate determining step (rds) and afterwards the atomic oxygen produced proceeds to react with oxygen to produce ozone. Only a small amount of atomic oxygen proceeds through the destruction processes laid out in table 1.1 (4a, 5a and b) and mostly dissociated ozone will recombine. Therefore altogether ozone and atomic oxygen are able to quickly interchange with each other on a timescale of seconds and overall, the process favours ozone production.[18]

Table 1.1: I. The Chapman mechanism for ozone photolysis. M is any molecule suitable for a collision event in the gas phase. v'' and v' represent the vibrational ground and excited states respectively. j'' and j' are rotational ground and excited states.[3,17]

I. Chapman Mechanism				
Reaction			Notes	
$\mathrm{O_2 + h\nu}$	$\longrightarrow$	$\mathrm{2\,O(^3P)}$	*1*	*UV light absorption yields groundstate atomic O*
$\mathrm{O_2 + h\nu}$	$\longrightarrow$	$\mathrm{O(^3P) + O(^1D)}$	*2a*	*UV light absorption yields ground and excited state O*
$\mathrm{O(^1D) + M_{v'',j''}}$	$\longrightarrow$	$\mathrm{O(^3P) + M_{v',j'}}$	*b*	*Excited state O is collisionally quenched to ground state*
$\mathrm{O(^3P) + O_2 + M}$	$\longrightarrow$	$\mathrm{O_3 + M}$	*3*	*Ozone production*
$\mathrm{O_3 + h\nu}$	$\longrightarrow$	$\mathrm{O_2 + O(^1D)}$	*4*	*Ozone destruction by light...*
$\mathrm{O + O_3}$	$\longrightarrow$	$\mathrm{2\,O_2}$	*5a*	*...or by recombination*
$\mathrm{O(^3P) + O(^3P) + M_{v'',j''}}$	$\longrightarrow$	$\mathrm{O_2 + M_{v'',j''}}$	*b*	

Initial investigations into Chapman's work indicated that calculated ozone levels in the stratosphere were much higher than those recorded. Due to this there was a search for additional loss processes which resulted in the discovery of a large variety of reactions involving ozone. It was found that atomic oxygen was not the only loss process and that there were catalytic cycles destroying ozone involving hydrogen (OH)[19,20], nitrogen (NO)[21,22], chlorine (Cl, ClO)[23–25], and bromine (Br, BrO)[26]. Of these chlorine is the most famous as this was found to stem from the decomposition of man-made chlorofluorocarbons (CFCs), direct evidence of a damaging anthropogenic effect on the atmosphere.

The Chapman mechanism showed how ozone was able to filter out harmful UV light. Removal of this layer causes increased damage to the organic life living underneath it. Farman *et al.*[2] revealed in 1985 that, contrary to models at the time which predicted largely invariant ozone layer fluctuations, a huge seasonal loss was occurring. Ozone was thinning markedly during the Antarctic spring and this was termed the ozone hole. The concern over this is still felt today and regular publications are produced on ozone depletion and its health effects.[27,28]

1.4 Ice in the Atmosphere

Not long after the ozone hole was revealed, it was discovered that heterogeneous ice chemistry was a major factor in its creation. A crucial point in the ozone depletion was that it occurred predominantly in the Antarctic during winter and spring. During this period polar stratospheric clouds (PSCs) become a feature of the stratospheric climate. PSCs, originally assumed to be composed mainly of water-ice particles, were found to be key component in the formation of the ozone hole. Experiments by Molina *et al.*[25] showed that the production of photolytically active chlorine was catalysed by the presence of ice particles. This was one of the earliest indications that ice was an important heterogenous component of atmospheric chemistry and now the role of ice in all its forms and locations in the atmosphere is addressed as a potential issue for climate science.

Nearly $100\,\%$ of all water is found in the troposphere and stratosphere, of which the troposphere contains $\sim 99\,\%$. Water is found on earth in all three states of matter making it unique amongst all other naturally occurring compounds. It is found mostly as a liquid divided between the oceans ($97\,\%$), lakes and rivers ($0.6\,\%$). Vapour, makes up the least form, and has a variable content in the atmosphere. It ranges from $1 \rightarrow 4\,\%$ of the entire atmosphere depending on the humidity in the troposphere. Above the tropopause humidity rapidly drops therefore much of atmospheric ice chemistry is devoted to investigation in the first two layers.

Ice at the surface is found mainly in the Arctic and Antarctic ($2.4\,\%$) and elsewhere in sea ice, snow and glaciers in varying amounts depending on season. Higher up in the atmosphere it is found in seasonal cirrus clouds in the upper troposphere and tropopause as well as in the contrails left by aircraft. In the stratosphere it is found mainly in PSCs in

the temperature range $190 \rightarrow 220\,\mathrm{K}$. The majority of ice exists in these two layers, but it is still found higher up in the mesosphere in form of polar mesospheric clouds.[29] These appear at temperatures in a range outside the scope of this project up to $\sim 130\,\mathrm{K}$.[1,9]

One of the earliest studies in atmospheric ice was its effect on stratospheric chemistry via PSCs. Following this it is now well known to have important roles in many different regions of the atmosphere but a particular focus in recent years has been in its effect on the biogeochemical cycle of carbon. Specifically ice's interaction with trace, volatile organic compounds (VOCs) released by geological, biological and anthropogenic sources has been investigated. VOCs impact the oxidative capacity of the atmosphere, often absorbing UV light to produce photochemistry. There is an enormous variety of chemistry that can take place which is discussed excellently across a large number of review papers.[10,30–33] The general chemical processes involved are the uptake of gases to the surface or incorporation into the bulk of ice followed by either release or reaction heterogeneously. Of these two key roles shall be looked at in a little more depth. First its role in heterogeneous catalysis via PSCs in the stratosphere, section 1.5, and then as a mechanism for the transport of trace gases, section 1.7.

1.5 Polar Stratospheric Clouds

Early studies on PSCs originally assumed them to be composed of water-ice. Although this is true, in fact, they have a more complicated nature first suggested in 1986 by Crutzen[34] and Toon[35] *et al.* Field measurements have shown there are three types of particles in PSCs. Type Ia and b form under typical stratospheric conditions at $195\,\mathrm{K}$, well above the frost point of water at this location in the atmosphere. In type Ia the particles are made of solid nitric acid trihydrate (NAT) and in Ib they are a supercooled liquid ternary solution of water, nitric and sulphuric acid. Type II PSCs are composed of water-ice particles. Type II particles are much rarer than type I PSCs. These form in the Antarctic winter at $\sim 185 \rightarrow 195\,\mathrm{K}$ when the temperature drops several Kelvin below the frost point of water in the stratosphere. This temperature is based on $5\,\mathrm{ppmv}$ water content at $60\,\mathrm{mbar}$ pressure, around $20\,\mathrm{km}$ above the earth's surface. Table 1.2 summarises the different compositions of PSCs.[9]

In contrast to type II clouds a precise formation mechanism for the observed NAT particles has been difficult to pin down despite its importance in ozone chemistry. Particulate distributions in the stratosphere are limited to mainly sulfate and associated water in aerosols ranging in size from $0.1 \rightarrow 2\,\mu\mathrm{m}$ which compose type Ib PSCs. Since only a few percent of stratospheric particles were believed to be mineral and soot based, NAT PSCs were initially believed to form by homogeneous nucleation in $H_2O/HNO_3/H_2SO_4$ aerosols.[36] However laboratory measurements by Koop *et al.*[37] demonstrated this was not the case. Another route to their formation was thought to be by nucleation onto existing ice particles, a mechanism that had been shown to occur in the laboratory and in the field. However field measurements in conditions without ice still observed NAT

clouds. Recent data now may indicate that in order to further explain observations a heterogenous mechanism involving solid particles of meteoric origin is required.[38]

Table 1.2: PSC types listed by chemical composition, formation temperature, T_{form}, particle diameter, $\varnothing_{\mathrm{particle}}$ and notes regarding their phase and structure.[9]

Type	Chemicals	T_{form} (K)	$\varnothing_{\mathrm{particle}}$ (μm)	Notes
Ia	H_2O/HNO_3	195	1	Crystalline, nitric acid trihydrate
Ib	$H_2O/HNO_3/H_2SO_4$	195	1	Supercooled ternary solution
II	H_2O	188	10-100	Crystalline, water-ice

1.6 PSC Chemistry

The first key reaction discovered in ice chemistry was involved in ozone chemistry. Chlorine gas in the stratosphere is an important source of ozone destroying chloride radicals. The main source of chlorine was initially from man-made CFCs which have now been phased out internationally. It is photolysis of these chemicals by solar UV which provides chlorine radicals for ozone depletion shown in the processes in table 1.3.III. Soon after its discovery it was suggested by Solomon *et al.*[39] that PSC ice surfaces provided a heterogenous catalyst facilitating release of chlorine gas. The mechanism of heterogeneous ice catalysis was determined and is shown in table 1.3.II.

Ozone depletion by chlorine begins with absorption of UV light by chlorine in the range $250 \rightarrow 450\,\mathrm{nm}$; this absorption region is continuous peaking around $350\,\mathrm{nm}$.[25,40] Following this, step III.2a and b occur regenerating atomic chlorine until it is terminated via either III.3a or b. Without the presence of ice, the $ClONO_2$ and HCl termination steps are relatively inert and end the ozone depletion cycle. However with PSCs present these compounds no longer remain inactive and are able to release chlorine as shown in II.1a and b. Type I PSCs are the dominant driver of the above reaction and although they also occur on type II PSCs they are less important.[10]

Nitric acid plays an important role inhibiting the termination of the chlorine depletion. N_2O_5 is formed from the gas phase oxidation of NO_2 with ozone to O_2 and NO_3. This is followed by the combination of NO_2 with NO_3 to create N_2O_5. It is thermally unstable and a temperature dependent equilibrium between N_2O_5 and NO_2/NO_3 is kept where cold weather promotes a shift to N_2O_5. N_2O_5 hydrolysis to HNO_3 in the gas phase is slow but heterogeneously reactions can occur at atmospherically relevant rates. This removes a vital source of NO_2 from the termination steps III.3a and b allowing chlorine to continue depleting ozone. This full cycle is summarised schematically below in figure 1.2.[10,18,41,42]

Table 1.3: II. Chlorine release from the reaction of stratospheric HCl and $ClONO_2$ heterogeneously on PSC ice surfaces. III. Destruction of ozone by chlorine.

II. Chlorine Release via Heterogeneous Ice Catalysis				
Reaction			Notes	
$HCl + ClONO_2$	$\xrightarrow{PSC}$	$HNO_3 + Cl_2$	*1a*	*Chlorine formation from III.3a...*
$HCl + HOCl$	$\xrightarrow{PSC}$	$H_2O + Cl_2$	*b*	*...and III.3b*
$N_2O_5 + H_2O$	$\xrightarrow{PSC}$	$2\,HNO_3$	*2a*	*Nitric acid formation by hydrolysis of dinitrogen pentoxide...*
$ClONO_2 + H_2O$	$\xrightarrow{PSC}$	$HNO_3 + HOCl$	*b*	*...and hydrolysis of chlorine nitrate*
$HNO_3(gas)$	$\xrightarrow{PSC}$	$HNO_3(surface)$	*3*	*Removal of gaseous HNO3 inhibiting termination step III.3a below.*
III. Ozone Depletion via Catalytic Chlorine Photolysis				
Reaction			Notes	
$Cl_2 + h\nu$	$\longrightarrow$	$2\,Cl$	*1*	*UV light absorption yields Cl*
$Cl + O_3$	$\longrightarrow$	$ClO + O_2$	*2a*	*Ozone destruction*
$ClO + O$	$\longrightarrow$	$Cl + O_2$	*b*	*Regeneration of Cl*
$ClO + NO_2 + M$	$\longrightarrow$	$ClONO_2 + M$	*3a*	*Termination of active Cl by NO_2...*
$Cl + CH_4$	$\longrightarrow$	$HCl + O_2$	*b*	*...or by CH_4 step.*

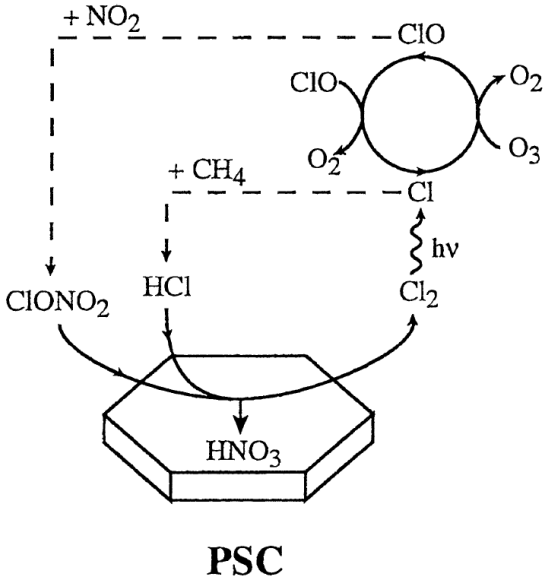

Figure 1.2: Schematic diagram of the ozone depletetion mechanism and its interaction with a PSC surface taken from Zondlo *et al.*[9]

1.7 Ice as a Vector for Transport

Most stratospheric reaction mechanisms are also able to occur in the troposphere along with many others. This is due to higher concentrations of trace gases, nitrogen oxides, sulfur oxides, and volatile organic compounds (VOCs) which are released from the combustion of fossil fuels and organic life. The significance and relevance of the heterogeneous reactions however now changes. As an example, tropospheric ozone is formed as a product from the oxidation of VOCs and CO by catalysis with NOx ($NO + NO_2$), radical OH (or any peroxy radical) or by transport from the stratosphere. In the troposphere ozone is considered a pollutant because it is a strong oxidant where high amounts at ground level are linked to respiratory diseases and the formation of reactive oxides. Removal processes, such as those found in the stratosphere, now become vital and sometimes even more complicated if the chemicals involved themselves are pollutants. In order to understand the formation and removal processes in the troposphere, a highly dynamic part of the atmosphere characterised by strong vertical mixing, gas distribution and transport mechanisms become very important.[43]

In the troposphere ice now becomes important not just for its role in heterogeneous chemistry but also as a vector for transport. Gas molecules are able to adsorb and be accommodated into the bulk of tropospheric cloud particulates, some of which are made of ice. Subsequent cloud movement or precipitation then allows them to be redistributed around the troposphere. A major drive for investigating these processes is in the formulation global tropospheric photochemistry models (GTPMs).[44–46] These attempt to simulate the chemistry occurring in the troposphere, an extremely difficult task requiring a large number of parameters across different literature sources. In particular lifetimes and transport details of the chemicals involved are needed.

Precipitation may move trace gases in two ways, the first is by precipitation scavenging. This occurs when particles form rain, snow and graupel. These are treated as falling with velocities $> 1\,\mathrm{m\,s^{-1}}$. If they reach the ground, which is essentially treated as a sink, they are regarded to remove any soluble/adsorbed trace gases from the atmosphere. However if the precipitation evaporates before reaching the ground their composition is released back into the gas phase at the lower level. A second process called gravitational settling affects cloud droplets and ice particles not heavy enough to form precipitation. This process was first considered by Crutzen and Gidel[47] in 1983 and was then shown by Fahey *et al.*[48] to be important in the stratosphere for denitrification and dehydration. This was followed up by Lawrence *et al.*[8] in 1998 looking at the effect of gravitational settling on concentrations of HNO_3 and H_2O_2 on GTPMs of the troposphere.

Although GTPMs were already taking into account precipitation in the form of rain, snow and graupel only $10\,\%$ of clouds are predicted to actually proceed to form precipitate in the first place. Instead as they dissipate over time, the motion of the cloud vertically can transport adsorbed or dissolved gases to lower levels. GTPMs such as those from

Wang *et al.* were over-estimating upper tropospheric HNO_3. Precipitation scavenging is accounted for within models in a couple of different ways. One is based on measurements of atmospheric gas concentrations before and after the precipitation event. A second is through complex algorithms designed to evaluate evaporation and redistribution as progress is made by precipitation through the atmosphere which is also used for for gravitational settling. For this, knowledge of uptake and evaporation coefficients is required that can be provided by laboratory based ice experiments.

1.8 Current State of the Field

Across the last two decades ice chemistry has been shown to play a significant part in the chemistry and dynamics of the atmosphere. There is a enormous volume of information that is barely touched upon by this brief overview and I would point the reader to the excellent reviews cited for more detailed information. The interest in ice is based on a need to model the atmosphere predicting its chemistry marked historically by the anthropogenic formation of the ozone hole in the stratosphere and photochemical smog in the troposphere. From this it has been shown that ice performs heterogeneous chemistry in both the troposphere and stratosphere and operates in the bulk uptake and transportation of trace gases to sinks and between layers in the atmosphere.

Recent laboratory experiments are now producing the information required for a wide range of trace gases and their interaction with pure water-ice and PSC compositions, such as the recent data summary by Crowley *et al.*[49] and collection of oxygenated VOCs by Symington *et al.*[50] The vast majority of laboratory data for uptake measurements however is provided at the temperatures of stratosphere and upper troposphere, $180 \rightarrow 230\,\mathrm{K}$. Here water is predominantly in the condensed phase. There continues to be a noticeable lack of data at warmer temperatures relevant to lower regions in the troposphere, in the range $230 \rightarrow 273\,\mathrm{K}$. This is in part due to experimental difficulties that are had working with ice close to its the melting point. While a wide array of surface adsorption studies are appearing, those studying the bulk phase are also distinctly lacking. In both areas many questions still remain and for accurate models precise information is required. As well as this there continues to be debate about well studied topics such as the precise formation of PSCs particularly with respect to their NAT form and composition.[38]

Overall this review of water-ice processes and chemistry has and will keep to the regime of temperatures most relevant to the troposphere and stratosphere. However it is pertinent to mention here the large body of work occurring outside of these temperatures between $20 \rightarrow 180\,\mathrm{K}$. These studies generally relate to higher atmospheric regions and space, that is astrochemistry and physics. Although occurring at lower temperatures much of the work provides data which is both complementary and underpins studies performed in the troposphere and stratosphere. There are far too many papers to cover fully within this short review. However a few of the more pertinent groups which have investigated the photochemistry of organic compounds on ice are included here for

completeness. Horn *et al.*[51,52] has studied the adsorption of stratospherically important molecules to water-ice between $80 \rightarrow 160\,\mathrm{K}$and Bouwman *et al.*[53,54] have looked at the interaction of organics with cosmic water-ice at $25 \rightarrow 125\,\mathrm{K}$. Finally Thrower *et al.*[55] has looked at the desorption of hot molecules from photon irradiated interstellar ice films at $80\,\mathrm{K}$. For further information the reader is pointed to these cited references and those related them.

A new experiment is proposed combining state-of-the-art gas phase techniques simultaneously with surface laser techniques for probing the ice bulk and inciting chemistry. Surface cooling with a peltier based set-up will be used to grow ice capable of reaching a large temperature range relevant to ice in the troposphere. It is hoped that this will prove itself able to add further detail to the other standard techniques used in the field to date. The key parts of this thesis are involved with the preliminary part of the build ascertaining the effectiveness of ice formation using a peltier based set-up. It also concerns itself with the continuing development and implementation of a novel laser technique for studying the gas phase reviewed in chapter 3. For the context of this experiment the study of ice, and its structure, and the experimental techniques used in its growth in a laboratory environment are discussed.

1.9 Water

Water is a simple triatomic molecule composed of two hydrogen atoms and one oxygen atom. In its ground state it has a bent structure with $\mathrm{C_{2v}}$ symmetry and bond length, $r_{\mathrm{OH}} = 0.9572 \pm 0.0003\,\text{Å}$ and bond angle, $\theta_{\mathrm{H\hat{O}H}} = 104.52 \pm 0.05\,^{\circ}$, derived from rotational spectroscopic data.[56] It is this bent structure that underpins the macroscopic behaviour of water in its different phases, as this affects its crystal structures and molecular formations that are made through hydrogen bonding (H-bonding). Each hydrogen atom yields one electron and the single oxygen atom provides eight, thus water contains ten electrons overall. Using the appropriate $\mathrm{C_{2v}}$ symmetry designations this yields a ground state molecular orbital configuration of $(1a_1)^2(2a_1)^2(1b_2)^2(3a_1)^2(1b_1)^2$ and from Walsh's rules[57] its bent structure and symmetry can be predicted.[58,59]

The electron density surface of ground state water has been calculated many times using a variety of ab initio methods. Most reinforce a Bjerrum four point charge model[60] for its fundamental structure; the water molecule forms a tetrahedral unit with a central oxygen atom, flanked by a pair adjacent of hydrogen atoms on two ends of the tetrahedron, along with an excess of negative charge in the remaining two tetrahedron corners; these are often referred to as the electron lone pairs in more basic structure theories such as Valence Shell Electron Pair Repulsion Theory (VSEPR). However, as Finney writes, we must take care in our assumptions of water as being a tetrahedral unit. Although inherent in early computational theories, it is now recognised to produce simulated water structures that are too ordered. In fact high quality quantum mechanical calculations use a trigonal electron distribution. Therefore the traditional Bjerrum model is best thought of in

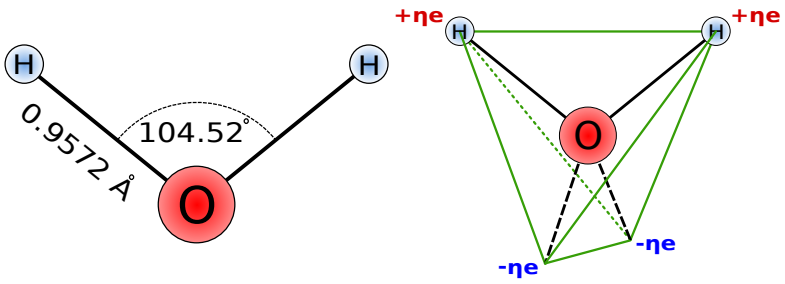

(a) Water Molecule

(b) Bjerrum Four Point Charge Model

Figure 1.3: *a)* Geometry of an individual water molecule[56] *b)* Bjerrum four point charge model of water presents the basic electrostatic model of a water molecule with fractions of charge $\pm\eta e$ placed at the four vertices.[58]

conjunction with an electrostatic model which positions a single lobe of negative charge trigonally disposed with respect to the hydrogens.[61]

From this basic molecular unit, the picture of how water arranges itself in the bulk phase starts to be understood. Key to its arrangement is this electrostatic unit and the way it may interact itself through H-bonding. This property is of immense importance as it underpins many interesting qualities of water, ice and the way it interacts chemically with other compounds. Water in the bulk form displays many unusual properties these including a negative volume of melting, a maximum density in the liquid at $4\,^{\circ}\mathrm{C}$, more than 9 crystalline polymorphs (see figure 1.4), a high dielectric constant and anonymously high melting, boiling and critical temperatures.

These qualities result from the formation of a complicated, extended H-bonded network. So far this has not been characterised by a single experiment or combination thereof. Liquid water can really only be described as a macroscopically connected, random network of H-bonds. These are continuously broken and reformed with anomalous properties arising from competition between ordering processes in the molecular architecture. Macroscopically we see a long range tetrahedral structure fitting the nature of the individual water molecules. Microscopically we see the momentary existence of small clusters due to thermal fluctuations. However despite tetrahedral long range order, the bond order is larger than 4.0, at $4.5 \rightarrow 5.0$, and the mean separation between molecules decreases by 0.1 Å relative to the ice phase. Overall the density is 9% higher relative to ice and as a result this causes ice to float on water.[62]

1.10 Bulk Structure of Ice

Relative to liquid water, ice is much easier to characterise experimentally. However it is still difficult due to the inherent disorder existing in the system, which makes a complete

experimental characterisation difficult. At $273.16\,\mathrm{K}$ enough energy has been removed from water for it to solidify, H-bonds become fixed and a crystalline structure emerges. In keeping with the complicated nature of water, there are a magnificent range of structures as shown in figure 1.4, each dependant on the pressure and temperature of system. New forms are still being found even after the years of heavy study that has already been performed such as Ice XV.[63] The bond order upon solidification decreases to four and an accompanying drop in density is observed. Each oxygen is H-bonded to four hydrogen atoms, except those at the surface, and the tetrahedral unit, as proposed by VSEPR and the Bjerrum model, reappears. Throughout all the polymorphs, this bond order is more or less maintained; the different pressures and temperatures only manage to distort the H-bonding as opposed to destroying or increasing it.[64]

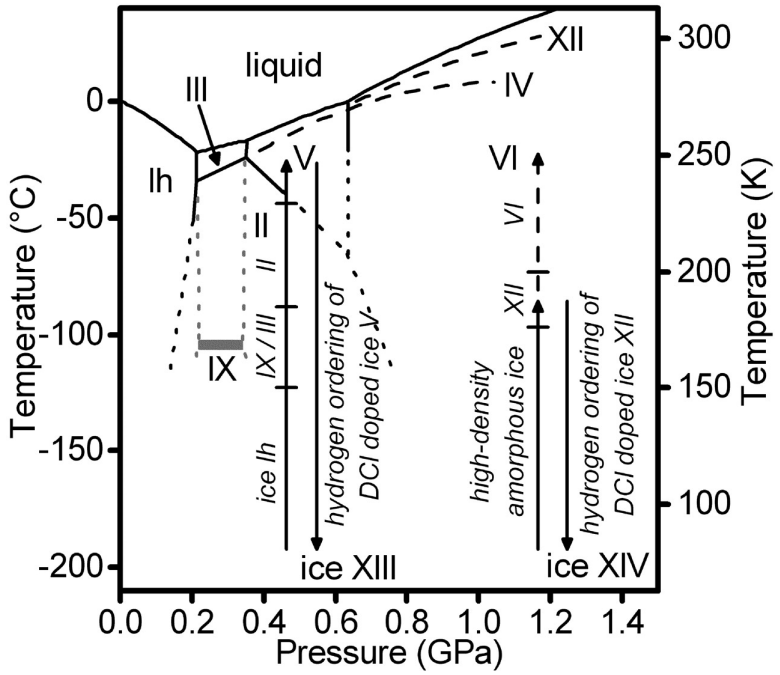

Figure 1.4: A phase diagram of ice showing the many crystal structures of water-ice. Figure taken from Salzmann *et al.*[65]

This project will look at ice chemistry not any lower than $190 \rightarrow 220\,\mathrm{K}$* and pressures less than the vapour pressure of liquid water at rtp ($\approx 20\,\mathrm{mbar}$). Under these conditions ice is produced in the hexagonal form, I_h. There are two other common forms of ice however these are of little relevance to this temperature's regime. Until only recently cubic ice, I_c, was thought not to be of much relevance to Earth's atmosphere, forming at around $130 \rightarrow 150\,\mathrm{K}$. Murray *et al.*[66] however found that given the right conditions cubic ice, could be the dominant form at temperatures up to $190\,\mathrm{K}$, when micrometre droplets of water and aqueous solutions were frozen homogenously under atmospheric conditions. Also Keyser and Leu *et al.*[67] have shown that it can be formed during vapour deposition at $200\,\mathrm{K}$ however here it is only metastable and converts to I_h ice over a period of

* The lowest temperatures of PSCs

minutes. This puts it into the lower end of the PSC temperature range and potentially atmospherically relevant. At extremely low temperatures, less than 130 K, ice is amorphous. In this form long range order breaks down and it resembles frozen liquid water. This is important in astrochemical studies, which also include other forms of ice such as CO_2, but are beyond the scope of this review.

I_h ice is named after the hexagonal lattice structure made by the oxygen atoms, based on a wurzite, ZnS, structure and generally it is formed at temperatures above $150\,\mathrm{K}$. This model was first proposed by Pauling and has been shown to be correct experimentally. Water molecules form a network of tetrahedrally bonded units at an angle, near to the optimum, $109.5\,^\circ$, with a distance, R_{OO} of $2.74\,\text{Å}$. Yet whilst, oxygen displays long range order, hydrogen does not. Rather they orientate themselves in any plausible direction in the tetrahedral units so long as there are only two hydrogens adjacent to an oxygen and one hydrogen per bond, maintaining the bond order; these are known as Bernal-Fowler rules and demonstrated in figure 1.5. Oxygen occupies two unique positions which together make up a bilayer; the first lies in its own plane with a second oxygen positioned diagonally above the it, marked on figure 1.5a. Each bilayer has a thickness that can be derived by trigonometry, $\approx 3.66\,\text{Å}$, this is backed up by half the lattice parameter, c, calculated by Röttger et al.[68] as $7.3616\,\text{Å}\,(265\,\mathrm{K}) \rightarrow 7.3332\,\text{Å}\,(175\,\mathrm{K})$.[56,58,59,69]

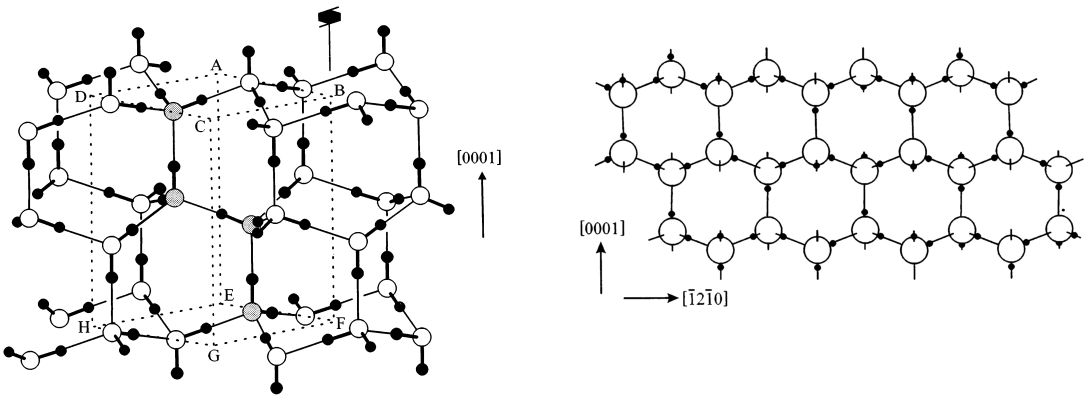

(a) I_h crystal structure based on the Pauling model. Figure taken from Petrenko[56]

(b) A layer of ice on the (1010) plane

Figure 1.5: Global structure of ice and in the (1010) plane. Notice the random orientation of hydrogens in the tetrahedral unit and the long range hexagonal order of oxygen. The central two shaded oxygen atoms in *a)* make up a single bilayer. Figure taken from Petrenko.[56]

1.10.1 Vapour Pressure and Density of Ice

For the work performed in chapter 5 several physical properties of ice are required. Behind each there is a significant body of work and a range of different measurements to choose from. Therefore a combination of the most recent, reliable, applicable and convenient sources for each property is used. Three main properties of water are used; the temperature dependent vapour pressure above water and ice, the temperature depen-

dent density of ice and wavelength dependent absorption coefficient of ice. Here the major sources are outlined for each property while appendix A.1 summarises the different constants and equations involved in their calculation.

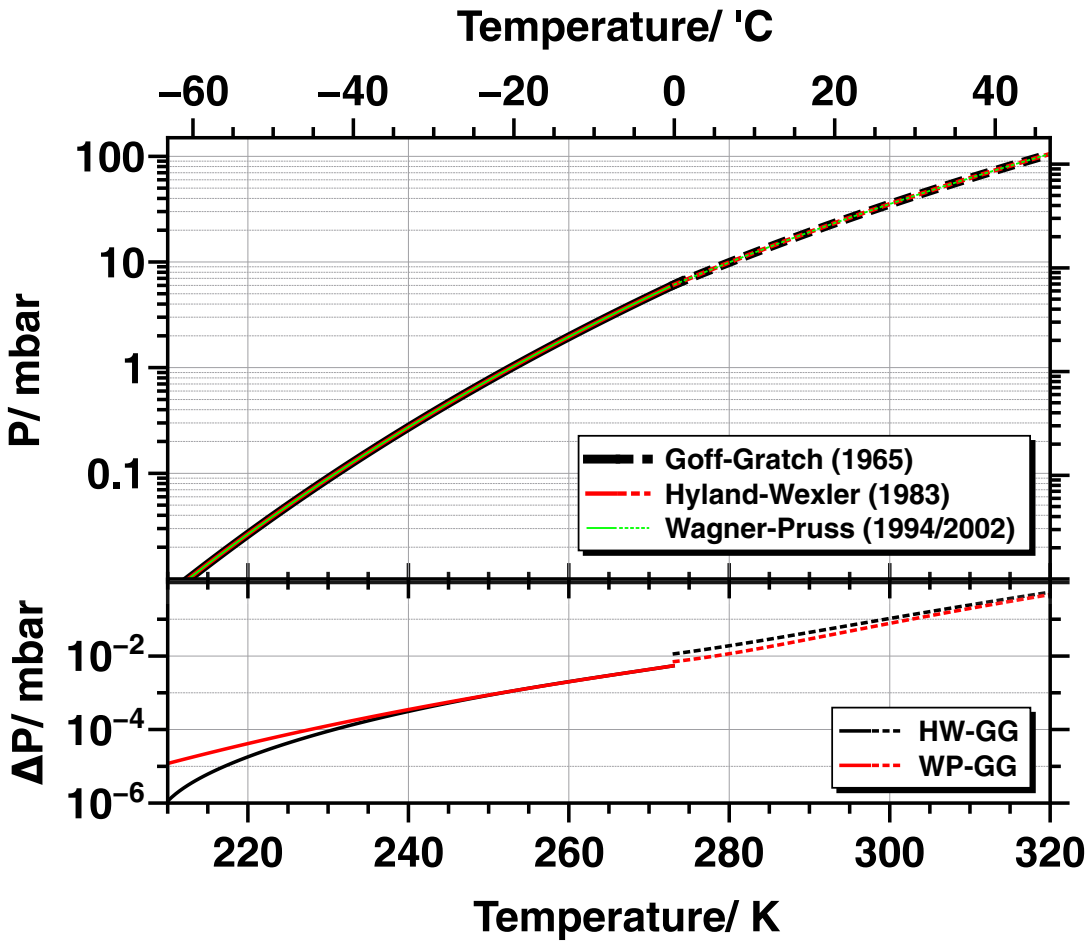

Figure 1.6: A comparison of the Goff-Gratchett (GG), Hyland-Wexler (HW) and Wagner-Pruß (WP) formulation for water vapour pressure above ice and water. Within the resolution of the top graph each model sits on top of each other. Deviation of the WP and HW from the GG model is shown in the figure below, $\Delta P = P_{\mathrm{WP}} - P_{\mathrm{GG}}$.

The vapour pressure of ice and water is significant in the formation of cirrus clouds, polar stratospheric clouds and any other source of ice in the atmosphere. It is particularly relevant in the formation of PSCs where a comparison between it and that over supercooled water becomes important for nucleation processes. The vapour pressure of water is also important for industry, stemming from its use as a coolant and in processes driven by steam. Therefore there have been a number studies over the years dedicated to ascertaining it to the best degree of accuracy. Murphy and Koop[70] provide a detailed review of the various formulations putting them in context for atmospheric applications. Goff and Gratch[71–73] formulated the first main derivation for the vapour pressure over ice and water with several updates produced afterwards by Goff. Following the Goff-Gratch formulation several other groups provided new formulations of which Hyland-Wexler and Wagner-Pruß is shown figure 1.6. From these the Wagner-Pruß is in most general

use today. Vapour pressure curves are formulated using the application of the Clausius-Clapeyron equation to measured thermodynamic data describing water including latent heats of sublimation, molar heat capacities and molar volumes. Figure 1.6 shows that for each of the measurements across the range shown and at the resolution given they are near identical. Beneath the difference from the GG equation is displayed for the HW and WP showing that each differs by only $0.02\,\%$ at low temperatures of ice to $0.4\,\%$ above water at higher temperatures across the range shown.

Another important property of ice required is its temperature dependent density. The formulation used is the recent one from Feistel and Wagner.[74] Here a Gibb's potential function is used from which many physical parameters of I_h ice can be derived. It has been based on the data from Wagner and Pruß[75] previously mentioned above and hence is why it is used here. The density derivation is included in full in appendix A.1 but for the full Gibbs function and any further physical properties derived from this study the reader is referred to the reference. Although the temperature dependent density of water is well-known in fact its application can be complicated by the way ice grows and structures itself. This is discussed further in section 1.14.

1.11 Absorption Spectrum of Ice

Pure ice is a highly transparent medium across the visible spectrum. This is a characteristic however rarely seen when observed under natural atmospheric conditions. Ice growth in the natural world consists of small crystals, granules and larger ice formations containing bubbles and small particles. This leads to scattering which increases the path length of photons travelling through the medium and in turn this causes the extinction coefficients to go up substantially from those measured in a pure crystalline ice. Despite this a variety of models for planetary atmospheres and the radiative energy balance of the earth's surface require good knowledge of the absorption coefficient of ice across the visible range which Grenfell and Perovich have measured.[76,77]

The first hurdle in this measurement is the formation of a large, metre long, bubble free ice in the laboratory environment. This has been achieved through the slow growth of ice in an Al tank from the bottom up using copper cooling pipes underneath. Mechanical stirrers were then used to ensure bubbles that might nucleate were forced out of the growing ice. Using this method a block of bubble free ice $2.83\,\mathrm{m}$ long, $0.26\,\mathrm{m}$ wide and $0.20\,\mathrm{m}$ high was grown. The absorption spectrum obtained using this shown in figure 1.7. These measurements continue to be used today but Warren and Brandt[78] have called them into question because of measurements taken by Ackerman *et al.*[79] Wavelengths between $250 \rightarrow 600\,\mathrm{nm}$ have measured absorptions an order of magnitude lower than those reported by Grenfell. This demonstrates the difficulty of taking these measurements accurately and currently this remains an unsolved issue. Across this range, and potentially the entire range, care must be taken in the application of the data; these measurements should be considered as upper limits to the actual values which might be lower.

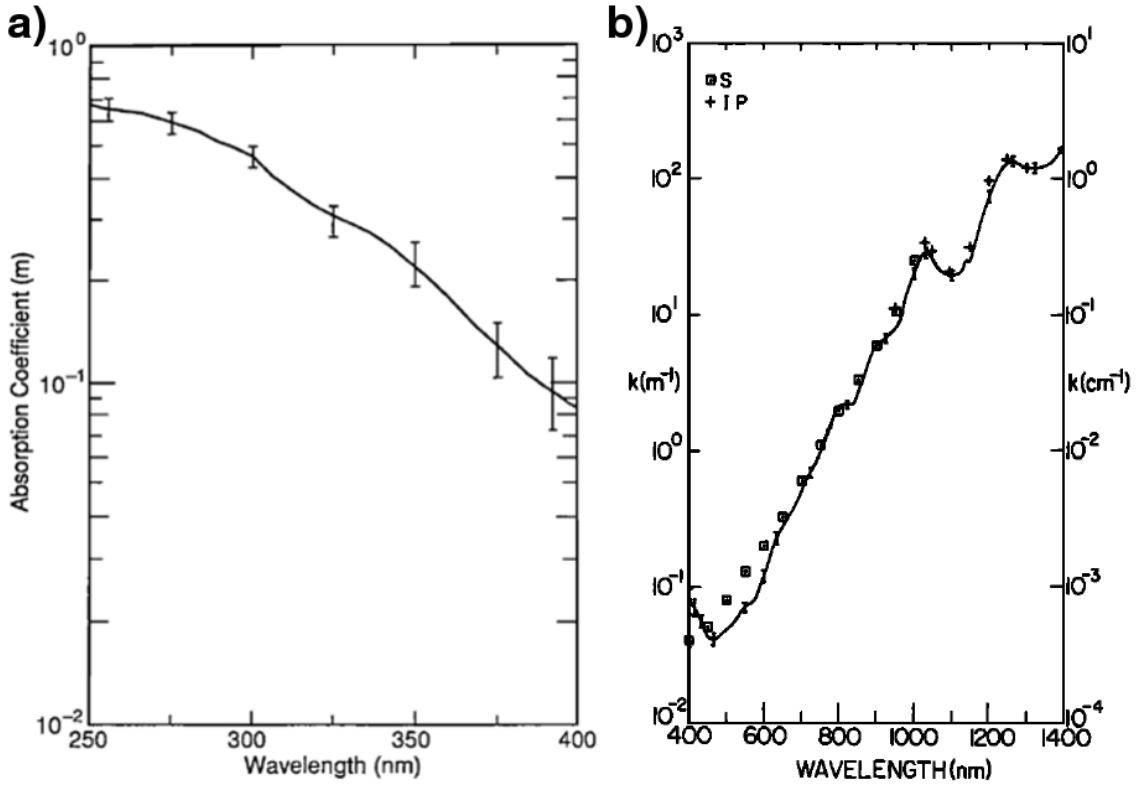

Figure 1.7: *a)* is taken from Perovich[77] showing the absorption coefficient as measured for pure bubble free ice between $250 \rightarrow 400\,\mathrm{nm}$. Error bars show the $90\,\%$ confidence level. *b)* shows the same for $400 \rightarrow 1400\,\mathrm{nm}$. Boxed and crossed values are a comparison to previous studys for which the reader is referred to the reference.[76]

1.12 Ice at the Surface

The surface of a material is often very different from the bulk. Water molecules which were able to bind with a full number of bonds in the bulk no longer can at the surface. Therefore energies change, molecules move from their usual sites and the chemical nature of the surface is altered allowing molecules to adsorb to the surface through chemisorption and physisorption. It has been shown that the surface of water-ice adsorbs trace atmospheric molecules, and also that it can accommodate them into its bulk. The ultimate aim for this project is to perform laboratory versions of this chemistry therefore it is necessary to understand what the structure of ice is like at the surface, a question that is not simple to resolve.

When modelling the idealised surface structure of ice, two potential forms can be devised. Shown in figure 1.8, these are a full-bilayer or a half-bilayer termination. In the former, the outermost O atom is H-bonded to three neighbours in the layer below. In the latter, it is bonded to a single neighbour. Various successful structural studies of ice surface at low temperatures around $25 \rightarrow 140\,\mathrm{K}$ have been performed using low energy electron diffraction[80] and scanning tunnelling microscopy.[81,82] These show that a fully terminated bilayer is the structure and that there are single dangling H-bonds at the sur-

face. Further investigations have shown the existence of three surface features, dangling O−H bonds, dangling bonds with no H and distorted tetrahedral units. The first of these is a proton donor and the second a proton acceptor and hence the ice surface is obviously structured for reactivity.[56] This is the structure as measured at low temperatures outside the temperature range of the troposphere and stratosphere. Investigations have shown that this depiction of ice is overly simple when moving to higher temperatures.

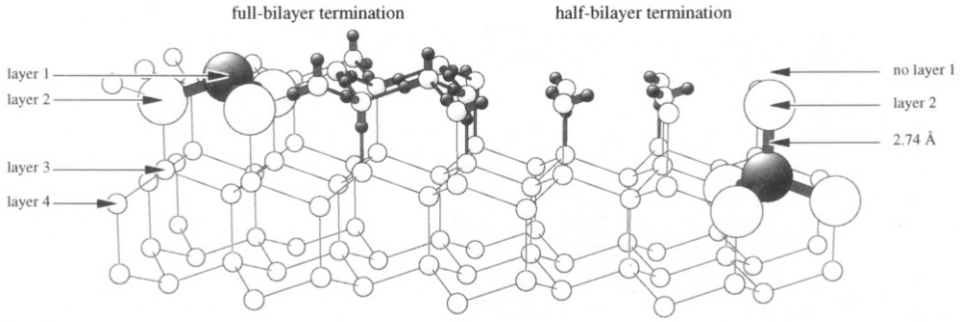

Figure 1.8: The surface structure of ice at low temperatures where the true ice surface structure is the full bilayer termination. Figure taken from Materer *et al.*[80]

1.12.1 Quasi-Liquid Layer

Complicating the depiction of ice, a thin film of liquid water coexists on the surface at temperatures higher than 160 K. This was first postulated by Michael Faraday in 1859, where he performed relegation experiments on ice cubes. Ice cubes will freeze together when two surfaces are brought into contact, hence he proposed that a liquid film was responsible. This curious property of ice is the result of a thermodynamically unfavoured region being created when the surfaces meet.[83] This has come to be known as the quasi-liquid layer (QLL) of ice. This feature is key to understanding the heterogeneous processes, adsorption and bulk accommodation shown by ice in the atmosphere up to the freezing point. It has previously been convenient for the QLL to be treated as an aqueous layer so that known reaction kinetics can be extended to those occurring on ice. While this layer is liquid-like it is however not strictly correct due to the restriction imparted to it by the ice bulk therefore this idea has been questioned.

Figure 1.9 demonstrates the disordered nature of the layer on top of the ice surface as shown by a molecular dynamics simulation.[84] Experimentally x-ray diffraction clearly showed a breakdown at the surface of the long range order shown in the bulk, while nuclear magnetic resonance studies indicated some protons exhibited increased motion. This was backed up further by experiments showing increased conductivity at the ice surface. Although defect motion, a process through which water molecules can migrate through the bulk, might have caused it, this alone was unable to account for the full range of results. As temperatures move towards the freezing point of water there is a large variance in the reported thicknesses of the QLL. Sadtchenko *et al.* reviewed data from papers up to 2002 showing the wide disparity amongst the quoted numbers, ranging

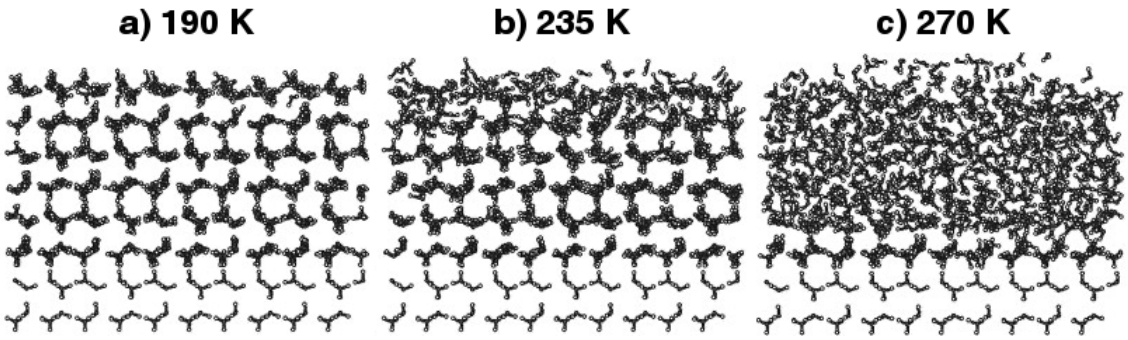

Figure 1.9: A classical molecular dynamics simulation of the ice surface at various temperatures. The disordered QLL is shown coexisting with bulk ice at temperatures well below freezing. At $190\,\mathrm{K}$ Ih ice is barely deformed but by $270\,\mathrm{K}$ disorder reigns throughout the upper bilayers. The bottommost layers are an artifact of the simulation which does not indicate thickness of the QLL.[84]

from $100 \rightarrow 0.1\,\mathrm{nm}$ over just $273 \rightarrow 263\,\mathrm{K}$. As well as this molecular dynamics simulations show this liquid layer continues to be relevant below $190\,\mathrm{K}$. The measurements reviewed also demonstrated the large array of techniques which have been used to study it including proton backscattering, atomic force microscopy, optical ellipsometry, grazing angle x-ray diffraction, photoelectron spectroscopy, molecular dynamics calculations, and optical reflections.

Further to this Sadtchenko *et al.* used attenuated total internal reflection (ATR) spectroscopy in an ice experiment to look into the nature of the QLL near to the triple point. Their findings indicated that the signal received from the QLL was nearly identical to that of water in the bulk. However later results from Kahan *et al.*[85] used glancing angle Raman spectroscopy to study H-bonding and glancing angle LIF to study pH changes in ice surfaces. Their results indicated this was not the case as H-bonding was occurring to a different extent than in water implying that it was quite different to an aqueous layer. To date the literature shows an array of conflicting measurements and no truly satisfactory theory has been put forward describing this behaviour.[10,56,69,86]

1.13 Experiments on Ice in the Laboratory

The main mechanism of cooling to sub-zero temperatures for ice formation in the lab is liquid refrigeration. In this there are two main implementations, the first involves a coolant pump used to maintain a liquid with specialised thermal properties at sub-zero temperatures. This is then pumped around a closed circuit flowing around the region to be cooled or a heat exchanger. Temperatures are then reached based on the cooling pump and liquid used as a coolant. The second method exists as an extension of this but specifically uses liquid nitrogen, or sometimes helium as the coolant. This extends from its wide use in cryogenic traps and its strength is its straightforward implementation combined with a powerful ability to cool. A liquid nitrogen/helium reservoir cools a heat exchanger either directly from contact with the liquid or indirectly passing the cold

nitrogen gas or cooled dry air around it. The heat exchanger can then be used to cool a substrate upon which ice may be grown or alteratively grown directly onto the heat exchanger itself. This method can then be combined with resistive heating on the heat exchanger or substrate to change temperatures.[87,88]

For both systems temperatures are controlled in similar ways. Sensors are installed on the ice growth region such as thermocouples or diodes. For liquid coolant pumps temperatures are usually managed on the control unit itself. For nitrogen set-ups the sensor information is often fed into a proportional-integral-derivative (PID) control which can then modify power to the resistive heating to maintain a set temperature. Precision in the instantaneous temperatures is based on the sensor and usually lies in the range of $\pm 0.05\,\mathrm{K}$. Absolute temperatures however, such as those derived from vapour pressure measurements, are less precise. These are highly dependent on the application but for a wide range of successful experiments, particularly using large ice growth regions, they are often quoted with an error up to $\pm 2\,\mathrm{K}$. Overall a huge range of temperatures can be reached using these two methods. For liquid coolant pumps the temperatures reached range from $180 \rightarrow 380\,\mathrm{K}$. Liquid nitrogen and helium set-ups range from $20 \rightarrow 35\,\mathrm{K}$[89,90] for helium and $85 \rightarrow 130\,\mathrm{K}$[91,92] for nitrogen reaching beyond $1000\,\mathrm{K}$ depending on the performance of the resistive heating.

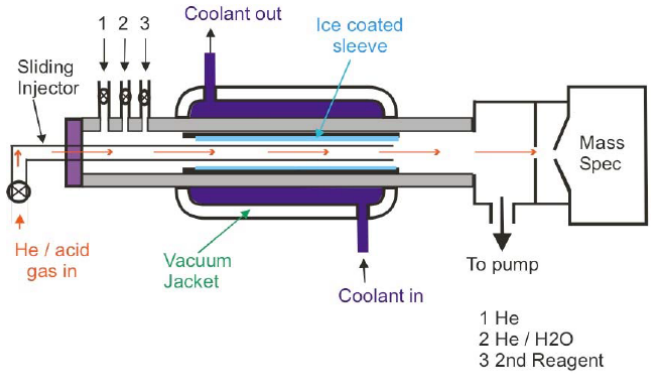

Figure 1.10: A coated wall flow tube, $\varnothing 1.5\,\mathrm{cm}$ by $\sim 50\,\mathrm{cm}$ length set-up as used by Symington *et al.* Ice is formed on the inside of an insert placed into the middle of the flow tube. Gases are introduced at points at the start and a cooling jacket is used to obtain sub-zero temperatures.[31,87]

There are two experiments that dominate many of the tropospheric and stratospheric ice studies performed in the laboratory, the Knudsen cell and flow tube reactors. Contained within each of these liquid nitrogen and liquid coolant based set-ups are employed. A coated wall flow tube experiment is shown in figure 1.10 from Symington *et al.*[50] The set-up essentially mimics a condenser used in conventional bench-top chemistry. Coolant is pumped around a central cylinder accessing temperatures in the range $180 \rightarrow 380\,\mathrm{K}$.* For the set-up used by Symington the coolant jacket is also jacketed by an evacuated cavity

* Using commercially available refrigeration units from the company Julabo as a guide.

improving insulation. The figure displays only one possible set-up and other versions have been implemented which are vertically orientated[93] and also set up for liquid surfaces.[94] In the latter an inner sleeve is rotated at a constant speed in order to achieve an even film thickness during a measurement.

In figure 1.10 ice films were created similarly using a glass inner sleeve. First the sleeve was prepared with sulfuric acid to create a wettable surface, then after putting a known amount of HPLC water onto the inside it was rotated to achieve an even film. The sleeve was then placed on the inside of the coolant jacket and frozen. Experiments were performed by flowing a carrier gas, noble (He, Ar) or N_2, through the system into a differentially pumped mass spectrometer. This set-up demands humidification of the carrier gas in order to maintain stable surface thicknesses. Trace gases are injected into the system from one end, and the point of entry modified to alter the exposure time of the gas to the surface. In this way measurements of gas uptake can be taken when the point of entry is kept at a fixed distance or adsorption rates when the distance is varied. Gas flow is generally modelled as a laminar plug flow, $500 \rightarrow 3000\,\mathrm{cm\,s^{-1}}$, that is without turbulence and equal across the cross-section of the tube. So a disadvantage in this set-up is that gas phase diffusion and remaining in the laminar flow state ultimately limits study of gases to a region $0.5 \rightarrow 4\,\mathrm{mbar}$. Also a full characterisation of the ice film can be difficult to perform precisely as access to it is severely limited.[31,50]

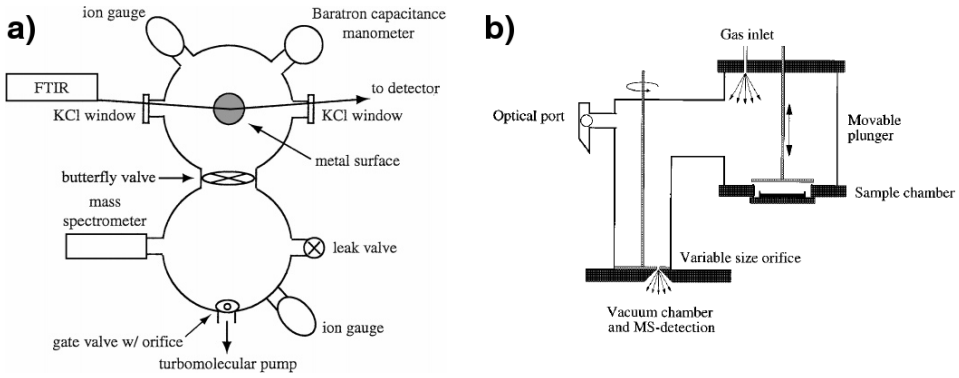

Figure 1.11: Figure shows two schematic set-ups for a Knudsen cell reactor. *a)* from Zondlo *et al.*[9,95] is a Fourier transform infra-red (FTIR) spectroscopy experiment directed over a metal surface in one and the gas flow in the other separated by a butterfly valve. *b)* from Carloz *et al.*[92] shows a version with a sealable sample holder positioned inside the chamber.

The Knudsen cell was first developed by Golden *et al.*[96] in 1973. It was designed to specifically compare a chemical system inside and out of the presence of a liquid or solid surface. Therefore one system needs to be able to shut off from the other in some way say by using adjacent chambers separated by a valve, figure 1.11a or by the isolation of a sample chamber inside a much larger chamber, figure 1.11b. Common to both set-ups is the combination of a gas entry point and an exit out to a low pressure detection system such as a mass spectrometer. A gas flow is setup, without the surface present, leaving via an orifice designed to be lower than the mean free path of the molecules inside the main chamber. This ensures that the gases behave as a molecular flow and it is the feature of

molecular effusion demonstrated by Knudsen in 1909 which gives the set-up its name. Measurements are then made by comparison of the gas concentrations between the flow set-up with and without the surface present.

In the examples in figure 1.11, ice is created using a liquid nitrogen cold finger or by flowing coolant under the sample tray. This is in part due to a limiting factor in the Knudsen cell as it can only be used with low pressures less than $\sim 1 \cdot 10^{-2}\,\mathrm{mbar}$ because the gas must behave as a molecular flow. Therefore it is not useful when it comes to higher vapour pressure ice studies, $> 210 \rightarrow 220\,\mathrm{K}$, in the troposphere and it is really only applicable to stratospheric studies and higher. Another disadvantage is that measurements happen over several seconds. This means that instantaneous measurements of surface uptake are not possible. They become time dependent unless further information from the experiments allows resolution of the problem.[31,92,97]

Although the Knudsen cell and flow tube experiments have been mentioned as the dominant experiments used to study ice dynamics there are other variants which have used the same cooling methods. Many of these have been designed to operate mainly at temperatures lower than those relevant to the troposphere and stratosphere where experiments are easier to run and more analytical techniques are available to be used. There are however two experiments which are of particular relevance to this project and exemplify versions of liquid coolant and nitrogen based cooling. The disadvantages of the Knudsen cell and flow tube experiments are their reliance on performing at low pressures. In this project the plan is to use the laser techniques CRDS and CELIF to study the gas phase dynamics above the surface of ice. Both of these, which are discussed further in the next two chapters, are highly sensitive and, crucially, able to function at a large range of atmospheric pressures and experimental environments.

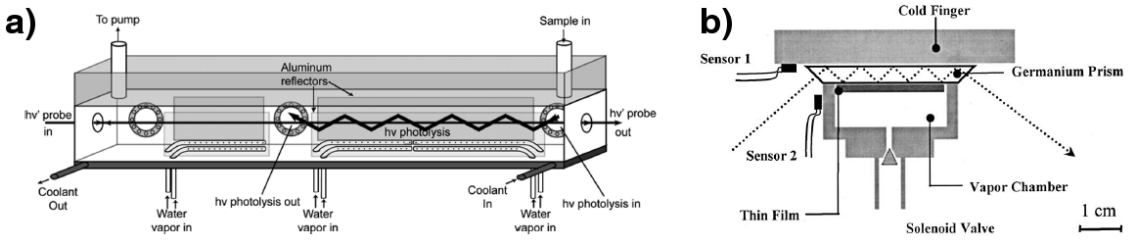

Figure 1.12: Figure shows the experimental set-ups for *a)* ice grown in the path of a CRDS beam from Zhu *et al.*[88] and *b)* for an ATR set-up on a cooled prism from Sadtchenko.[98]

Zhu *et al.* used CRDS to measure the photolysis of nitric acid on ice grown on an aluminium surface. Figure 1.12a shows the set-up that was constructed for this purpose. It is based on a double walled flow cell. Underneath the cell a liquid cooled block using ethanol freezes out ice onto pairs of aluminium reflectors mounted on the inside. Water vapour is delivered to the surface using pipes with holes drilled into them, mounted horizontally along the bottom of the cell. The set-up was used at temperatures of $253\,\mathrm{K}$ but the full capacity of the set-up to cool was not discussed. A laser was reflected between the aluminum plates promoting photolysis for any nitric acid adsorbed onto the ice, which

was then measured using CRDS running through the centre of the cell. Ice was formed $10\,\mu\mathrm{m}$ thick confirmed visually by the geometric area and estimated using mass flow rates of the water vapour put into the cell, ice deposition time and bulk density.

Further to this current the build is looking towards the integration of evanescent-wave CRDS (EWCRDS) which would like to be used to study dynamics within the ice surface concurrently with CRDS and CELIF. This will require the growth of ice isolated on the upper surface of a prism. To date no other experiment has done this, however Sadtchenko[98] has investigated the interfacial melting of ice films near to the triple point of water using attenuated total internal reflection (ATR*) spectroscopy. The set-up is shown in figure 1.12b and was based around a liquid nitrogen cold finger. An ATR prism was sandwiched between a solenoid valve, acting as a water doser, and a cold finger. The valve was heated resistively creating a decreasing temperature gradient towards the cold finger. Importantly this meant that the coldest surface in the interfacial region was the upper surface of the ATR prism. The temperatures reached on the surface of the prism using this method were quoted as $243 \rightarrow 273\,\mathrm{K}$ with an accuracy of $\pm 0.05\,\mathrm{K}$ from diode sensors positioned around the prism however the full accessible range might be larger. Thin ice films were grown, $10 \rightarrow 20\,\mathrm{nm}$ thick, monitored by the ATR spectrum. A thin film is defined as being several hundred water bilayers in thickness on the order of nanometres to micrometres. This is contrasted with ultrathin films which are generally less than a nanometre in thickness and only consist of a few to tens of bilayers. Since access to the film was restricted by the solenoid valve there was no visual method for confirming the surface morphology of the ice. There was also no absolute temperature measured since localised vapour pressures above the ice surface were not monitored and ice temperatures were only derived from the diode sensors.

1.14 The Surface Structure of Ice

Water ice films in our target temperature range, $210 \rightarrow 273\,\mathrm{K}$, are generally formed by very slow vapour deposition to a pre-cooled surface. In comparison to freezing directly from a liquid the properties of ice formed in this manner can vary significantly depending on the precise growth mechanism. Using scanning electron microscopy (SEM) outfitted for high humidities and pressures Leu and Keyser have published a number of papers characterising the morphology of ice surfaces used in tropospheric and stratospheric laboratory measurements.[99–101]

SEM micrographs were taken, showing the surface structure of water-ice films on both borosilicate glass and polished aluminium surfaces. Since the work in chapter 5 occurs on a metal SS surface micrographs from the aluminium work are shown in figure 1.13. Ice was formed passing a mixture of air and water vapour over an aluminium plate

* This is sometimes referred to as ATIR but to avoid confusion with terms like Fourier transform infra-red (FTIR) spectroscopy, where the IR stands for infra-red, the I is often dropped.

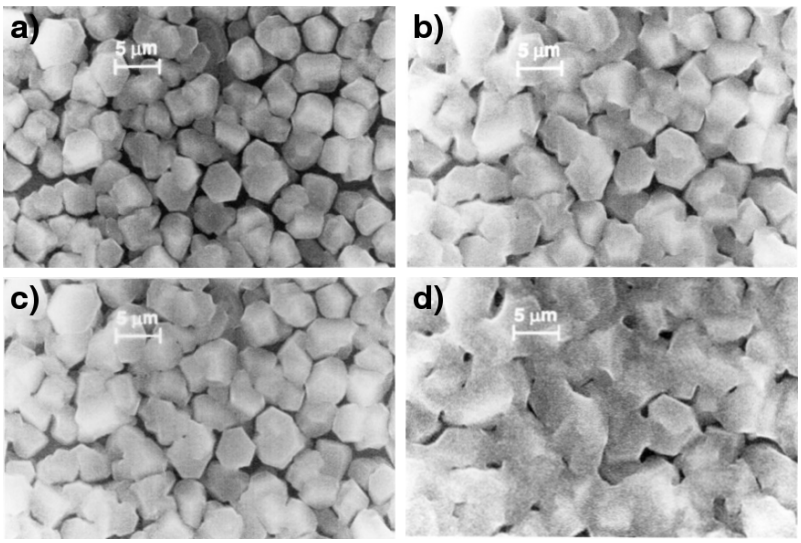

Figure 1.13: SEM micrographs of vapour deposited water-ice films on a polished aluminium plate, formed at $180\,\mathrm{K}$, then annealed at *a)* $200\,\mathrm{K}$, *b)* $215\,\mathrm{K}$, *c)* $220\,\mathrm{K}$ and *d)* $230\,\mathrm{K}$. Figures taken from Keyser[99]

cooled to $180\,\mathrm{K}$ and no thickness, area or deposition data is provided. The figures show a clear granular ice structure referred to as polycrystalline. The ice grains ranged in size from $2 \rightarrow 8\,\mu\mathrm{m}$ with an average of $5\,\mu\mathrm{m}$, where granules increase in size with the deposition time. The surface was annealed by raising the temperature incrementally from $200 \rightarrow 220\,\mathrm{K}$ and from this process the grain structure changed. The well defined grains increased in size and sintered together. By $230\,\mathrm{K}$ they were no longer well defined creating instead a porous network.

The resulting polycrystalline structure has an effect on several of the other properties of ice. First it leads to an understatement in the total surface area available and secondly it reduces its density. True surface areas that take into account the granular structure of a solid can be measured using Brunauer-Emmett-Teller (BET) adsorption isotherms. BET theory relates the adsorption of a gas, typically nitrogen or a noble gas, to its specific surface area, S ($\mathrm{cm^2\,g^{-1}}$). Leu *et al.* measured specific surface areas for ice grown on borosilicate glass and compared them to those derived from a simple relationship calculating it based on the true density* and average grain diameter, D in equation 1.4.

$$S_{\mathrm{ice}} = \frac{6}{\rho_{\mathrm{ice}} \cdot D} \tag{1.4}$$

Experiments found that equation 1.4 held up well against BET measurements above $215 \rightarrow 230\,\mathrm{K}$. But at $200\,\mathrm{K}$ and $80\,\mathrm{K}$ the BET surface area was calculated to be 3 and 6 times larger respectively. This was ascribed to the emergence of an internal porosity at colder temperatures that was not present in the annealed surfaces at warmer ones. Gener-

* Differentiated from bulk density, the true density is that of a solid ice crystal see appendix A.1

ally internal porosity in ice is observed in much colder temperature regimes, $< 200\,\mathrm{K}$, as measured recently by several groups, Bossa *et al.* and Isokoski *et al.* which are concerned with astrochemistry.[102–104] However in this case overall porosity is caused externally by the granular structure, and internally by either the lower temperatures or from the unannealed surface. Together it means that the ice formed has a lower bulk density than that expected from the true density. The average bulk density, ρ_{bulk}, for unannealed ices was measured at an average of $0.64 \pm 0.03\,\mathrm{g\,cm^{-3}}$ across $83.5 \rightarrow 263\,\mathrm{K}$ with little variation across the range. When compared to a true density of $0.925\,\mathrm{g\,cm^{-3}}$ averaged across the range, this provides a value for the bulk porosity in ice of 0.32 ± 0.03.*[101,105]

1.15 Ice Film Volumes, Areas and Thicknesses

For atmospheric experiments concerned with dynamics at the interface, knowledge of the ice volume, and therefore area and thickness is required. These values can be tricky to derive with a great degree of accuracy however there are various methods that are used. One such method for area calculations that is ubiquitously used is the BET adsorption isotherm described previously in section 1.14. The BET adsorption isotherm however requires specific experimental conditions to be run, conditions which unlikely facilitate reuse of the same ice surface. Thus measurements are only applicable in that instance. For flow tube experiments film thicknesses can be calculated using a mass flowmeter combined with values for the deposition time, geometric area and density of ice. However with the ice often covering large areas assumptions have to be made and measurements have some uncertainty to them.[50,88]

Deposition to surfaces with a more discrete area and flexible experimental set-up, such as in a Knudsen Cell, allow the use of both a similar geometric and mass based estimation as well as spectroscopy. Zondlo *et al.* use one method to determine ice thickness by monitoring an IR absorption line in crystalline ice. However a second powerful tool for measuring the thickness of crystal films was developed by Hollenberg and Dows in 1961.[106] This technique was successfully used to study ice growth by Haynes *et al.* in measurements of condensation, evaporation and sticking coefficients in water vapour to water-ice. Following this several other groups studying ice have used it as it can produce strong results with a very simple set-up.[95,107,108]

When a sample condenses onto an optically flat substrate in a thin film, light reflected from the surface produces an interference pattern that varies with film thickness. A schematic of this process is shown in figure 1.14. The process works by directing a laser onto an ice film such that the angle of incidence is not greater than the critical angle in order to avoid total internal reflection and ensure transmission into the film. Reflections occur before transmission into the film at the vacuum/vapour-ice boundary and afterwards at the ice-substrate boundary. The resulting two reflections can then inter-

* where bulk porosity is equal to $1 - (\rho_{\mathrm{bulk}}/\rho_{\mathrm{ice}})$

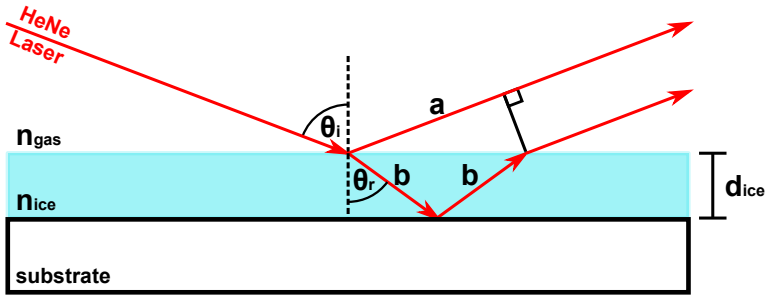

Figure 1.14: A HeNe laser interacting with an ice layer grown on a substrate. The laser reflects from the air-ice and ice-substrate boundaries producing two reflected beams which may interfere to produce fringes as the ice layer grows in thickness.

fere, assuming that the thickness of the film, d_{ice}, is not so large that the reflections do not overlap or are absorbed before exiting the surface. Constructive interference is observed when the path length difference is an integral number of wavelengths. Similarly destructive interference occurs when the path length is a half number of wavelengths in difference.

From this observation we can calculate d_{ice}. It is derived using a combination of Snell's law with the geometry of the laser travelling through the ice. Snells law is used to find the angle of refraction, θ_{r}, in the ice using the angle of incidence from the set-up, θ_{i}, the refractive index of gaseous medium in which the laser starts, n_{gas}, and that of the ice, n_{ice}. For most applications n_{gas} is the vapour pressure of ice at low temperatures which is negligible and can be equated to the refractive index in a vacuum. For constructive interference the difference between path length a above the ice and $2b$ through the ice is equal to $m\lambda$, the integer number, m, of wavelengths, λ, producing equation 1.5. Geometry relates the two paths to θ_{i} and θ_{r} producing equation 1.6 which can be rearranged to find the d_{ice} in equation 1.7. Therefore using a standard HeNe laser, $\lambda = 632.8\,\mathrm{nm}$ and setting n_{ice} to 1.3, approximately the refractive index of ice, varying $\theta_{\mathrm{i}} = 1 \rightarrow 50\,^{\circ}$ produces $d_{\mathrm{ice}} = 243.4 \rightarrow 378.7\,\mathrm{nm}$ at the first fringe.

$$m\lambda = 2\,b\,n_{\mathrm{ice}} - a\,n_{\mathrm{gas}} \tag{1.5}$$

$$= \frac{2\,n_{\mathrm{ice}}\,d_{\mathrm{ice}}}{\cos\theta_{\mathrm{r}}} - 2\,n_{\mathrm{gas}} d_{\mathrm{ice}} \tan\theta_{\mathrm{r}} \sin\theta_{\mathrm{i}} \tag{1.6}$$

$$d_{\mathrm{ice}} = \frac{m\lambda\,\cos\theta_{\mathrm{r}}}{2\,(n_{\mathrm{ice}} - n_{\mathrm{gas}}\cos\theta_{\mathrm{r}}\sin\theta_{\mathrm{i}})} \tag{1.7}$$

CHAPTER 2

Laser Spectroscopy using CRDS, LIF, and CELIF

2.1 Introduction

The invention of the laser has allowed spectroscopists to delve deeper than ever into the molecular realm over the past fifty years. A huge array of experimental techniques have been developed to use lasers for a variety of different objectives. Cavity ring-down spectroscopy (CRDS) is one such technique that, since its development in the 1980s, has established itself as powerful, flexible, sensitive and applicable to a huge number of molecular problems. Along with this laser induced fluorescence (LIF) is another simple and versatile technique with greater sensitivity than CRDS but is more difficult to apply. In our group LIF has been combined with CRDS to form a variation on both techniques named cavity enhanced laser induced fluorescence (CELIF). This new technique combines the advantages of both CRDS and LIF whilst accounting for some of their disadvantages. The further application and development of the CELIF technique accounts for the work reported in chapter 3 while in chapter 5 CRDS is used in experiments on ice. Future experiments on ice surfaces will use a combination of these techniques to monitor gaseous species above an ice film. Since CRDS, LIF and CELIF form the core analytical techniques used, this chapter will spend some time discussing them.

2.2 Direct Absorption Spectroscopy

CRDS is a technique which derives from spectroscopy at its most basic. A simple direct absorption experiment might occur in the following manner. A source of light of intensity, I_L, and wavelength, λ, is shone onto a detector, passing through a region of space containing an absorbing species. The light intensity will decrease and this will be related to the concentration of the absorber. If light is then varied over a range of wavelengths then an absorption spectrum can be recorded, characteristic of the molecular composition of the sample. By comparing this spectrum with a background, where the region is

devoid of the absorbing species, and knowing only a few experimental parameters, information on the composition is obtained. This is a direct absorption method, where I_L is related to the intensity after absorption in the sample, I, by the Beer-Lambert law.

$$I = I_L \exp(-\alpha s) \tag{2.1}$$

α (cm^{-1}) is the absorption coefficient and s* (cm) is the sample length across which absorption takes place. As light passes through the absorbing species it decays exponentially and thus a measurement of I, I_L, and s advantageously allows the acquisition of α directly. However since this set-up is a single-pass technique, where a target is probed only once, it suffers from low sensitivities as it measures a small attenuation in a large background signal.

There are a couple of methods which can be used to improve these issues. Firstly an indirect absorption technique may be used, many of which are highly sensitive such as LIF[110] or resonance enhanced multi-photon ionisation (REMPI).[111] In these methods α is not available directly and instead must be calculated back from a secondary process. For LIF this is the emission of fluorescence after the absorption of light by a species, and for REMPI, the formation and detection of ions. It is only after this secondary process that information can then be derived on the original absorption. However if the probe is a laser then another method can be used increasing sensitivity while retaining the advantages of a direct absorption process. Rather than a single pass experiment instead a multi-pass one can be designed by simply introducing mirrors into the direct absorption set-up. Although several multi-pass techniques using mirrors have been developed such as the Herriott cell[112] and White cell,[113] by far the most successful is CRDS.

2.3 Cavity Ring-Down Spectroscopy

CRDS was first implemented as a spectroscopic tool by O'Keefe and Deacon[114] in observing the vibrational overtones of oxygen in air. However the technique itself derives from a clever method for resolving problems characterising mirror reflectivities, developed by Herbelin *et al.*[115] in 1980, and Anderson *et al.*[116] in 1984. Fundamentally CRDS is an extremely simple set-up. A stable cavity (an optical resonator) is created between two identical, highly reflective mirrors, $R > 99.9\,\%$, separated by a distance, d, and with a radius of curvature, $\mathcal{R}_\mathrm{c} > d$. A pulsed laser is then directed axially between the mirrors. At the first mirror most of the light is reflected away, but a small portion, $1-R$, is coupled into the cavity. The mirrors are aligned such that this light is trapped, bouncing between the same spots on the mirrors in the cavity. Thus each reflection between the end mirrors allows a small portion of the trapped light, $1-R$, to leak out. Although this amount of

* Here we use s for the sample length and d for the cavity length. This is because in the CELIF analysis we use L for the cavity loss c.f. Berden[109]

light is small, if a suitably sensitive light detector, such as a photo multiplier tube (PMT) is positioned after the end mirror, an exponential decay of light is observed. In the analysis of light exiting a CRDS cavity it is not the intensity, rather the lifetime of the decay that is important; this is called the ring-down time (RDT). Any absorbing or scattering feature within the cavity will cause the RDT to decrease from its theoretical maximum, so an empty cavity may be compared to one with an absorber present and α obtained for that species. The empty cavity itself need not be a vacuum, but any atmosphere so long as a difference in RDTs can be detected between the absorber being present and not present. Figure 2.1 shows a basic CRDS setup with distance between the cavity mirrors of d.

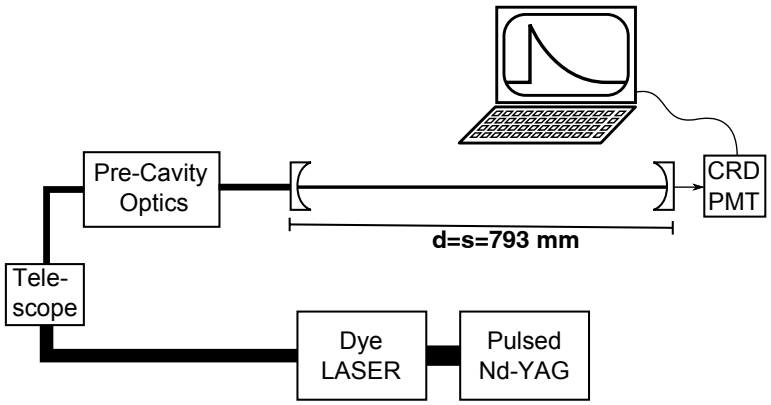

Figure 2.1: A typical pulsed CRDS experiment. A nanosecond laser pulse from a Nd:YAG pumped dye laser is directed into a cavity of length, d, confined by two highly reflective mirrors. A telescope is used to clean up the laser beam and pre-cavity optics including a mode-matching lens are positioned in front of the cavity. A PMT detector with appropriate data acquisition equipment resides behind the output of the rear mirror.

This set-up has many advantages over a single pass absorption technique. The multiple passes through the absorption region produce a long path length which dramatically increases sensitivity; for our cavity with at least $R > 99.99\,\%$, and $d = 0.793\,\mathrm{m}$, the minimum effective cavity path length is $7.9\,\mathrm{km}$ as derived from equation 2.8. In a single pass technique stability in the laser source is an issue as a comparison must be made of laser intensity before and after absorption through the sample. CRDS, however, is a time dependant technique with measurements based on only changes in the RDT. Therefore it is largely immune to shot-to-shot intensity fluctuations in the laser source.

Compared to indirect absorption techniques like LIF and REMPI it measures absorptions absolutely and has a general applicability to the gas, liquid and solid phases. In contrast LIF and REMPI require several different parameters, which are not straightforward to derive, in order to obtain absorptions and concentrations from their spectra. As well as this suitable routes to fluorescence emission and ion generation must be available in the target species for them to work in the first place. Both of these also generally require quite low pressure environments to function effectively where CRDS can be set-up for use over nearly any pressure range. The sensitivities of LIF and REMPI are greater than CRDS as

to a certain extent these measure their signal on a zero background. But overall CRDS has very good sensitivities, easily reaching parts per billion (ppb) and trillion (ppt)* detection limits.[109,117,118]

2.4 The Ring-Down Time and Absorption Coefficient

The RDT is the most important characteristic of CRDS as from the changes in this value absorption cross sections or concentrations are derived. The RDT is the time taken for light in the cavity to decay to $1/e$ of its initial value and is represented by τ. In order to derive a relationship for the variation of the τ with time the ring-down event needs to be looked at in more detail. Using the Beer-Lambert law, equation 2.1, produces the amount of light seen by the detector after the first pass through the cavity, I_0, by a laser pulse of intensity, I_L, with mirrors of transmission, T. Here the loss to absorption is calculated using the sample length, s, although often this is equal to the cavity length, d.

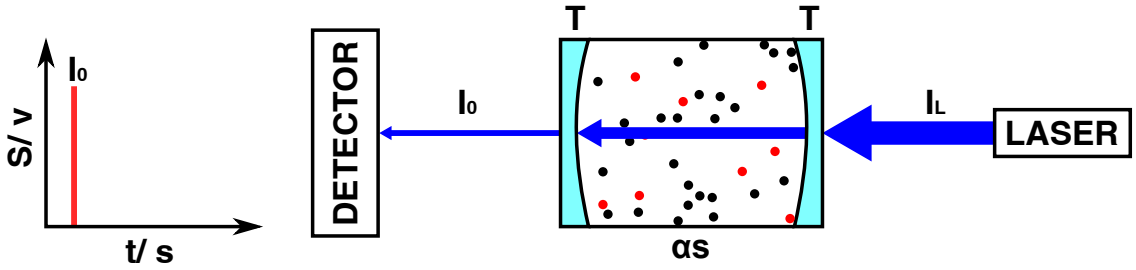

Figure 2.2: The light seen by the detector after the first pass through the cavity.

$$I_0 = I_L \cdot T^2 \exp(-\alpha s) \tag{2.2}$$

After I_0 is emitted, the remaining light inside the cavity is reflected back towards the first mirror and then returns emitting a smaller amount I_1. Now a full round trip in the cavity occurs, where mirror reflectivities, R, are needed. Substituting in for I_0, this is shown mathematically as,

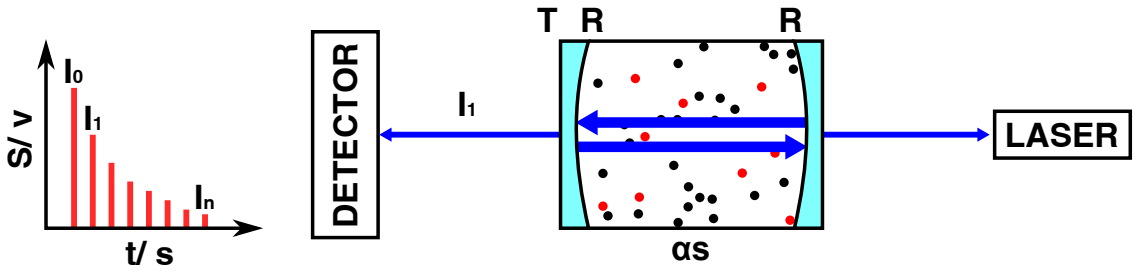

Figure 2.3: The light seen by the detector after the second pass through the cavity, I_1, depicted on the CRD setup and marked on the graph. The light seen is also shown for each subsequent pass, I_n, but on the graph alone.

* spectrometers for specific species are available off the shelf with ppt sensitivities

$$I_1 = I_L \cdot T \exp(-\alpha s) \cdot R^2 T \exp(-2\alpha s)$$
$$= I_0 \cdot R^2 \exp(-2\alpha s) \tag{2.3}$$

Thus each subsequent round trip after the first adds an extra term of $R^2 \exp(-2\alpha s)$, so after a number of round trips of the cavity light received at the detector is represented by,

$$I_n = I_0 \cdot R^{2n} \exp(-2n\alpha s) \tag{2.4}$$

n is the number of round trips and has a relationship, based on the distance travelled in the cavity, the speed of light, c ($\mathrm{cm\,s^{-1}}$), multiplied by the time over which light has been travelling, t (s), divided by its the cavity length, d (cm).*

$$n = \frac{ct}{2d} \tag{2.5}$$

Substitution of equation 2.5 into 2.4 and with knowledge that $R^{2n} = \exp(2n \ln R)$ produces equation 2.6. This leads to equation 2.7, which is the key one for CRDS, relating the time dependent light intensity, $I(t)$, at the detector, to the cavity and absorptions inside it using the approximation that $\ln R \approx R - 1$ which is true for mirrors of high reflectivity.

$$I(t) = I_0 \exp\left(\frac{ct(\ln R - \alpha s)}{d}\right) \tag{2.6}$$
$$= I_0 \exp\left(-\frac{ct(1 - R + \alpha s)}{d}\right) \tag{2.7}$$

From this equation we can derive the RDT, τ,

$$I(t) = I_0 \exp\left(\frac{-t}{\tau}\right), \ \tau = \frac{d}{c(1 - R + \alpha s)} \tag{2.8}$$

For a pulse width shorter than the round trip time of the cavity the ring-down signal is received at the detector as a series of peaks indicated in the figure 2.2 and 2.3 above. Depending on the response time of the detector and sampling of the ring-down event this may or may not be visible in the signal. For pulse widths on the order of the cavity round trip and longer, the ring-down traces become less like a discreet series of peaks. A real example of a ring-down trace, shown for our system, is shown in the next chapter

* Assuming that the absorption coefficient continues to be used in $\mathrm{cm^{-1}}$

in figure 3.4. τ can be obtained simply by using a fitting algorithm or by plotting the natural logarithms of the light intensity decay from which a linear relationship is formed where the gradient gives τ. Subsequently a comparison between the cavity filled with and without an absorbing species of interest allows the calculation of α,

$$\alpha = \left(\frac{1}{\tau'} - \frac{1}{\tau_0}\right)\frac{1}{c} \tag{2.9}$$

Without an absorber present this is called the background RDT represented by τ_0, and with it present, τ'. As previously noted often the sample length over which the light is absorbed in the cavity is equal to its length, $s = d$. However in some set-ups such as in the CRD of flames this does not the case.

By varying the wavelength of a measurement, an absorption spectrum can be taken characterising all loss processes in the cavity. In each case a new background measurement of τ_0 is required as R is wavelength dependent. α can be expanded for all absorbers, i, in terms of their wavelength dependant absorption cross-sections, $\sigma_i(\lambda)$ (cm^2) and the line integrated number density, or concentration, $\int_0^\infty N_i(x)dx$, with the number of particles, N_i over length, x, producing,

$$\alpha(\lambda) = \sum_i \sigma_i(\lambda) \int_0^\infty N_i(x)dx \tag{2.10}$$

Sometimes it can be convenient to provide the absorption spectrum not in terms of absorption but instead the so called photon loss per pass through the cavity. This as shown in the examples in the next chapter is simply a unitless value composed of the absorption multiplied by the length of the cavity.

$$\text{Photon Loss}(\lambda) = \alpha(\lambda) \cdot d \tag{2.11}$$

Accompanying molecular absorptions in the cavity there are usually other loss processes. Two key processes for this are Rayleigh and Mie scattering. Rayleigh scattering of light is an elastic process related to the electric polarisability of particles. It applies when the particles are smaller than the wavelength of the incident light and therefore almost always occurs to some degree, usually insignificantly, in a spectroscopic experiment. Light scatter by this method is discussed in further detail in section 2.10. Mie scattering derives from an electromagnetic treatment of Maxwell's equations, when the wavelength of light is similar in size to the target. It only comes into play under specific conditions such as when studying aerosols or measuring particulate sizes held in a dispersion using wavelengths near to their size. Although these additional losses are present when performing a CRD experiment very often when considering a narrow band laser pulse these losses are effectively negligible.

The sensitivity of a cavity can be characterised in terms of its minimum detectable absorption, $\alpha_{\min}$.

$$\left[\alpha(\nu)\frac{s}{d}\right]_{\min} = \frac{1-R}{d}\left(\frac{\Delta\tau}{\tau_0}\right) \tag{2.12}$$

$\alpha_{\min}$ is related to the minimum change in the RDT, $\Delta\tau/\tau_0$, that can be detected by the set-up. $\Delta\tau$ therefore is just the shot-to-shot noise generated by the experiment. From this it can be seen that one simple way to improve the sensitivity of CRDS is to reduce sources of noise in the experiment for example by improving the detector and reducing shot-to-shot fluctuations in the laser power. Alternatively one may increase the cavity length or the mirror reflectivities. Increasing mirror reflectivities however has the effect of lowering the amount of light entering into the cavity and thus the gain in the detector has to be able to cope with the drop in signal. It also changes a characteristic of the cavity called the finesse which impacts measurements in several ways. The coupling of light into the cavity is a key point in the CELIF method and therefore this is discussed further.[118,119]

2.5 Cavity Finesse and Mode Structure

The injection of light into a cavity is integral to the operation of CRDS and also the new CELIF technique and therefore warrants discussion. For the laser experiments described previously a pulse of light is used. When light is coupled into a cavity, the pulse can either be longer than the round trip time or shorter. This produces different results depending on the extent of the overlap the pulse has with itself while maintained inside the cavity. When the pulse overlaps interference occurs and only wavelengths that create a standing wave between the mirrors are able to remain across the ring down event. For our cavity the round trip time is $5.3\,\mathrm{ns}$, and a nanosecond dye laser is used typically producing pulse widths of $\sim 4 \rightarrow 6\,\mathrm{ns}$. Therefore only a small amount of light in the cavity will overlap.

The wavelengths, or frequencies, sustained inside the cavity from the interfering pulse are called the longitudinal modes (eigenmodes) of the cavity. In addition to longitudinal modes there are also different transverse modes. Each transverse mode has a different path around the cavity involving multiple reflections from the end mirrors. Therefore each has its own longitudinal structure and a different, shorter, τ. Each transverse mode is referred to as a $\mathrm{TEM_{q\,m\,n}}$ (transverse electromagnetic mode) and is characterised by three integers q, m and n. q is the longitudinal mode integer characterising the number of nodes in a standing wave supported by the cavity. Similarly m and n together describe the nodes in the transverse modes. Adjacent q with the same m and n, where $\Delta q = 1$, are separated by a frequency that is defined by the cavity called the free spectral range (FSR).

The longitudinal modes supported by the cavity start from the lowest supported frequency derived from the mirror separation, and are increase incrementally by the FSR. Therefore q is often dropped when referencing the mode structure and it is shortened to $\mathrm{TEM_{m\,n}}$. Typically CRDS looks to excite only the shortest, most axial path between the mirrors the mode, $\mathrm{TEM_{0\,0}}$ which ensures the best spatial resolution and optimum sensitivities. Only half or full numbers of wavelengths form standing waves in the cavity producing,

$$\mathrm{FSR} = \frac{c}{2d\,n} \tag{2.13}$$

The FSR is in Hz, and the other parameters are c ($\mathrm{cm\,s^{-1}}$), the speed of light, d (cm), the length of the cavity and the refractive index of the optical medium, n, which in most gas phase regimes is approximately 1.

Along with the FSR a second value describes the width of the modes supported by the cavity. This value is called the finesse, F, and is related to the reflectivity of the cavity mirrors. It is the ratio of the FSR to the full width half maximum (FWHM) of adjacent maxima. Essentially it characterises the degree to which constructive interference is maintained inside the cavity. Thus the reflectivity of the mirrors is related to its calculation as this effects the RDT and therefore the length of time over which interference occurs. For high reflectivities it can be approximated to produce the following relationship,

$$F = \frac{\mathrm{FSR}}{\mathrm{FWHM}} = \pi\frac{\sqrt{R}}{1-R} \tag{2.14}$$

An example of the $\mathrm{TEM_{00}}$ mode structure for our cavity is shown below in figure 2.4. For pulsed CRDS systems, which have a bandwidth larger than the FSR, many modes are covered spatially and the output of the end mirror represents all modes covered by the pulse width shown below in figure 2.4. For our cavity of length, $79.3\,\mathrm{cm}$ and mirror reflectivity of 99.99%, $\mathrm{FSR} = 6\cdot10^{-3}\,\mathrm{cm^{-1}}$ and $F = 31,414$, hence the calculated FWHM of the modes is $1.9\cdot10^{-7}\,\mathrm{cm^{-1}}$.

As previously stated the above mode structure applies to any cavity where there is significant overlap of the pulse inside it. For pulses shorter than the cavity this mode structure is not seen and as might be expected there is a range in between the two extremes as well. In figure 2.5, the transmittance of the cavity is shown at different frequencies where for a pulse of light much shorter than the cavity length no interference occurs and all the light frequencies are transmitted. However as pulses of light become longer overlap occurs and the mode structure is seen.[118–122]

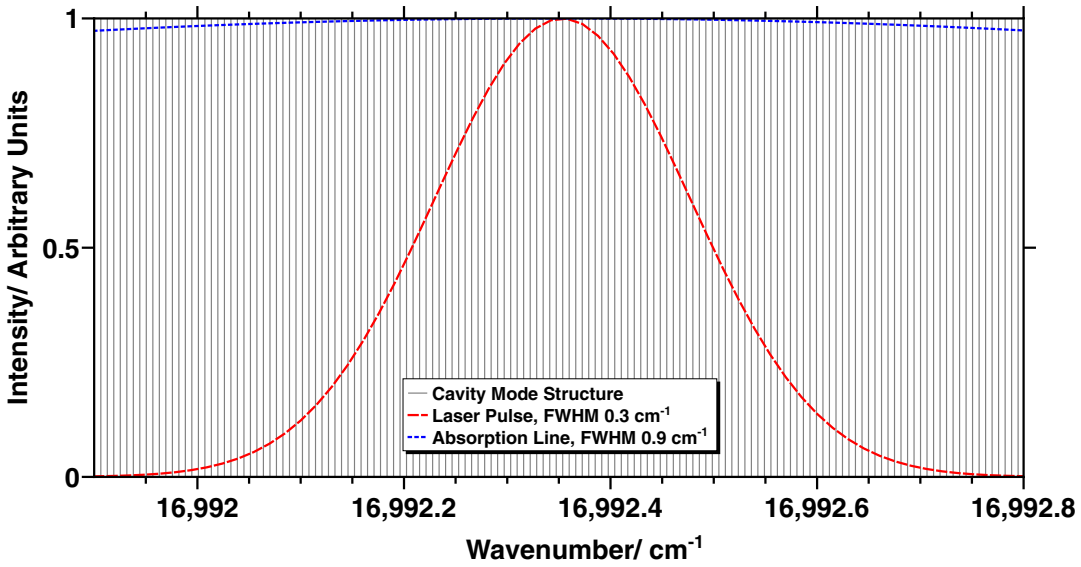

Figure 2.4: Figure shows the positions of TEM_{00} modes for our cavity of length, $79.3\,\mathrm{cm}$ and $R = 99.99\%$, showing how densely packed they are. A pulsed laser line at $588.5\,\mathrm{nm}$, as used in chapter 3, is shown with a bandwidth FWHM of $0.3\,\mathrm{cm}^{-1}$ similar to ours, smaller than a molecular absorption, with an arbitrary FWHM of $0.9\,\mathrm{cm}^{-1}$.

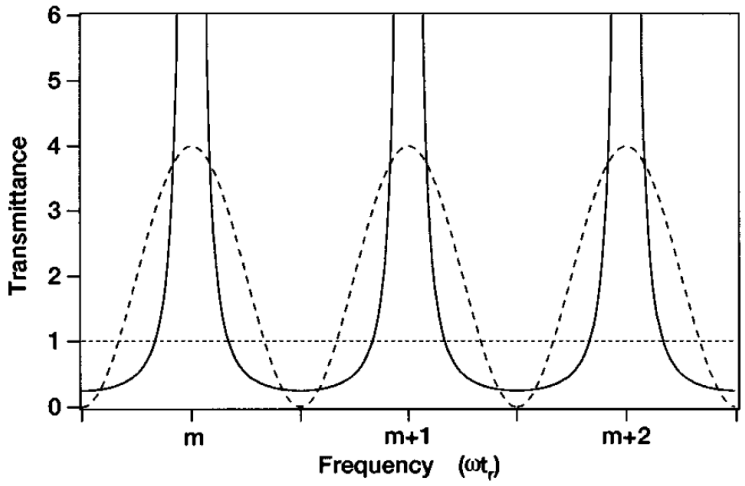

Figure 2.5: Figure of cavity transmittance varying with pulse length. The mode structure is calculated for a long pulse on the order of the RDT (solid), a medium pulse twice the length of the round trip time (dashed) and one shorter than the round trip time (dotted). Figure has been taken from Zalicki *et al.*[119]

2.6 Measuring Absorption Lines with CRDS

In order to take absorption spectra or monitor concentrations of species using a CRD set-up several different issues must be accounted for. The problems encountered will vary given the exact application of CRD used. Therefore those mentioned here assume the pulsed CRD experiment using a nanosecond dye laser as employed in this work. As previously mentioned the laser pulse length is $\sim 4 \rightarrow 6\,\mathrm{ns}$, on the order of the round trip time of our cavity, $5.3\,\mathrm{ns}$, so the cavity mode structure lies somewhere between the short

and medium pulse shown in figure 2.5. Any mode structure inside the cavity means an absorption feature needs to have a linewidth larger than the modes in the cavity as indicated in 2.4. Otherwise a narrow absorption could fall between the modes and be missed altogether, however in our cavity this is unlikely an issue.

Secondly if the cavity is not aligned properly a multi-mode excitation is obtained, where several transverse modes are excited with the TEM_{00} mode. This causes oscillations in the RDT signal, termed mode beating, to appear on a ring-down trace. These reduce accuracies in the measurements from the different competing RDTs of the modes causing instabilities in the exponential and a poor fit. A good CRD alignment can take care of some multi-mode excitation but not all as some modes can still be excited by a poor beam quality which unfortunately often affects dye lasers. To cope with this, two actions may be performed first to filter the beam and second to align it better to the TEM_{00} mode. Spatial filtering can be used to optimise a Gaussian beam shape before the cavity and inside the cavity to restrict the beam inside to the TEM_{00}. Alternatively in front of the cavity a mode-matching lens may be used to shape the beam to the curvature and radius of the mirrors.

Another problem that can be encountered occurs if the probe laser has a bandwidth that is larger than that of the molecular absorption line being probed. Again a multi-exponential decay is seen in the RDT. For some CRDS experiments, such as broadband CRDS this problem is inherent, but for narrower band CRD experiments these features are a problem. If a laser with a large bandwidth is probing one or multiple absorptions then the different exponentials, from the pure cavity and any other absorption feature covered by the spectral range, become combined as shown in figure 2.6.[120]

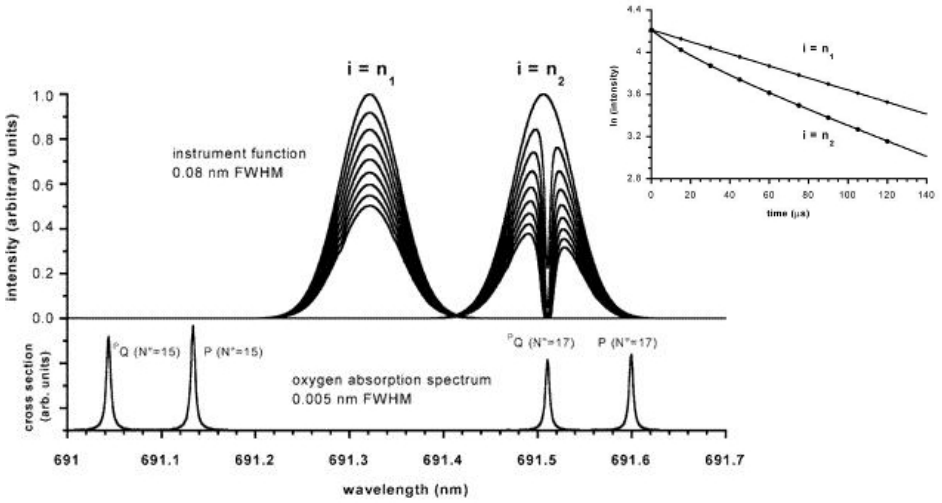

Figure 2.6: Multi-exponentials in a simulated 10% oxygen absorption spectrum at atmospheric pressure are shown. n_1 shows a single exponential for a pure cavity, laser pulse with a bandwidth of $0.08\,\mathrm{nm}$ FWHM, and no absorption feature present. n_2 shows a multi-exponential where an absorption feature is present. Inset are the natural logarithms over time of each decay, where non-linearity is observed in n_2. Figure taken from Ball *et al.*[123]

For a laser of bandwidth equal to or lower than an absorption line saturation can be observed if molecules cannot relax quickly within the lifetime of the ring-down. When this occurs molecules located within the probe region become excited before the lifetime of the ring-down trace has expired and decreased absorption intensities are obtained.* Solutions to saturation caused by this involve reducing the bandwidth of the laser or reducing the time over which the measurement is observed, though in CRDS these are not always straightforward to implement. Saturation may also occur purely from a strong absorption alone. However this is difficult to achieve in pulsed systems and is mainly found in the continuous wave variant of CRDS, since molecules can be continuously pumped to dark excited states.[109,118,122]

2.7 Spatial Profiling of the Cavity Beam

In our application of CRDS, it will be passed above an ice surface to monitor the gas dynamics above it. Zhao *et al.*[124] have shown that extending CRDS to surface studies causes it to suffer from additional sensitivity losses due to the presence of the surface. To date, their paper remains the only literature source investigating these losses with respect to CRDS. The losses themselves have been shown to not be caused only by the geometrical obstruction from the surface, but also from diffraction processes as the beam passes over it. Therefore as the beam path becomes nearer to the surface, the RDT lowers faster than the rate expected from a purely geometrical obstruction alone.

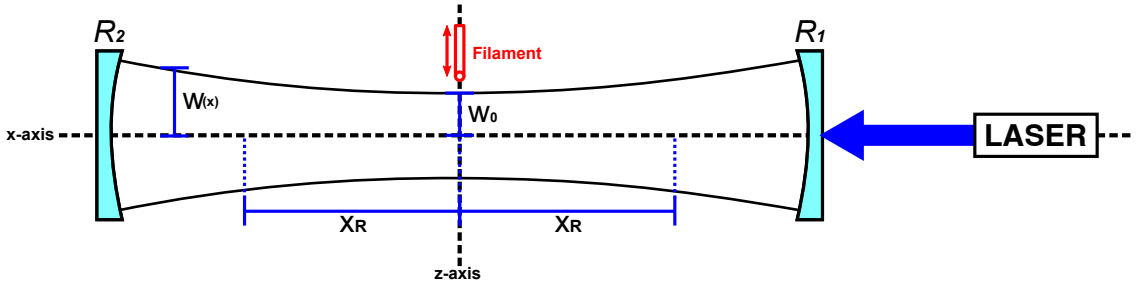

Figure 2.7: Depiction of a Gaussian beam inside a symmetric cavity with an obstructing surface, a filament, put into the path of the beam. For further details of the parameters see the text. Note that $\mathcal{R}_{1,2}$ here refers to the curvature not the reflectivity of the mirrors.

To understand this effect, knowledge of the spatial profile of the beam inside the cavity is required. As previously stated, the optical cavity used for a standard CRD set-up is a symmetric cavity with mirrors of curvature greater than the distance between them. A Gaussian beam is assumed with all light coupling onto the TEM_{00} mode. Under these conditions the beam can be described spatially through defining two parameters, the beam waist, w_0, and the wavefront curvature at a point along the beam. Distance along the cavity axis is defined with x, where $x = 0$ lies at the centre between the mirrors.

* This is not always a problem. Lamb dip spectroscopy actively looks to saturate as a method of detecting the centre of transitions very accurately.

Vertical distance from cavity axis is defined by z, where $z=0$ lies on the x-axis.*

w_0 (m) occurs in a Gaussian beam at its focus, after it has passed through a lens or, as in this case, at the centre of a stable optical resonator. It is the radius at which light intensity has dropped to $1/e^2$ of its maximum and presents the minimum radius of the beam from the cavity axis. It is depicted in figure 2.7 and calculated by,

$$w_0 = \sqrt{\left(\frac{\lambda \cdot X_{\mathrm{R}}}{\pi \cdot n}\right)} \tag{2.15}$$

$$X_R = \sqrt{\left(\frac{g_1 g_2 (1 - g_1 g_2)}{(g_1 + g_2 - 2 g_1 g_2)^2}\right)} \cdot d \tag{2.16}$$

$$g_{1,2} = 1 - \frac{d}{\mathcal{R}_{1,2}} \tag{2.17}$$

It has dependencies on the wavelength of the incident light, λ, the refractive index of the optical medium, n, and on X_{R} (m) the Rayleigh range. The Rayleigh range is a measure of the depth of focus of the beam along the x-axis as shown in the figure 2.7. X_{R} is dependent on the mirror set-up, based on d and the optical stability parameters for each mirror, $g_{1,2}$, where each index represents a different mirror and $\mathcal{R}_{1,2}$ (m) is the radius of curvature for each mirror. Following on from this a general expression for the beam waist at any point along the cavity can be formed. The characteristic beam shape along our cavity is depicted in the final chapter in figure 5.2a.[118,125]

$$w(x) = w_0 \sqrt{\left[1 + \left(\frac{x}{X_{\mathrm{R}}}\right)^2\right]} \tag{2.18}$$

2.8 CRDS with Surfaces

Zhao *et al.* used CRDS in a chemical vapour deposition to measure concentrations of gas phase species above diamond films formed using either a hot-filament reactor or a plasma-activated reactor. Although both methods were used to demonstrate near-surface effects the hot-filament method will be looked at in more detail alone. The filament was inserted into the path of the ring-down beam, as indicated in figure 2.7, measuring its effect on the RDT. It can essentially be modelled as infinitely thin along the x-axis and infinitely long in the orthogonal plane. As the filament was inserted a reduction in τ was observed and measured as a function of distance from the cavity axis, z. The reduction effect was calculated for an obstruction based on the geometry of their filament

* Note that in some texts, such as Silvfast,[125] the terminology is reversed with the z-axis as the cavity beam and the x-axis as the vertical distance from it. Therefore here the Rayleigh range Z_{R} is called X_R.

alone,

$$\alpha_c = \frac{1}{2}\left[1 - \mathrm{erf}\left(\frac{\sqrt{2}z}{w_0}\right)\right] \tag{2.19}$$

α_c is the additional loss calculated which can be used in equation 2.8 to calculate the expected overall RDTs for a particular CRD set-up. It was found that the observed reductions in τ were underestimated using a purely geometric description of the obstruction. In order to simulate the data observed diffraction effects needed to be incorporated into the model. The results found are shown in figure 2.8. They show that compared to the geometrical clipping, diffraction effects nearly double the distance at which τ drops to zero. Therefore passing close to a surface will both lower the sensitivity of CRDS and limit the range at which it can operate.

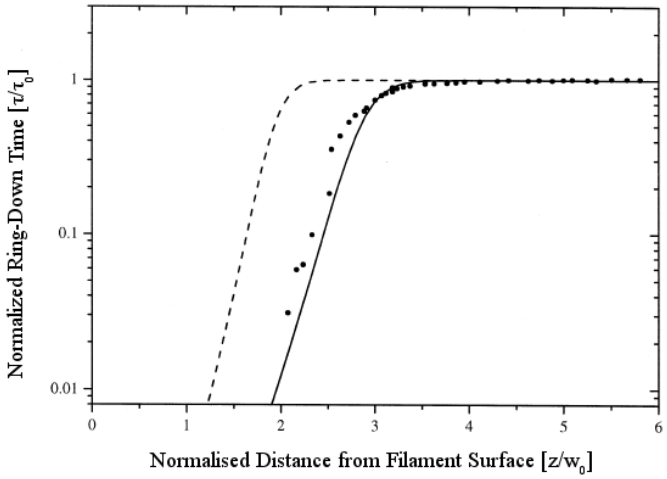

Figure 2.8: Measured ring down reductions of a filament moved towards a CRD beam. τ is normalised against τ_0 and the distance to the filament has been normalised against the w_0 of $0.431\,\mathrm{mm}$. The solid line is the model including diffraction effects, the dotted line is the for the geometrically clipped effect alone. Figure taken from Zhao *et al.*[124]

In this project CRDS is passed over an ice surface that is much larger than the filament studied by Zhao. Therefore diffraction effects are likely to be larger still. This effect leaves two options for a CRD set-up running near to a surface. The first option is to run an experiment with the laser far enough away from the surface for zero or acceptable losses. Otherwise the only other option is for the beam waist to be made smaller, by reducing the operating wavelength or Rayleigh range of the mirrors. Using the data of Zhao *et al.* the minimum beam distance can be predicted based on their results and minimum loss conditions. For our experiment, the mirrors have a curvature of $1\,\mathrm{m}$ producing a beam waist of $0.3\,\mathrm{mm}$ at $588.5\,\mathrm{nm}$, in a cavity of length, $79.3\,\mathrm{cm}$. Using the work of Zhao *et al.* they predict for a minimum absorption loss of 10% using mirrors of reflectivity 99.99%, the beam must be at least $3w_0$ above the surface. This however excludes the size difference between our surface and the filament which will likely make this distance even

greater.[124]

2.9 Indirect Absorption Spectroscopy

CRDS is a direct absorption method. However many laser spectroscopic techniques exist which are indirect. An indirect method relies first upon the absorption of radiation and then some subsequent change or emission in the molecule which is then recorded. A variety of these indirect techniques exist ranging from REMPI of molecules to create ions which can be recorded by ion time-of-flight, and photo-acoustic spectroscopy where heat and pressure changes create sound waves which have an amplitude that can be related to the absorption. However one of the most used techniques is LIF which involves recording the light emission in a molecular sample after using a laser to promote electronic transitions within it. The main advantage of these techniques over direct absorption ones is that low background signals offer extremely high sensitivities. For those which measure emission, so long as a single photon is detected above the background, a signal can be recorded. However accompanying this advantage is the disadvantage that by relying on a secondary process analysis is far more complicated with greater uncertainties.

When light interacts with a molecule two different events may occur depending on the nature of the interaction, absorption or scattering. In an absorption process the incident photon causes a transition to an excited energy level in the molecule. Following this the molecule may then either re-emit the energy or redistribute it internally followed by either radiation at a different wavelength or not at all. It is upon this process that LIF is based. In a scattering process the electric field of the incident radiation interacts with the particle but is not absorbed by it; whereas an absorption process requires the existence of a resonant energy level in the molecule a scattering process does not. Thus it is able to occur at any frequency. It occurs elastically though Rayleigh or Mie scattering, or inelastically through Raman scattering. The newly developed CELIF mechanism uses CRD combined with LIF spectroscopy and it was investigated using both Rayleigh scattering in nitrogen and fluorescence in acetone in order to characterise it. Therefore these two processes are discussed in further detail.

2.10 Rayleigh Scattering

Rayleigh scattering refers to the elastic scattering of light by particles whose sizes are much smaller than the wavelength of the incident radiation. John Strutt (also called Lord Rayleigh) first observed this phenomenon and wrote several papers about it for Philosophical Magazine.[126,127] He used the classical theory of electromagnetic fields to derive quantitative expressions for calculating scattering cross-sections. The key process behind scattering involves light interacting with the electrons of the atoms, molecules and small particles involved. When a wave of light is in range of a particle, within its scattering cross-section, σ (cm^2), its electromagnetic field can interact with it. It causes the electron cloud of the particle to interact resonantly with it, oscillating with the frequency of the

incident light, displacing electrons in the particle from equilibrium. Classically this electron motion will then radiate the wave scattering it. In a non-polar molecule, which has a zero electric dipole moment, this causes an induced dipole moment to be created and scattering to occur. Rayleigh scattering is thus related to the electronic polarisability of a particle. This is the ability of the electron cloud to distort, equal to the ratio of the dipole moment to the electric field.

In a standard experiment observing Rayleigh scattering from gas molecules, a laser at a single wavelength is directed through a probe volume and light collected from an angle off the laser axis. The scattered signal collected at the detector is not just composed of light at the incident wavelength but also includes inelastic scattering. Unless filtered, the complete signal combines three elements, the Rayleigh line (sometimes referred to as the Cabannes line[128]), and rotational and vibrational Raman side peaks. The largest component is the Rayleigh line which is the main elastically scattered peak. In reality it is quasi-elastic as the peak is widened by doppler and pressure broadening. Raman scattering occurs when the internal energy of the molecule changes during the scattering process. Changes in the rotational and vibrational levels of the molecule are then reflected by an inelastic scattering process. The next largest component is rotational Raman scattering, side peaks where energy in the scattered light changes based on the separation of rotational levels in the molecule. These often fall within the range of the Rayleigh line and it is hard, but not impossible, to separate them out. Accounting for only $0.1\,\%$ of the detected signal vibrational Raman peaks occur further out from the rotational Raman and Rayleigh lines. They are formed similarly to rotational Raman peaks but between vibrational states. In Raman scattering energy can be both lost (Stokes) and gained (Anti-Stokes) based on the separation of the energy levels and thus emission is found both above and below the Rayleigh line.[128]

To date there have been several approaches to solving the problem of light scattering by small particles including both a quantum mechanical treatment[129] and a more generalised Mie theory. The latter of these was a theory formulated by several people, with the credit usually given to Gustav Mie. In his seminal paper of 1908[130] he extended the work of Rayleigh, solving the simplest model for scattering of a plane, monochromatic, electromagnetic wave by a homogenous sphere of any composition in a homogenous medium. Mie theory is long and complicated and yields expressions that are often not insightful and necessitating a computer for calculation. It is also often misquoted as only applying to scattering where the incident wavelength is equal to or smaller than the particle size. This is not the case as it is applicable to any particle which can be characterised by the ratio of its circumference with the incident wavelength, λ. This is called the size parameter, X.

$$X = \frac{\pi D}{\lambda} \tag{2.20}$$

where, D is the diameter of the particle. Scattering properties derived from the Mie solutions are divided into three regimes, $X \gg 1$, $X \approx 1$ and $X \ll 1$. The first of these $X \gg 1$ is known as the geometric scattering regime relating to large particles where the scattering is dominated by optics of reflection, refraction and diffraction; important examples of this in the atmosphere are water droplets. $X \approx 1$ is the Mie scattering regime which finds application in the scattering of UV-visible light by aerosols and measuring particle sizes in liquid dispersions. Finally when $X \ll 1$ the Mie solutions for scattered radiance reduce to a proportionality with $1/\lambda^4$ a result first obtained by Rayleigh 37 years earlier analysing the problem geometrically. For a spherical particle, smaller than the wavelength of the incident light, in the electric dipole approximation the scattering cross-section, σ_{R} is,

$$\sigma_{\mathrm{R}} = \frac{32\pi^3}{3\lambda^4 N^2} \left(n(\lambda) - 1\right)^2 \tag{2.21}$$

$$= \frac{24\pi^3}{\lambda^4 N^2} \left(\frac{n(\lambda)^2 - 1}{n(\lambda)^2 + 2}\right)^2 \cdot F_{\mathrm{k}}(\lambda) \tag{2.22}$$

It has dependencies on λ, the refractive index of the medium, n, and the molecular density, N ($\mathrm{molecules\,m^{-3}}$). Equation 2.21 is the original approximation which was derived by Rayleigh.[127] Equation 2.22 is an improved approximation which contains an additional local field correcting factor, $(3/(n^2+2))$, which largely holds true for gases, and the dimensionless King correction factor, $F_{\mathrm{k}}(\lambda)$. The local field correction occurs because the localised field acting near a molecule is not necessarily the same as the macroscopic field. The King factor corrects the Rayleigh equation for non-spherical particles. For exactness it must be added as this can significantly effect a measurement.

Nitrogen Rayleigh scattering is used to calibrate fluorescence quantum yields for acetone and test the CELIF method in chapter 3. Naus *et al.* demonstrated the effect of non-sphericalness in particles measuring Rayleigh cross-sections for several gases including nitrogen using CRDS.[131–133] It was found that inclusion of the corrective factors allowed σ_{R} to be measured and predicted correctly within $1\,\%$. The net result is that σ_{R} in gases of non-spherical molecules does not precisely follow a $1/\lambda^4$ relationship because the corrective factors themselves are dependent on λ. Therefore a mathematical function to predict scattering cross sections over specified wavelength ranges was formulated using work by Teillet,[134]

$$\sigma_{\mathrm{R}} = \frac{\sigma}{\lambda^{4+\epsilon}} \tag{2.23}$$

where ϵ is a dimensionless parameter and the dimension of σ depends upon it. The parameters of this equation for Rayleigh scattering in nitrogen are shown in table 2.1. For further information the reader is referred to the cited references.[1,128,135,136]

Table 2.1: Table of collected Rayleigh cross section parameters for use with equation 2.23 from Sneep[132] and Ityaksov[133]

Wavelength Range (nm)	σ **(** $/10^{-47}$**)**	ϵ
$197.70 \rightarrow 270.15$	18.0 ± 0.6	0.534 ± 0.003
$400 \rightarrow 1000$	18.83 ± 0.09	0.0817 ± 0.005

2.10.1 Anisotropy of Rayleigh Scattering

Rayleigh scattering described in the previous section, using polarised light on a non-polar spherical particle, is not an isotropic process. Scattering is rapid and instantaneous,[128] taking place on a timescale faster than a molecule can rotate. The following description is discussed relative to figure 2.9. In this figure laser light is directed along the x-axis and interacts with a particle at the origin. Signal detection occurs along the z-axis. A scattering plane is defined by the axis of incident light and the detection axis which in this figure is the zx-plane. The probability of scattering occurring in a particular direction is highest in the plane perpendicular to the electric field of the incident photon and thus the induced dipole moment of the particle. In this way interacting particles behave like dipole antennas. Therefore scattering is not isotropic when polarised light is used and a spatial pattern is observed. Scattered intensity follows a function of $\sin^2\phi$, where ϕ is the angle between the dipole axis, essentially the electric field vector of the incident light, and the scattering direction. Thus this has maximum intensity in the plane perpendicular to the dipole axis, at $90\,^\circ$, and zero intensity along it at the poles.

A depiction of the $\sin^2\phi$ function for light polarised p and s relative to the scattering zx-plane is displayed in figure 2.9a and b. Light polarised perpendicular (s) to the scattering plane has maximum intensity on the detector while light polarised parallel (p) has zero intensity. Using p-polarised light the induced dipole axis is coincident with the z-axis and the maximum would be seen in the xy-plane. For unpolarised light the scattering intensity is the addition of the s and p polarisations, $\sin^2\phi_\mathrm{p}+\sin^2\phi_\mathrm{s}$. Following a trigonometric proof this can be related to a single measurement of the observation angle, θ, about the origin of the scattering plane producing a phase function, $\Pi(\theta)$, which is rotationally symmetric about the incident light direction. The normalised phase function for unpolarised light is,

$$\Pi(\theta) = \frac{3}{4}(1+\cos^2\theta) \tag{2.24}$$

Where the intensity of linearly p-polarised light is $\propto 1$ and s-polarised light is $\propto \cos^2\theta$. This is depicted in figure 2.9c.

For polarised light this anisotropy can be useful under laboratory conditions to minimise or maximise Rayleigh scattering by choosing the correct polarisation with respect

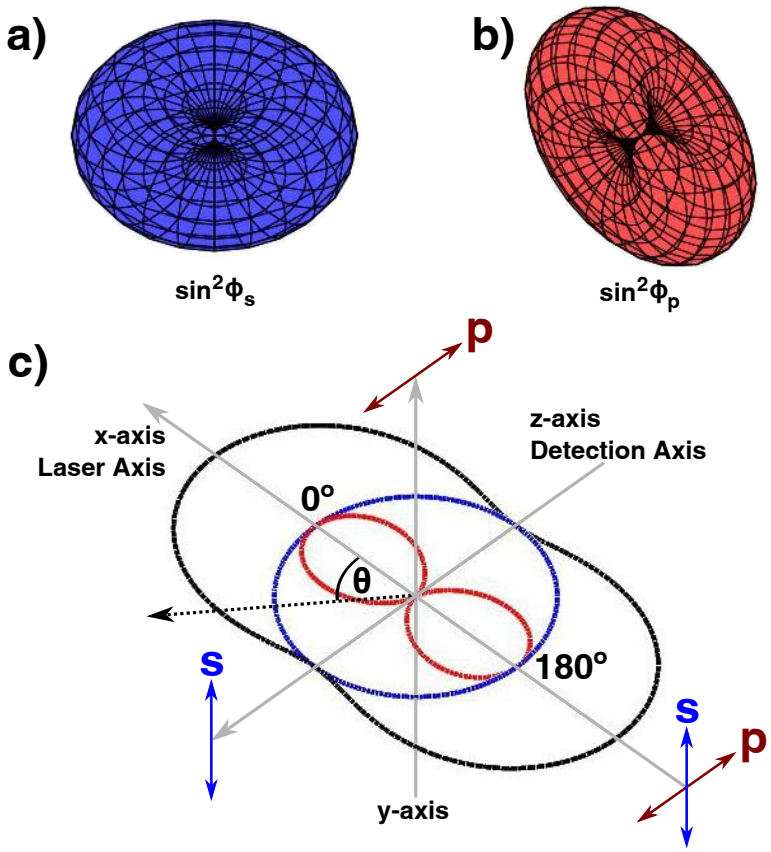

Figure 2.9: In each plot a spherical scattering particle is assumed to be at the origin and all plots have the same axes as displayed in *c)*.
a) shows the 3D surface on which light scatters when interacting with light s-polarised and *b)* p-polarised to the scattering zx-plane.
c) The particle phase function, $\Pi(\theta)$ is displayed for Rayleigh scattering of unpolarised light. Light enters along the x-axis and detection of scattered light occurs along the z-axis. The particle phase function is shown in the xz-plane for the two scattering extremes. $\Pi_s(\theta) \propto 1$ (blue line) and $\Pi_p \propto \cos^2(\theta)$ (red line). Also shown is $\Pi_s + \Pi_p$ (black line) which occurs for unpolarised light.

to the detection plane. Therefore by aligning the laser p-polarised with respect to the zx-plane, Rayleigh scattering in the detected signal can be minimised, or maximised with s-polarisation. Sometimes it can be important to have equal intensity contributions from both vertically and horizontally scattered light. In this case equation 2.24 is set to zero and solved for $\theta = 54.7\,^\circ$; this is known as the magic angle and has uses across several different scientific fields.[1,135,136]

2.11 Laser Induced Fluorescence

LIF was first developed by Zare in 1967[137,138] soon after the development of the first lasers. It has quickly grown due to its simple implementation producing extreme sensitivities and ability to work in harsh operating conditions such as flames. As with the other indirect absorption techniques, being essentially background-less, signal-to-noise ratios in the signal are excellent and single photon detections are possible; using this

method even single molecules have been detected with it. Concentrations and cross-sections can be calculated from LIF measurements but a disadvantage is that absolute measurements depend on a good calibration or using geometric and LIF efficiency parameters which can sometimes have large uncertainties on them.

Similar to Rayleigh scattering a typical LIF experiment involves passing light through a molecular sample and recording any emission from it at a detector. However in contrast the incident light is not scattered. Light, impinging upon a molecule, is absorbed by it, promoting the molecule into a higher electronic state. After excitation the absorbed energy may undergo several different processes before de-excitation of the molecule releases the absorbed energy via emission processes and light of varying wavelengths is received at the detector. Traditionally the example used for fluorescence emission is one with singlet ground state, S_0, singlet excited, $S_{1,2...n}$ and triplet $T_{1,2...n}$ states. A Jablonski diagram for the different radiative and non-radiative pathways in such a molecule is shown in figure 2.10. A molecule occupying a ro-vibrational level in the ground singlet state can absorb light to move to a ro-vibrational level in an excited singlet state, so long as the energy difference between the two levels, ΔE_{laser}, matches the energy of the incident laser. Once in an excited state the molecule can non-radiatively relax trickling down through the ro-vibrational levels, releasing the energy into kinetic modes via collisions with other molecules. This is called vibrational relaxation (VR) and it occurs on a $10^{-14}\,\text{s}$ timescale.

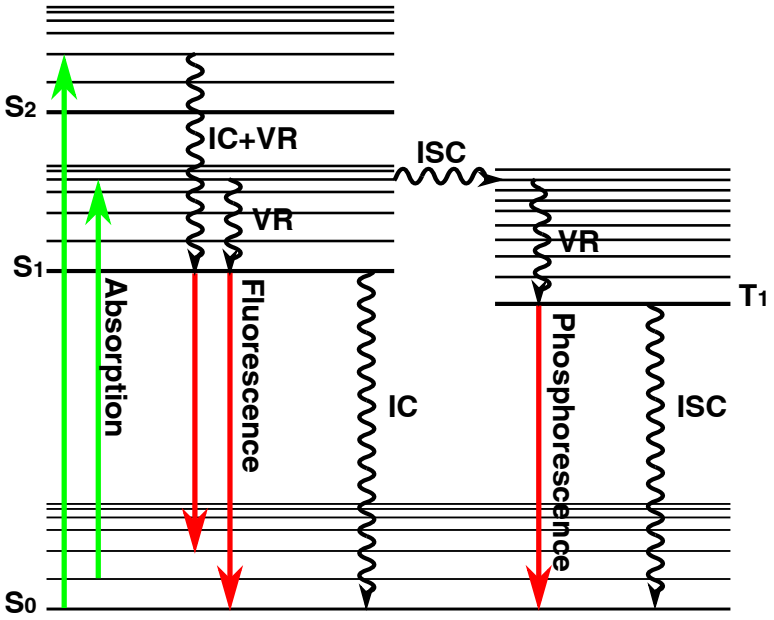

Figure 2.10: Jablonski energy level diagram outlining the traditional fluorescence and phosphorescence pathways. Thick lines represent an electronic energy level and thinner ones a vibrational levels. For clarity rotational levels are not shown. Each process is discussed further in the text.

During VR, a transition to a lower electronic state may occur either through a non-radiative process, internal conversion (IC), or a radiative one, fluorescence. During IC

energy exchange occurs again through collisions but a strong overlap between vibrational levels in the two electronic states, $S_2 \rightarrow S_1$, $S_1 \rightarrow S_0$ or $T_2 \rightarrow T_1$, permits a non-radiative transfer to the lower state. This is a longer process than vibrational relaxation occurring on a $10^{-12} \rightarrow 10^{-7}$ s timescale. During fluorescence, emission occurs releasing a photon with wavelength equal to the energy of the transition occurring. The Franck-Condon principle states that because nuclei in the molecule are stationary relative to the movement of electrons the probability of a transition is dependent upon the strength of the overlap between the wavefunctions describing the two states. Therefore a characteristic spectrum of light is seen during emission depending on the overlap between the upper and lower states in the transition and the excitation wavelength(s) initiating the process. Emission is relatively fast and proceeds on a timescale of 10^{-9} s. In comparison to vibrational relaxation however fluorescence is slow and it can often be assumed that relaxation to the lowest ro-vibrational levels in the excited state has occurred before fluorescence is emitted. Although typically shown for singlet states fluorescence occurs whenever spin multiplicity is conserved during the transition. Therefore it could occur in triplet states as well such as $T_2 \rightarrow T_1$ in the above example.

When spin multiplicity is not conserved it is a significantly slower emission process and thus given a different name, phosphorescence. This happens when triplet states, $T_{1,2...n}$, are accessed through a process of intersystem crossing (ISC) from an excited singlet state again resulting from overlap between the wavefunctions of the two states. Following crossing into a triplet state it may vibrationally relax and then radiatively emit while crossing back to the singlet ground state. Singlet to triplet state transitions are spin forbidden and the process of ISC and the radiative emission involves changing the spin of an electron. Therefore the process of phosphorescence is much slower occurring on the $10^{-7} \rightarrow 10^{-5}$ scale, but can take up to hours depending on the molecules and pathways involved. As well as this, competing at the same time, ISC can allow a non-radiative transition back to the ground state. A final non-radiative process can occur which competes with both fluorescence and phosphorescence called quenching. This is a collisional process whereby the contact and subsequent energy exchange with another molecule, often unexcited, causes a return to the ground state without emission. In the case where that molecule is of the same type as the excited molecule this is termed self-quenching.[139]

Each of the processes outlined above, when measured and characterised, are usually described by a rate constant, k, with a subscript relating to the process being observed i.e. for fluorescence, k_{f}, or phosphorescence, k_{p}. Mostly rate constants are first order (s^{-1}) but depending on the exact process being described it can have a higher order. The rate constant in a first order process can be related to the lifetime, τ, of the process occurring $k = \tau^{-1}$. This is the time take for the population of the excited state to decay to $1/e$ of its initial population via the process it describes. Furthermore to characterise the efficiency of a fluorescence process the wavelength dependent quantum yield of fluo-

rescence, $\Gamma(\lambda)$,* is used. Conceptually simple, this is just the ratio of photons emitted, N_{emi}, to the photons absorbed, N_{abs}, by a molecule. In this way a particular LIF scheme can be characterised in terms of the processes producing fluorescence competing against those which do not, non-radiative processes, phosphorescence, collisional quenching and dissociation/pre-dissociation.

$$\Gamma(\lambda) = \frac{N_{\mathrm{emi}}}{N_{\mathrm{abs}}} \tag{2.25}$$

As displayed by Rayleigh scattering, fluorescence and phosphorescence are also fundamentally anisotropic processes when excited by polarised light; since electronic transitions are involved the photons must interact with the electron cloud along the correct axis and therefore they are polarisation sensitive. However whether this is observed or not is entirely dependent upon the speed of the emission process relative to the rate of rotation in the molecule being probed. If a molecule has time to rotate before emission occurs then photons are emitted randomly in all directions, isotropy is observed and the photons become depolarised. Since molecular rotation generally occurs on a picosecond scale, isotropy and depolarisation are observed in many fluorescent and most phosphorescent processes.

Acetone has been used by our group as a test gas in advancing the methodology of the CELIF technique. Moreover in atmospheric chemistry it is a trace gas that has been shown to have significant uptake rates to ice surfaces and thus represents a potential trial molecule for early ice experiments with the peltier based set-up.[50] Therefore the case of fluorescence in acetone is discussed further.

2.11.1 Photoemission Processes in Gas Phase Acetone

Research into the absorption of UV light and subsequent photolysis of acetone and the closely related molecule biacetyl ($[CH_3CO]_2$) was started as early as 1913 by Henri and Wurmser[140]. This was followed up later by Damon and Daniels[141] in 1933 who recorded some of the earliest evidence of green acetone fluorescence. Today acetone (CH_3COCH_3, di-methyl ketone or 2-propanone) is a well characterised molecule in part due to its widespread use as a tracer molecule in planar LIF (PLIF). PLIF is used to image species concentrations in flow fields and jets in a plane using acetone, along with 3-pentanone ($CH_3CH_2COCH_2CH_3$). For this purpose acetone brings obvious benefits. It is low in toxicity with a high vapour pressure therefore easy to handle, whilst also being readily and cheaply available, even in a high purity form, for immediate and consistent use in high or low concentrations in an experiment.[142] Acetone represents a relatively typical example molecule for the emission processes involved with LIF. A depiction of these in a standard Jablonski diagram is shown for acetone in figure 2.11.

* It is usually represented by Φ in many texts, Γ is used here to avoid confusion with parameters in the CELIF method

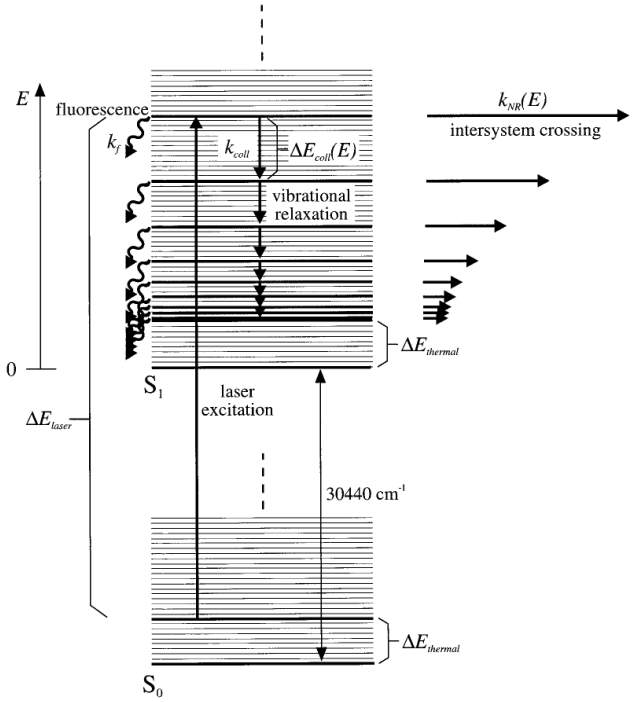

Figure 2.11: Jablonski energy level diagram outlining the fluorescence and phosphorescence pathways of acetone. Further information is available in the text. Figure obtained from Thurber *et al.*[143]

Excitation of acetone from its ground singlet state to first excited state, $S_0 \rightarrow S_1$, occurs in the wavelength region $\sim 225 \rightarrow 328.5\,\mathrm{nm}$. This is a symmetry forbidden, perpendicular transition from the n orbital of the oxygen to the π^* orbital of the carbonyl group. After excitation photoemission occurs from $S_1(I^1A_u)$, or, through intersystem crossing, the excited triplet state $T_1(I^3A_u)$ back to $S_0(A_g)$. As such acetone demonstrates the classic mechanistic example of a photoemission spectrum. Each electronic state has a rich vibrational structure and excitation at energies of $30440\,\mathrm{cm}^{-1}$ ($328.5\,\mathrm{nm}$) or higher allow access to the S_1 state. Fluorescence occurs as a broad emission at lower energies than the excitation energy from relaxing through the S_1 vibrational manifold. Alternatively the extensive system of vibrational levels allows a facile intersystem crossing to the triplet state, whereupon phosphorescence may occur.

The mechanism for photoemission in acetone is depicted in figure 2.11. $\Delta E_{\mathrm{thermal}}$ shows the amount of thermal energy above the ground vibrational state the molecule resides in. After excitation by a photon with $\lambda \leq 328.5\,\mathrm{nm}$ the molecule resides in some vibrational level in the S_1 state equal to the sum of thermal energy, $\Delta E_{\mathrm{thermal}}$, and laser energy, $\Delta E_{\mathrm{laser}}$. Once in the excited state fluorescence may occur at a rate, k_f, and collisional relaxation at a rate, $k_{\mathrm{coll}}(T, P)$, dependent on temperature and pressure. Alternatively intersystem crossing to T_1 may occur at rate, $k_{\mathrm{NR}}{}^*$, followed by relaxation and phosphorescence.

* NR = Non Radiative

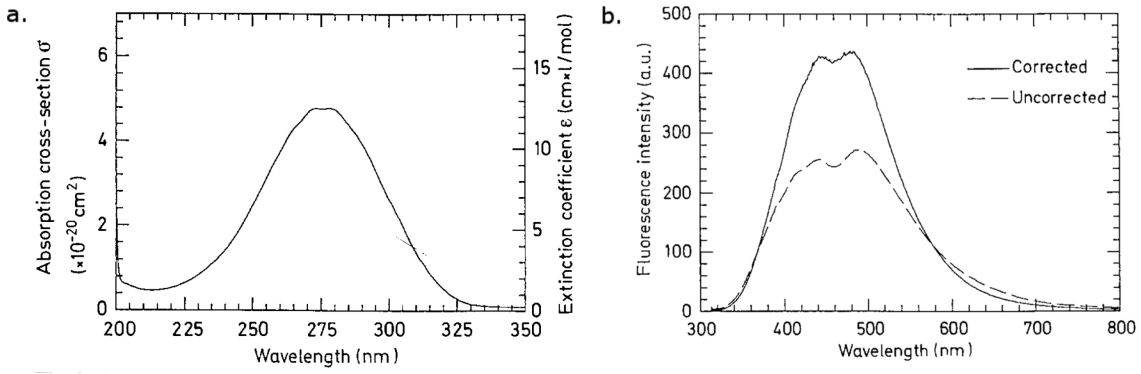

Figure 2.12: *a)* Absorption spectrum of acetone taken using a Perkin-Elmer Lambda 9 Spectrophotometer. *b)* Fluorescence spectrum of acetone, seeded in a planar jet of air and excited at $308\,\mathrm{nm}$. This was measured with a prism spectrograph and is shown corrected for the spectral response of the detector (solid) and uncorrected (dashed). Figures taken from Lozano *et al.*[144]

Acetone has a weak and broad absorption band in the range $\sim 225 \rightarrow 328.5\,\mathrm{nm}$, producing fluorescence in the band $\sim 350 \rightarrow 550\,\mathrm{nm}$ shown in figure 2.12. These two features lend themselves well to easily constructed set-ups using high energy, pulsed UV dye lasers and low noise detectors without a need for amplification. After excitation the majority of the molecules cross to the triplet state, with nearly $\sim 100\%$ efficiency, and any left in the singlet state fluoresce before or after a period of collisional quenching. Fluorescence lifetimes have been measured by Breuer,[145] Halpern[146] and Blitz.[147] Breuer and Lee analysed acetone at pressures, $P_{\mathrm{ace}} = 26.7\,\mathrm{mbar}$, measuring nanosecond fluorescence lifetimes, $\tau_{\mathrm{f}} = 2.7 \pm 0.3\,\mathrm{ns}$ at $313\,\mathrm{nm}$, dropping to $1.7 \pm 0.3\,\mathrm{ns}$ at $280\,\mathrm{nm}$. Data from Halpern showed a measurement at $313\,\mathrm{nm}$ of $2.4\,\mathrm{ns}$. Echoing this data Blitz *et al.* derived lifetimes from Stern-Volmer plots of $\sim 2\,\mathrm{ns}$. The shorten9ing fluorescence lifetime at shorter wavelengths is significant due to the increasing probability of a competing photodissociative process, $CH_3COCH_3 + h\nu \longrightarrow CH_3CO + CH_3$, which operates through the triplet state. A wavelength threshold relating to the T_1 state for this process is reported at $305.8\,\mathrm{nm}$ so at longer wavelengths the rate of dissociation is very small.[147]

Phosphorescence in comparison to fluorescence has been studied far less. However, as previously stated nearly $100\,\%$ of the molecules cross into the triplet state after excitation. Following crossing into the triplet state phosphorescence in acetone is met with non-radiative processes from a variety of quenching mechanisms. It is susceptible to both self-quenching with un-excited acetone and with other excited triplet states. In this latter process two acetone molecules collide and one non-radiatively decays to the ground singlet state and the other is excited into higher triplet levels. Since acetone is often measured in air another known effective quenching molecule is oxygen. It has such a strong quenching effect on the acetone triplet state that while measured in air virtually no phosphorescence signal is received. Thus the lifetime for phosphorescence is very much dependent on the conditions it is measured in. Groh *et al.*[148] measured phosphorescence from acetone vapour in a collisionless environment measuring lifetimes of $\sim 200\,\mu\mathrm{s}$. In

comparison Hu[149] measured lifetimes at $308\,\mathrm{nm}$ of a few microseconds in ambient pressure streams of nitrogen and tens of nanoseconds in ambient air. Charogiannis[150] agreed with the nitrogen data finding that acetone phosphorescence decayed with a lifetime of $920\,\mathrm{ns}$ in nitrogen.

2.12 Combination LIF-CRDS Techniques

A new technique is presented in chapter 3 combining LIF and CRDS into a single beam experiment where LIF emissions are monitored at the centre of a CRDS cavity. By doing this CRDS can calibrate the LIF signal allowing absolute measurements to be made for concentrations and cross-sections removing one of the disadvantages of LIF. This is however not the first time that CRDS and LIF have been combined in an experiment. Previous work with combinations have mainly derived from spectroscopy in flames,[151–155] but it has also been applied to pulsed molecular beam studies[156] and in the detection of aerosols.[157] To date no group has specifically set out to identify the advantages and disadvantages of a single beam experiment combining LIF and CRD.

The idea of using a CRDS measurement to calibrate LIF is not new. But it has only been used in measurements which were not taken simultaneously or used different lasers for each technique. In flame measurements CRDS is used to determine total column densities of the species being observed. This is then used to calibrate the LIF measurement avoiding the need to calculate geometric and sensitivity factors derived from the LIF detection system. In two cases, Richman *et al.* and Tokaryk *et al.* use LIF and CRDS quite similarly in a single beam experiment as in the CELIF method where the CRD signal is used to normalise the LIF signal but this idea was not progressed any further to look at the advantages or disadvantages this gives over using CRD or LIF individually.

2.12.1 LIF-CRDS in Flames

LIF and CRDS have mainly been used together in the spectroscopy of flames. The general method has a circular burner placed at the centre of a CRD cavity or LIF cell. By monitoring a choice fluorescent species, either native to the flame being analysed or a seeded tracer molecule, such as acetone, characteristics of the flame can be extracted. One such native fluorescent species is OH, which has importance in flames as a chemical intermediate with large populations and long lifetimes. It has strong radiative transitions in the $A^2\Sigma^+ \leftarrow X^2\Pi$ band hence LIF is a suitable method to analyse it. Spaanjaars *et al.*[151] used a combination of LIF and CRD to measure laser-induced predissociative fluorescence (LIPF) to obtain relative predissociation rates of OH ($A^2\Sigma^3$, $v' = 3$). By monitoring short-lived, $< 100\,\mathrm{ps}$, predissociative states, problems with collisional quenching were avoided allowing the determination of 2D temperature distributions in the flame. They ran a pulsed dye laser through a beam splitter to produce a high and low intensity beam. The high intensity beam was then used to run LIF, and the low intensity one CRDS crossing centrally, at an angle to each other, over a burner plate. So although both

the CRD and the LIF experiments ran simultaneously they were not directly combined into a single beam set-up; one beam was used for a fluorescence measurement while the CRD beam was used for an independent absorption measurement of different molecules over a different section of the burner plate. After normalisation of the fluorescence signal against the laser power, comparison with the absorption signal yielded quantum yields which were then used to calculate the predissociation lifetimes.

Dreyer *et al.*,[152] Luque *et al.*,[153] and Lamoureux *et al.*[155] all used a similar set-up to Spaanjaars on a range of chemical species, OH, CH, NCN. Mostly they made measurements for CRDS and LIF independently rather than simultaneously but with a few variations in the experiment. In each case during a LIF measurement, CRD mirrors were either removed or replaced by transparent windows with little or no attempt to study and analyse LIF born from the centre of the CRD set-up. Dreyer *et al.* also observed OH in atmospheric pressure methane-air flames and used CRDS to calibrate their LIF measurements. For this they used a premixed methane-air flame which had a near unity quantum yield. Similarly, in section 3.2 it is demonstrated that CELIF is capable of obtaining quantum yields in a single beam experiment using near unity quantum yields of Rayleigh scattering for the calibration.

Luque *et al.* independently measured LIF and CRDS and combinations thereof for monitoring CH radical concentrations. CH radicals have a direct relationship with NO concentrations produced in hydrocarbon flames and performing measurements at low pressures is useful for testing flame models. They used LIF derived from two CH bands, $A^2\Delta \leftarrow X^2\Pi$ excited at $430\,\mathrm{nm}$ and $B^2\Sigma \leftarrow X^2\Pi$ at $390\,\mathrm{nm}$, in low pressure ($53\,\mathrm{mbar}$) flames of propane/air. Two combination experiments are described, firstly by monitoring LIF fluorescence along the cavity (as in CELIF) in a CRD experiment they were able to spatially profile the cavity alignment with respect to the flame and optimise it accordingly. Secondly they used a sequential LIF-CRD technique to make quantitative, spatially resolved, measurements of the inhomogeneous CH concentrations in the flames. They calibrated standard single pass LIF data taken sequentially after CRD measurements as a function of height above the burner. Importantly the focus was mainly on the sequential LIF-CRD as the technique for obtaining absolute values, where CRD provided the sensitive method of absorption with which to calibrate spatially resolved LIF data. Lamoureux *et al.* also looked at CH as well as NCN radicals and NO species. CH and NCN radicals were measured using combination LIF-CRDS in the aforementioned scheme where the LIF signal was calibrated using a separate CRD measurement. Finally Bahrini *et al.*[154] made use of combination LIF-CRDS to take spectra of CaBr and CaI radicals. Unfortunately less information is provided on the specifics of their set-up but the indication is that it was within the premises described above. There is, however, no discussion of a single beam technique.

2.12.2 LIF-CRDS in Molecular Beams and Aerosols

Tokaryk *et al.*[156] used CRD and LIF similarly to the CELIF method but did not take the investigation of the results into much depth. They were attempting to locate a hitherto undetected $B^2\Sigma^+ \leftarrow X^2\Sigma^+$ transition in CaCCH in order to complete the detection of its theoretically predicted three lowest lying states. They formed CaCCH using laser ablation on a calcium rod passing a molecular beam of methane and helium through the resulting cloud of Ca ions. On this beam, LIF was used to optimise the laser alignment before the CRD cavity was built. After optimisation CRDS was then run with no real expectation to see much LIF signal, if any, from the centre of the CRD cavity due to such weak laser intensities involved. Surprisingly however they found the time integrated LIF signal across the ring-down time was comparable to the original LIF result.

2.13 CELIF Spectroscopy of BPEB

The combination of LIF and CRDS as CELIF, where fluorescence born from the centre of a ring-down cavity is recorded, has first been used in the spectroscopy of 1,4,bis-(phenylethynyl)benzene (BPEB, Ph−C≡C−Ph−C≡C−Ph) in our group by Sanders *et al.*[158,159] The scientific motivation behind BPEB is its potential role as a molecular wire in electronic devices. BPEB structurally consists of three benzene rings linked by acetylene groups in the para position on a central benzene ring. There are two structural conformations for the molecule of which the lowest energy structure exists with the entire molecule in a planar arrangement. A second higher energy, unstable, conformation exists with the central ring twisted perpendicularly with respect to the two end phenyl groups. In the planar case a delocalised π-electron system across the entire molecule is created perfect for the transmission of electrons across its length. Thus BPEB is seen to be a prototypical backbone molecule for use as a molecular wire. To this end electron withdrawing and donating substituents can be positioned on its opposite ends to mimic the effects of an electrical circuit. Also modification to the backbone using structurally enhancing or diminishing groups along the molecule's length allows BPEB to be fine tuned for specific applications.

In the twisted conformation the π-electron system is localised to each phenyl group, destroying the extended π system and thus killing the method of electron transmission. The barrier to rotation between the planar and twisted conformations is very low, $\sim 230\,\mathrm{cm}^{-1}$,[160] thus structurally enhancing groups can be used to increase the size of this barrier. This has two useful effects, first inhibiting rotation improves the ability of the molecule to be used as a wire as a low barrier means that performance can be inhibited by the twisted conformation. Secondly by increasing the barrier a more selective process can be initiated to switch the molecule off pushing the utility of the molecule from wires to switches. It is this torsional twisting motion that was under investigation which led to creation of CELIF.[158–160]

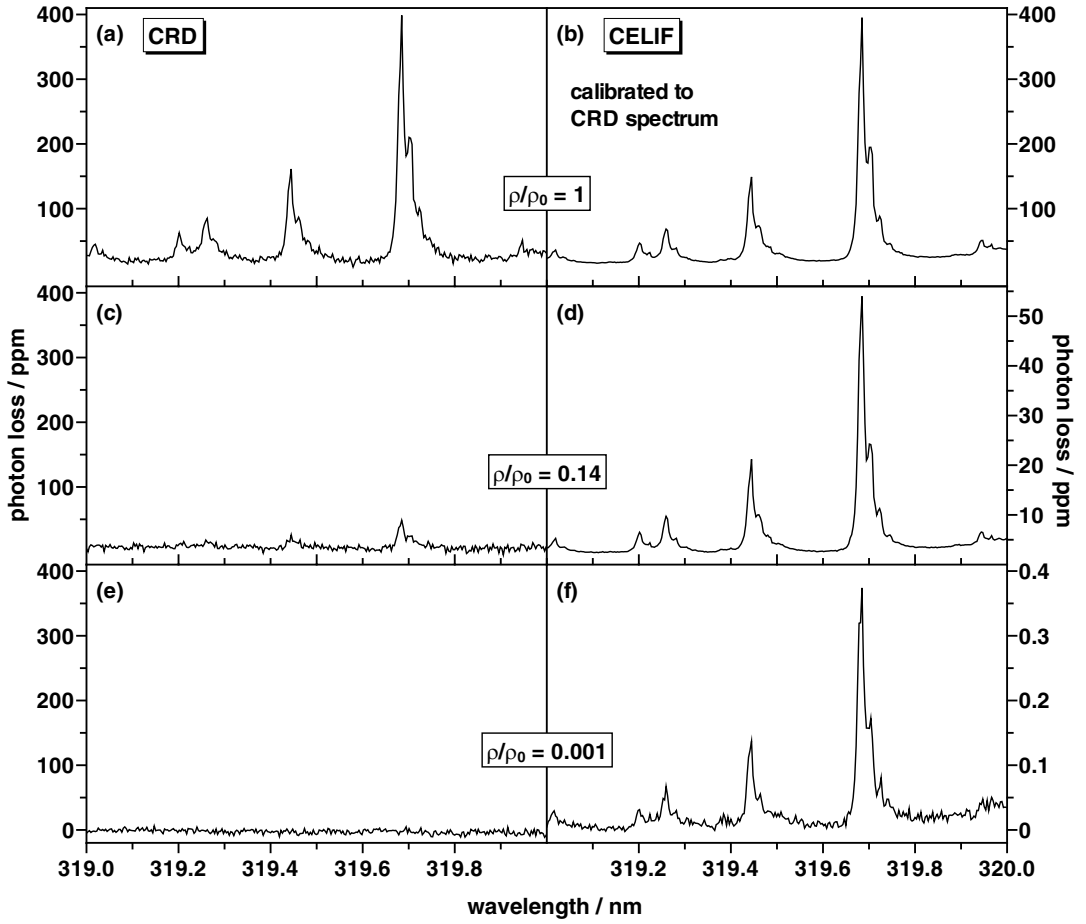

Figure 2.13: Comparison of data recorded simultaneously with CELIF and CRD monitoring BPEB. Jet-cooled BPEB is seeded into a molecular beam using an oven to vapourise it. It is seeded at different concentrations, ρ, labelled relatively here in terms of the maximum concentration, ρ_0 , hence ρ/ρ_0. Spectra (d) and (f) are calibrated with respect to (b) which is calibrated by the CRD spectrum (a).[159]

BPEB and substituted relatives of it are solid at room temperature with a negligible vapour pressure. Heating is therefore required to promote vapourisation. BPEB is heated in an oven and seeded into a molecular beam of argon positioned at the centre of a CRD cavity. The molecular beam is pulsed through the CRDS beam and where its the width intersects with the CRD axis is the probed sample. Scans were being taken around $320\,\mathrm{nm}$ and initially CRDS was the primary spectroscopic technique to analyse the BPEB. However difficulty was encountered finding signal and for this reason a LIF set-up was introduced in order to locate the best alignment of the CRD set-up much as Luque *et al.*[153] had done. During the course of the experiment it was then found that by monitoring LIF born from the centre of the CRD cavity during a ring-down event significantly higher signal-to-noise Ratios (SNR) were produced.

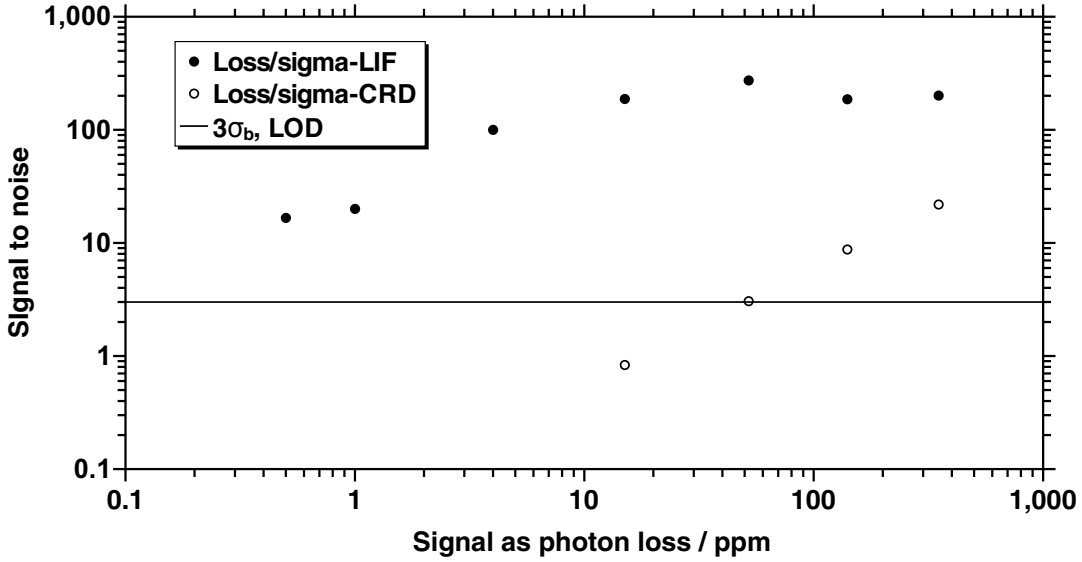

Figure 2.14: Limits of detection (LODs) for CELIF and CRD are shown from data presented in figure 2.13. LODs are extracted from transients at $319.69\,\mathrm{nm}$ where the signal-to-noise ratio is made from the signal divided by the standard deviation of the baseline noise, σ_b. The usually quoted LOD of $3\sigma_b$ is shown indicated on the figure.[159]

Examples of the spectra taken are shown in figure 2.13 in terms of the relative concentrations of BPEB seeded in the molecular beam where the advantage of CELIF used in this experiment over CRD is displayed. Figure 2.14 shows this advantage in terms of limits of detection (LOD) and indicates how starkly CELIF outperforms CRD at low concentrations. However at high BPEB concentrations (i.e. high relative photon loss), the SNR is dominated by the shot-to-shot fluctuations in the molecular beam, hence the CRD and CELIF LODs become similar. Although this is not shown here, CELIF has also been compared to straight LIF of BPEB. It was shown to have a much better SNR, although less significantly than in its comparison to CRD. The fluorescence lifetime of BPEB is significantly shorter than the pulse length of the probe laser, which makes high SNR single-pass LIF measurements impossible. The data altogether showed that CELIF extended the dynamic range of CRD by three orders of magnitude covering about six altogether. With such profound results further investigation was pursued to develop the CELIF technique and investigate it on a more fundamental level.

CHAPTER 3

Advancing the Methodology of Cavity Enhanced Laser Induced Fluorescence

A novel technique which combines the advantages of LIF and CRDS whilst compensating for some disadvantages of each has recently been developed in the groups of Wrede and Nahler. It was first implemented with great success in the spectroscopy of wire-like molecules[158] outlined in the previous chapter. This new technique, dubbed cavity enhanced laser induced fluorescence (CELIF), was demonstrated to produce high SNRs relative to the standard LIF and pulsed CRD counterparts used in the same experiment. Previous literature in the area indicates that CELIF is the first implementation of LIF where the signal is normalised using a simultaneous CRD measurement in a single beam experiment. CELIF, which includes a standard CRD measurement as part of its operation, was first used on BPEB seeded in a molecular beam and allowed absolute absorption and fluorescence measurements to be made covering six orders of magnitude. With such interesting results further investigation into the fundamental methodology of the technique was pursued and it was applied to other problems outside of the first set-up in which it was implemented.

3.1 Signal Analysis in CELIF

In a CELIF measurement the ring-down and fluorescence signal are recorded simultaneously so that in order to calibrate the fluorescence measurement the relationship between signal received at the LIF detector, S^{LIF}, needs to be related to that at the CRD detector, I^{CRD}. The standard CELIF set-up is shown in figure 3.1.

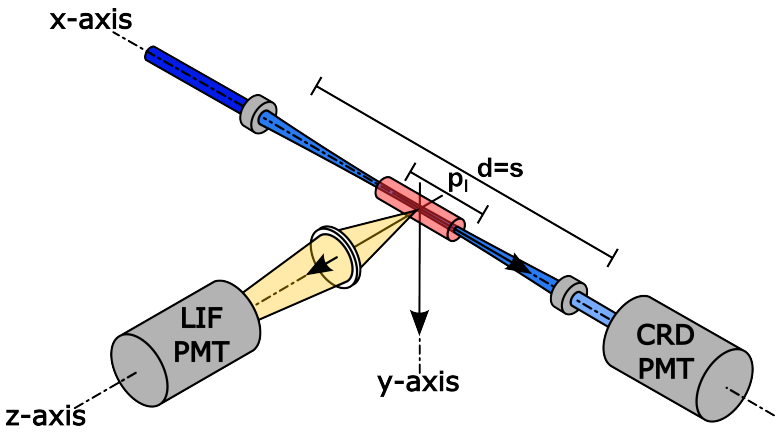

Figure 3.1: A schematic diagram of the CELIF experimental set-up. Light enters a cavity, enclosed by high reflective mirrors, along the x-axis from left to right and the ring-down trace from the cell of length, d, is detected at the CRD PMT. Fluorescence is generated along the sample length, s, where in this experiment $s = d$. LIF collection optics are situated on the z-axis and probe a set volume of light of length, p_l, from the centre; this is the LIF probe volume.

Assuming there are no saturation effects occurring the time integrated LIF signal should be proportional to the light intensity interacting within the probe region.

$$S^{\mathrm{LIF}} = I^{\mathrm{LIF}} \cdot \alpha(\lambda) \cdot \Gamma(\lambda) \cdot g \tag{3.1}$$

where I^{LIF} is the light intensity interacting with the sample (in the LIF probe volume) and α is the absorption coefficient, Γ is the quantum yield of fluorescence. g is composed of several factors which includes the geometry of the fluorescence collection optics, and the quantum efficiency and gain of the detector. The geometry of the collection optics is important as only a certain portion of light formed is collected and received by the detector. Both α and Γ depend on the fluorescence wavelength including, in theory, g. A wavelength dependence in g needs consideration as the wavelength dependence in the quantum yield of the detector means that if the fluorescence spectrum changes depending on the state excited then the detector will record a different amount of LIF signal. This can be accounted for by dispersing the fluorescence which allows the quantum yield of the detector to be taken into account and the LIF signal corrected.

For continued analysis knowledge of the I^{LIF} is required. A symmetrical sample of length, s, positioned at the centre of the CRD cavity is assumed as depicted in figure 3.1. It should be noted for all experiments pursued in this study that $s = d$, the full length of the cavity.* Light initially passes through the first cavity mirror and at the centre we

* As opposed to Sanders[158] where $s \neq d$ since the sample length is the intersection of the laser with molecular beam

find,

$$I_0^{\mathrm{LIF}} = I_{\mathrm{L}} T \left(1 - \frac{\mathcal{L}}{2}\right) \tag{3.2}$$

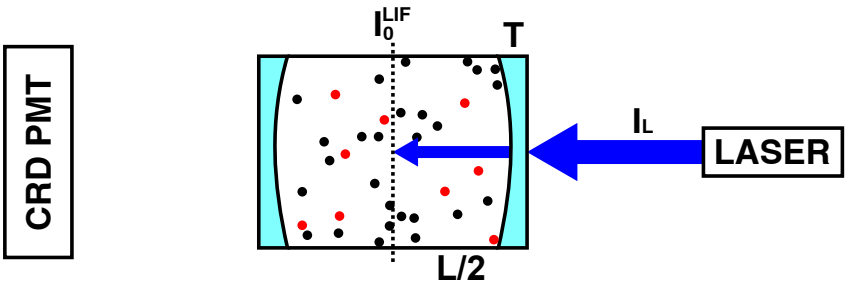

Figure 3.2: The light available for LIF at the centre along the CRD cavity during the first pass.

where I_{L} is the light intensity incident to the cavity entrance and T is the transmission through the first mirror. There is significance in using T originating from the light passing through the mirror substrate and coating. As a result, an assumption of $T = 1 - R$ is not necessarily valid from additional absorption losses caused by passing through the mirror. It is assumed that all light can be resonantly coupled into the cavity (see section 2.5) and it does not act as a spectral filter therefore these equations do not account for it. We define the fractional absorption per pass, $\mathcal{L} = \sigma \rho s$ dependent on the absorption cross-section, σ, the number density, ρ, and s. At the end of each single pass in the cavity light bounces back from the mirrors with reflectivity, R. After i passes through the cavity light intensity at the centre, I_i^{LIF}, is,

$$I_i^{\mathrm{LIF}} = I_0^{\mathrm{LIF}} [(1 - \mathcal{L})\, R]^i \tag{3.3}$$

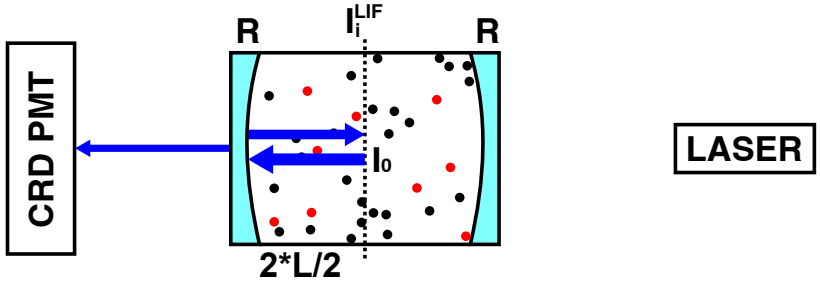

Figure 3.3: Subsequent passes through the centre after a reflection from either of the mirrors can be represented by equation 3.3.

Therefore the total light integral passing through the centre is represented by the sum of all parts. This can be simplified using the summation rule for a geometric series*

* The sum of a geometric series of n terms $S_n = a + ar + ar^2 + ... + ar^{n-1}$ simplifies to $S_n = a\frac{(1-r^n)}{(1-r)}$ and when $n \to \infty$, $S_n = \frac{a}{(1-r)}$

producing,

$$
\begin{aligned}
I_n^{\mathrm{LIF}} &= I_0^{\mathrm{LIF}} \sum_{i=0}^{n} [(1-\mathcal{L})\,R]^i \\
&= I_0^{\mathrm{LIF}} \frac{1-[(1-\mathcal{L})R]^{n+1}}{1-(1-\mathcal{L})R} \\
\lim_{n\to\infty} I_n^{\mathrm{LIF}} &= \frac{I_0^{\mathrm{LIF}}}{1-(1-\mathcal{L})R} \qquad (3.4)
\end{aligned}
$$

In the same manner we may derive the relationship for the time integrated light intensity, I^{CRD}, collected at the CRD detector. The major differences are in the second factor of T from passing through the rear mirror, and that after the first pass through the cavity light is only collected at the CRD detector every two passes. Additionally during the first pass light must travel fully through the sample in order to reach the detector.

$$
\begin{aligned}
I_0^{\mathrm{CRD}} &= I_{\mathrm{L}} T^2\,(1-\mathcal{L}) \qquad (3.5) \\
I_n^{\mathrm{CRD}} &= I_0^{\mathrm{CRD}} \sum_{j=0}^{n/2} [(1-\mathcal{L})\,R]^{2j} \\
&= I_0^{\mathrm{CRD}} \frac{1-[(1-\mathcal{L})^2R^2]^{n+1}}{1-(1-\mathcal{L})R} \\
\lim_{n\to\infty} I_n^{\mathrm{CRD}} &= \frac{I_0^{\mathrm{CRD}}}{1-(1-\mathcal{L})^2R^2} \qquad (3.6)
\end{aligned}
$$

By substituting equation 3.2 into 3.4, and 3.5 into 3.6, and then rearranging for I_{L} we obtain a relationship between the intensities at the LIF and CRD detector.

$$
I^{\mathrm{LIF}} = I^{\mathrm{CRD}} \frac{[1+(1-\mathcal{L})R]\left(1-\frac{\mathcal{L}}{2}\right)}{T(1-\mathcal{L})}
$$

In the limit of low loss, $\mathcal{L} << 1$, and for high reflectivity mirrors, $R \approx 1$ this condenses further producing the simple relationship,

$$
I^{\mathrm{LIF}} \approx I_{\mathrm{CRD}} \left(\frac{1+R}{T}\right) \approx I_{\mathrm{CRD}} \left(\frac{2}{T}\right) \qquad (3.7)
$$

The error in this approximation holds well even under harsh operating conditions, where mirror reflectivities are poor and absorptions are large shown in greater detail table 3.1. Even in the most unreasonable CRD conditions, with mirrors of $R = 0.9$ and huge losses of $\mathcal{L} = 0.1$, the error in the approximation is still only 5%.

We define the CELIF signal, S^{CELIF} (unitless), in terms of the time integrated LIF signal

Table 3.1: Example errors in CELIF approximation used in equation 3.7 for given cavity path losses and mirror reflectivities.

R	Error/ %				
	$\mathcal{L} = 1 \cdot 10^{-5}$	$\mathcal{L} = 1 \cdot 10^{-4}$	$\mathcal{L} = 1 \cdot 10^{-3}$	$\mathcal{L} = 1 \cdot 10^{-2}$	$\mathcal{L} = 1 \cdot 10^{-1}$
0.99999	0.0005	0.0005	0.0005	-0.002	-0.28
0.9999	0.0050	0.0050	0.0050	0.002	-0.27
0.999	0.050	0.050	0.050	0.05	-0.23
0.99	0.50	0.50	0.50	0.50	0.20
0.9	5.0	5.0	5.0	5.0	4.5

normalised by the CRD intensity over the same time frame,

$$S^{\mathrm{CELIF}} = \frac{S_{\mathrm{LIF}}}{I_{\mathrm{CRD}}} \tag{3.8}$$

In order to extract an absorption coefficient calibrations with absorptions based on the measurements of the RDT from equation 2.9 must be made. The calibrated CELIF signal is related to an absorption coefficient by,

$$\alpha = \sigma\rho = \mathcal{K} \cdot S_{\mathrm{CELIF}} \tag{3.9}$$

$\mathcal{K}$ is defined as a proportionality factor which combines the complicated geometry factor of the LIF volume, that needs to be known along with the transmission of the cavity exit mirror, T. Herein lies a fundamental necessity of the CELIF measurement as in order to be able to calibrate the data it must have an accompanying RDT measurement (with a reference/empty-cavity measurement). Currently therefore the technique only exists to extend the dynamic range of a CRD measurement and can only be used when the LOD of CRD is surpassed so that a valid measurement can be taken. Finally we may express $\mathcal{K}$ in terms of the RDT measurements by combining equations 3.8 and 3.9 with any valid expression for deriving the absorption from a CRD measurement, here using equation 2.9.

$$\mathcal{K} = \frac{I_{\mathrm{CRD}}}{S_{\mathrm{LIF}}} \left(\frac{1}{\tau'} - \frac{1}{\tau_0} \right) \frac{1}{c} \tag{3.10}$$

3.2 Absolute Fluorescence Quantum Yields

Absolute fluorescence quantum yields and quenching rates have been previously measured using combinations of CRDS and LIF in groups such as Spaanjaars *et al.* and Bahrini *et al.* discussed in the previous chapter. In particular Hagemeister *et al.*[161] and Koch *et al.*[162] used a method to calibrate fluorescence data using Rayleigh scattering measurements. Considering equations 3.1, 3.7 and 3.9 an expression can be created for

α in terms of the two factors of the experiment which are difficult to obtain, $T(\lambda)$ and $g(\lambda)$.

$$\alpha(\lambda) = \frac{T(\lambda) \cdot S^{\mathrm{CELIF}}}{2g \cdot \Gamma(\lambda)} \tag{3.11}$$

In this expression it becomes evident that to derive $\Gamma(\lambda)$ we must obtain T, g and S^{CELIF}. S^{CELIF} is simply obtained experimentally but the others are more problematic. However if an experiment with a known quantum yield can be performed they may be extracted as a single factor, $\mathcal{K}$. Fortunately such an experiment can be done by using the same set-up to observe Rayleigh scattering in which $\Gamma_{\mathrm{R}}(\lambda) = 1$. Thus an expression for $\mathcal{K}$ is formed as follows,

$$\mathcal{K}_{\mathrm{R}}(\lambda) = \frac{\alpha_{\mathrm{R}}^{\mathrm{CRD}}(\lambda)}{S_{\mathrm{R}}^{\mathrm{CELIF}}(\lambda)} = \frac{T(\lambda)}{2g} \tag{3.12}$$

where the subscript R designates a value obtained by Rayleigh scattering (contrasted with the subscript F for a value obtained from a fluorescence measurement). In the knowledge of the transmission and geometric factors of the experiment a fluorescence experiment may then be run and $\Gamma_{\mathrm{F}}(\lambda)$ extracted.

$$\Gamma_{\mathrm{F}}(\lambda) = \mathcal{K}_{\mathrm{R}}(\lambda) \cdot \frac{S_{\mathrm{F}}^{\mathrm{CELIF}}(\lambda)}{\alpha^{\mathrm{CRD}}(\lambda)} \tag{3.13}$$

3.2.1 Normalisation of S^{LIF}

The normalisation of S^{LIF} by I^{CRD} to create S^{CELIF} in equation 3.8 is shown graphically in figure 3.4. As an example, typical experimental data from this study is shown displaying a single trace from a nitrogen Rayleigh scattering and an acetone fluorescence measurement. If this process of normalisation is accurate then it should be found to hold under different laser powers, PMT voltages and sample pressures. Thus this is investigated further as part of the results of this study.

With a high enough emission intensity the fluorescence and Rayleigh scattering data is expected to mirror the shape of the ring-down trace; the data although demonstrating a broadly similar shape does not do this. In comparison data obtained by BPEB fluorescence measurements did fill out the trend mirroring the CRD trace very well. One reason for this is that BPEB has a much higher quantum yield, 0.58[163] at $320\,\mathrm{nm}$, in comparison to acetone, $1.1 \cdot 10^{-3}$ at $308\,\mathrm{nm}$,[162] and relative to the small cross-sections for nitrogen Rayleigh scattering in the order $10^{-26}\,\mathrm{cm}^2$ in the same wavelength range.[132,133] Secondly limits on the input laser powers for the CRD measurement restricts the available the fluorescence and Rayleigh scattering signal. If too much light is put onto the detection PMT it can saturate affecting the signal received and making the CRD trace deviate from its

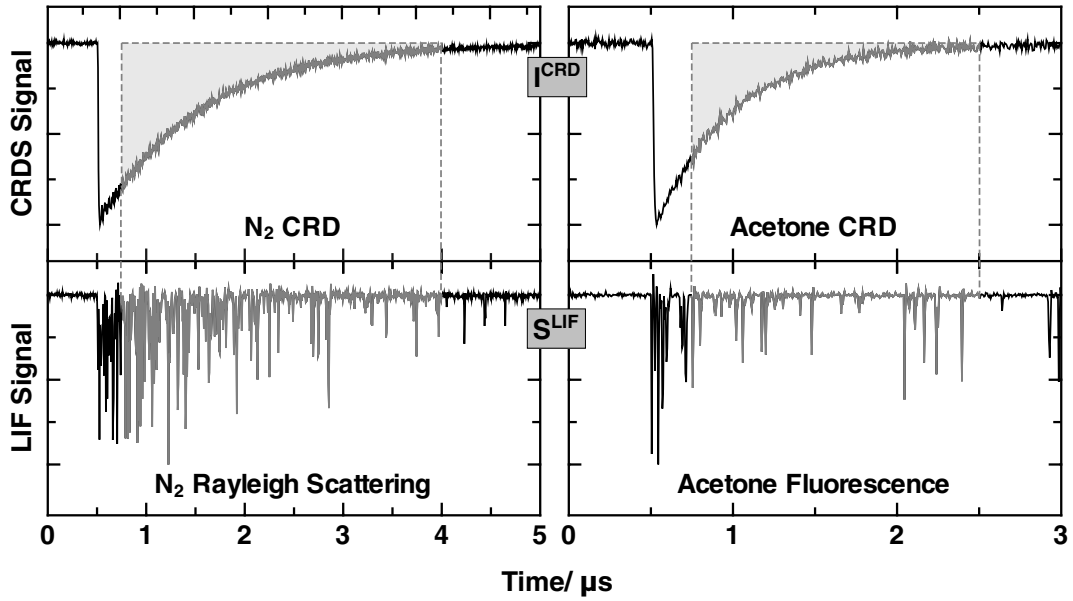

Figure 3.4: Example of normalising integrated LIF signal, S^{LIF} by integrated CRD signal, I^{CRD} per equation 3.8. Two examples are shown, one using Rayleigh scattering by nitrogen and another, fluorescence from acetone. Measurements have all been normalised on the peak signal. Nitrogen measurements have been taken at 200 mbar N_2 at 318 nm. Acetone measurements have been taken at 0.08 mbar at 313 nm.

exponential trend. This same process does not affect LIF due to the significantly lower amounts of signal produced.

Saturation in the signal can be partially solved up to a certain power level by reducing the voltage gain across the PMT. However the PMT operating voltage must remain high enough to produce signal properly. For fluorescence measurements, since multiple passes are made through the absorption region, unless molecules have short fluorescence lifetimes, much lower than the RDT, then bleaching of the molecules can limit the maximum power which may be put into cavity. The molecular beam based CELIF set-up used in the study of BPEB is understood to alleviate this. The molecules in a pulse from the molecular beam move through the probe region much more slowly than the sequential passes of light between the mirrors. But over the course of a ring-down event lasting microseconds in time, partial refreshment of the molecules in the probe volume does occur.[158] In a straight gas cell set-up replenishment of molecules in the probe volume is more limited being dependent on diffusion rates. Thus overall for molecules with a low quantum yield or scattering cross-section S^{LIF} operates in a near photon counting regime.

3.3 Overview of the Experimental Set-up

The set-up used is outlined in far greater detail in chapter 4. Briefly, for the CELIF experiment a laser cavity designed for CRDS and operating as a gas cell is used including optics for monitoring fluorescence trained on the centre. The cavity is constructed from

a 6" stainless steel cube with CF100 ports on each side. Along the main cavity axis (x-axis) side arms were constructed from CF16 nipples supporting the mirror mounts and extending the cavity to a length, $d = 793 \pm 2\,\mathrm{mm}$. The modifications needed to integrate CELIF into any existing CRD experiment are straightforward; suitable fluorescence collection lenses should be added and trained on the position in the ring-down path where fluorescence is to be monitored. This was implemented by customising a CF100 flange for the central cube to seal 1" fluorescence collection lenses along the LIF axis; two set-ups were used which are detailed and compared in terms of their LIF probe volumes in section 4.5. Figure 3.1 shows the simplified schematic of the experimental set-up, while figures 4.1-4.3 in chapter 4 provide more detailed plans.

Two dye laser systems were used for these measurements referred to as System Ia and System II. System Ia, used in the earlier measurements, was a $10\,\mathrm{Hz}$ pulsed Nd-YAG laser (Continuum Minilite II) producing a maximum of $28\,\mathrm{mJ}$ at $532\,\mathrm{nm}$ pumping a dye laser (Quanta Ray PDL-1 outfitted with a custom delay line). System II, used in the latest measurements of acetone spectra and absolute fluorescence quantum yields, was a $10\,\mathrm{Hz}$ pulsed Nd-YAG laser (Continuum Surelite SL-I) producing a maximum of $\sim$250 mJ at $532\,\mathrm{nm}$ pumping a dye laser (Sirah Cobra-Stretch). Further details of the lasers, dyes, wavelengths and powers are given in section 4.2. The laser is passed through spatial filter, comprising a focussing telescope and pinhole, to clean up the beam and collate it to a near-Gaussian beam shape. Before entering the cavity, a mode-matching lens is used to match the curvature of the beam to the cavity mirrors. A pair of PMT modules (Hamamatsu H7732-10, wavelength range$= 185 \rightarrow 900\,\mathrm{nm}$) are used to detect I^{CRD} and S^{LIF}. Further details on the cavity, its mirrors and set-up are in section 4.3.

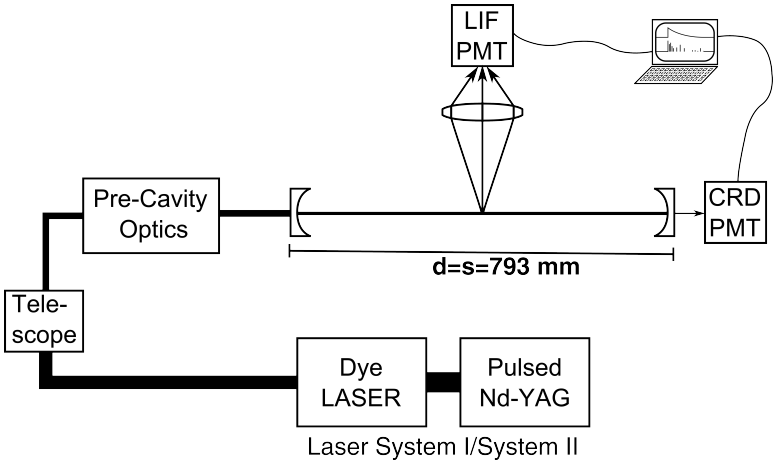

Figure 3.5: A schematic layout of the specific CELIF and CRD laser and optical set-up used for all CELIF experiments reported in this chapter. The experiment is shown in the xz-plane. A pulsed Nd-YAG laser pumps a dye laser. The resulting beam is passed through shaping optics (focussing telescope and pinhole) to achieve a near Gaussian beam shape. Before the cavity resides any polarisation rotating optics used and a mode matching lens to shape the beam further to the cavity TEM_{00} mode. Signals are recorded from the CRD and LIF on PMTs which are digitised by a scope card inside a pc. All measurements are made using NI LabVIEW.

Gases are admitted through the bottom of the cube (y-axis) using a custom made line made from $\varnothing 6\,\mathrm{mm}$ Ham-Let and Swagelok fittings. Admission is performed via individual lines dedicated to the gases being admitted and purged through an independent exhaust connected to the main chamber. Gas flow is controlled by diaphragm valves and using a series of low (Hamlet H1300), high (Hamlet HXF1300) and very high precision (Chell CMV) needle valves. The cavity is purged using rotary pumps down to $2{\cdot}10^{-3}\,\mathrm{mbar}$ and towards ultra-high vacuum pressures using two turbomolecular pumps (TMPs), one large (Oerlikon Leybold Vacuum SL300) positioned directly above the central cube on the y-axis and one smaller (Oerlikon Leybold Vacuum SL80) offset from the experiment for pumping the cavity arms. The TMPs were sealed from the chamber using pneumatic gate valves. Pressures were monitored by a series of three capacitance manometers (Oerlikon Leybold CTR100-10, and MKS 626A, 627D) and an ion gauge (AML AIG17G). Together these provided a full range of pressure measurements from $3{\cdot}10^{-11}$ to $1333\,\mathrm{mbar}$. In optimum working conditions a bottom end pressure of $3{\cdot}10^{-8}\,\mathrm{mbar}$ with a leak rate of $4{\cdot}10^{-7}\,\mathrm{mbar\,s^{-1}}$ was achieved.

3.4 Nitrogen Rayleigh Scattering Measurements

An initial investigation was performed to extend the generality of the CELIF method beyond the molecular beam study of BPEB. Therefore the case of Rayleigh scattering by a molecule that broadly maintains the spherical particle approximation was studied. Nitrogen was chosen due to it being readily and cheaply available in the laboratory, and because of recent, detailed investigations by Sneep *et al.*[132] and Ityaksov *et al.*,[133] quantifying the deviation of its scattering cross-section from the λ^{-4} dependence on frequency. Measurements of N_2 Rayleigh scattering were taken at $583.5\,\mathrm{nm}$ by continuously varying the pressure between $0 \rightarrow 1000\,\mathrm{mbar}$.

3.4.1 Experimental Setup

The experimental set-up consists of the standard CRD gas cell set-up outfitted for CELIF outlined briefly in section 3.3 and in much greater detail in chapter 4. Pulsed dye laser system Ia (see section 4.2) and the cavity (see section 4.3) was set-up for $532\,\mathrm{nm}$ pumped Pyrromethene-597 in MeOH producing light in the range $560 \rightarrow 600\,\mathrm{nm}$. Rayleigh scattering measurements were carried out at $583.5\,\mathrm{nm}$ obtaining empty ring-down times, $\tau_0 = 35 \rightarrow 40\,\mu\mathrm{s}$. Maximum powers used were tuned down to acceptable levels using the Q-switch on the pump laser when necessary to avoid saturation effects when they were observed on the CRD signal detectors. A double Fresnel rhomb and Glan-Taylor prism were used to change the polarisation angle of the incident light and inserted into the experiment as part of the pre-cavity optics in figure 3.5. The polarisation of the incident light was set at the magic angle and all measurements were taken at room temperature. Measurements were performed using mirror mounts (see section 4.4) which were designed to be more stable when taking CRD measurements that vary with pressure.

Pressures were monitored using the capacitance manometer array mentioned in section 3.3 and discussed fully in section 4.6. N_2 was admitted into the chamber in a slow and controlled manner to avoid destabilising the cavity and for good equilibration. Measurements were taken continuously, simultaneously admitting N_2 up to $1000\,\mathrm{mbar}$, and afterwards pumping it out, while concurrently recording I^{CRD} and S^{LIF}. Pressures were admitted to the gas cell, which has a volume of $\sim$5 L, at three distinct flow rates set using needle valves and evacuated in a controlled manner through a needle valve by a rotary pump. The flow rates for admission and removal were left to evolve naturally and so the leak rate changed over time, depending on the backing pressure in the chamber. Table 3.2 provides approximate details of the N_2 admission and removal processes used in the measurement.

Table 3.2: Rough breakdown of leak rates used for filling the cavity during the Rayleigh scattering measurements contained in figure 3.6. Each region occurs sequentially after the previous.

	Pressure Range (mbar)	Leak Rate (mbar cm^3 s^{-1})*
Region 1	$0 \rightarrow 7.5$	120
Region 2	$7.5 \rightarrow 300$	5500
Region 3	$300 \rightarrow 1000$	13600
Region 4	$1000 \rightarrow 0$	-3000

* Assuming a total volume in the gas cell is $\sim$5 L

3.4.2 Results

CRD data has been processed using equations 2.8 and 2.9, and CELIF data using equations 3.8 to 3.10. The continuous data has been binned into points each with 311 shots and the results are shown in figure 3.6. Results are shown in terms of the photon loss as per equation 2.11 based on a cavity length, $d = 79.3 \pm 0.2\,\mathrm{cm}$. S^{LIF} data has been calibrated by the CRD absorption at $1000\,\mathrm{mbar}$ and gradients of a least squares fit to each data set based on this are virtually indistinguishable. Rayleigh scattering cross-sections were derived from the CRD measurements using the ideal gas law at 292 K. The CRD derived cross-section from the pressure range, $200 \rightarrow 1000\,\mathrm{mbar}$ at $583.5\,\mathrm{nm}$ is $3.67 \pm 0.1 \cdot 10^{-27}\,\mathrm{cm}^2$. This compares favourably with a literature value of $3.64 \cdot 10^{-27}\,\mathrm{cm}^2$.[132] The standard error of the averaged cross-section measurements is displayed and is within error of the cited literature value.

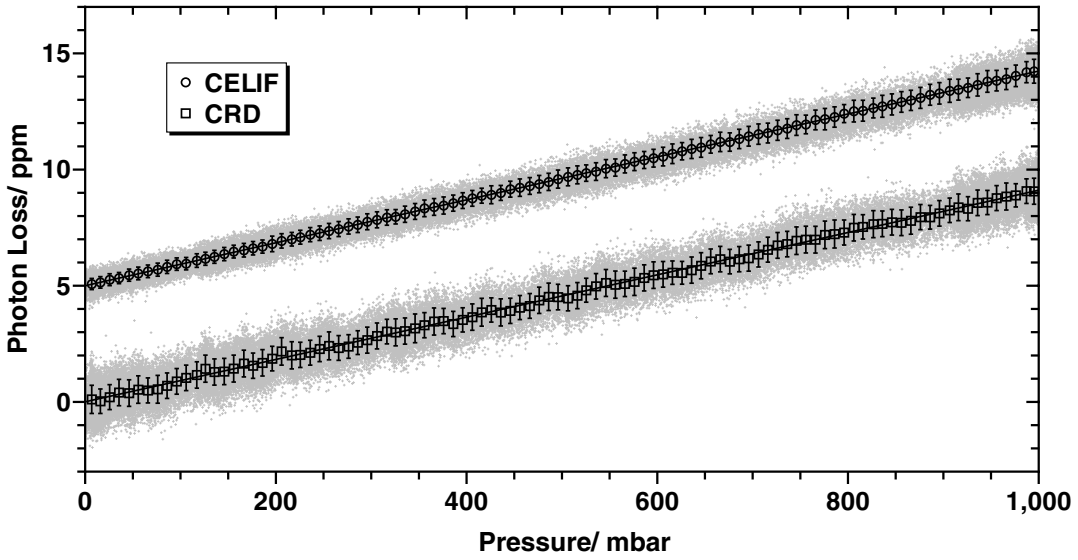

Figure 3.6: Rayleigh scattering measurements taken with varying pressures of N_2 at 583.5 nm with the polarisation set at the magic angle. Fractional absorption is shown against pressure. CELIF signal is calibrated by the CRD signal at 1000 mbar and offset by 5 in order to better compare the two data sets. Large data points shown are based on an average of the data they lie on, each is the average of 311 data points in a 10 mbar range. The error displayed represents the standard deviation in the data.

3.4.3 Analysis

Calibration of the CELIF data by the CRD data at 1000 mbar has shown confidently that equations 3.8 to 3.10 are valid in their description of the CELIF process and demonstrate a linear trend with varying pressures of nitrogen. The quality of the data is indicated by the CRD derived cross-sections. Whilst data is within the standard deviation of the literature it is outside of the standard error. Any errors in the cross-section might derive from several sources with most contributing to an over-estimation. One potential source of underestimation known of is a systematic error from the Rayleigh scattering process itself. Forward and backward scattered light is able to couple into the CRD measurement but can only happen over a very small acceptance angle. It has been shown able to produce an underestimate of $\sim 0.01\%$ [132] but this error is insignificant in the face of other existing errors that might add to an overestimate in the result.

A major error contribution may arise from impurities in the gas and any future repeat should aim to remove these if they exist. In accordance with Ubachs et al.[132] greater care can be taken over the N_2 source which could be purged through a sintered stainless steel filter with $0.5\,\mu$m pores. This removes dust and aerosols from the gas. Additionally a water filter could be installed in the N_2 source to make certain that residual water vapour in the gas, if any is present, is removed since the gas cylinder is housed outside the building with a long section of piping, the cleanliness of which is unknown. As well as this the main purpose of the cavity is for ice experimentation and it is often subjected to heavy concentrations of water. Water contamination was partially accounted for by

ensuring to probe the scattering on a frequency off resonance with any water lines. In the measurement however a small mistake was made positioning the laser at $583.5\,\mathrm{nm}$ when previous scattering measurements were taken at $585.5\,\mathrm{nm}$. The reason for sitting at $585.5\,\mathrm{nm}$ was that it is clear of any water transitions ensuring that if any contamination in the sample had occurred it would contribute as little as possible to the measurement. At $583.5\,\mathrm{nm}$ measurements were performed sitting on the shoulder of a water transition with a cross-section in the order of $1 \cdot 10^{-26}\,\mathrm{cm}^2$. If the N_2 source was contaminated with $0.5\,\%$ water vapour then this could account for the observed over-estimate in cross-section.

A final error source exists in the pressure readings from the capacitance manometers. The quality of the CRD data shown demonstrates a linear trend that is markedly noisy with an irregular pattern on the data. Readings in the range 200-1000 mbar were taken using a capacitance manometer (MKS 626A) which has an instrument error of 0.25% and readings will reliably fluctuate in the pattern seen on the data within this instrument error. It is believed that the pattern is related to the heating and cooling cycles of the air conditioning system maintaining the temperature of the laboratory combined with the intrinsic function of the capacitance manometer.

3.4.4 Pressure Varied CELIF Measurements

The data shows two clear advantages of the CELIF technique over standard CRDS. Firstly the standard deviation in the data, although increasing linearly towards higher absorptions, is lower overall; in contrast CRD absorptions have a data spread which remains the same at all absorptions. This is due to the response from the PMT in which noise increases with increasing LIF signal detected. At low pressures the errors are twice as big for CRD than for the CELIF and only at high pressures are they comparable. This does however contrast measurements made in the very first incarnation of CELIF shown in figures 2.13 and 2.14 where CELIF outperforms CRD dramatically across the board. The major reason for this is from the sample length probed in the two different measurements. CELIF observes a probe volume set by the optics which collects light into the detector; in this set-up it is approximately 45.5 mm in length with a beam waist, set by the cavity, of $\approx 0.3\,\mathrm{mm}$ (see section 4.5.1) However the CRD measurement samples the entire cavity length, $793\,\mathrm{mm}$ long, approximately 18 times greater. In this way it gains back over the smaller sample volume of the CELIF measurement and for nitrogen Rayleigh scattering at this wavelength it is at the very least competitive with CELIF.

More interestingly, the CELIF data shows it follows the linear trend in the pressure varied measurements with greater precision than CRDS. In fact the quality from the CELIF measurements is rarely superseded by CRD. This is supported by evidence from regular laboratory experimentation over a period of three years. This potentially has several contributions such as the essentially background free nature of LIF signal born from a well aligned cavity and the relative sensitivities of the individual techniques. However

this does not explain how resistant to the overall shot-to-shot pressure variations that the CELIF signal is. As a cavity is filled from vacuum to some pressure the forces that exist on the mirrors will increase and change. In an ideal situation this effect would be negligible or non-existent on the mirrors which would maintain the alignment of the cavity. However in reality the cavity must adjust to accommodate them. Combined with additional vibrations and shot-to-shot changes in the general environment and laser this affects the data obtained by CRDS.

It may be that CELIF is largely immune to many of the shot-to-shot fluctuations that CRDS is not. Any shot-to-shot changes in the cavity alignment should be reflected by the light integral from CRD which then normalises the LIF signal. So every measurement is made relative to a correct depiction of the cavity environment at that point in time. In contrast the RDT measurement is referenced against a background cavity that is not simultaneously taken but must be taken at a different time before or after the absorption or scattering measurement. Overall the quality of the CELIF data was found to be better than the CRD but not as much as hoped. Further analysis of data near the LOD for CRD showed that CELIF tended to show greater sensitivity than CRDS but not as much as the BPEB data demonstrated. From these generally positive results efforts were turned to analyse CELIF further by looking at the polarisation dependence of nitrogen Rayleigh scattering and also studying a fluorescent molecule.

3.5 Polarisation Dependence of Rayleigh Scattering

Another simple test used to investigate the performance of CELIF was measuring the polarisation dependence of nitrogen described in section 3.4. The data obtained was used to characterise the polarisation dependence for use in measuring absolute quantum yields of fluorescence for acetone at the magic angle and also to verify a simulation program designed to calculate and assess probe volumes for LIF set-ups.

3.5.1 Experimental Setup

The experimental set-up was as in section 3.4 with the following changes and clarifications. A double Fresnel rhomb (Thorlabs, FR600HM) was used to rotate the polarisation of the laser. Linearity in the resulting polarisation was ensured by passing it through a Glan-Taylor prism (Thorlabs, GT10) set to match the polarisation of the incident light. Measurements were made in intervals of $5\,^\circ$ between $0 \rightarrow 90\,^\circ$ recorded by installing the double Fresnel rhomb into a rotational mount (Thorlabs, RSP1C); this translates to rotating the polarisation in $10\,^\circ$ intervals between $0 \rightarrow 180\,^\circ$. The polarisation was rotated around the CRD cavity axis and described in terms of the zx-scattering plane. $0\,^\circ$ is when the laser polarisation is parallel (p), $90\,^\circ$ is when it is perpendicular (s). Polarisation measurements were carried out at $585.5\,\mathrm{nm}$, well clear of any water transitions, and 1000 laser shots per point were taken. Three pressures of nitrogen were used to take measurements 30, 60 and $120\,\mathrm{mbar}$.

3.5.2 Results

Results are shown in figure 3.7 for recorded data and also for simulated data. Recorded data was fit using the function, $f(\theta) = A\cos^2(\theta + d\theta) + b$, where A is the normalised amplitude of the signal received, b is the minimum scattered light signal and θ is the polarisation. $d\theta$ is an offset to the polarisation caused by the angular scale on the fresnel-rhomb and derived from the fit; it had an angle of $-2.9\,^\circ$ at $30\,\mathrm{mbar}$, $-2.6\,^\circ$ at $60\,\mathrm{mbar}$, and $-2.1\,^\circ$ at $120\,\mathrm{mbar}$. The recorded data follows the expected trend for the polarisation dependence of Rayleigh scattering well. Errors in the standard deviation decrease towards lower intensities as previously discussed. Data has been simulated using the same program used to analyse the LIF probe volumes described in section 4.5.1. Parameters for the simulation were drawn from the set-up, which is described in figure 4.3b and then scaled to the measured data set. For an accurate fit 9% elliptical polarisation had to be included into the incident laser.

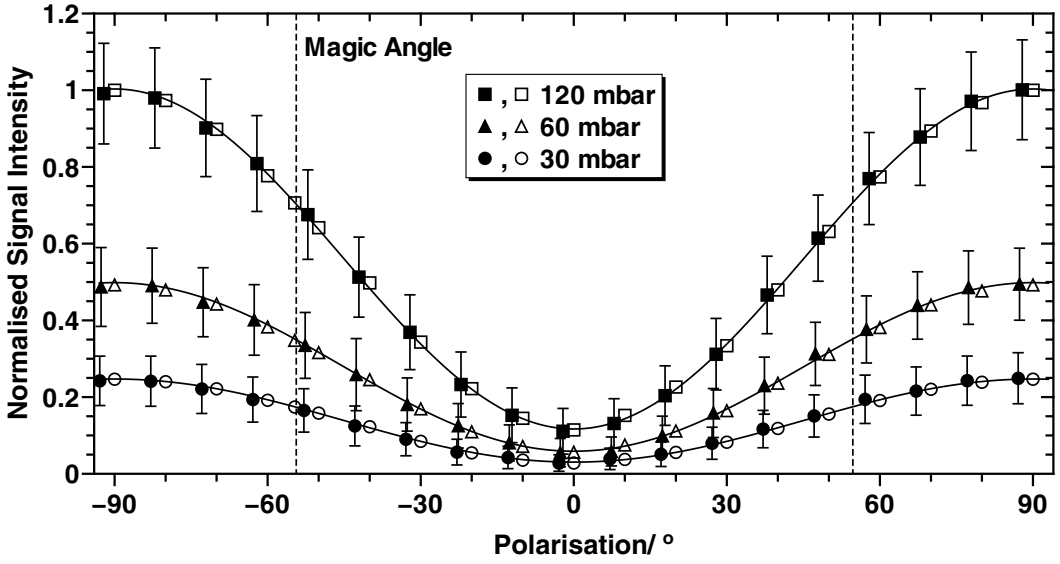

Figure 3.7: Rayleigh scattering CELIF intensity measurements taken at three different pressures of nitrogen, 30, 60 and $120\,\mathrm{mbar}$ (●,▲,■) while varying the polarisation of the incident laser light. Filled points are recorded data and empty points (○,△,□) are simulated data. All data is normalised with respect to the maximum intensity at $120\,\mathrm{mbar}$. The solid line shows a fit to the the recorded data. The magic angle is marked using dashed line and the errors displayed represent the standard deviation.

3.5.3 Analysis

At first glance the results mirror the expected data trend as well as the simulated data. However initial simulations using linearly polarised light did not match the intensities correctly at the angle for minimum scattering detection and to simulate the correct data 9% elliptical polarisation in the laser had to be added. The Glan-Taylor prism was positioned as the last optic that the incident laser light went through, before the mode-matching lens preceding the CRD cavity. Incident light is therefore assumed to be linear

up to this point. The mode matching lens is unlikely to cause elliptical polarisation in the incident beam, which only leaves the cavity mirrors. The manufacturer of the cavity mirrors, Layertec, indicated that these might have been the cause. The design specification of the mirrors was for light with an angle of incidence of $0\,^{\circ}$. The material used in the mirror coating was Ta_2O_5, specified by the manufacturer, which is known to display birefringence.[164] Therefore any light which passes through the mirror at an angle off the design specification might be depolarised.[165] The mirrors have a curvature of $1\,\mathrm{m}$ so to avoid this the mode matching lens preceding the cavity was designed to match the laser to the curvature of the cavity. It may be that all light was not matched perfectly and this was the cause. One effect of the depolarisation of light entering the cavity is that it has altered the magic angle measurement. From section 2.24 the intensity of normalised light at the magic angle should be 0.66, from figure 3.7 the intensity at the magic angle is 0.71. As a result this will effect the measurements of absolute fluorescence quantum yields slightly which use nitrogen Rayleigh scattering at the magic angle in their calculation.

3.6 Application to Simple Fluorescing Molecules

N_2 Rayleigh scattering measurements demonstrated that CELIF data correlated better than equivalent CRD data to expected linear, pressure versus absorption trends at concentrations on or near the LOD for CRDS. In order to investigate CELIF further and see if this extended to a simple fluorescing molecule a suitable candidate for initial study needed to be chosen. Originally nitrogen dioxide, NO_2, was chosen for several reasons. Firstly there had been previous, recent, work in the study of NO_2 which meant it was well understood spectroscopically and readily accessible by our group. Work had been undertaken previously in the creation of an undergraduate laboratory experiment studying the detection of NO_2 by CRDS. Additionally it had been used in the work of Wrede *et al.* in the photostop process so a sample was on hand for immediate testing. Furthermore NO_2 has great relevance in its role as a pollutant in the atmosphere and is a potential target molecule for study with the ice surface experiment.

NO_2 has an easily accessible visible fluorescence band when excited from its ground state to first excited state, $\tilde{A}^2B_2 \leftarrow \tilde{X}^2A_1$. Fluorescence is broad and red-shifted, occurring in a near continuum from the excitation wavelength to the infra-red only limited by the wavelength range over which the detector can function. It is due to the presence of a strong conical intersection between the ground and first excited state that strong vibronic interactions are observed between the dense, highly excited vibrational levels of the ground state and low lying levels of the excited state. After excitation by visible light the redistribution of energy down many different pathways creates a multitude of fluorescence pathways and hence a broad fluorescence spectrum. In our case NO_2 was excited at $585.5\,\mathrm{nm}$ therefore detecting fluorescence between $585.5 \rightarrow 901\,\mathrm{nm}$ (from the excitation wavelength to the cut-off point of the PMT). An example of a dispersed fluorescence

spectrum for NO_2 from excitation at $435.04\,\mathrm{mbar}$ is shown below in figure 3.8. The other potentially favourable aspect of NO_2 was its seemingly reasonably sized cross-sections in the order of $(\sim 1 \rightarrow 10 \cdot 10^{-20}\,\mathrm{cm}^2)$[166] between $580 \rightarrow 590\,\mathrm{nm}$, the wavelength region at which it was to be tested.

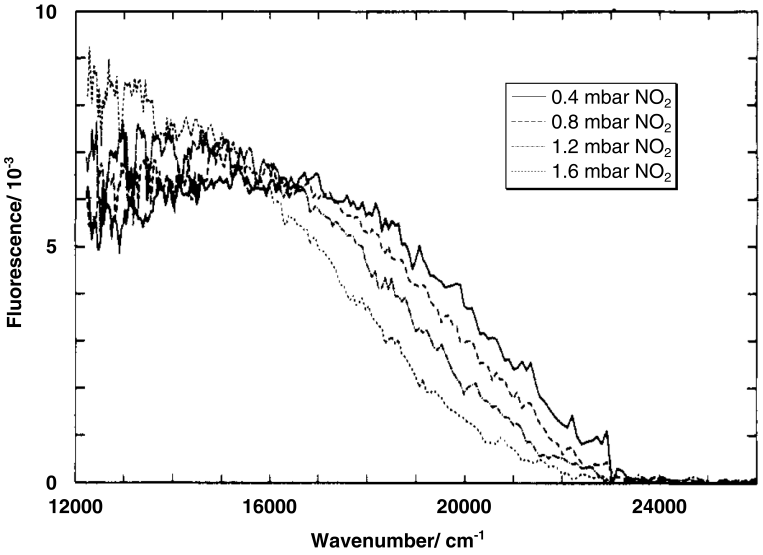

Figure 3.8: Dispersed fluorescence spectra of NO_2 excited by a $435.04\,\mathrm{nm}$ $(22986\,\mathrm{cm\,s^{-1}})$ pulsed dye laser showing fluorescence from the excitation wavelength to at least $833.33\,\mathrm{nm}$ $(12000\,\mathrm{cm\,s^{-1}})$. Each fluorescence profile has been normalised to unit total area under the curve. Different lines show measurements at different pressures varying between $0.4 \rightarrow 1.6\,\mathrm{mbar}$.[167]

Experiments were run at $585.5\,\mathrm{nm}$ with pure NO_2 and also in a helium buffer gas. Several problems were encountered indicating NO_2 to be far less favourable than originally thought. Firstly, its cross-sections in this wavelength range proved too high. σ is $\sim 5{\cdot}10^{-20}\,\mathrm{cm}^2$ at $585.5\,\mathrm{nm}$ so only relatively low concentrations of NO_2, $< 0.02\,\mathrm{mbar}$, could be used whilst still retaining measurable RDTs. Moreover, in this wavelength range, the cross-sections only changed by plus or minus a single order of magnitude hence changing the testing wavelength did not produce a significant enough change in the testable pressures. Using lower concentrations of NO_2 lowered the available LIF signal making CELIF measurements far more difficult to perform. Secondly, and most importantly, NO_2 was found to be highly susceptible to quenching due to extremely long fluorescence lifetimes of between $55 \rightarrow 90\,\mu\mathrm{s}$[168] in the $400 \rightarrow 600\,\mathrm{nm}$ excitation region, where a higher excitation wavelength tends towards longer fluorescence lifetimes. This meant that the amount of LIF signal dropped to virtually nothing at higher pressures, $> 0.5\,\mathrm{mbar}$. Moreover using a buffer gas of helium was found to be ineffective and did not solve any issues.[167,169,170]

3.6.1 Quenching in CELIF

Quenching can be an issue with a standard gas phase LIF experiment but in comparison it can be dealt with more easily. Pressures can usually be dropped to the point where

collisions are infrequent or collision-less and in conjunction with this LIF laser powers can be maximised to produce more LIF signal. Quenching particularly affects CELIF because it has to use much lower light levels (some 99.99% having been reflected from the front mirror) in the CRD cavity, thus each pass through the sample yields far less fluorescence. Moreover the combination technique is such that simply increasing the incident laser power or increasing the concentration of sample may interfere with CRD measurements. Armed with this knowledge the search was made for an alternative molecule. One that would be far less susceptible to quenching by having a shorter fluorescence lifetime on a scale of nano or picoseconds, and that was readily available with cross-sections which could provide a good dynamic range for CRD and LIF to work at the same time. After a short investigation the molecule settled on for further measurements was acetone.

3.7 Acetone CELIF Measurements

Acetone is much better suited for CELIF measurements in comparison to NO_2. As discussed in section 2.11.1, when excited around $320\,\mathrm{nm}$ it has broad fluorescence emission band, $350 \rightarrow 550\,\mathrm{nm}$, with a fluorescence lifetime $\sim 2\,\mathrm{ns}$ long. At $\sim 1 \cdot 10^{-20}\,\mathrm{cm}^2$ cross-sections in the region are weak enough to allow decent pressures to be used without saturation of the CRD signal. In order to further extend the preliminary results of the scattering measurements experiments were performed using acetone, testing the validity of the CELIF equations and looking into whether the dynamic range of basic CRDS was extended or improved upon by the most generalised CELIF experimental set-up. Three different CELIF measurements were made,

1. Power Dependence
2. Pressure Dependence
3. Absolute Quantum Yields

3.8 Power Dependence of Acetone CELIF

Power dependencies of acetone were measured to ensure that variations in the PMT gain and sample density remained linear during the normalisation process with respect to changing incident laser powers. From this it would be confirmed that both the laser power and detection sensitivity could be changed as and when an experiment demanded.

3.8.1 Experimental Setup

The set-up used is described in section 3.4 with the following modifications. Pulsed dye laser system Ia (see section 4.2) and the cavity (see section 4.3) was set-up for $532\,\mathrm{nm}$ pumped DCM in MeOH producing light in the range $600 \rightarrow 660\,\mathrm{nm}$. A BBO doubling crystal was installed and optimised producing light in the range $300 \rightarrow 330\,\mathrm{nm}$. Measurements were carried out at $313\,\mathrm{nm}$ where the cross-section of acetone is $1 \cdot 10^{-20}\,\mathrm{cm}^2$ and empty ring-down times of $1 \rightarrow 1.3\,\mu\mathrm{s}$ were obtained. Laser power was varied man-

ually during the experiment using the built-in attenuator in the pump laser (Continuum Minilite II). The polarisation of the laser was set to minimise Rayleigh scattering, at $0\,^{\circ}$ on the zx-plane. The maximum and minimum power was consistent between all measurements however due to the manual nature of the power attenuator data points were taken at similar but not identical powers between the two extremes. Pressures were admitted to the chamber through the gas system specified in previous sections. High purity Acetone was used (Fisher Scientific, HPLC grade, $> 99.9\,\%$), degassed and stored in a glass bulb that was connected to an acetone only gas line. Admission was controlled using the very high precision (Chell CMV) or high precision (Hamlet HXF1300) needle valve as required.

3.8.2 Results and Analysis

Results are shown in figure 3.9. Each data point was averaged over 5000 shots at a temperature of $\sim 293\,\mathrm{K}$. Standard errors produced are smaller than the symbol size, therefore the standard deviation of the data is shown instead. Power dependencies are shown for two different pressures of acetone, 0.1 and $0.3\,\mathrm{mbar}$ with the PMT at $1094\,\mathrm{V}$, and three voltage settings on the S^{LIF} PMT detector, 1000, 1050 and $1094\,\mathrm{V}$ at a pressure of $0.3\,\mathrm{mbar}$ acetone.

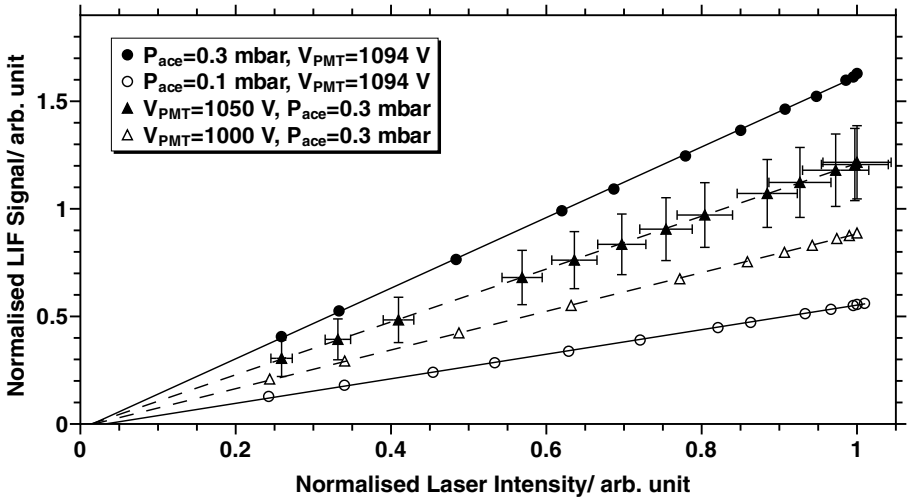

Figure 3.9: The dependence between incident laser intensity, as measured by its proportional relationship with I^{CRD}, and S^{LIF} is shown. Data has been recorded at $313\,\mathrm{nm}$. The pressure of acetone was varied, $P_{\mathrm{ace}} = 0.1$, $0.3\,\mathrm{mbar}$ with the PMT voltage set, $V_{\mathrm{PMT}} = 1094\,\mathrm{V}$. PMT voltage was recorded at $V_{\mathrm{PMT}} = 1000$, $1050\,\mathrm{V}$ with an acetone pressure, $P_{\mathrm{ace}} = 0.3\,\mathrm{mbar}$. For each data set, x and y, has been normalised with respect to the peak integrated signal I^{CRD}. A linear least squares fit has been applied to the data. Errors displayed show the standard deviation for one data set and are similarly proportional in the other data sets.

The measurements confirm a linear power dependency for both sets of data. This proves that normalisation of S^{LIF} by I^{CRD}, as depicted in figure 3.4 and equation 3.8, is valid when changing the input power under different pressures of acetone and detector gains.

3.9 Pressure Dependence of Acetone CELIF

The performance of CELIF with respect to CRDS was then investigated to see if it could potentially extend the dynamic range of the CRDS to lower LODs in a generalised manner as opposed to the specific molecular beam set-up employed by Sanders *et al.* to study BPEB.

3.9.1 Experimental Setup

The experimental setup used was exactly the same as section 3.8.1 with no difference. Acetone was degassed and put into the chamber using the high precision needle valve through a dedicated gas line. Pressure was varied between $1 \cdot 10^{-4} \rightarrow 1 \cdot 10^{-2}\,\mathrm{mbar}$. 5000 shots were taken per data point at a temperature of $\sim 293\,\mathrm{K}$. Data was taken at $313\,\mathrm{nm}$ with the polarisation of light set to minimise Rayleigh scattering on the LIF signal.

3.9.2 Results and Analysis

The results are shown in figure 3.10 shown in terms of the photon loss as per equation 2.11 based on a cavity length, $d = 79.3 \pm 0.2\,\mathrm{cm}$. Linear least squares plots have been performed on the $P_{\mathrm{ace}} > 0.1\,\mathrm{mbar}$ avoiding the poorer quality data at the lowest pressures near the LOD. Broadly both data sets demonstrate a linear trend for absorption with increasing pressure. However it is clear that the CELIF data is no better in quality than the CRD data. Moreover at the lowest pressures of acetone used the RDT measurements seem to outperform CELIF.

The CELIF measurement of acetone fluorescence under these conditions does not increase the dynamic range of CRDS and in this example CRD outperforms it. Although the quality of data can be improved, regardless CELIF is unlikely to extend the dynamic range of CRD by the three orders of magnitude seen previously by Sanders *et al.* The data quality is dependent on several factors. First of all at the lowest pressures the PMT is photon-counting and the analysed data is composed of a seemingly random series of voltage spikes during the ring-down event. A result of this is that a direct signal integration is no longer necessarily the best method for calculating S^{LIF}. This is compounded by being unable to integrate S^{LIF} at the beginning of the ring-down event where the largest amount of fluorescence is observed. The earliest part of the ring-down can be subject to jitter and include uncoupled light from ASE in the incident laser beam. This increases the error in the ring-down fit and therefore normally the best fit would not include the very early part of the ring-down.

Secondly at these low signals, near the LOD, the standard deviation on the recorded CELIF absorption increases for the lowest few pressure measurements. This is because the background is increasingly becoming similar in value to the recorded LIF signal. One detail of this experiment is that when it was performed background light levels were higher than necessary as it was performed with the lights on in the laboratory; later

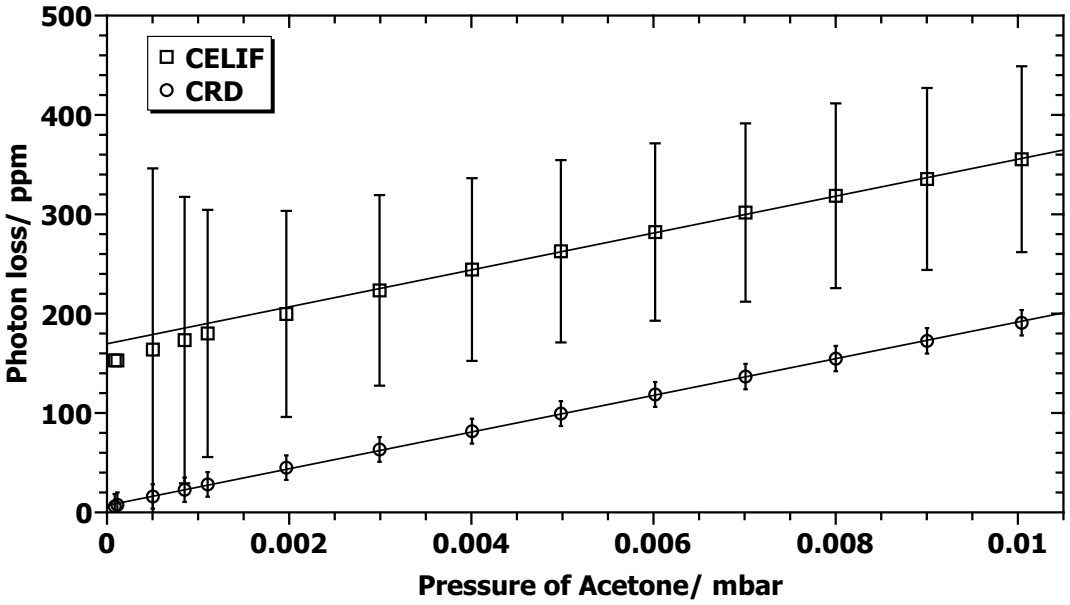

Figure 3.10: Fluorescence measurements of acetone are shown using CELIF and CRDS. Pressures were varied between $1 \cdot 10^{-4} \rightarrow 6 \cdot 10^{-3}\,\mathrm{mbar}$ and data taken at $313\,\mathrm{nm}$. CELIF data has been normalised using the CRD data and then shifted on the y-axis to aid comparison between the data sets. Data is plotted with a linear least squares trend for $P_{\mathrm{ace}} > 0.1\,\mathrm{mbar}$. Errors shown represent the spread in the data, where missing errors lay beyond the graph range.

measurements were performed in darkness which has a noticeable effect decreasing the background. Any repeat of this experiment should aim to minimise background light levels and also change the method by which the LabVIEW program records the LIF signal to account for photon counting.

3.10 Absolute Quantum Yields of Acetone Fluorescence

Absolute quantum yields of acetone were measured by first taking a high resolution spectrum of the target scan region, $313 \rightarrow 318\,\mathrm{nm}$. The high resolution scan was used to ensure that acetone data matched with current literature and also to test the installation of a newer dye laser system. This data was also used to determine an appropriate resolution and the experimental settings for the absolute quantum yield measurements.

3.10.1 Experimental Setup

The experimental set-up continued with the use of the standard gas CRD cell outfitted for CELIF, as outlined in previous sections, with the following alterations. Pulsed dye laser system II (see section 4.2) and the cavity (see section 4.3) was set-up for $532\,\mathrm{nm}$ pumped DCM in MeOH producing light in the range $600 \rightarrow 660\,\mathrm{nm}$. A BBO doubling crystal was installed and optimised producing light in the range $300 \rightarrow 330\,\mathrm{nm}$. The laser system, due to a higher power pump laser, was capable of maximum powers in this wavelength range of $\approx 4\,\mathrm{mJ}$ using both the oscillator and the amplifier. These were much

too high for suitable CRD measurements and required overly low PMT voltage settings to accommodate output signals. Therefore only the oscillator was used and tuned down using the Q-switch until appropriate powers, $\sim 100\,\mu$J, were obtained.

Measurements were carried out at $313 \rightarrow 318\,\mathrm{nm}$ producing empty ring-down times of $\sim 1 \rightarrow 2\,\mu$s, increasing towards longer wavelengths. Polarisation of incident light was controlled using a half-wave plate (Photonics Solutions, WPZ1215-2-308), instead of the double fresnel rhomb, combined with a Glan-Taylor prism situated in the pre-cavity optics. Acetone was used as previously, degassed and admitted through a dedicated gas line. In order to further improve the optical set-up for CELIF, the experiment was altered to place a lens closer to the probe volume increasing the solid angle of light accepted by the PMT detector. For this a plano-convex uv fused-silica lens, $f = -40$ (Thorlabs, LA4765) was placed the $20\,\mathrm{mm}$ from the CRD axis and combined with a plano-convex uv fused-silica lens, $f = -50$ (Thorlabs, LA4148) mounted into the CF100 flange in front of the CELIF detector. Figure 4.3b contains more detailed schematic information of the set-up while section 4.5.1 analyses the changes to the LIF probe volume in more detail.

3.11 Acetone High Resolution Scan Results

Measurements were made recording acetone at a pressure of $2 \cdot 10^{-2}\,\mathrm{mbar}$ and temperature of $\sim 293\,\mathrm{K}$. Data was taken across $313 \rightarrow 318\,\mathrm{nm}$ at a resolution of $0.01\,\mathrm{nm}$, in scans $0.5\,\mathrm{nm}$ in length. Each section had an overlap region of only a single data point. 300 laser shots per data point were taken and voltage levels on the CRD PMT were set for each scan interval to maintain maximum voltages of $\sim 8 \rightarrow 10\,\mathrm{mV}$ on the CRD detector, and $\sim 40\,\mathrm{mV}$ on the LIF detector. Background scans were run in between each measurement using the TMPs to evacuate the cavity. Results are shown in terms of the photon loss as per equation 2.11 based on a cavity length, $d = 79.3 \pm 0.2\,\mathrm{cm}$. Fresh acetone was used for each measurement and background scans were taken consecutively after each absorption measurement. Short scans lasting $\sim 30\,\mathrm{min}$ were necessary so that the background scans remained as relevant as possible to the absorption measurement. Over time exposure to the acetone causes the cavity mirrors to become dirty from adsorption to their surface. In addition, over long wavelength scans, changes are required to the laser power and PMT settings to accommodate the changing mirror reflectivities and fluorescence absorption/emission process. For this the Q-switch on the laser was used to lower powers to acceptable levels. Measurements were performed in darkness to ensure noise on S^{LIF} was kept to a minimum. Although CELIF data was also taken, calibration with the CRD data means that it sits directly on top. The wavelength dependence of the PMT and voltage changes in between measurements ensured that normalisation coefficients had to be made for every wavelength point taken, therefore only the CRD data is displayed.

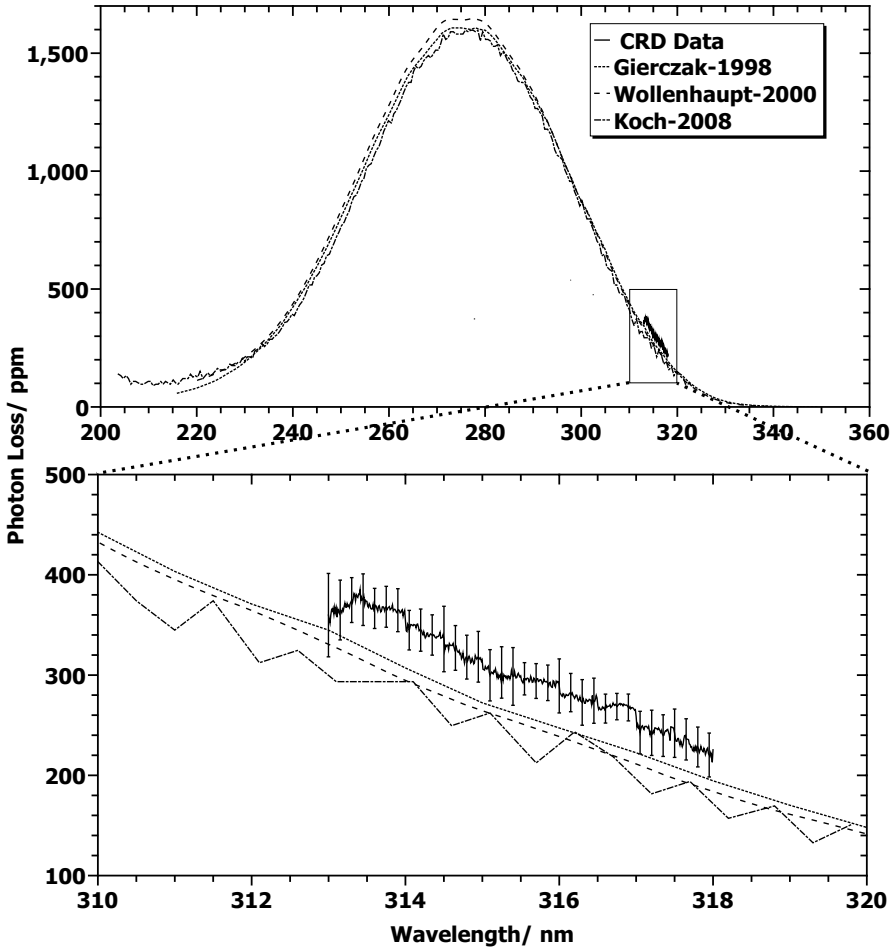

Figure 3.11: High resolution absorption scan of acetone, $P_{\mathrm{ace}} = 2 \cdot 10^{-2}\,\mathrm{mbar}$, taken from $313 \rightarrow 318\,\mathrm{nm}$ at a resolution of $0.01\,\mathrm{nm}$. Data was taken in $0.5\,\mathrm{nm}$ intervals. The upper figure shows the data in reference to the broad absorption feature as measured by several recent publications using cross-sections for acetone at $P_{\mathrm{ace}} = 2 \cdot 10^{-2}\,\mathrm{mbar}$.[171–173] The lower figure zooms into the region $313 \rightarrow 318\,\mathrm{nm}$ for a more detailed comparison. The error displayed shows the standard deviation in the data.

3.11.1 Analysis

The scan shows a broad, structureless absorption band as expected. The recorded absorptions are nearly in agreement with the those sourced from the literature but relative to them are slightly too high. The literature lies outside a standard deviation of the recorded data which is $\sim 10\%$ too large. This could be linked to several experimental errors. First truly accurate background ring-down traces may be difficult to obtain in the face of an unquantifiable and changing amount of acetone adsorption to the cavity mirrors. When acetone is first put into the cavity it equilibrates with the interior of the gas cell and some is adsorbed to the surfaces including the mirrors. This is observed in the short term by a general reduction in acetone pressure as it equilibrates in the cavity and in the longer term by a reduction in the measured τ_0.

Other error sources include the method used to degas acetone. This could be improved

and was not necessarily as rigourous as it could have be. Measurements were made in the early stages of setting up a new laboratory within a limited time frame and a MeOH/CO_2 bath used. Ideally degassing would have taken place using a liquid nitrogen bath. Finally although the sample used was high purity, $> 99.9\%$, it could also be purified further by distillation. Although a potential error, an absorption above the expected value would only be caused if any impurity was also an absorber. Since the main gas evolved is nitrogen it is unlikely. The pressure of acetone is recorded using a capacitance manometer with an error of 0.2% and is unlikely to be the main contributing factor unless its calibration was off. It should also be noted that ideally the overlapping parts of the $0.5\,\mathrm{nm}$ scans comprising the data should be longer than only a single point.

3.12 Acetone Fluorescence Quantum Yield Scan Results

Measurements were made again recording acetone at a pressure of $2 \cdot 10^{-2}\,\mathrm{mbar}$ and temperature of $\sim 293\,\mathrm{K}$. Since higher resolution data showed the absorption band at $220 \rightarrow 340\ \mathrm{nm}$ to be broad and featureless, data was recorded at a lower resolution. Measurements were taken between $313 \rightarrow 318\,\mathrm{nm}$ at a resolution of $0.05\,\mathrm{nm}$ in three sections $\sim 2\,\mathrm{nm}$ in length. Each section had an overlap region of $0.5\,\mathrm{nm}$. 500 laser shots per data point were taken, and the PMT gain combined with tuning of the dye laser doubling crystal was used to maintain maximum output voltages of $\sim 8 \rightarrow 10\,\mathrm{mV}$ on the CRD detector, and $\sim 40\,\mathrm{mV}$ on the LIF detector. Background scans were run in between each measurement using the TMPs to evacuate the cavity.

Measurements were made varying the polarisation of the laser while monitoring the acetone fluorescence signal and no anisotropy in the signal was observed. Therefore polarisation of the incident laser light remained at the magic angle for all measurements. Acetone fluorescence data was calibrated to a nitrogen measurement taken using exactly the same settings at $200\,\mathrm{mbar}$. Figure 3.12 shows the absolute quantum yields calculated and figure 3.13 shows the nitrogen data used to calculate it. As with the high resolution acetone data the CELIF data is omitted in figure 3.13.

3.12.1 Analysis

Figure 3.13 shows CRD derived cross-sections and compares them to recent data from Ityaksov *et al.* As discussed in section 2.10, the wavelength dependence of the refractive index and the King correction factor means that Rayleigh scattering is not proportional to $1/\lambda^4$ as is commonly stated. Ityaksov *et al.* created a mathematical fit, equation 2.23, describing the variation of the nitrogen Rayleigh cross-section, in terms of two variables which are provided for specific wavelength ranges in table 2.1. Nitrogen Rayleigh scattering cross-sections have been shown in reference to the data from Ityaksov in figure 3.13. The fit despite being outside the wavelength range, $197.70 \rightarrow 270.15\,\mathrm{nm}$, valid for the data correlates well. In comparison data from their previous paper by Sneep *et al.*[132] scaled by a $1/\lambda^4$ relationship does not correlate with these recorded nitrogen scans. From

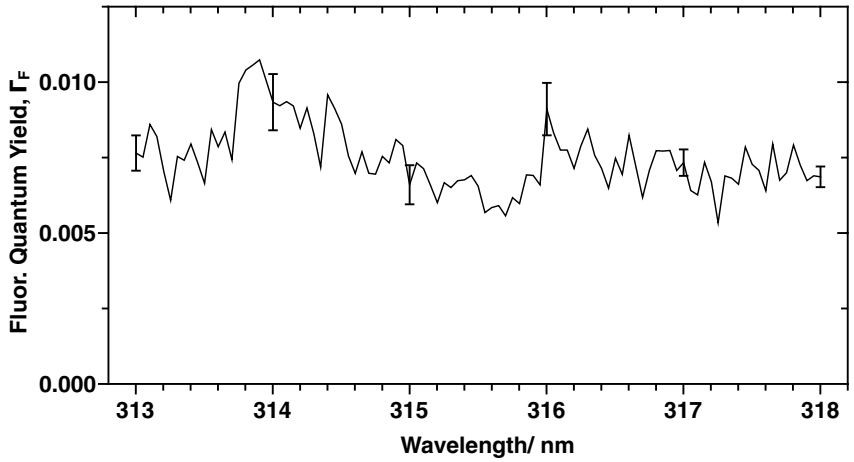

Figure 3.12: Absolute quantum yields of acetone fluorescence are shown. Data was taken in three scans between $313 \rightarrow 318\,\mathrm{nm}$, each $\sim 2\,\mathrm{nm}$ in length with a resolution of $0.05\,\mathrm{nm}$. Results have been calibrated using a CELIF measurement of nitrogen Rayleigh scattering at $200\,\mathrm{mbar}$. The standard error in the data is shown.

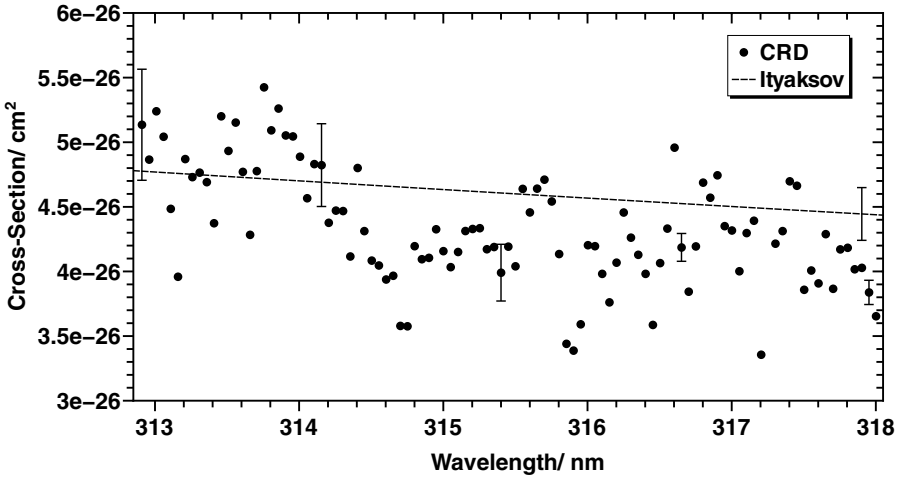

Figure 3.13: Nitrogen Rayleigh scattering cross-sections derived from the CRD results used to calibrate the acetone fluorescence quantum yield. Data was taken in three scans between $313 \rightarrow 318\,\mathrm{nm}$, each $\sim 2\,\mathrm{nm}$ in length with a resolution of $0.05\,\mathrm{nm}$. The standard error of the data is displayed for a select points; larger errors are from averaging over the overlapping data sets. Data is compared to derived data from Ityaksov *et al.*[133] with an error shown derived from the reference.

this strong correlation the calibration measurement is understood to be good.

The calculated acetone fluorescence quantum yields for the range $313 \rightarrow 318\,\mathrm{nm}$ are displayed in figure 3.12. Data has been processed with the scheme laid out in equations 3.12 and 3.13 and S^{LIF} data has been background subtracted for each data point. Previous work measuring absolute quantum yields is laid out in table 3.3 and indicates although data is of the correct order it is higher than previous measurements. Errors shown are the standard error but the standard deviation is approximately of equal magnitude to the measurement value. Thus, in terms of the standard deviation the measurements are within error of the previously recorded data though this is misleading.

Table 3.3: Comparison of studies measuring absolute quantum fluorescence yields for acetone from most recent to oldest. Table partially adapted from Koch *et al.*[162]

Author	λ (nm)	Γ_F ($\cdot 10^{-3}$)	Notes
This work	313	8.6	$P_{ace} = 2 \cdot 10^{-2}$ mbar, $T = 19\,^{\circ}$C
This work	318	6.8	
Koch *et al.*[162]	308	0.71	$P_{ace} = 4$ mbar, $P_{N_2} = 0$ mbar, $T = 23\,^{\circ}$C
		0.84	$P_{ace} = 40$ mbar, $P_{N_2} = 1000$ mbar, $T = 23\,^{\circ}$C
Halpern *et al.*[146]	313	1.2	$P_{ace} = 267$ mbar, $P_{air} = 733$ mbar, $T = 24\,^{\circ}$C
Heicklen[174]	313	2.07	$P_{ace} = 103 - 271$ mbar, O_2 present, $T = 40\,^{\circ}$C

The results, in light of previous measurements, are over-estimating the fluorescence quantum yield by $\sim 4 \rightarrow 5$ times increasing to an order of magnitude in light of the lower quantum yields reported by Koch at $308\,\mathrm{nm}$. It is not unreasonable to expect quantum yields to change at different wavelengths but assuming that the quantum yield is over-estimated by up to an order of magnitude potential sources of error should be discussed. From section 3.2, we can expand the equation for the calculating the quantum yield into its individually measured components,

$$\Gamma_F = \frac{I_R^{CRD}}{S_R^{LIF}} \cdot \frac{\alpha_R}{\alpha_F} \cdot \frac{S_F^{LIF}}{I_F^{CRD}} \tag{3.14}$$

where R is a Rayleigh calibration and F is a fluorescence measurement. Equation 3.14 shows that in order to gain or lose an order of magnitude from the calculation an order of magnitude needs to be gained or lost across one or several measurements from either the integrated signal across the PMTs or CRD derived absorptions. An error in these values of this magnitude is unlikely to occur without it being observed within the data. CRD derived cross-sections for acetone in this measurement match even better than those displayed in figure 3.11. Similarly nitrogen cross-sections in the calibration measurement were also seen to be good. Therefore problems equating to an order of magnitude from the RDT measurements seem unlikely.

This leaves only a few options that can be contributing to the over-estimate in quantum yield. One involves accounting for the relative spectral sensitivity of the LIF detector. The LIF detector sees a completely different wavelength range to the CRD detector and this is not accounted for in the normalisation process. The PMT detector used has a higher sensitivity at wavelengths longer than $313\,\mathrm{nm}$ peaking around $400\,\mathrm{nm}$ and dropping towards $550\,\mathrm{nm}$ as much as it rises initially. This is good evidence that the LIF signal is over-estimated as desired, however the difference in sensitivities alone is not sufficient to explain the error. Another option is that the quantum yield observed is real.

From the literature and observation in the example acetone data in figure 3.4 the answer is found. It was understood that acetone phosphorescence had a long lifetime of

$\sim 200\,\mu$s. However in high enough concentrations self-quenching may occur and this value decreases dramatically to $\sim 1\,\mu$s according to Lozano *et al.*[144] When the data was taken acetone pressure were kept relatively low in order to avoid amongst other things possible quenching effects. Figure 3.4 however shows large peaks occurring at the $\sim 2\,\mu$s mark. These reliably appear in other data shots and may be evidence of phosphorescence appearing from self-quenching. If true the absolute quantum yields derived from the data also include phosphorescence as well as fluorescence. With this in mind further investigation should be pursued retaking the data and integrating it over a shorter time frame to avoid including the phosphorescence peaks. However with this knowledge, it is likely that the absolute quantum yields displayed accurately represent the measurements taken by the experiment.

3.13 Analysis of the CELIF Technique

CELIF has been shown so far to be competitive with CRD measurements. Often it is better in quality owing to generally lower errors from smaller standard deviations in the data that decrease, up to a certain point near the LOD. This stems from a number of points about the CELIF technique. First the PMT detector produces lower noise in the signal when there is less LIF being received. As well as this, CELIF is, at least in theory, a background free technique and noise from background light scatter is virtually eliminated through the use of a well defined cavity; any light that is not coupled into the TEM_{00} correctly is quickly eliminated.

Observations in the pressure varied N_2 Rayleigh scattering data showed that it is more robust with respect to shot-to-shot changes in the cavity caused by pressure fluctuations, vibrations, temperature changes, mode fluctuations or any event which might cause the ring-down to be affected. Where these affect the CRD data they do not appear so strongly, if at all, in the CELIF data. This is because CELIF is focused on the normalised total integral of light in the cavity as opposed to CRDS, which is interested in the time evolution thus it is effected strongly by changes to its shape. Also on a shot-to-shot basis the ring-down time is compared to a single averaged background trace in order to obtain a measurement. In comparison each CELIF measurement is normalised against the instantaneous state of the cavity at the time of the measurement thus shot-to-shot noise is lower than in the determination of the ring-down time.

Another advantage of the CELIF technique that has not been mentioned so far exists in the way that it obtains the fluorescence spectrum in comparison to an equivalent single pass LIF experiment. In a single pass LIF experiment such as the equivalent for acetone the light collected must be measured over the timescale of the fluorescence lifetime. For acetone, which has a nanosecond fluorescence lifetime, this means digitising the signal over a very short period. In CELIF this same fluorescence signal is spread over the time frame of the ring-down event making it significantly easier to digitise it with greater precision.

The results of this study indicate that these improvements seem to be the main advantages to using CELIF in the broad scope found so far. The acetone and nitrogen data demonstrate that beyond this the dynamic range of CRDS is not extended unlike in the BPEB molecular beam experiment where CELIF increases the dynamic range by 3 orders of magnitude. The reasons for this are threefold,

1. Path Length
2. Fluorescence
    - Strength
    - Lifetime
3. Quenching

Firstly CRDS has the advantage of the increased path length from using the full gas cell in these tests. The cell path is nearly 20 times the length of the probed volume in the BPEB experiment where it was the width of the molecular beam at the point it intersected the cavity axis, $\sim 3\,\mathrm{mm}$. This idea can be expressed further in terms of the minimum detectable absorptions, equation 2.12, shown in table 3.4. For an experiment run at $313\,\mathrm{nm}$ theoretical $\alpha_{\min}$ are shown over sample lengths, s, equal to the full length of the cavity, d, the LIF probe volume for our optical set-up, p_{l}, and for the BPEB experiment. By increasing the path length from the width of a molecular beam to the full gas cell, $\alpha_{\min}$, changes by three orders of magnitude. This is also shown in terms of the pressure of acetone or nitrogen that would be required to meet $\alpha_{\min}$. Since the higher pressures needed to meet $\alpha_{\min}$ are not always feasible, CELIF is able to out-perform CRD. The drop in performance level for CRDS from decreasing s has no impact on the CELIF detection limit as CELIF only ever observes the LIF probe volume and nothing more. Moreover crucially for the CELIF technique the experiment must always be able to work in a region where both CRDS and CELIF operate. Therefore the path length can effect CELIF negatively as if $\alpha_{\min}$ for CRDS is not surpassed then CELIF cannot be used.

Table 3.4: $\alpha_{\min}$ for several CRDS experiments have been derived using equation 2.12 combined with the parameters, $\tau_0 = 1.11\,\mu\mathrm{m}$ and $R = 0.9975$, derived from measurements at $313\,\mathrm{nm}$ using the experimental set-up described in previous sections.

Experimental Set-Up	$\boldsymbol{\alpha_{\min}}$ **($\mathbf{cm^{-1}}$)**	$\mathbf{P_{min}^{ace}}$ * **(mbar)**	$\mathbf{P_{min}^{N2}}$ † **(mbar)**	**d (cm)**	**s (cm)**
Gas Cell	$2.1{\cdot}10^{-7}$	$8{\cdot}10^{-4}$	180	80	80
Probe Volume	$3.8{\cdot}10^{-6}$	$1.5{\cdot}10^{-2}$	3200	80	4.5
Molecular Beam	$5.7{\cdot}10^{-5}$	0.21	48400	80	0.3

* Acetone pressures calculated using Gierczak[171]
† Nitrogen pressures calculated using Ityaksov[133]

Gas cell path length versus absorption path length is a feature affecting the success of both CRDS and CELIF. For CELIF alone, fluorescence is one of two factors governing its LOD. The quantum yield of the fluorescence emission directly governs the strength

of S^{LIF}. The stronger and more efficiently a LIF pathway is able to perform the better it can operate below the minimum detectable absorption for the CRD technique, which ultimately governs to what degree the CELIF technique can extend the dynamic range of CRDS. Tied up with this a second key factor in CELIF is quenching. Standard CRD usually takes place on a time-scale of microseconds. For long lived fluorescers on the scale of the ring-down event at pressures where collisions between the molecules in the sample occur frequently quenching and self-quenching can occur. As was seen with NO_2 this can significantly interfere with a measurement, killing off LIF signal almost entirely at longer times in the ring-down. Thus an advantage of using a molecular beam is that it can avoid this issue by simulating a near quenchless environment.

From these reasons, a picture is constructed as to why the BPEB experiment has been so much more successful than the implementation of CELIF as a general technique so far. In the case of BPEB, it is a strong fluorescer, which as a solid at room temperature promoted Greaves *et al.* and Sanders to use a molecular beam oven to seed it in the gas phase.[158,160] This provides a near quenchless environment for fluorescence to occur and moreover partially refreshes the molecules in the probe volume across a measurement. Furthermore the quantum yields for BPEB have yielded values of $\Gamma_{\mathrm{F}} = 0.58$,[175] two orders of magnitude higher than acetone at $\sim 1 \cdot 10^{-3}$. The short absorption path length equal to only the width of the molecular beam ensures that CRD is not able to work far beyond the its LOD but the strong fluorescence ensures that CELIF is capable of producing excellent results.

3.14 Conclusion and Future Work

In this study CELIF has been examined exploring it practically to test the theory developed behind the technique and use it to calculate absolute quantum yields of fluorescence. It has been investigated as a stand alone technique in its own right and in its role extending the dynamic range of standard pulsed CRDS in its simplest form, an $\sim 80\,\mathrm{cm}$, gas cell enclosed by highly reflective mirrors. CELIF has been successfully used to monitor pressure varied nitrogen Rayleigh scattering, at $583.5\,\mathrm{nm}$, and acetone absorption, at $313\,\mathrm{nm}$. They have shown that CELIF signal is linear with respect to increasing concentrations of a sample, expressed mathematically in equations 3.7-3.10. They have shown that the time integrated signal from CRDS can be used to calibrate LIF signal born from the centre of a cavity in a novel single-beam experiment where both signals are obtained simultaneously. By calibration with a CRD measurement absolute absorption coefficients, cross-sections and particle densities can be derived from the CELIF data. For these measurements it has been shown that the two techniques are comparable in the dynamic range covered. They only differ in the quality of the data and in this CELIF surpasses CRDS.

Polarisation measurements have clearly demonstrated the dependence of Rayleigh scattering with the polarisation of the incident laser, a well-known phenomenon. This has

highlighted a potential problem where a $9\,\%$ elliptical depolarisation of incident light coupled in through the cavity mirrors was observed. For measurements where absolute polarisation of the light in the cavity is necessary this should be dealt with for the most accurate measurements. Measurements varying the power entering the cavity, and hence the I^{CRD}, have been taken with different pressures of acetone and different S^{LIF} detection gains at $313\,\mathrm{nm}$. As with the pressure varied measurements, trends were observed indicating that S^{LIF}, scales linearly with I^{CRD}. This proves scaling remains linear during modification of the two main experimental parameters used to take unsaturated absorptions and maximise fluorescence signal.

Absolute quantum yields of fluorescence for acetone have been measured using equation 3.13 through calibration using a nitrogen Rayleigh scattering measurement at the magic angle. During this a high resolution scan of acetone absorption was taken between $313 \rightarrow 318\,\mathrm{nm}$ agreeing with previous literature scans which show a broad featureless absorption and our reported absorptions are within $10\,\%$. The Rayleigh scattering data across the same range has agreed with the deviation of the scatter from the traditional $1/\lambda^4$ relationship discussed by Ityaksov *et al.* Quantum yields for acetone measured by this process have been calculated at $\Gamma_{\mathrm{F}} = 7.5 \pm 0.6 \cdot 10^{-3}$ averaged across the range $313 \rightarrow 318\,\mathrm{nm}$. They are overstated relative to literature values of $\sim 1 \cdot 10^{-3}$ measured at $308\,\mathrm{nm}$. Two main factors likely contribute towards this, firstly there is the possibility of the inclusion of some phosphorescence occurring at shorter than expected lifetimes from acetone self-quenching. Secondly the data needs to be modified to account for the relative spectral sensitivity of the PMT detector with respect to the Rayleigh scattering calibration. However within this framework the acetone quantum yields are believed to be a reliable measurement and proof of concept.

Future work on CELIF is available improving the set-up and running further experiments on acetone quantum yields. CELIF has been shown to be comparable to CRD, however unlike the pulsed CRD experiment, there are significant modifications that can be made to the set-up to further improve CELIF detection. In the experiments run the signal received by the PMT was in a near-photon counting regime. Appropriate modifications to the signal analysis program and acquisition of a PMT designed for photon counting would improve detection sensitivities potentially by orders of magnitude. Another experimental improvement is to the LIF detection optics. Discussed in the section 4.5.1 these can be improved by using the simulation program to simulate the LIF collection optimising the types of lenses used and their position along the CELIF axis. As well as this there is the potential to install along the z-axis on the opposite side of the cavity beam relative to the LIF detection optics, a mirror. This can be designed to reflect LIF, which has been emitted away from the detection optics, back into them and improve the amount of light collected. As discussed the acetone quantum yields may include phosphorescence and a repeat is encouraged to see if exclusion of this signal from the measurement can solve the majority of the overstatement from this work. Lastly investigation into the literature shows that there is still further work that can be performed on the gas phase

fluorescence spectroscopy of acetone where there is limited data available and conflicting measurements of the quantum yields. This work would also be applicable in future measurements of the dynamics of acetone with ice films.

In summary the data presented here shows how CELIF is an excellent companion technique to CRDS but in order to extend the dynamic range for the generalised case further improvements are required to the set-up. Currently its best use is in a more specialised set-up with a specific probe molecule. Ideally this is an experiment where the absorption path length, s, is much smaller than the CRD path length, d, on the order of the length of the LIF probe volume, and where the molecule being probed has a high quantum yield and a fast fluorescence.

CHAPTER 4

Experimental Build

The goal of this project is to design and build an experiment for probing the interaction and dynamics of trace atmospheric gases with ice, initially using small, well characterised molecules such as acetone, methanol and nitric acid. Literature shows that ice surfaces play a key role in atmospheric dynamics yet despite a large amount of research many aspects remain poorly understood. The key temperature region to be looked at is between $273 \rightarrow 210\,\mathrm{K}$, that of the troposphere and stratosphere, where nearly $100\,\%$ of the earth's atmospheric water content is found.

Despite this the majority of spectroscopic research to date takes place at low temperatures below $210\,\mathrm{K}$. The reasons for this are twofold, first the far temperature regime is of interest to groups investigating and modelling interstellar ices. Moreover at lower temperatures the vapour pressure of ice drops off to easily manageable values, $< 1{\cdot}10^{-2}\,\mathrm{mbar}$, facilitating a broader array of spectroscopic techniques, such as mass spectrometry, which can be difficult to use at high vapour pressures. Many ice surface experiments use liquid nitrogen combined with resistive heating or a liquid coolant based set-up to access temperatures across a wide range between $77 \rightarrow 273\,\mathrm{K}$ with varying degrees of accuracy from $\pm 0.1 \rightarrow 1\,\mathrm{K}$.

CRDS and CELIF, outlined in chapters 2 and 3, are sensitive techniques which can be used at a large range of vapour pressures from UHV right up to and exceeding atmospheric pressures. Combining these two techniques to study ice films will prove a valuable method to probe processes occurring at a complete range of tropospheric and stratospheric pressures and temperatures. For this a different cooling system is proposed directed towards the tropospheric and stratospheric temperature range. The use of peltier modules is suggested which might offer greater control, accuracy and an ease of set-up not found with liquid nitrogen based methods. These are robust devices used in modern technology as heat sinks, for example in computers. They are also used in commercial scientific analysis for the cooling and heating of samples across wide temperature ranges, such as in scanning electron microscopes. They are capable of reaching and maintaining large temperature differences up to $130\,\mathrm{K}$ with the surrounding environment.

The goal of this thesis is to investigate the potential of a peltier set-up targeted towards ice film growth for use in experiments measuring chemical dynamics at the ice-air/vacuum interface. Success could potentially provide a "dial up" approach to setting up a thin ice film for study with CRD based techniques. Ultimately the long term goal is to combine CRDS and CELIF with Evanescant Wave CRDS (EWCRDS) for the study of bulk processes to provide a complete characterisation of dynamics in and on the ice film. Although laying outside the scope of this thesis, this fact plays a strong role in parts of the design. Briefly, evanescent waves both penetrate into and propagate along the boundary of a totally internally reflecting interface, such as a prism. This allows interaction with medium above the boundary providing absorption measurements or promoting chemistry. The depth of penetration is set by the TIR angle where at the critical angle it tends towards infinity becoming shallower as the reflection angle increases and changing with the refractive indices of the media involved. Generally it is in the order of the incident wavelength therefore to probe molecular species in and on ice, thin films need to be deposited nanometres to micrometres in thickness. EWCRDS has been used previously to study a variety of interfacial processes on prisms including water.[176–179]

Combining the different goals of the research project, the main aims of this experimental build can be summarised,

1. Develop an Experimental System
    - For use with CRDS, CELIF
    - Using a peltier driven cooling system
    - But with an outlook to EWCRDS
2. Create and control the growth of thin ice films in the laboratory
    - Ice temperatures, $T_{\mathrm{ice}} = 273 \rightarrow 210\,\mathrm{K}$
    - $0.1 \rightarrow 10\,\mu\mathrm{m}$ in thickness
    - Maximising the ice area (across a prism sized surface)
    - Uniform in character

4.1 Experimental Figures

Discussion of the different details in the build process continues after this section introducing the build figures. The set-up has been split into the two different parts of the experiment, the CELIF setup (including the CRD setup) and the peltier surface cooling. Both constructions are centered around a pre-existing, 6", CF100, cube. This central feature lends itself well to gas phase laser experiments, in particular for CRDS as it has a wide range of access ports and small volume for rapid pumping. All constructions placed within the body of the cube can be no larger than $\varnothing 100\,\mathrm{mm}$ and designs are made with this in mind. Reference is made to figures 4.1-4.7 throughout the main body of the text. These show the layout and design of each part in full. Table 4.1 contains the information on the descriptive annotations and markers used in the figures.

Table 4.1: Table, for reference with the experimental build figure series 4.1-4.7, provides descriptions of the different parts of each diagram.

Part Main	Part Sub	Description
1		**CRD entrance mirror and alignment housing** Mirrors are sealed and aligned by compression against viton o-rings on a CF40 flange. The end is supported in a frame aiding the stability of the cavity.
2		**CELIF optics and signal PMT**. Hardware is contained on a CF100 flange. Optics are o-ring sealed. A vented lens tube/light scatter shield sits inside the flange.
3		**CRD exit mirror and alignment housing**. See (1) for detail.
4		**CRD signal PMT**. Sits behind the exit mirror (3). It is encased in a delrin frame to shield it from background light and supported on an optical mount.
5		**Ice surface assembly**. This is split into two sections, the external port aligner and the internal equipment which contains the peltier driven cooling set-up.
		5a - e, the external apparatus and port aligner partition.
	a	Partition pumping ports connected to a rotary pump and TMP
	b	Liquid cooling unit inlet and outlet
	c	Windows for surface/evanescent wave laser
	d	PSU and thermocouple (TC) feedthroughs
	e	Port aligner surface alignment screws
		5i - vi, the peltier surface cooling mechanism.
	i	Fused Silica prism or metal surface block glued to Al plate
	ii	3 stage peltier
	iii	stainless steel (SS) heatsink and lid. Liquid cooled internally by a reservoir linked to 5b
	iv	Thermally isolating bolts for fixing Al plate to peltier cold surface
	v	PT1000 temperature probe glued to upper prism or metal block surface
	vi	Miniature optical mount for guiding a surface laser through prism internally reflecting from the upper surface.

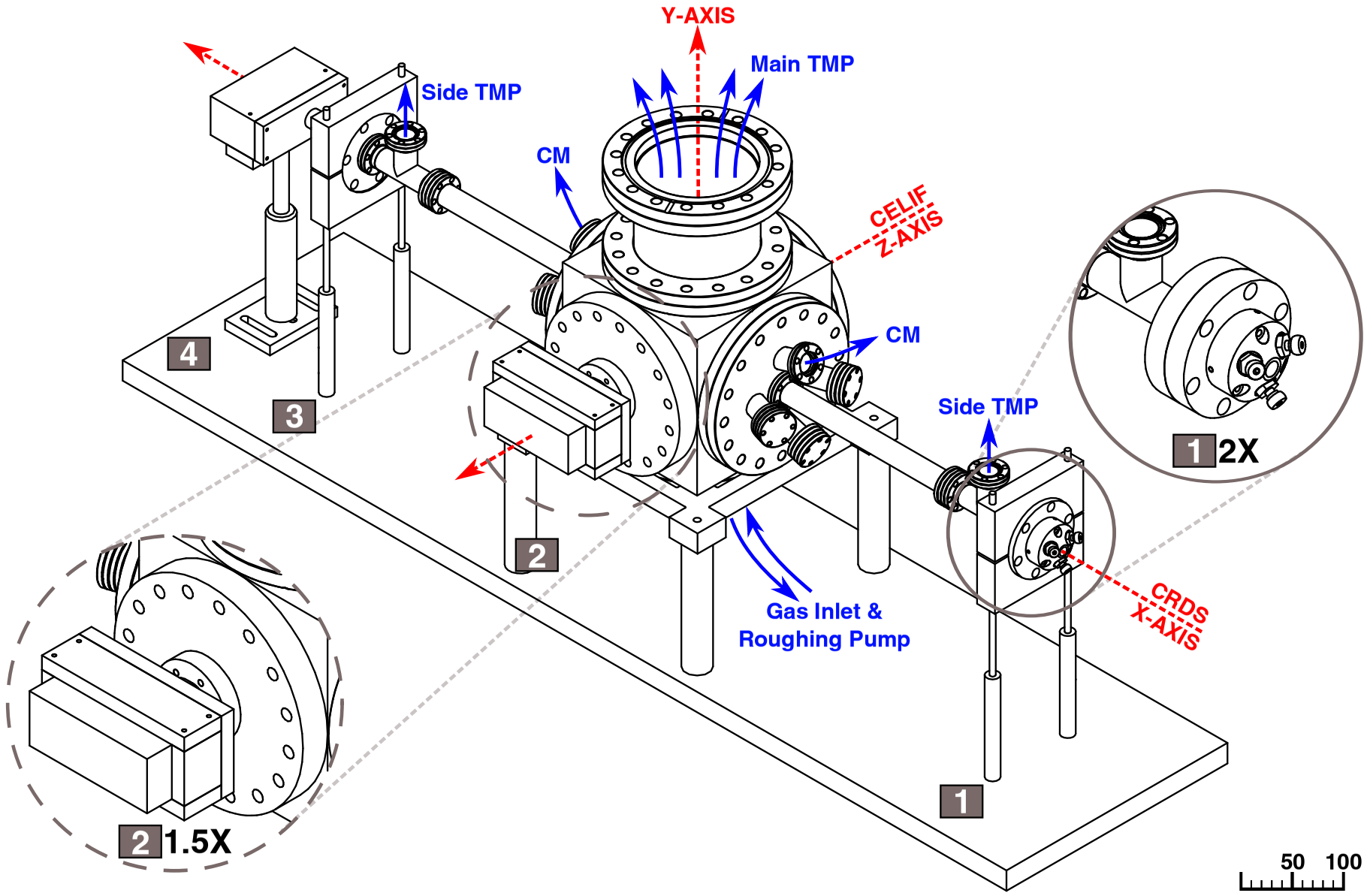

Figure 4.1: This diagram should be referenced along with table 4.1. Distances are in millimetres. A complete schematic of the general CELIF set-up is displayed. Key details (dashed and solid circles) are shown in further detail in figures 4.2 and 4.3. The CRD laser enters from the right into the first CRD mirror (1) along the cavity to the exit mirror (3) received by the PMT (4). LIF monitoring occurs in the centre (2) directed into another PMT. The main axes are displayed (red) with further experimental details (blue).

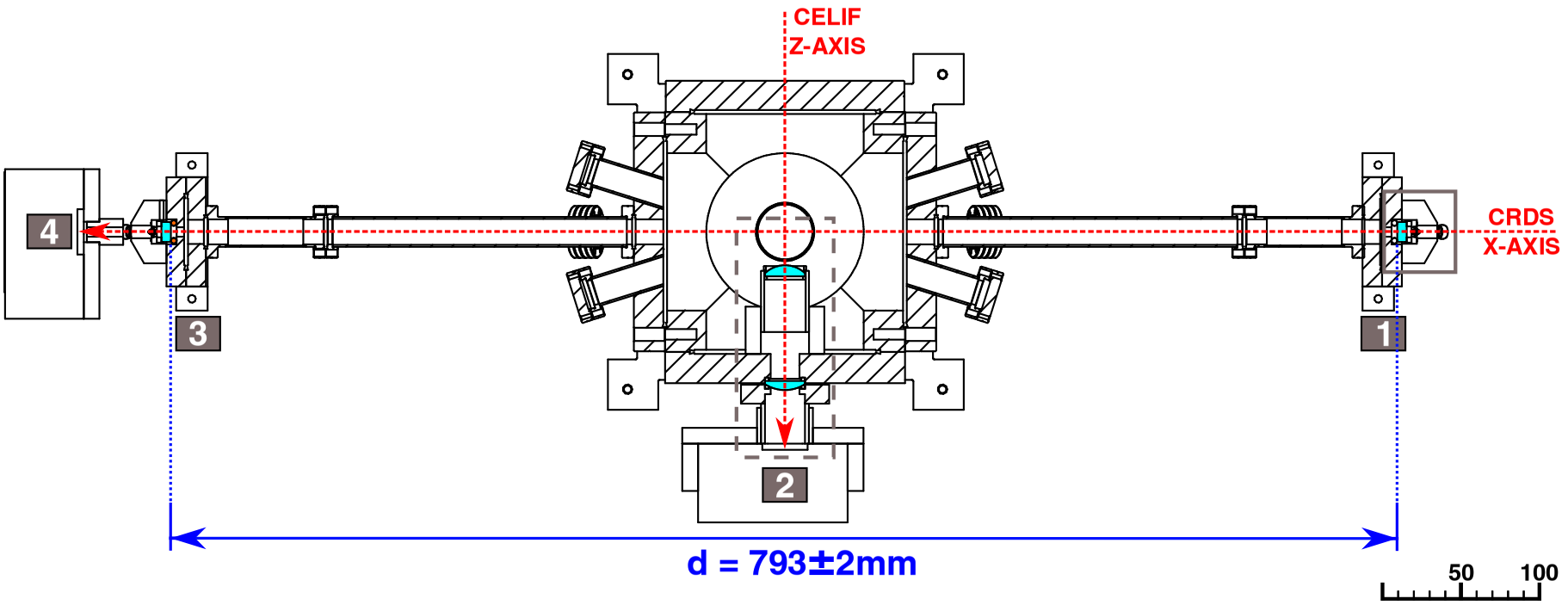

Figure 4.2: This diagram should be referenced along with table 4.1. Distances are in millimetres. A cut-through of the CELIF set-up from figure 4.1 in the xz-plane is shown. Axes are displayed (red) with further experimental details (blue). Elements in light blue are the optical components of the CRD set-up and LIF. Boxed regions are presented in further detail in figures 4.3a and 4.3b.

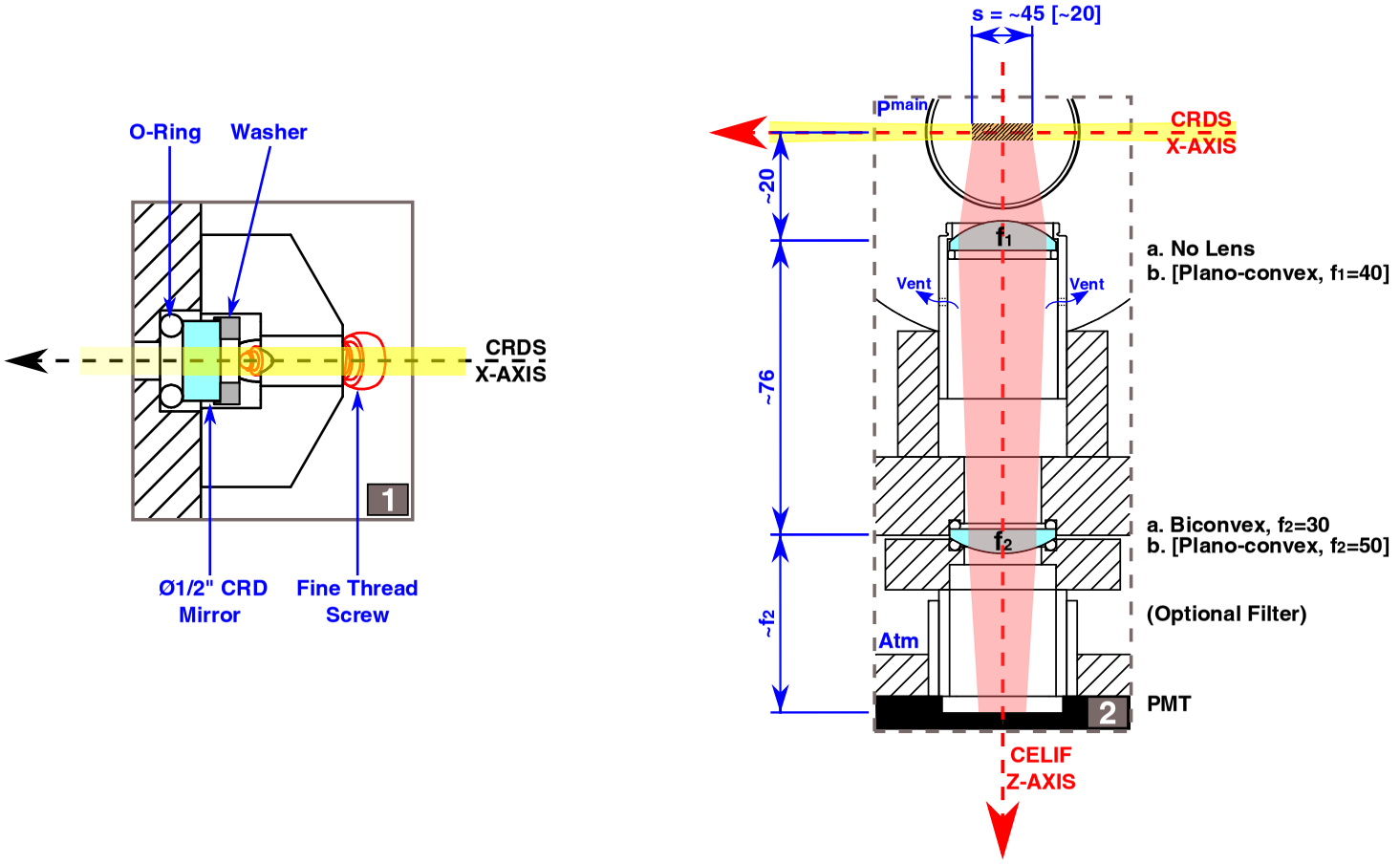

(a) CRD mirror alignment housing detail view

(b) CELIF optical axis detail view

Figure 4.3: Expanded details from figure 4.2. The CRD laser is depicted (not to scale) in each figure (yellow) with the experimental axes. Distances are in millimetres.
a) shows the mirror housing used to align and support the cavity mirrors along the main cavity axis. The fine thread screw (red) lies under the plane of the cut.
b) shows the CELIF axis and optics used to image the source volume onto the PMT. The LIF volume is indicated by the region with black diagonal lines crossed with the CRD laser. s is the sample length probed by the CELIF optics. Two lens combinations were used during the experiments a and [b], distinguished by brackets. f_1 and f_2 are the focal lengths of each optical component. P^{main} is the pressure inside the set-up.

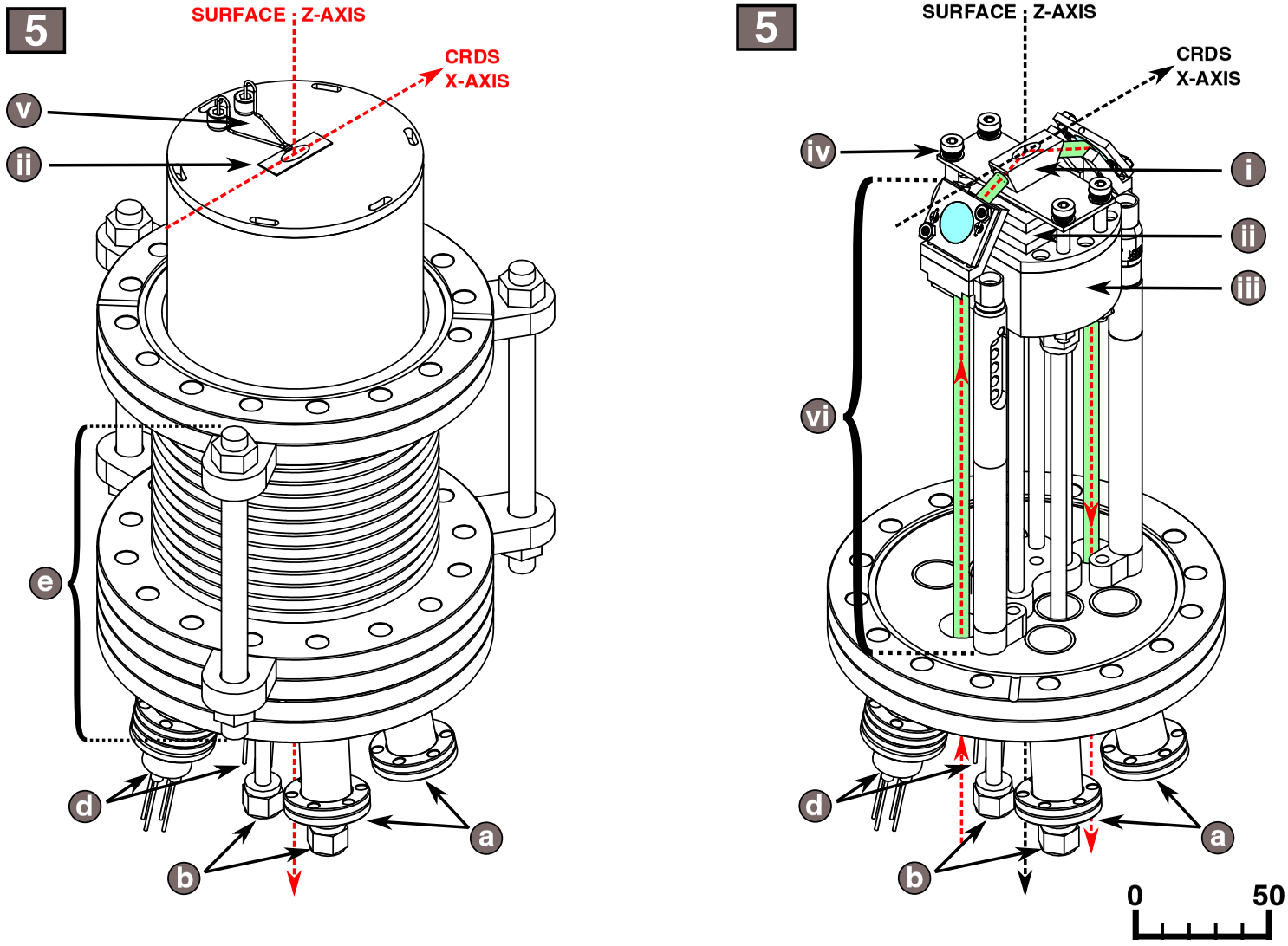

(a) Surface port aligner

(b) Peltier cooling set-up and surface laser

Figure 4.4: This diagram should be referenced along with table 4.1. Distances are in millimetres. *a)* shows the complete port aligner set-up with main axes (red). Detailed cut-throughs are shown in figure 4.5. *b)* shows the set-up without the top of the port aligner. It includes the mirror components designed to direct a surface laser (green) internally reflecting through a glass prism. The surface laser path is shown in red, axes from *a)* are in black.

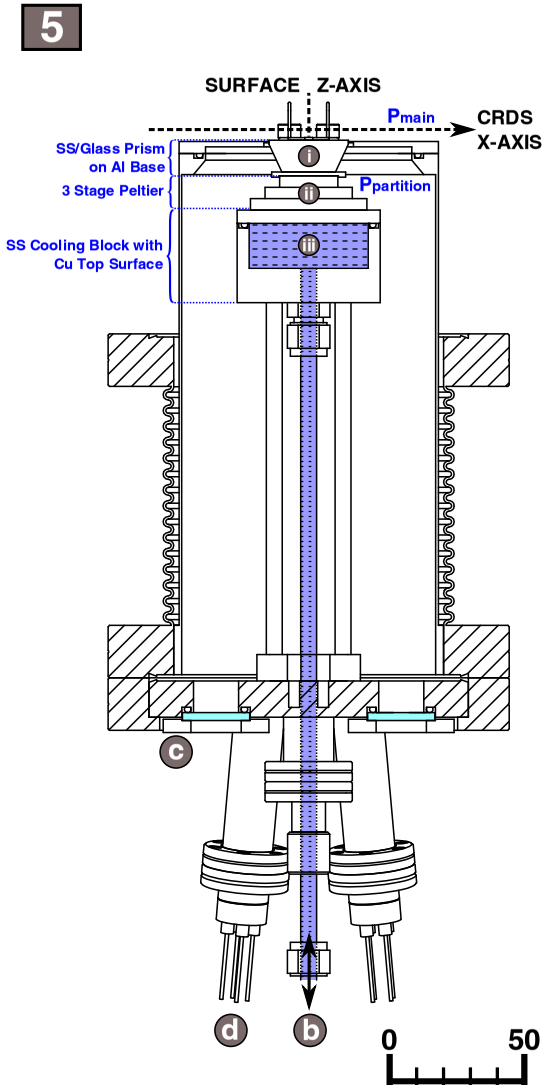

(a) Cut-through of the Surface cooling apparatus

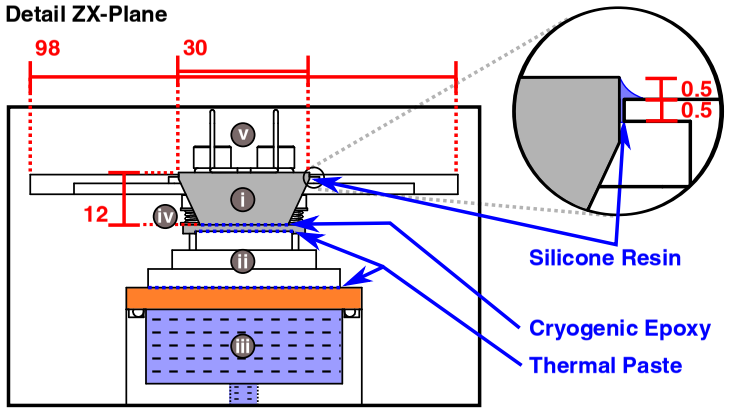

(b) Surface layering detail (zx-plane)

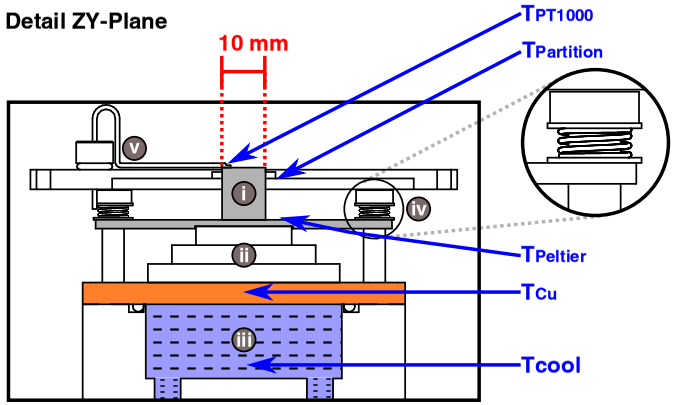

(c) Temperature monitoring detail, (zy-plane)

Figure 4.5: This diagram should be referenced along with table 4.1. Distances are in millimetres. The figure shows a cut-through of the peltier driven surface cooling system acting on a SS or glass prism. *a)* and *b)* display the zx-plane. *b)* details out the different interfacial layers. *c)* shows the ZY-plane and details the temperature probes, see section 4.12.

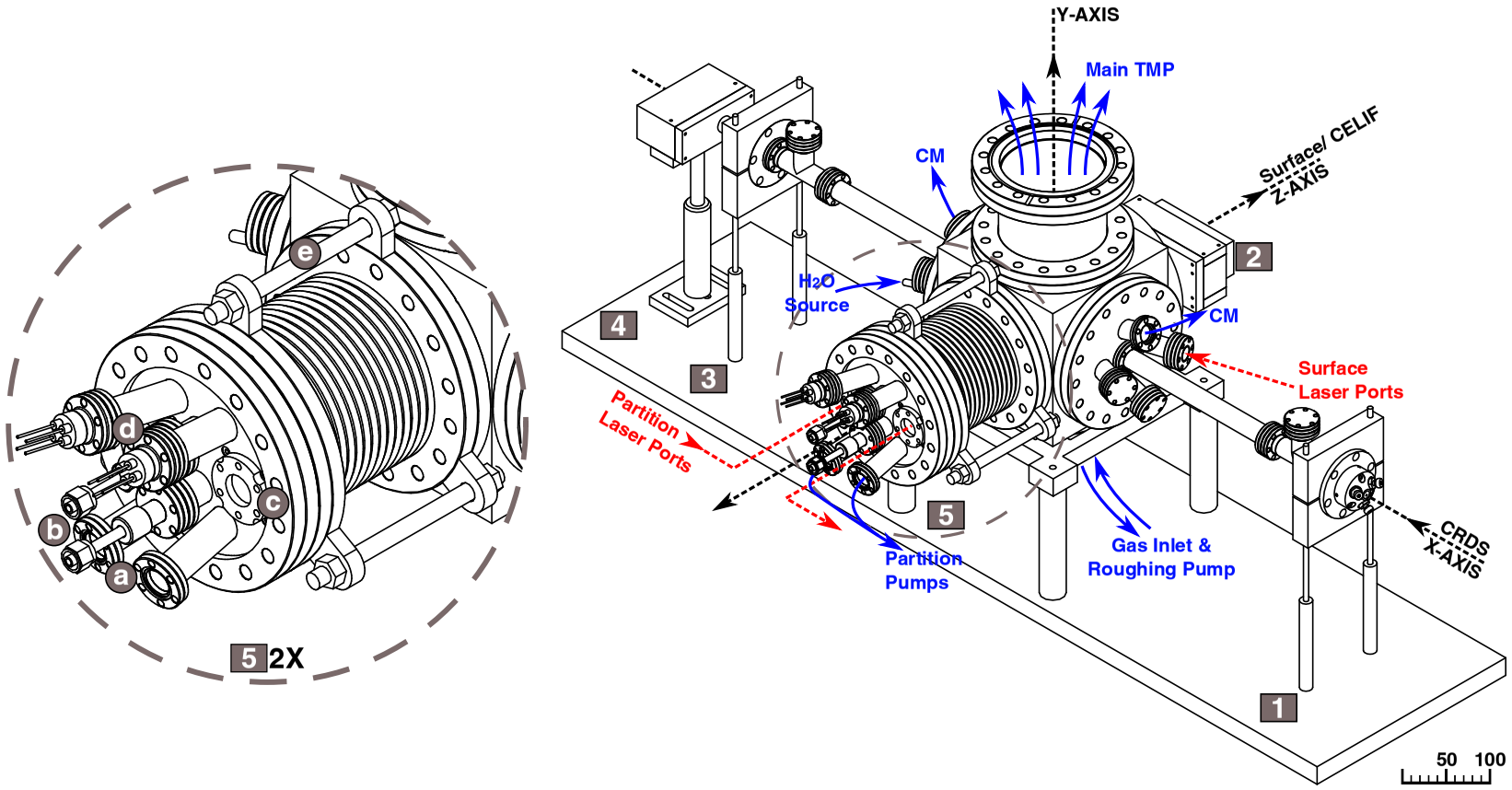

Figure 4.6: This diagram should be referenced along with table 4.1. Distances are in millimetres. The complete surface experiment is displayed. The main difference with figure 4.1 is the surface flange (5) now in place of the CELIF flange (2) which is now on the opposite side. Core experimental axes are shown (black) along with those for the optional surface probing lasers (red). Further details of the set-up, not depicted, are also shown (blue). For greater information refer to the main body of the text.

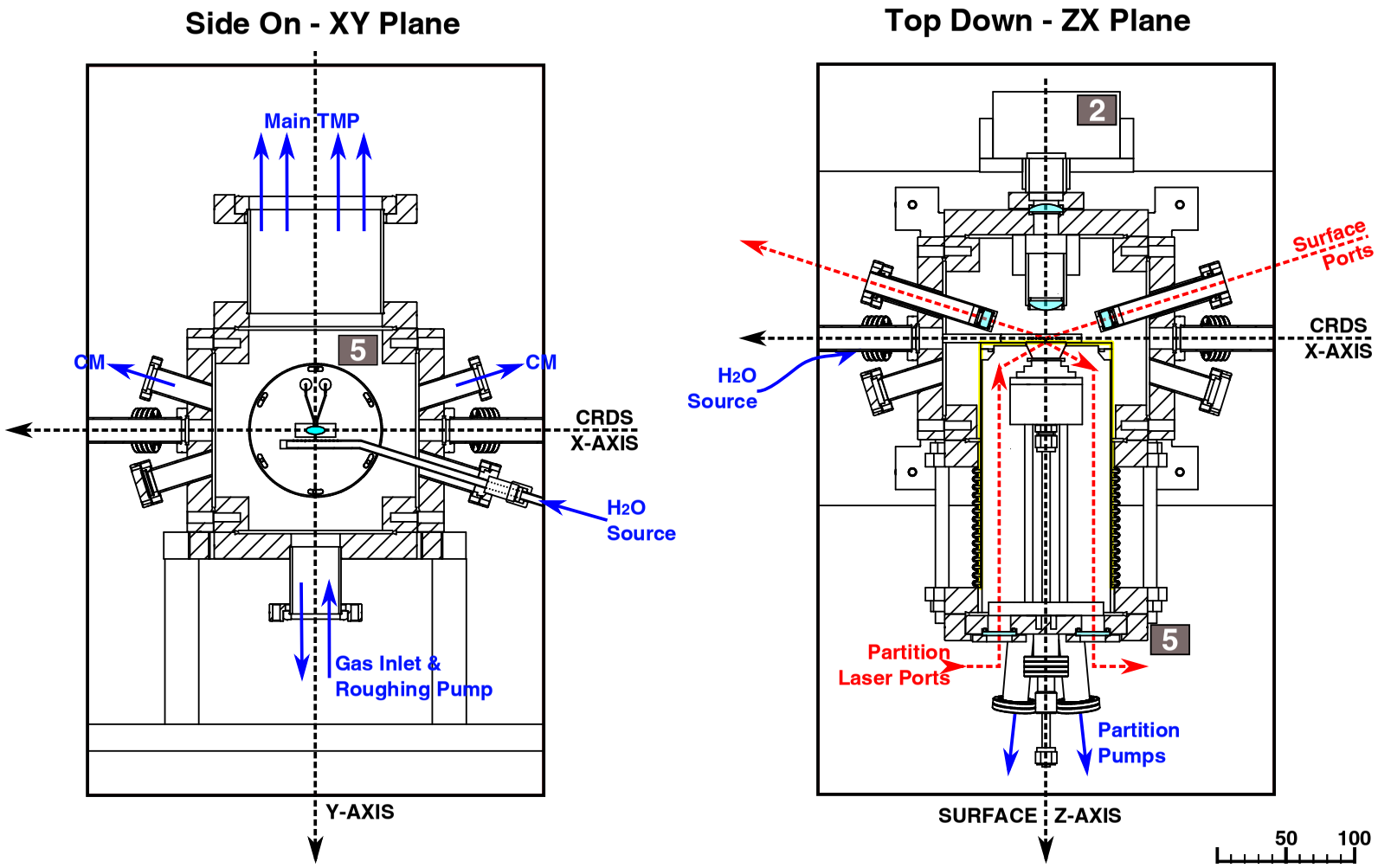

Figure 4.7: This diagram should be referenced along with table 4.1. Distances are in millimetres. Two cut-throughs of the central cube are shown. One is in the XY-plane facing the surface flange and the other the ZX plane facing down. As in figure 4.6 experimental axes are displayed (black) with further details (blue). The optional surface laser probes (red) are shown but without the mirrors inside the partition to aid clarity. For greater information refer to the main body of the text.

4.2 Laser Systems

Two different dye laser systems, labelled I, with two different configurations a and b, and II, were used during the experiments in chapter 3 and 5. Laser system I predated laser system II and was technically less superior in terms of Gaussian beam shape and collimation due to the age of the dye laser. The different laser dyes are provided in table 4.2, while table 4.3 provides details of the different laser systems used, their powers and bandwidths.

System Ia was a Quanta Ray PDL-1 outfitted with custom internal optics pumped with a $10\,\mathrm{Hz}$ pulsed Nd-YAG laser (Continuum Minilite II, $532\,\mathrm{nm}$, $28\,\mathrm{mJ}$). System Ib used the stock optics but was pumped with a stronger laser (Continuum Surelite SL-I, $532\,\mathrm{nm}$, max energy $250\,\mathrm{mJ}$). A delay line was installed to improve the overlap in time between the seed beam from the oscillator into the pre-amp to reduce amplified stimulated emission (ASE). In both set-ups the main amplifier was not used and moved out of the beam path. For Ia the pump was passed through a $50:50$ beam splitter into the oscillator instead of the stock $8\,\%$. A high reflector was used for the pre-amp beam and a cylindrical telescope was used to achieve an elliptical beam profile. Ib used the stock optics for the laser with the pump beam to the main amplifier directed into a beam dump. System II used a Sirah Cobra-Stretch laser combined with the Surelite and had a much improved beam shape and collimation.

In all set-ups the laser was passed through a focussing telescope and pinhole to clean up the beam and collate it to a near Gaussian beam shape. This was particularly necessary for the output of system I. Before entering the CRD/CELIF set-up a mode-matching lens was used to match the curvature of the beam to the cavity mirrors. Saturation issues from the signal on the PMT and from gas samples meant lower powers tended to be required for experiments. CRD requires only low laser powers to function and is largely unaffected by shot-to-shot fluctuations however it is not the best regime to run in. They were most significant with system Ib, and to a lesser extent II. System Ib was run at low pump powers, modified by tuning the Q-switch. II was tuned down by using only the oscillator without the pre-amplifier.

Table 4.2: Table of dyes used in the CELIF and surface experiments.

Code	Dye	Solvent	Pump[a]	λ_{peak}	λ_{min}	λ_{max}	Double[b]
			(nm)				
P597	Pyrromethene-597	MeOH	532	582	560	610	
DCM	DCM	MeOH	532	635	607	676	
DCM-BBO				317.5	303.5	338	BBO

[a] Pulsed, 10 Hz [b] Crystal type listed if dye is doubled, dye used is included in code.

Table 4.3: Laser systems and typical power outputs produced in the CELIF and surface experiments. Maximum powers are quoted though often the powers used were modified using the Q-switch or by only running only on the oscillator circulator.

	Dye Laser [Pump (Nd:YAG)][a]	$P^{532}_{\max}$ (mJ)	Dye	Typical Power Output		
				P (mJ)	λ (nm)	$d\lambda$ (pm)
Ia	Quanta Ray PDL-2 [Continuum Minilite II]	28	P597	$0.4^{b\,c}$	589	10
Ib	Quanta Ray PDL-2 [Continuum Surelite SL-I]	$260^{\,d}$	P597	$4.4^{b\,c}$	589	10
			DCM	$5.4^{b\,c}$	626	10
			DCM-BBO[e]	$0.25^{b\,c}$	313	···
II	Continuum Sirah Cobra-Stretch [Surelite SL-I]	$160^{\,f}$	DCM	$21^{\,g}$	627	···
			DCM-BBO[e]	$4.3^{\,g}$	313.5	···

[a] Pulsed, 10 Hz [b] Measured behind a large iris used to clean up initial output of dye laser. [c] A beam expander used causing a small amount of power loss in the measurement, $\sim 11 \rightarrow 16\,\%$. [d] Pump beam tuned down to $100 - 120\,\mathrm{mJ}$ using $50:50$ beam splitter [e] Using input from DCM. [f] Lower max power compared to Laser system Ib from Type I SHG generation of $532\,\mathrm{nm}$. Pump beam tuned down to $75\,\mathrm{mJ}$ using $50{:}50$ beam splitter. [g] Values shown for oscillator/pre-amp with main amp. However during experiments only the oscillator and main amp was used to reduce output powers to $\sim 0.1 \rightarrow 0.25\,\mathrm{mJ}$.

4.3 CRD and CELIF Set-up

A set-up was designed for pulsed CRDS combined with the monitoring of LIF emission borne from the centre of the cavity. Figures 4.1 and 4.2 show a 3D and cut-through of the complete set-up. The cavity is composed of two mirror mounts, parts 1 and 3 in the figures. These attach directly to side arms made from a CF40-CF16 zero length converter attached to a CF16 tee and nipple; each arm from the mirror face to its end is approximately $294\,\mathrm{mm}$ long. The arms are mounted centrally on a custom-made CF100 flange, positioned on two opposing faces of a 6" cube. Running through the centre of all these parts is the x-axis along which the CRD cavity is aligned.

Each custom CF100 flange contained four CF16 ports angled 17.5° towards the centre of the cube. On the uppermost of these the capacitance manometer (CM) bank was mounted which was used to monitor pressures, P^{main}, inside the cavity. During a standard CELIF experiment, in chapter 3, CF16 ports not used for pressure monitoring were blanked off. The total cavity length was measured by a fast fourier transform of the CRD signal obtained using a fast PMT (ps response time). A frequency of $189{\pm}0.5\,\mathrm{MHz}$ was obtained giving a cavity length, $d = 793{\pm}2\,\mathrm{mm}$. Including some additional spaces from gaskets and o-rings between components this agrees well with CAD drawings which place the d at $790.1\,\mathrm{mm}$. Two mirrors sets were used during experimentation. One set was designed for

a peak reflectivity at $585 \rightarrow 605\,\mathrm{nm}$ (Layertec #108840, $\varnothing 12.7\,\mathrm{mm}$, $\mathcal{R} = 1000\,\mathrm{mm}$) and used for nitrogen rayleigh scattering and water absorption measurements. The other set was for $330\,\mathrm{nm}$ (Layertec #105139, $\varnothing 12.7\,\mathrm{mm}$, $\mathcal{R} = 1000\,\mathrm{mm}$) used also in nitrogen rayleigh scattering measurements and acetone absorption measurements.

Table 4.4: Cavity characterisation in terms of the various parameters defined by the cavity construction and available mirrors sets. Values are derived from experimental data for τ_0 and the cavity length, $d = 793 \pm 2\,\mathrm{mm}$. λ_{dsgn} is the design wavelength for the cavity mirrors, λ_{expt} is the wavelength τ_0 and w_0 have been measured at. $\sigma_{\tau 0}$ is the standard deviation in τ_0 and $SEM_{\tau 0}$ is the standard error in the mean. R is the mirror reflectivity derived from τ_0, F, the cavity finesse and α_{min} the minimum detectable absorption based on $\sigma_{\tau 0}$.

$\boldsymbol{\lambda_{\mathrm{dsgn}}}$ $\boldsymbol{(\lambda_{\mathrm{min}} \rightarrow \lambda_{\mathrm{max}})}$[a]	$\boldsymbol{\lambda_{\mathrm{expt}}}$	$\boldsymbol{w_0}$	$\boldsymbol{\tau_0}$	$\boldsymbol{\sigma_{\tau 0}(\mathrm{SEM}_{\tau 0})}$	$\boldsymbol{R}$	$\boldsymbol{F}$	$\boldsymbol{\alpha_{\mathrm{min}}}$[b]
$\mathbf{(nm)}$	$\mathbf{(nm)}$	$\mathbf{(mm)}$	$\mathbf{(\mu s)}$	$\mathbf{(\mu s/10^{-2})}$	$\mathbf{(\%)}$		$\mathbf{(cm^{-1})}$
$585 \rightarrow 605$	583.5	0.301	34.7	$2(0.2)$	99.992	41100	$6{\cdot}10^{-10}$
	589.5	0.303	36.6	$2(0.2)$	99.992	43400	$5{\cdot}10^{-10}$
330 $(310 \rightarrow 350)$	313	0.221	1.08	$0.7(0.03)$	99.75	1280	$2{\cdot}10^{-07}$
	318	0.223	1.68	$0.8(0.04)$	99.84	1990	$9{\cdot}10^{-08}$

[a] Where $R > 99\%$, if not represented by a design wavelength.
[b] Typical as derived from experimental data, multiply by 5 for 5σ limit.

For the CRD and CELIF signal detection a pair of PMT modules (Hamamatsu H7732-10, wavelength range $185 \rightarrow 900\,\mathrm{nm}$) were used. Shown in 4.1 and 4.2 at (4) and (2) they were mounted in a Delrin enclosure to shield them from scattered room light. During standard operation, lights were brought to a low level in the laboratory. PMTs were matched to avoid any complications that might have arisen matching sensitivities and for convenience. The CELIF set-up is shown in figure 4.3b and the cavity has been characterised in terms of its different parameters in table 4.4.

4.4 CRD Mirror Mount, Design and Set-Up

Mounts were designed for the CELIF experiment replacing older, simpler designs in use at the beginning of the project. Both the older and the new CRD mirror holders operate by compressing a $\varnothing 1/2$" high reflective ($> 99.9\,\%$) mirrors against an o-ring to create a seal. Commercially available mounts use 1" mirrors which make for easier engineering and alignment but also are twice as expensive. Fine thread screws (Photonics Technologies, 170 TPI*) were used to compress the mirror against the o-ring and create the seal inside a CF40 flange. Three screws were positioned equidistantly around the x-axis as seen in figure 4.1 and angled towards the mirror. Each acts to center the mirror pushing against a lipped SS washer, in which the mirror sits. The balance between each of these screws was used to align the mirror with the cavity axis. A cut-through of the mirror mount is shown in detail in figure 4.3a.

* Threads Per Inch

During early CELIF experiments measurements varying pressure were needed. The original mirror mounts were inadequate since varying P^{main}, particularly going from vacuum to the first few mBar, caused the cavity alignment to shift during a measurement. Adjustments were made by changing the design of the mirror mounts to the ones displayed in the figures. The difference between these improved mounts and the older versions is in the exact compression method on the o-ring and the fine thread screws. Shown in further detail in figure 4.8, the current mounts push against the mirror in the centre using screws which are angled in. In comparison, the older mounts used lower grade fine thread screws (Thorlabs, 80 TPI) and pulled the mirror, fixed in a front plate housing, towards the cavity.

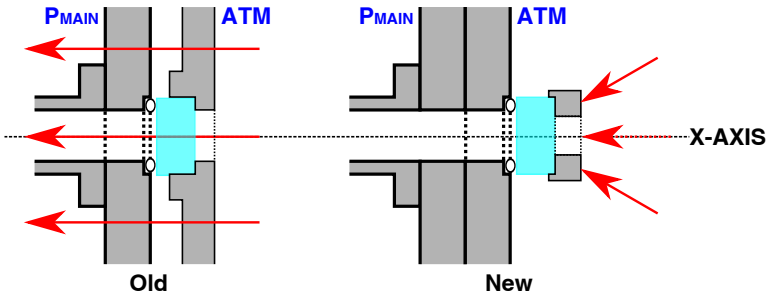

Figure 4.8: Comparison of the sealing method of the old mirror mounts relative to the improved versions are shown in a top down (zx-plane) schematic of the cavity mounts. Thick black lines mark the fixed cavity relative to the mobile mount face in thinner lines. Dashed lines show information behind the foreground. Each mount has three alignment screws placed around the cavity axis shown in a circle indicated by the red arrows. Mirrors are shown in light blue at the centre of each diagram.

The new mirror mounts were a large improvement over the older ones allowing measurements over wide pressure ranges $P^{\text{main}} = 0 \rightarrow 1000\,\text{mbar}$ demonstrated by the measurement of nitrogen Rayleigh scattering in figure 3.6. A second advantage was designed into the mount so that the end piece up to the first CF40 flange could be removed from the cavity and replaced whilst maintaining a partial mirror alignment; previously the mirror mount had to be fully dismantled. They are however more difficult to setup and clean. Unlike the older mounts the mirrors inside are not fixed into the front plate but freestanding, held in place only by the force of the alignment screws on the washer. This means a careful horizontal assembly onto the first CF40 flange must occur before it is mounted onto the front of the cavity. If the alignment screws are too far forward or too far from a neutral alignment then the mirror can slip from a centered position on the o-ring making alignment impossible. The assembly process then has to begin again and the mirrors recleaned. Mirrors were cleaned thoroughly before use in the set-up by washing with optical grade tissue and high purity solvents, acetone and isopropanol.

4.5 CELIF Set-up

One of the advantages to CELIF (and LIF) spectroscopy is its ease of implementation. All that is required is access to some part of the ring-down event which probes the tar-

get sample. Suitable optics were added and trained on the centre of the ring-down path where the ice surface was to be positioned along the z-axis. A CF100 flange was customised for the central cube to accommodate 1" lenses. One was installed into the flange and sealed with an o-ring. Others could be mounted in lens tubes, which also doubled as a light scatter shields, fixed on the inside and outside where desired. The CELIF flange, part (2), is shown in figures 4.1 and 4.2 and in further detail in 4.3b.

Two set-ups were used the first, (a) in figure 4.3b, was designed with simplicity in mind. It placed a 1" biconvex lens (Thorlabs LB1757, BK-7, $f2 = 30\,\mathrm{mm}$) at the entrance, $\approx 96.2\,\mathrm{mm}$ from the central cavity axis, and used a light shield on the inside of the flange. The second set-up, (b), focussed on fluorescence emitted more centrally in the cavity, i.e. from an ice surface. It employed a lens tube with venting holes on the inside to hold the a plano-convex lens, (Thorlabs LA4306, fused silica, $f2 = 50\,\mathrm{mm}$) and another in the flange (Thorlabs LA4148, fused silica, $f2 = 40\,\mathrm{mm}$). Both set-ups were imaged onto a PMT at a distance $\sim f_2$, avoiding the PMT being at the focus of the lens.

4.5.1 Analysis of the LIF Probe Volume

The LIF probe volume for our cavity of length $d = 793 \pm 2\,\mathrm{mm}$ and mirrors of curvature $1\,\mathrm{m}$, occupies a cylinder of length, p_l, through the sample with a radius equal to the beam waist, w_0 assuming that $p_l << d$; figure 3.1 adds detail to the parameters used in this analysis. A ray tracing simulation, written in C by Wrede,[180] was used to model the probe volume observed by the detector. The program traces rays through lenses and media, modelling their physical dimensions, refractive indices and mimicking the physical obstructions along the path to the detector. Using a Monte-Carlo system it randomly generates LIF vectors. These are traced through the system until they either make it to a successful point within the imaging plane of the detector or do not; vectors that reach the imaging plane are separated out from those that do not. It is used to create set-ups, optimise lens positions, and has also been extended for other uses such as the simulation of the polarisation dependence in a Rayleigh scattering measurement shown in section 3.5.

By using this method parameters characterising the probe volume can be calculated such as p_l, and the solid angle, Ω, of light seen by the detector. Parameters are measured relative to the sample length which is the maximum length light can be collected over.* Solid angles of light, reported by the program, are given relative to the maximum solid angle as derived from the sample length. The reported value is called the fractional solid angle, Ω_{frac}, which is that observed by the lens setup relative to the total solid angle as set by the sample length.

* e.g. For a sample filling the whole cavity this will be the equal to the probe length as although light is generated across a longer distance it cannot be collected. For a molecular beam intersecting with the cavity axis it will likely be set at the width of the molecular beam unless the probe length is shorter.

Table 4.5: CELIF probe volume analysis performed at $585\,\mathrm{nm}$, $w_o = 0.302$ sampled with 100 million laser vectors.

Sample Length	CELIF Optics			$\Omega_{\mathrm{frac}}{}^{a}$	p_l
	Set	f_1	f_2		
		(mm)		$(\cdot 10^{-3})$	(mm)
45.5	(a)	-	30	1.929(5)	45.5
	(b)	40	50	1.046(3)	20.5
20.5	(a)	-	30	2.421(5)	20.5
	(b)	40	50	2.320(5)	20.5

[a] Quoted numbers in brackets are the calculation errors in the last digit.

Comparison has been made between the two lens set-ups (a) and (b) in table 4.5. The sample length was set first to $45.5\,\mathrm{mm}$, approximately the same size as the p_l calculated for (a), then to $20.5\,\mathrm{mm}$, the same size as (b). The sample length set to $45.5\,\mathrm{mm}$ simulates the CELIF cavity where the sample fills the whole length; in order to compare (a) with (b) the sample length was then set to the lens which sees the longest portion of the cavity, in this case (a). When the sample length was set to $20.5\,\mathrm{mm}$, it simulated a restricted sample length in the centre of the cavity like an ice surface. Here the LIF probe volume is limited to a region in the centre which is assumed to be the smaller sample length observed, set-up (b).

In the first case there is little advantage in placing a lens closer to the source image as it observes a smaller amount of the sample length. Thus Ω_{frac} is $46\,\%$ smaller in (b) than (a) as it is unable to see part of the sample length. So, for long sample lengths over the distance of the cavity, using our set-ups above, there was no advantage placing a lens closer as any gain in solid angle was lost observing a shorter portion of the sample. The advantage in moving a lens closer to the subject becomes apparent when the sample length is reduced in size. Now set-up (a) observes a longer sample length for no benefit and the lens could be moved closer to improve its solid angle. Unfortunately for set-up (b) this advantage was not seen and fractional solid angles were only similar to (a) due to a non-optimal lens positioning. In the future an improvement to this experiment would be to use this simulation to optimise the positions of lenses and maximise Ω_{frac} for ice experiments. In this way an increase of at least 4 times more solid angle relative to set-up (a) should be seen.*

* Observed using a different set-up not used in this experiment or shown above.

4.6 Gas Manifold

Linked into the main CELIF and ice surface machine, displayed in the aforemention figures, was a system used to control gas admission and pumping for CELIF and ice surface measurements. It was composed of $6\,\mathrm{mm}$ and $1/4$" pipes connected together using Ham-Let and Swagelok fittings. These connected with the main machine via CF and KF fittings. A simplified schematic of the pipework using standard process symbols is shown in figure 4.9.

All gases were admitted through the bottom of the cube (y-axis) except water which had its own dedicated line admitted in through the side of the chamber (see section 4.7). Pumping in the main chamber from atmosphere to $\sim 3 \cdot 10^{-3}\,\mathrm{mbar}$ was performed using a roughing line consisting of a MeOH(l)-CO_2(s) slush trap cooled to between $198 \rightarrow 228\,\mathrm{K}$ connected to a rotary pump. Pumping to high vacuum was performed using turbomolecular pumps (TMPs). Two were used. One, the main TMP (Oerlikon Leybold, SL300) was positioned on top of the cube. A second, smaller, TMP (Oerlikon Leybold, SL80) was used to either pump the side arms concurrently with the main TMP in a standard CELIF experiment or was used to pump down the inside of the surface partition during an ice measurement. Both TMPs sat inside pneumatic gate valves.

Table 4.6: Pressure gauges utilised during experimentation.

Code[a]	Model	Type	Range (mbar)	Error (%)
C1	MKS 626A-1000	CM[b]	$0.013 \ldots 1333$	0.25
C2,C4	Oerlikon Leybold CTR100-10	CM	$1 \cdot 10^{-3} \ldots 13.3$	0.20
C3	MKS 627D-0.02	Heated CM	$5 \cdot 10^{-7} \ldots 0.027$	0.12
C5	Oerlikon Leybold TTR101	Combination Pirani/CM	$5 \cdot 10^{-5} \ldots 1500$	$50\ [0.5 \cdot 10^{-4} \ldots 1 \cdot 10^{-3}]$ $15\ [1 \cdot 10^{-3} \ldots 100]$ $5\ [100 \ldots 950]$ $2.5\ [950 \ldots 1050]$
IG	AML AIG17G	Ion gauge	$1{\cdot}10^{-11} \ldots 1{\cdot}10^{-3}$	$\cdots$
P1,P2	AML PVB3	Pirani	$1 \cdot 10^{-3} \ldots 1000$	$\cdots$

[a] See figure 4.9 [b] Capacitance Manometer (CM)

Pressures were monitored inside the experiment using a series of gauges laid out in table 4.6. Their positions are shown in figure 4.9. Together C1-C3 and the IG provided a complete range of measurements from $3{\cdot}10^{-11}$ to $1333\,\mathrm{mbar}$. C4 measured pressures inside an isolated volume used for ice formation in the morphological analysis and HeNe monitoring experiments. C5 monitored background pressures inside the partition to ensure safe operation of the partition TMP in case of a leak into the partition from the main chamber. The backing lines use the Pirani gauges.

All the pressure gauges were connected to a custom made control box using a software

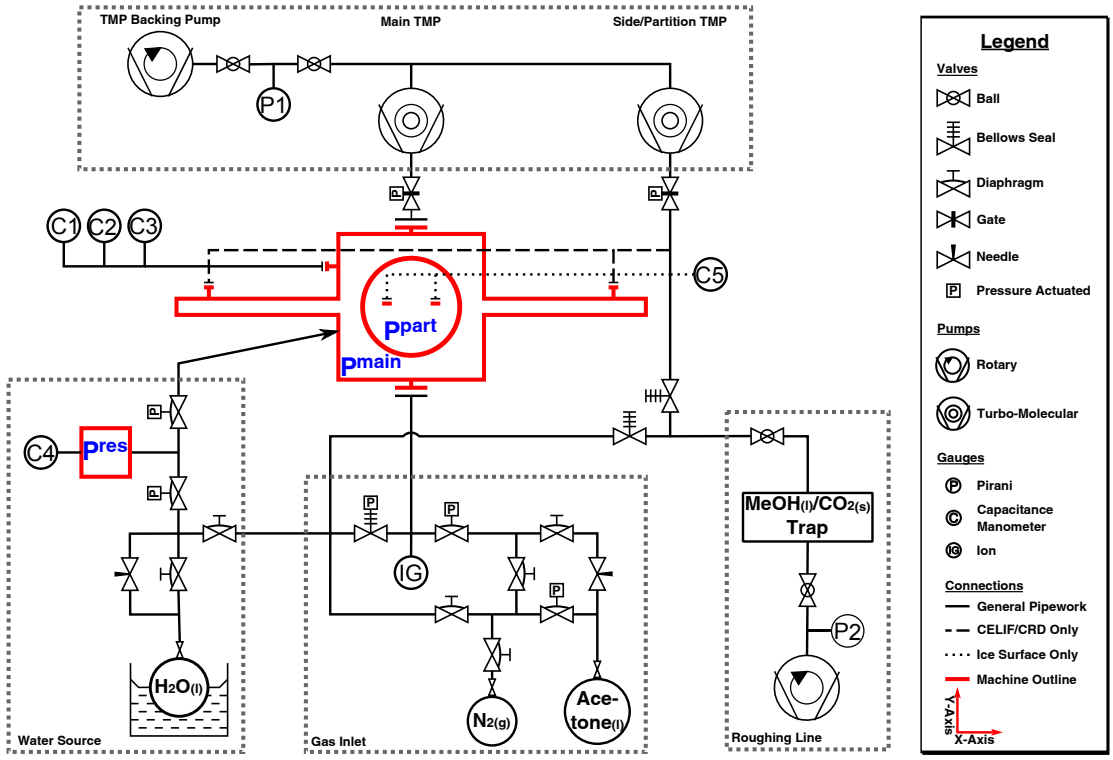

Figure 4.9: Gas control and pressure monitoring manifold linking up with the main machine as shown by a highly simplified schematic in the xy-plane. Flange-to-flange fittings are shown by lines ending perpendicular to the pipework and limited to those connected to the main machine; additional CF and KF parts are contained within the body of pipework but simplified to straight lines for clarity. During a pure CELIF experiment the surface partition indicated by the circle in the centre of the machine was absent. P^{main}, $P^{\text{partition}}$ and P^{res} are the pressures inside the cavity, surface partition and water reserve (used in the expansion across the surface to form ice) respectively.

controlled programmable logic controller designed to implement safe operation of the pneumatic gate valves, TMPs and rotary pumps. Briefly, pressure gauges were connected to a controller (AML NGC2D Ion Gauge Controller) which was able to connect them to relays. These relays were set to activate at pressures programmed by the operator. They were combined with relay outputs on the gate valves and pumps and fed into the logic controller. This controlled the status of the pumps and gate valves based on the relay inputs from all the connected devices. It could also automatically override unsafe operator commands such as opening the gate valve to a TMP when the pressure in the cavity was above an unsafe limit. Altogether under optimum working conditions a bottom end pressure of $3{\cdot}10^{-8}\,\text{mbar}$ with a leak rate of $4{\cdot}10^{-7}\,\text{mbar}\,\text{s}^{-1}$ was achieved.*

* These values take a week/two weeks of continuous pumping to achieve if the chamber has been continuously exposed to atmosphere for a long period i.e. weeks.

4.7 Vapour Preparation, Control and Admission

Three chemicals were used during the experiments nitrogen, acetone and water. nitrogen was supplied using a standard gas cannister, (oxygen free) and regulator. Acetone (Fisher Scientific, HPLC grade, $> 99.9\,\%$) and water (Fisher Scientific, HPLC grade) were sourced in high purity form. Vapour flow was regulated using a series of low, high (Hamlet H1300, HXF1300) and very high (Chell CMV) precision needle valves as required. Acetone and water were kept in custom round bottomed Schlenk flasks connected to the gas line with o-ring sealed metal to glass compression connections. Water vapour flow was further regulated through the use of a water bath (Julabo F25-HL) usually set to maintain a temperature of $19\,^{\circ}\mathrm{C}$ as referenced by a PT1000 probe angled into the centre of the flask.

Acetone and water were degassed thoroughly before use by a standard freeze-pump-thaw method as referenced in many papers.[41,50,181] A round bottomed flask was filled with $\approx 100\,\mathrm{mL}$ of chemical, attached to a rotary pumped vacuum line and pumped down from atmosphere to the vapour pressure of the chemical. A dewar of liquid nitrogen was used to freeze the chemical promoting effervescence of the dissolved gas, predominantly nitrogen. After freezing pumping continued for a period before slowly defrosting with light heating from a heatgun applied to the flask. This process was repeated three to four times.

Water was admitted to the surface using a custom dispersion nozzle designed as a rudimentary method to direct water vapour across the cooled surface detailed in section 4.10. This is seen in figure 4.7 labelled as the H_2O source. Early experiments chronologically admitted water in the bottom along with the rest of gas manifold the details of which are included in the experimental sections where pertinent. It was found that a targeted delivery system was needed due to the nucleation of water vapour at isolated sites on the surface using undirected methods, discussed in chapter 5. Other experiments have been designed using pulsed molecular beams and specialised dosers.[91,182,183] They represented a costly and major design investment which was not accounted for during these early build stages. The dispersion nozzle was simply a sealed off piece of $6\,\mathrm{mm}$ SS pipe. It was angled to run parallel and close to the surface, underneath it outside the range of the CRD beam. Angled towards the surface $1\,\mathrm{mm}$ holes were cut at $3\,\mathrm{mm}$ intervals (center to center) across the width of the cooled surface, $30\,\mathrm{mm}$. During ice deposition water vapour, either released from a set reserve into vacuum or passed continuously out via a needle valve, was emitted through this nozzle directed towards and across the cold surface.

4.8 Design of a Peltier Cooled Surface

One key component in this experiment was the peltier. Briefly, these thermoelectric devices operate using the Peltier-Seebeck effect. They are composed of two ceramic faces

with a circuit of alternating p and n semiconductor (SC) units sandwiched between. When current is passed through the peltier electrons move around the circuit. In passing from the n to p-type SCs they deposit thermal energy as they move down from high energy levels to lower ones. In order to move from p to n-type SCs, the opposite has to be done and they must gain energy to move across. In doing this they draw on thermal energy from their surrounding. Thus heat is absorbed at the cold junction which is pumped to the hot junction at a rate proportional to the current passing around the circuit and the number of couples. To operate effectively heat moved to the hot junction must subsequently be pumped away by a heatsink in thermal contact with it. Thus this component is an important part of any peltier set-up.[184]

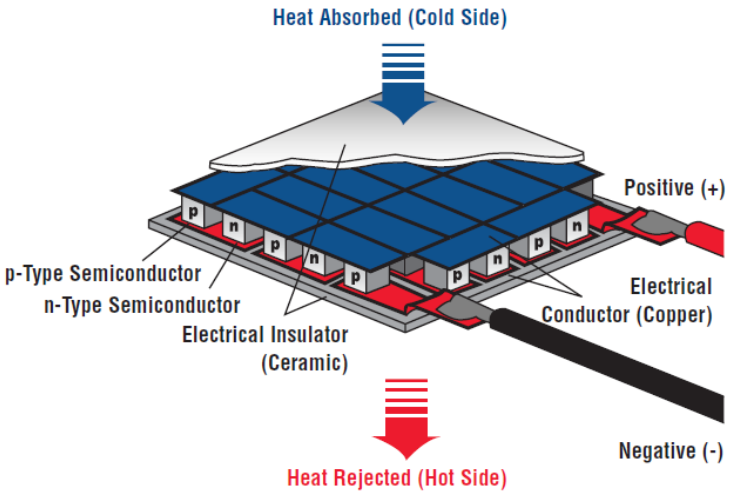

Figure 4.10: A schematic diagram of a peltier. Taken from the Thermoelectric Handbook.[184]

There are several characteristics which made these devices an appealing component for this cooling experiment. Firstly they are compact in size and lightweight making them suitable for tight spaces and applications requiring localised cooling. They have good reliability in a variety of operating conditions, are functional in a vacuum and contain no mechanically moving parts. They also have a fast response and good accuracy to which the temperature can be controlled. When choosing a peltier for surface cooling there are however several factors that need to be considered. These are mostly inter-related making what might be an easy decision more complicated.

1. Type
2. Size and Shape
3. Peltier Performance
   - $Q_{\max}$, the maximum heat power which may be absorbed at the cold face
   - $I_{\max}$, current required for largest $\Delta T_{\max}$
   - $V_{\max}$, voltage required for largest $\Delta T_{\max}$
   - $\Delta T_{\max}$, the maximum temperature difference
4. Implementation

Peltiers come in two commonly available types, single-stage and multi-stage (MS). Single-stage peltiers as depicted in 4.10 and 4.11a are the most commonly available unit and cheapest, varying widely in shape and size. Usually they are square, however, circular ones may be obtained and other specialised versions with central holes. Commercially they tend not be bigger than $40 \rightarrow 50\,\mathrm{mm}$ square. In principle, however, they may be any size so long as it can be engineered. However usually to cover larger areas multiple peltiers would be added side by side and run together in series or parallel depending on the implementation.

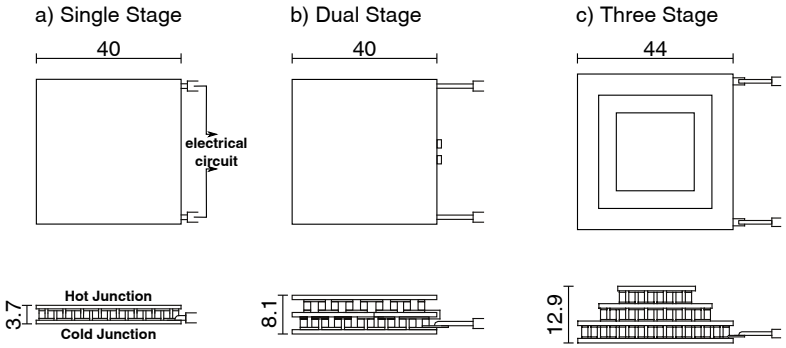

Figure 4.11: Figure showing the structural differences between three commonly available peltiers. These figures have been adapted from commercially available peltiers* and were involved in prototyping the ice surface experiment. Each shows a top down view and side on view of the peltier.

MS peltiers are similar to single-stage peltiers but formed from several devices stacked on top of each other. Now the cold junction of the bottom stage becomes the hot junction of the stage above it. They come in two main forms. One (figure 4.11c) resembles a square, stepped pyramid as each further peltier added is smaller than the one beneath it. The area of each subsequent layer is, very roughly, $50\,\%$ of the layer below it. They are found commercially in stacks of two to four. A second type exists (figure 4.11b) which is generally only seen as a dual stage device largely because of additional complexity in the peltier construction. Here the top layer has the same surface area as the one below it but instead has a lower density of SCs inside it. Similarly for single-stage peltiers the largest, common base size is around $40 \rightarrow 50\,\mathrm{mm}$ square. Sacking peltiers in this way $\Delta T_{\max}$ is increased where each additional stage added allows access to larger $\Delta T_{\max}$. However, this comes at a cost and each stage reduces $Q_{\max}$, the capacity of the peltier to pump heat.

Peltiers are listed by four characteristics, $Q_{\max}$, $V_{\max}$, $I_{\max}$, $\Delta T_{\max}$. These can be a misleading in the design process as they represent values that are not reached under normal working conditions. $V_{\max}$ and $I_{\max}$ are no issue as a power supply can be appropriately built to meet those limits, superseding these reduces the lifetime of peltier and does

* Laird Technologies. See website www.lairdtech.com for further details. Model depicted are a) ZT5-16-F1-4040, b) MS2-192-14-20-11-18, c) MS3-119-20-15.

not necessarily improve performance. $Q_{\max}$ and $\Delta T_{\max}$ are values that are only reached under unrealistic operating conditions. So these two values alone are not overly useful.

Q_c, represents the current heat pumping capacity of a peltier. Q_c is equal to $Q_{\max}$ when $\Delta T_{\max} = 0$ and $I = I_{\max}$. Similarly $\Delta T_{\max}$ occurs when $Q_c = 0$ and $I = I_{\max}$. This results in a peltier performance curve such that as ΔT increases Q_c decreases. This is broadly linear in form and examples are shown in appendix A.3. The performance curve is dependent on V and I powering the peltier such that a drop in performance is seen if $I < I_{\max}$ ($V < V_{\max}$). There is also a drop in performance when $I > I_{\max}$ ($V > V_{\max}$) where this also causes a faster degradation of the peltier due to wear from harsher operating conditions and raises the risk of a short occurring. Since any peltier is used specifically to create a temperature difference in the first instance a drop in Q_c is inevitable.

It was therefore important to characterise the experimental restrictions on the build in order to make sure that the design achieved the objectives laid out at the beginning of this chapter. First a prototype stage was pursued to test a variety potential designs and choose an appropriate peltier. In choosing an appropriate peltier an estimate of the heat load of our system, Q_{L}, was needed. Q_{L} limits the achievable ΔT, as Q_c has to match it so this was looked at in order to better decide upon a suitable peltier.

4.8.1 Prototyping of the Surface Build

Before the final design discussed in 4.10, several prototypes were created and tested. Initial designs concentrated on the simplest idea a heatsink, peltier, and surface combined mechanically by clamping the set-up together. The ultimate build was to form ice on a fused silica prism (for EWCRDS), so for the surface a glass substrate was used. A glass substrate with an area, $80\,\mathrm{mm}$ by $40\,\mathrm{mm}$, and thickness, $3\,\mathrm{mm}$, was used. A strip of at least $10\,\mathrm{mm}$ was designed to be near the path of the CRD beam (x-axis) after clamping. The size of substrate used was designed to maximise the area of ice produced and was limited from fitting apparatus onto a CF100 flange. The surface was cooled by a pair of peltiers, testing single-stage and dual stage ones, each $40\,\mathrm{mm}$ by $40\,\mathrm{mm}$ in area. A simple copper heatsink was built, refrigerated by coolant, which is shown in figure 4.12.

Together the surface, peltiers and heatsink were tested with a series of different mechanical clamps compressing them together. Prospective materials were analysed in terms of different factors such as cost effectiveness, outgassing, mechanical properties, chemical reactivity and importantly thermal conductivity and thermal expansion coefficients. Materials such as polymer plastics and ceramics, which are expensive, were avoided in preference for those with which the mechanical workshop had most experience, stainless steel (SS), Aluminium (Al), Oxygen-Free Copper (Cu) and similar. Appendix A.4 collects a few of the standard material properties that were important during the prototyping phase and in the final build.

It was demonstrated unequivocally that a purely mechanical method of fixing the setup was not feasible. Parts, despite being machined and polished for flatness (where applicable) were not able retain good thermal conduction across the heatsink, peltier, substrate sandwich while under sub-millibar pressures. The result was that the temperature of the substrate, after it had been cooled at atmospheric pressures, collapsed back towards room temperature when placed under vacuum. To counteract this clamping methods were tried with increasingly heavy forces but it did not rectify the problem. The forces across the set-up ended up uneven from trying to maintain an exposed part of the substrate for ice layering and CRDS. This created a situation that could fracture brittle glass and ceramic components which was made worse as the prototype was cooled where the different thermal expansion coefficients increased the stresses in the set-up. As well as this, during ice formation on a sub-zero substrate, ice was found to form mainly on the parts of the peltier closest to the cold junction; by having the entire cooling system exposed to the water vapour, ice would form on the coldest part of the set-up which was not the top of the substrate.

Instead a partition would need to be created so that thermal paste could be used to create a good thermal junction between layers in the set-up. The partition would also allow the cold surface of the substrate to be isolated from colder parts of the set-up upon which ice would preferentially layer. In order to avoid direct pressure onto the substrate, glue would be used to bond it to a metal plate that could be evenly compressed onto the cold junction of the peltier avoiding any unnecessary damage. The use of single and dual stage peltiers indicated strongly that a multi-stage set-up was definitely the way to proceed to reach temperatures below $243\,\mathrm{K}$.

4.9 Peltier Heat Load, $\mathrm{Q_L}$

MS peltiers represented a significant cost and design investment over single-stage ones. Our target temperature regime was $273 \rightarrow 210\,\mathrm{K}$ therefore MS peltiers, which produce the largest ΔT, were necessary. However the larger ΔT comes at the cost of its capacity to pump heat, since ΔT and Q_c are interdependent. An estimate of the heat load, Q_L, for our system was required for an informed peltier decision. Q_L represents the minimum amount of thermal energy that needs to be constantly pumped away by a peltier in a set-up, hence limiting the accessible ΔT. This heat load originates from thermal contact with surrounding bodies and fluids, and black body radiation in the set-up. By using cheap peltiers with defined performance curves a rough estimate was made for Q_L. Combined with performance graphs this helped to decide the actual ΔT that was likely to be reached using the more expensive peltiers.

A small system was built from a pre-existing, prototype liquid cooled (Julabo FL300) copper block, and two cheap single-stage peltiers (Global Component Sourcing ET-031-10-20-RS, $5.1\,\mathrm{W}$ and ET-031-10-13-RS, $9.3\,\mathrm{W}$) glued to a SS plate as shown figure 4.12. On each peltier a glass block was placed designed to approximate the size of a prism

upon which ice would like to be grown. A PT1000 temperature probe monitored the upper surface of each glass block in the centre and the temperature of the cooling block was monitored by a k-type thermocouple (TC) attached near the surface on one side. Cryogenic epoxy, as discussed later on, was used to glue each layer of the set-up together. The whole rig was mounted on a CF100 flange with feedthroughs for power, the TCs and cooling liquid.

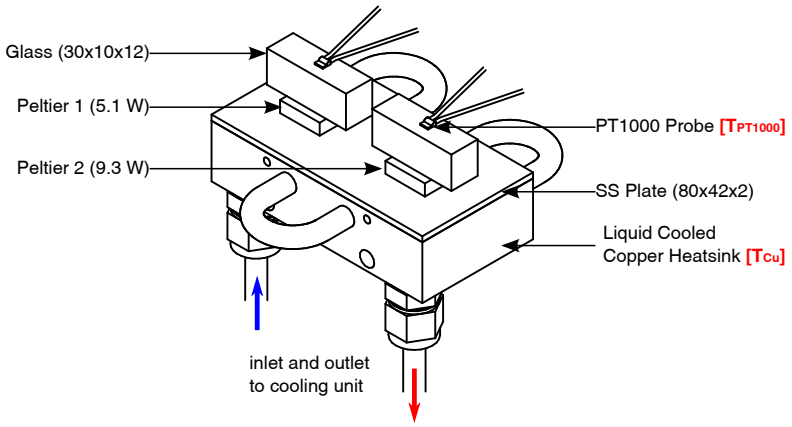

Figure 4.12: Figure showing set-up to test approximate heat load on a glass block inside the main chamber of the machine while under vacuum. Each of the layers is glued with a thin layer of cryogenic epoxy as described later on in section 4.10.

The experiment was performed as follows. The cooling unit was set to maintain the copper block at $T_{\mathrm{Cu}} = 298.7 \pm 0.1\,\mathrm{K}$, near to $300\,\mathrm{K}$ the temperature of the hot junction at which the performance curves are provided. A bench top power supply fed current at $I = I_{\max}$ into the peltier. Thermal energy was removed at the cold junction from the prism and pumped away at the hot junction by the copper block forming a ΔT across the peltier and the glass block. Simultaneously with the increasing ΔT, Q_c reduced from $Q_{\max}$ until, $Q_c \approx Q_{\mathrm{L}}$. $\Delta T = T_{\mathrm{Cu}} - T_{\mathrm{PT1000}}$, between the copper block and prism, was measured and compared to the performance graphs for each peltier, shown in appendix A.3. This value then provided the rough estimate of the heat load in this system.

Data was obtained in a vacuum and in the presence of nitrogen to test the effects of gas levels e.g. water vapour inside the chamber on Q_{L}. Heat load in this set-up was estimated at $2.8 \pm 0.5\,\mathrm{W}$. The effects of gas were tested at intervals from $1 \cdot 10^{-3}$ to $1000\,\mathrm{mbar}$ and found to increase the Q_{L} by comparatively little; at $1000\,\mathrm{mbar}$ it increased by only $0.6\,\mathrm{W}$. Moreover it was seen that across the range 0.5 to $100\,\mathrm{mbar}$, Q_{L} increased by only 0.3 to $0.4\,\mathrm{W}$. Since the vapour pressure above ice at $273\,\mathrm{K}$ is $\sim 6\,\mathrm{mbar}$ any surface experiments run should be effected minimally and be very similar across a large range of ice temperatures.

4.9.1 Design Implications

4 and 5 stage peltiers offer the best ΔT, up to $120\,\mathrm{K}$, but only with a $Q_{\max}$ of $2 \rightarrow 3\,\mathrm{W}$. These are not useful in light of the estimated load in our system as they are expensive

for little gain in $\Delta T_{\max}$ compared to peltiers with smaller numbers of stages. They also have an upper surface area on the final stage that is very small. 3 stage peltiers can be obtained with ΔT, up to $100\,\mathrm{K}$ and Q_c up to $15\,\mathrm{W}$ which are more cost efficient. Cost efficiency matters for although peltiers are generally reliable they are composed of brittle parts. If they are used unpotted or uninsulated then they can be prone to shorts and if used aggressively their performance can also drop over a faster time than desired.

Single-stage, 2-stage and 3-stage peltiers were compared looking at $Q_{\max}$ and ΔT. A 3-stage one was chosen (Lairdtech, MS3-119-20-15-11-W8, $\Delta T_{\max} = 100\,\mathrm{K}$, $Q_{\max} = 14.9\,\mathrm{W}$, $I_{\max} = 8\,\mathrm{A}$, $V_{\max} = 8.2\,\mathrm{V}$) for which the performance graph is shown in appendix A.3. A heat load of $3\,\mathrm{W}$ on this peltier should create a temperature difference of $\sim 80 \pm 3\,\mathrm{K}$. These measurements correspond to a hot junction temperature, in essence the copper cooling block, of $298\,\mathrm{K}$ and $I = I_{\max}$. This gives a predicted cold junction temperature of $218\,\mathrm{K}$ very close to our lowest temperature boundary. This can be further improved by dropping the temperature of the copper cooling block,* however this will also cause a drop in performance in the peltier reducing ΔT. Therefore this is only possible up to a certain limit but can be performed to lower the temperature further.

4.10 The Surface Set-Up

Using the information discovered during the prototyping phase of the experiment, a set-up was built around a port aligner to partition the peltier cooled surface away from the main chamber. Cryogenic adhesive was used for gluing the substrate to a metal plate that could be evenly clamped to a peltier and heatsink. The partitioned volume could then be independently pumped from the main chamber allowing the use of any outgassing materials within. The upper surface of a glass prism or metal block protruded out of the port aligner into the main chamber through a sealed hole. This positioned the upper surface as the only cold object exposed to the main chamber upon which ice was then grown. The partition can be split into two different sections, the exterior referred to as the port aligner, 4.4a, and the interior, the surface set-up, 4.4b. Figure 4.5 shows further important details of the port aligner, while figures 4.6 and 4.7 show the peltier surface cooling setup as it was installed onto the main CRD and CELIF experiment.

4.10.1 The Port Aligner

The port aligner comprised a custom CF100 bellows fixed to a base made from a custom rotatable CF100 flange. This was chosen so that the surface inside the experiment could be aligned relative to the CRD axis. Inside the port aligner was a tube welded to the bottom. On top of the tube sat an o-ring groove so that a circular plate, the partition plate, could seal it. A rectangular hole, precision cut by electrical wire cutting, was designed to create the closest mechanical fit around a prism substrate. The substrate could then

* By dropping the temperature of unit cooling the liquid inside the copper block

protrude out of the plate by an amount set by the cooling mount inside fixed to the base. In this set-up it was set at $0.5\,\mathrm{mm}$. Three bolts (5e in 4.4a) were positioned equidistantly around the port aligner which align the surface in the xy-plane along the z-axis. Each was secured by four nuts, two at each end to tabs on the port aligner. The surface can be aligned by loosening one nut on each bolt and making small incremental adjustments with the companion nut on the other side of the tab until a desired alignment and vertical height is reached. Then the loosened nut is secured tightly to fix the position. Two threaded holes were cut into the partition plate, feedthroughs for a PT1000 temperature gauge (5v in 4.4a). This was used as a feedback measurement for the PID controller which supplied power to the peltiers. They were constructed from M5 vented screws through the centre of which vacuum compatible wire was placed and glued into position using a low vapour pressure epoxy (Torr Seal). The M5 screws were sealed to the partition plate using o-rings.

A custom CF100 rotatable flange contained all feedthroughs for the function of the surface. It was composed of three pairs of CF16 ports and one pair of windows. During the standard function of the machine one pair of ports (5a in 4.4) was dedicated to pumping, connected to a rotary and TMP (Oerlikon pirani, SL80) in the gas system in figure 4.9. A pressure gauge (C5 in 4.9) was used to monitor background pressures in the partition. Another pair of ports (5b in 4.4) was used for liquid feedthroughs passing $1/4$" piping through a Wilson seal to the heatsink. The final pair (5d in 4.4) connected up k-type TCs, the PT1000 temperature probe and peltier power supply. The TCs were connected to a pc via an analogue input module (National Instruments, NI-9211). The PT1000 and power supply were connected to a custom made programmable PID control unit based around a thermal controller (Lairdtech, TC-XX-PR-59). Finally a pair of windows (5c in 4.5a/4.6) in the flange were designed for a surface laser to enter and exit the partition. This was for future use with a glass prism substrate in an experiment using evanescent waves to interact with ice grown on the prism.

4.10.2 The Surface Cooling Set-Up

The surface set-up, shown in figures 4.4b and in detail in 4.5, was designed to perform two roles. Firstly it was to cool a surface within a partitioned space inside the main chamber. Secondly, with a view to the future, it needed to allow room for a surface laser to be directed through the substrate when set-up with a glass prism. Custom miniature mirror mounts were designed to be positioned around the cooling set-up. These were successfully trialled but did not form part of the set-up used in chapter 5. The addition of mirror mounts for future experimentation influenced decisions made in the overall design process hence their inclusion in the diagram in figure 4.4b.

Starting at the bottom, a liquid cooled heatsink was seated on posts which were fixed to the feedthrough flange. Liquid feedthroughs circulated ethylene glycol from a cooling unit (Julabo FL300) around the heatsink. The body of the heatsink was made from SS with

a Cu lid sealed using an o-ring. Inside a hollowed out cylinder formed a tank around which the coolant circulated, entering and leaving through $1/4$" pipe fittings in the base. Centrally on top sat the 3-stage peltier (Lairdtech, MS3-119-20-15-11-W8, $\Delta T_{\max} = 100\,\mathrm{K}$, $Q_{\max} = 14.9\,\mathrm{W}$, $I_{\max} = 8\,\mathrm{A}$, $V_{\max} = 8.2\,\mathrm{V}$).

Seated on the cold junction was an Al plate which was fixed to the body of the heatsink by four bolts (5iv in 4.5c). These were designed to minimise heat transfer. Each compressed down on the plate usiwng two Teflon washers with a spring between. Good thermal contact between the plate, peltier and heatsink was achieved using a thin layer of silicone thermal grease (RS Silicone Thermal Adhesive, $2.9\,\mathrm{W\,m^{-1}\cdot K^{-1}}$). The substrate to be cooled was fixed to the Al plate using a cryogenic epoxy (Oxford Instruments, C5-102). A hole in the partition allowed the prism to fit through protruding above by $0.5\,\mathrm{mm}$ where it was sealed to the partition using a silicone resin leak sealant (Kurt Lesker KL-5). Thermal conduction between the partition and the prism was reduced by decreasing the thickness of the partition where it met the prism to $0.5\,\mathrm{mm}$. By doing this $\Delta T = 50\,\mathrm{K}$ could be maintained between the two regions for well over $30\,\mathrm{min}$; appendix A.2 provides further details on the experimental testing of this.

4.11 SS Surface Build and Preparation

In chapter 5 the surface used was a SS block. It was designed as a replica of a glass prism, upon which ice films might ultimately be grown. The prism, seen in figures 4.5b and c, had an upper surface area of $30\,\mathrm{mm}$ by $10\,\mathrm{mm}$, and height of $12\,\mathrm{mm}$. A $2\,\mathrm{mm}$ flat band around the top of the prism was cut in order to create a tight mechanical fit to the hole in the partition plate.

The build was prepared as follows. All parts were cleaned using acetone or methanol in a sonic bath before use. The custom CF100 feedthrough flange was fixed to a stand, knife edge up, which had clear access to both sides. The heatsink on its base was fixed to the CF100 flange and the temperature and PSU feedthroughs attached. The peltier and Al plate were then fixed in position with a thin layer of thermal grease between each interface. After compression any excess was wiped away. Once complete, TCs were bonded to surfaces using screw fixings or TC cement (Oxford Instruments, C5-105) and the peltier was hooked up to its PSU feedthroughs.

The port aligner, without the partition plate, was then placed over the surface set-up, orientated correctly and fixed to the feedthrough flange with the PT1000 feedthrough wires and partition plate TC poking out the top of the tube. These were then connected to the partition plate, which was suspended above the port aligner during this process; the feedthroughs have to be long enough to facilitate this. Once secure, the partition plate was then lowered and sealed to the top of the port aligner.

The SS surface itself was prepared using a grinding and polishing machine. The upper surface was ground down using wet and dry sandpaper to a grade of P1200/P2400. It

was then finished using $6\,\mu\mathrm{m}$ followed by $1\,\mu\mathrm{m}$ diamond paste. To bond it to the Al plate on the peltier cryogenic epoxy (Oxford Instruments, C5-102) was made up and spread on the bottom. It was then gently* slid through the hole in the partition and weighted down firmly until cured ($\sim 24\,\mathrm{Hr}$), taking care not to scratch the upper surface. The PT1000 temperature probe was then fixed on the upper surface and hooked up to the feedthroughs on the partition. Epoxy could be used for a strong permanent connection or TC cement for a more temporary one.

The last part involved sealing the partition hole edge to the substrate in the centre. For this a silicone resin leak sealant (Kurt Lesker, KL-5) was used. Details of this is shown in figure 4.5b. Several different sealing compounds were trialled by adding nitrogen up to $100\,\mathrm{mbar}$ and monitoring the background pressure inside the partition, both at rtp and when peltier was running. Most failed creating a slow leak when the surface was cooled caused by the shrinking volumes during the cooling process or were too soft. Silicone resin was sealed around the edge added dropwise using a pipette. Usually the resin should be cured at $230\,^{\circ}\mathrm{C}$ or higher however due to the nature of the build this was not possible. Instead curing was performed at room temperature over a couple of days.

Following this preparation the surface was attached to the main experiment and pumped down slowly while maintaining an overpressure on the outside of the seal, $P^{\mathrm{main}} > P^{\mathrm{partition}}$, around $5 \rightarrow 50\,\mathrm{mbar}$. The partition could be completely pumped down when P^{main} was less than $50\,\mathrm{mbar}$ but if the seal was not completely cured then residual solvent in the resin would boil off at the lower pressures. Care was taken to avoid this as much as possible by a slow pump down maintaining the quality of the seal.† During the dismantling process this build was reversed. The substrate-partition edge seal was easily removed through the use of toluene solvent. Any epoxy glue could also be softened using a toluene and/or an acetone bath, plus if necessary gentle sonication. After the set-up was complete, and the glues set, the surface was thoroughly cleaned with HPLC acetone before use.

4.12 Operation and Temperature Monitoring

Once assembled the port aligner was mounted onto the CELIF set-up as displayed in figure 4.6 and as a cut-through facing the surface in figure 4.7. Peltiers were connected to the PID controller which interfaced with a PC. This supplied power to the system based on temperature feedback from the PT1000 probe, T_{PT1000}, on the surface to reach a temperature set point. Cooling began by running the liquid cooling system for the heatsink and waiting for it to get to temperature, followed by turning on the peltier. The program was run and a target temperature set with appropriately sized PID parameters in order to minimise hysteresis in the system. Due to the large distances between the

* Particularly applying to glass prisms which are easily fractured at corners and edges. † If necessary then bubbles can be carefully lanced, however the more bubbles the less the seal has managed to cure before use.

upper surface and peltier a state of hysteresis was easy to get into without proper PID parameters due to the long delays between the peltier cooling and the PT1000 probe responding.

The PID works by running the peltier until T_{PT1000} is reached, at which point it switches to maintain the set point. This is done by the PID software modifying and scaling the power output and current direction (which allows switching between cooling and heating mode) in the peltier based on the PID parameters entered. For our set-up, heating mode was not used as this was found to cause severe hysteresis. Instead the peltier just switched off when cooling was no longer required, turning back on only to maintain T_{PT1000}. It should be noted that single-stage peltiers can be run in both cooling and heating mode by simply reversing the current. MS peltiers however are designed specifically to pump heat in a single direction, and running them in heating mode can damage them. As a general rule MS peltiers can only heat to half the ΔT_{max} reported in the specifications.

Five temperatures were monitored throughout the running of the surface, T_{cool}, T_{Cu}, T_{peltier}, $T_{\mathrm{partition}}$ and T_{PT1000} shown in figure 4.5c. T_{cool} was internally measured by the Julabo cooling unit feeding the heatsink. This was set to maintain the hot junction near its optimum temperature of $298\,\mathrm{K}$ as measured by T_{Cu}. T_{peltier} measured the temperature of the cold junction fixed to the Al metal plate as close to the centre of the peltier as possible. $T_{\mathrm{partition}}$ measured the temperature of the partition plate near to the edge bond with the surface substrate. T_{Cu}, T_{peltier} and $T_{\mathrm{partition}}$ were all measured by k-type TCs. During a typical experiment running temperatures were recorded at $T_{\mathrm{Cu}} = 301 \pm 0.3\,\mathrm{K}$ with $T_{\mathrm{PT1000}} = 230\,\mathrm{K}$ and $T_{\mathrm{peltier}} = 220\,\mathrm{K}$. The partition plate temperatures recorded under these conditions showed that the partition edge temperature was generally held between $273 \rightarrow 268\,\mathrm{K}$ across the course of an experiment.

CHAPTER 5

Peltier Controlled Ice Film Growth on a Stainless Steel Surface

Once the surface set-up was constructed, work characterising it began. The work presented in this chapter was performed in two areas. Firstly the experiment was characterised in preparation for future experiments, such as the adsorption, desorption and photolysis of trace gases with CRD and CELIF spectroscopy. The second topic discusses the different techniques investigated to layer ice onto the substrate, the stainless steel prism. For the different spectroscopic techniques that are wanted to be used ice should be layered on the surface maximising coverage with a well defined thickness, nanometres to micrometres in size. The best method found for layering ice was then characterised in area with video monitoring and morphological analysis, and thickness with HeNe interference measurements. By doing this the strength of the set-up was assessed and the system placed in context with other experimental methods used for ice film growth in the temperature range, $210 \rightarrow 273\,\mathrm{K}$.

5.1 Near-Surface Reduction Measurements of the Cooled Surface

CRDS is to be used to detect and monitor the gas phase above the surface. It is important that the ring-down beam passes as close to the surface as possible without being affected by it, only interacting with the gas phase above it. The beam needs to be as close as possible to the surface to keep the number of gas-phase collisions before detection to a minimum. Previous work from Zhao *et al.*[124] (as discussed in section 2.8) demonstrated the effect of introducing an obstruction into the path of the ring-down event. Calculations based on the surface geometry alone underestimated the sensitivity loss and suggested diffraction was important; when diffraction was accounted for in the calculations they mirrored the observed results more closely. Their tests were performed by the insertion of an obstructing filament, essentially blade-like, orientated coincidentally with

the beam waist of the cavity. Their calculations, being based on this specific setup, are not directly applicable to this one where the ring down beam runs above a large surface area, $\varnothing 98\,\mathrm{mm}$. Therefore this is investigated to realise the minimum measurable distance above the surface that must be used for this experiment.

5.1.1 Experimental Setup

The experiment is depicted in figure 5.1 and was performed as follows. A HeNe laser (JDSU Model 1125/P, CW, $5\,\mathrm{mW}$, Beam $\varnothing 0.81\,\mathrm{mm}$) was aligned perpendicular to the cold surface along the z-axis. It was directed through two irises and a window opposite the surface which replaced the CELIF optics originally mounted on that flange. The HeNe was aligned in two stages. In the first stage an initial alignment was made through the window centrally, under vacuum, onto a blank flange which temporarily replaced the surface mount. Two back reflections a small one from the window and a larger one from the blank flange were then aligned onto the incident beam and the two irises used to mark this alignment. This alignment is assumed to be as coincident to the z-axis as can be managed with this system.

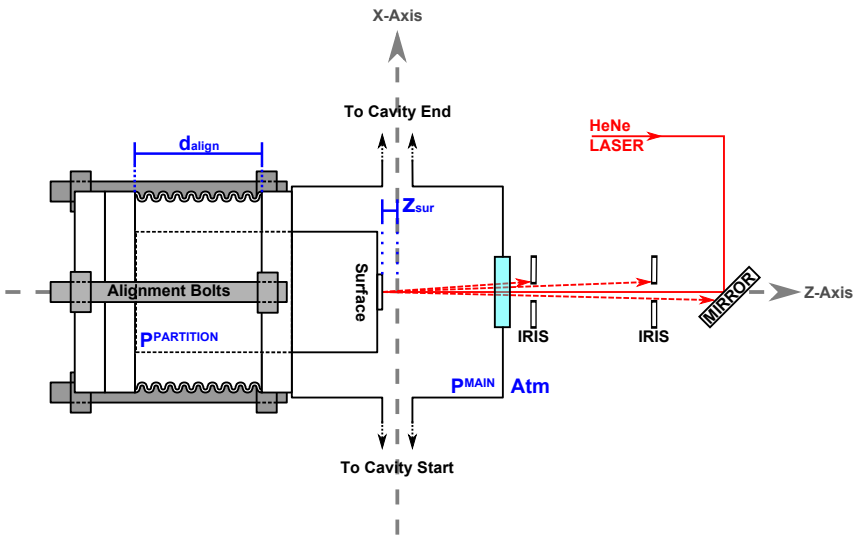

Figure 5.1: A schematic diagram is shown looking down onto the experiment used for near-surface reduction measurements of the substrate surface. The HeNe laser is directed through two irises and a windows before reflecting centrally from the substrate surface.

Stage two replaced the blank flange with the SS surface. This was set to its neutral position and mounted in place of the blank flange. Realignment of the surface then proceeded until the main reflection and back-reflections ran through the irises again. The CRD set-up was optimised and operated at $583.4\,\mathrm{nm}$ in high vacuum, pumped fully by the TMPs in both the partition, $P^{\mathrm{partition}}$, and main chamber, P^{main}. The experiment was run by withdrawing and extending the surface towards the CRD axis, changing z_{sur}, whilst maintaining alignment. RDTs were recorded along with a measurement of d_{align}, taken using calipers. Since z_{sur} cannot be measured directly, d_{align} is used in conjunction

with a CAD drawing of the set-up and subsequent drop to zero CRD signal to calculate it.

5.1.2 Results

Ring-down times were sampled at 2000 laser shots per measurement at various distances from the CRD axis. The near-surface data is displayed in figure 5.2 along with a graph showing the variation of cavity beam waist, $w(x)$, along the x-axis (CRD axis) derived from equations 2.15 and 2.18. Included with the near-surface data is the expected trend for a purely geometrically clipped line as derived by equation 2.19 in section 2.8 using the current cavity at the experimental wavelength. For guidance the experimental data has been fit using the same equation although it is known that the fit will not mirror the data exactly due to the difference in the shape of the obstructing feature between the two measurements and missing contributions resulting from the surface diffraction. It is mathematically more involved to introduce surface diffraction into a treatment. This fit uses a beam waist, $w_0^{\text{fit}} = 1.43\,\text{mm}$, and presents the beam waist that would be required to produce a similar drop in τ_0 from geometric clipping alone in the filament case described by Zhao. For reference, in this measurement τ_0 was equal to $49.6\,\mu\text{s}$.

5.1.3 Analysis

The results show that at $3.8\,\text{mm}$ ($12.6w_0$, where $w_0 = 0.302$ for our cavity, see figure 5.2) τ_0 begins to measurably reduce and that after just $1.2\,\text{mm}$ of travel to $2.6\,\text{mm}$ ($8.6w_0$) it has reduced by $90\,\%$ of its original value. Zhao *et al.* set their maximum loss condition in τ_0 to $10\,\%$* which occurred for them at $2.7w_0$. In comparison to the data for this surface, which is much larger in our system, it occurs at $10.4w_0$. From the fitting to a geometrically clipped beam it is seen that to produce the same loss in ring-down a factor of 4.74 to the beam waist in our cavity is required. It also shows a deviation to this fit plotted in figure 5.2 as expected, from a combination of surface diffraction effects and also from experimental error due to the increased difficulty optimising the alignment at distances close to the cavity beam where the RDT approaches zero.

The set-up used here differs from that used by Zhao *et al.* who inserted a thin filament into the path of their beam. Their filament is very thin along the length of the cavity but wider than the diameter of the beam. In our case it is not thin along the x-axis; the surface is $30\,\text{mm}$ wide, sitting at least $\approx 0.5\,\text{mm}$ above the partition plate, which itself is $98\,\text{mm}$ in diameter. Since equation 2.19 has been designed with the filament based set-up it might not be valid to extend its use to our set-up. However from figure 5.2 the beam waist only changes marginally from 0.302 to $0.307\,\text{mm}$ across the entire diameter of the partition plate. Therefore additional geometric clipping from the larger surface area is unlikely to be responsible for the increase in τ_0 losses at longer distances from the surface. Instead

* This is also the maximum loss condition used for any ring-down measurements that have been taken in this thesis.

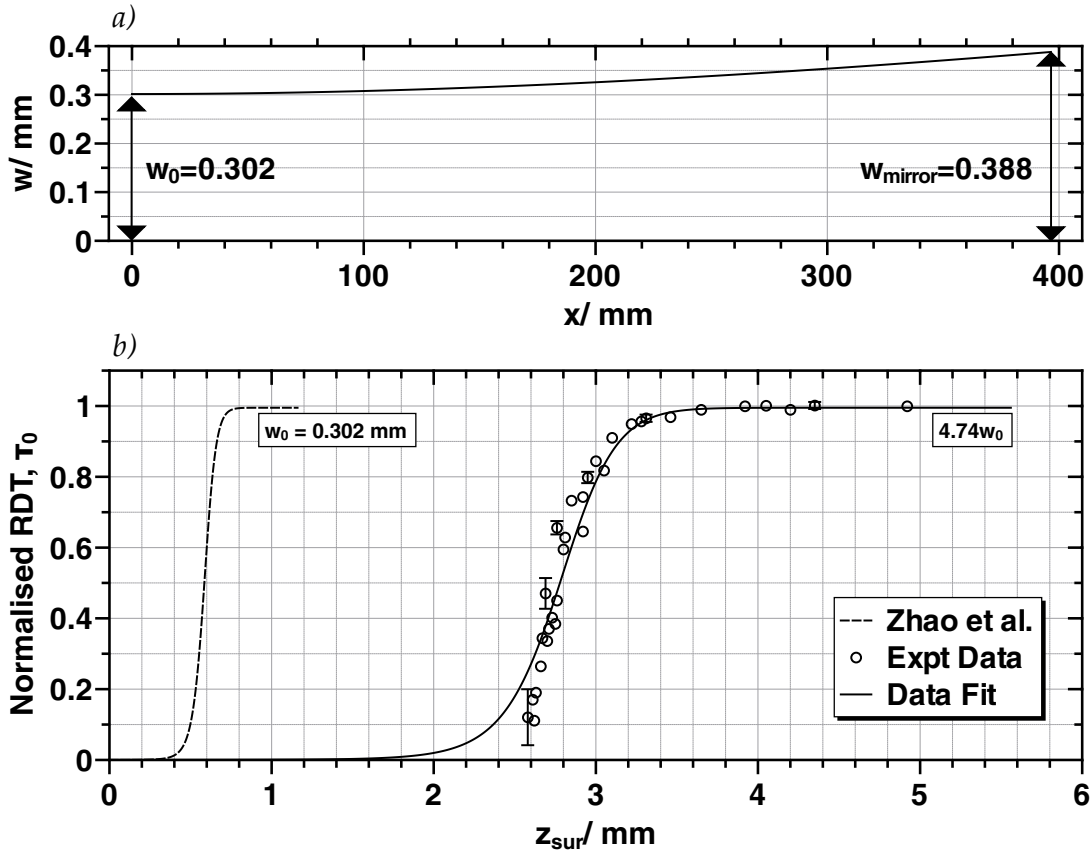

Figure 5.2: $a)$ displays the variation of the beam waist along the cavity length, $d/2$, showing the beam waist at the centre of the cavity, w_0 and at each end of the cavity w_{mirror}. $b)$ shows the surface data ($\bigcirc$) and two curves. The dashed curve represents the expected trend for a geometrically clipped Gaussian beam with the cavity beam waist, $w_0 = 0.302$. The solid curve has been fit to the data using the same equation with $w_0^{\mathrm{fit}} = 1.43$; it is meant as a guide to the trend of the data recorded. Errors in the normalised ring-down times show the standard deviation in the data.

an increase in surface diffraction effects must be the more significant factor.

One error in this experiment stems from the method with which z_{sur} has been derived. Measurements of distance made by the calipers have an error of $\sim 0.1\,\mathrm{mm}$ but in order to calculate z_{sur} at all several assumptions have to be made. One is that the cavity is fully aligned to the TEM_{00} mode and runs centrally through the cavity from mirror to mirror. This should be the case as the ring-down time was both long and cleanly fitted to a single exponential as demonstrated by a good flat residual. Another assumes that the plane of the surface is fully coincident to the yx-plane and perpendicular to the z-axis in the centre of the surface. Lastly the measurement made by the calipers is assumed to correlate to z_{sur} through measurements derived via CAD drawings of the experimental set-up.*

* There is nothing assume this is not the case but due to the construction of the port aligner it is not straight forward to check distances manually to an accuracy much greater than $\sim \pm 0.5\,\mathrm{mm}$

It is therefore possible that the z_{sur} has been over or under estimated. For instance if the aligned cavity lies particularly off the x-axis or was accidentally aligned to different cavity mode increasing the width of the beam waist. A situation might even have be seen where an error was produced as large as $\pm 1\,\mathrm{mm}$. However even an error of this magnitude would not produce a change in z_{sur} large enough to bring our measurements in range to mirror the observations made by Zhao *et al.* It is concluded that the larger surface area has a much greater effect on τ_0 and that the surface must be positioned at least $12w_0$ away to avoid interference effects. Further improvements to this experiment could be performed by introducing a full treatment of the losses due to surface diffraction effects into a model of our set-up. Any repeat of the experiment should seek methods to improve the alignment of surface, such as monitoring multiple reflected beams, and also find greater accuracy in the measurement of z_{sur}.

5.2 Monitoring Water in the Vapour Phase

Throughout testing of the ice surface experiment and during any future experimentation phase the monitoring of water vapour will be required. This is eventually to be used in monitoring any dynamics occurring in the vapour phase near ice and in the presence of trace gas VOCs. However in this study it is used to relate the vapour pressures of water in the gas phase to the temperature of ice on the surface. CRDS has a sensitivity covering of approximately three orders of magnitude but access to the full range in a single experiment is usually not possible. Discussed in Berden,[118] very early times in the ring down trace can be subject to a number of distortions. These occur for a number of reasons including ASE from the dye laser and jitter in the signal recording process. Normally this can be avoided during the data fitting by delaying it until shortly after ring-down has stabilised. However as $\Delta\tau$ increases and the exponential reduces there are ever smaller numbers of data points to fit over. Also when fitting across the same data range for all ring-down measurements, as τ becomes smaller the background signal (to which τ decays) occupies an ever growing proportion of it. These two features degrade the correlation between τ and τ_0 as $\Delta\tau$ increases. Therefore, where possible, τ/τ_0 is kept to a value of $\sim 0.8 \rightarrow 0.9$ across the course of a measurement. For this reason, and to test the operating functionality of the CRD set-up, the most suitable water absorption lines were sought for monitoring water vapour over ice at temperatures between $220 \rightarrow 273.15\,\mathrm{K}$ and while maintaining a ring-down reduction of $\sim 10\,\%$.

5.2.1 Experimental Setup

The experimental set-up consisted of the standard CRD gas cell described in section 4.3. The overall set-up used varied across the different absorption scans taken depending on the current purpose of the machine at the time of the scans.* Pulsed dye laser

* Depending on whether the set-up was being used solely as a CRDS or CELIF machine with/without the ice surface section installed.

system Ib (see section 4.2) was used, set-up for $532\,\mathrm{nm}$ pumped Pyrromethene-597 in MeOH producing light in the range $560 \rightarrow 600\,\mathrm{nm}$. Absorption measurements were carried out in the wavelength range $580 \rightarrow 590\,\mathrm{nm}$ using high reflectivity mirrors (Layertec, $\lambda_{\mathrm{dsgn}} = 585 \rightarrow 605\,\mathrm{nm}$) for the CRD cavity and empty ring-down times of $\sim 35 \rightarrow 40\,\mu\mathrm{s}$ were obtained. Maximum powers used were $\sim 4\,\mathrm{mJ}$ per pulse tuned down to acceptable levels using the Q-switch on the pump laser to avoid saturation effects when they were observed on the CRD signal.

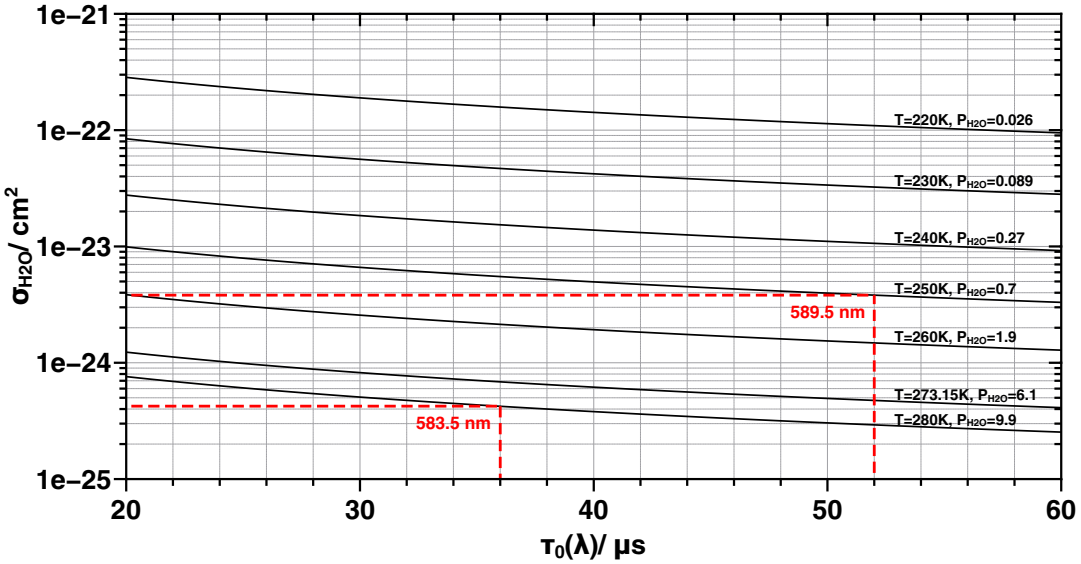

Figure 5.3: Theoretical absorption line cross-sections, σ_{H2O}, calculated for water at a series of different vapour pressures at the corresponding ice temperature derived from the Wagner-Pruss equation. σ_{H2O} has been calculated assuming a desired $\tau/\tau_0 = 0.9$ at the corresponding vapour pressure. The baseline ring-down signal, τ_0 is varied across the range of displayed by the mirrors used in the experiment. Marked are the two wavelengths investigated.

Pressures were measured using the capacitance manometer array discussed in section 4.6. High purity H_2O was degassed and admitted into the chamber by the method in section 4.7. Background measurements in vacuum were taken before and after each run. For each H_2O measurement, time was allowed for equilibration with the system before it was taken. Wavelength regions to be scanned were decided by an analysis of the CRDS system described in figure 5.3 combined with literature of the absorption line spectra derived from the HITRAN database shown in 5.4. Figure 5.3 shows idealised cross-sections for water that would be required to produce $\tau/\tau_0 = 0.9$ across different τ_0 and vapour pressures of water. Marked on the figure are the two wavelengths that were used in this study. Vapour pressures of water-ice have been split into two rough regions, $0 \rightarrow 1$ and $1 \rightarrow 10\,\mathrm{mbar}$. The first region covers a range of ice temperatures from $220 \rightarrow 250\,\mathrm{K}$, within which measurements were largely taken. The latter covers any higher temperatures or pressures that were used. Based on this figure 5.4 is split into two regions. Region 1 where $\lambda = 586 \rightarrow 590\,\mathrm{nm}$ containing $\sigma_{H_2O} = 1 \rightarrow 6 \cdot 10^{-24}\,\mathrm{cm}^2$, and region 2 where $\lambda < 586\,\mathrm{nm}$ containing lines with $\sigma_{H_2O} < 1 \cdot 10^{-24}\,\mathrm{cm}^2$. Figure 5.3 shows that for $\tau/\tau_0 = 0.9$ at $P_{\mathrm{H2O}}^{\mathrm{main}} \sim 10\,\mathrm{mbar}$ requires a line in region 2, and for $P_{\mathrm{H2O}}^{\mathrm{main}} \sim 1\,\mathrm{mbar}$ a line in

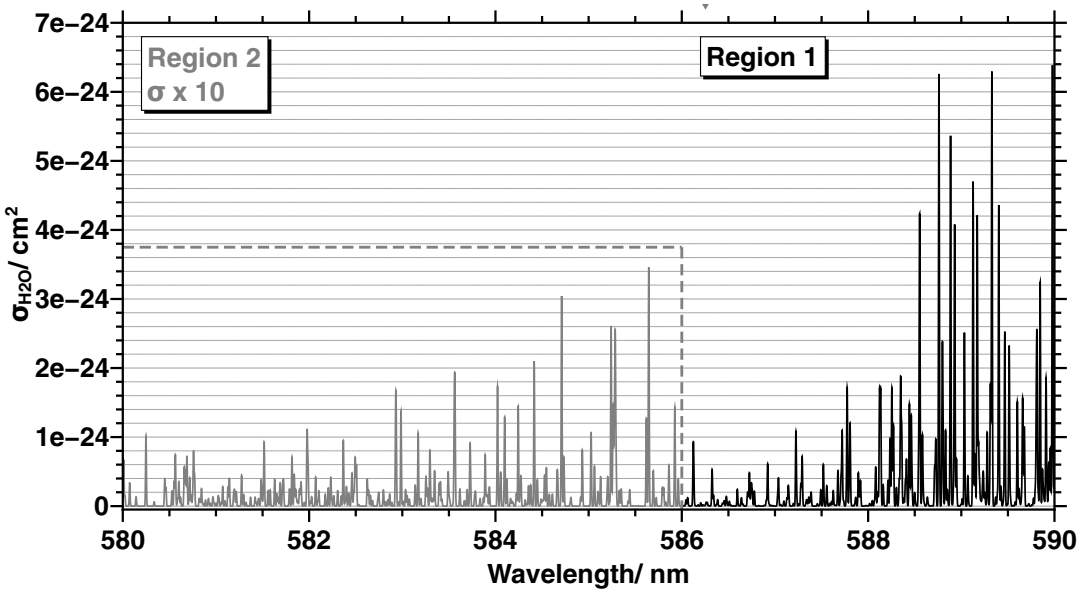

Figure 5.4: HITRAN data for water absorption cross-sections between $580 \rightarrow 590\,\mathrm{nm}$ and pressure broadened at $P_{\mathrm{H2O}}^{\mathrm{main}} = 1\,\mathrm{mbar}$. Region 1 covers $586 \rightarrow 590\,\mathrm{nm}$. Region 2 covers $580 \rightarrow 586\,\mathrm{nm}$ and has been enlarged 10 times.[185]

region 1.

5.2.2 Results and Analysis

Results of the water absorption line scans are shown in figure 5.5. Details of the wavelength ranges, resolution and experimental parameters are contained within the figure. Two lines were picked out for the two pressure bands, one at $583.563\,\mathrm{nm}$, the other at $589.514\,\mathrm{nm}$. The longer low resolution scan in figure 5.5a shows that cross-sections are not matched for many of the strongest peaks. Alterations were made to laser system Ib, lowering powers, improving the collimation of the beam and optimising its bandwidth but this was not able to improve the measurement better than that shown. It was found that cross-sections greater than $\sim 2.5 \cdot 10^{-24}\,\mathrm{cm}^2$ were consistently under-estimated with this set-up. This problem might arise from the resolution of the laser being too low and scanning past the peak of the absorption. However higher resolution scans, not shown here, also produced the same result. Another potential issue is the acquisition of missed CRD shots being averaged into the data however this would be expected to affect all lines and was also largely accounted for during the acquisition process. It is therefore believed that the main limitation to the accessible line strengths is from bandwidth limitations in the laser alone.

Choosing a typically underestimated line centered at $589.979\,\mathrm{nm}$ a Gaussian fit to the HITRAN data produces a bandwidth of $8.8\,\mathrm{pm}$. This can be compared to the bandwidth of the laser which was at best $\sim 10\,\mathrm{pm}$.* When the line width is comparable to or narrower

* Wavemeter measurements indicated it might fluctuate to produce even higher bandwidths up to $17\,\mathrm{pm}$

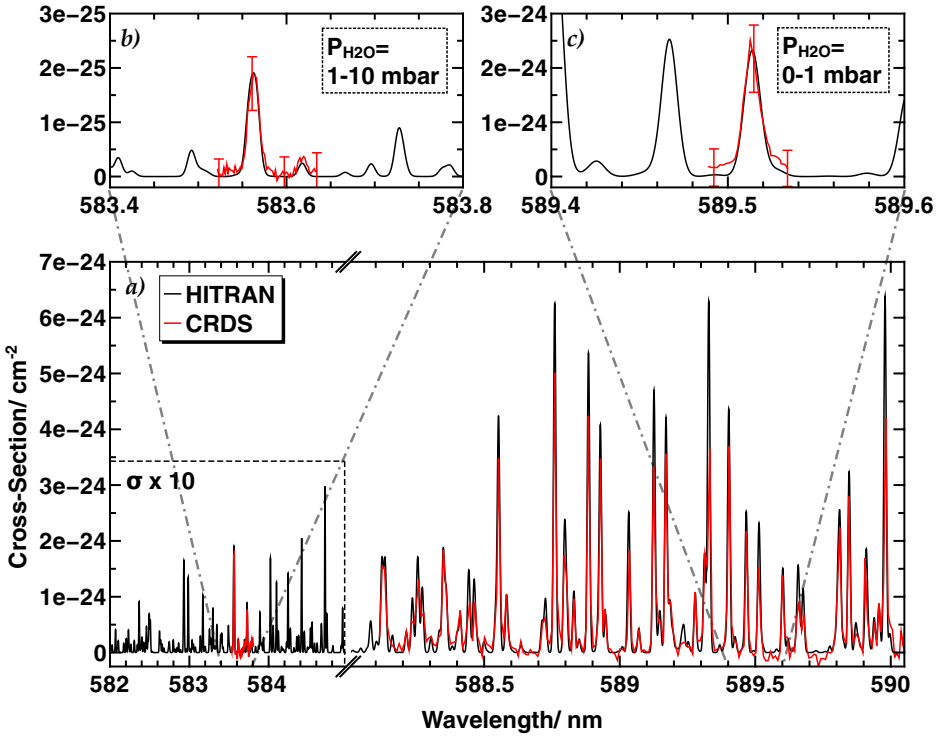

Figure 5.5: All figures show H_2O spectra derived from the HITRAN[185] database (black) and measured using CRDS (red). The vacuum wavelength is displayed, measured with a wavemeter. HITRAN data has been pressure broadened in line with the experimental conditions. Errors are displayed on b) and c) which show the spread in data and are similar in a) although these are not shown.
a) shows data in the range $588 \rightarrow 590\,\mathrm{nm}$ recorded at $P^{\mathrm{main}}_{\mathrm{H2O}} = 0.5\,\mathrm{mbar}$, a resolution of $0.009\,\mathrm{nm}$, and at 100 laser shots per point. HITRAN data is also shown for the range $582 \rightarrow 585\,\mathrm{nm}$ with measured data in the range $583.4 \rightarrow 583.7\,\mathrm{nm}$. It is recorded at $P^{\mathrm{main}}_{\mathrm{H2O}} = 10\,\mathrm{mbar}$, a resolution of $0.0036\,\mathrm{nm}$, and at 100 laser shots per point. It has been magnified by 10 to aid viewing.
b) expands the water line, $583.563\,\mathrm{nm}$ to be used to monitor the pressure range $1 \rightarrow 10\,\mathrm{mbar}$. It is recorded at $P^{\mathrm{main}}_{\mathrm{H2O}} = 10\,\mathrm{mbar}$, a resolution of $0.0018\,\mathrm{nm}$, and at 200 laser shots per point.
c) expands the water line at $589.514\,\mathrm{nm}$ to be used to monitor the pressure range $0 \rightarrow 1\,\mathrm{mbar}$. It is recorded at $P^{\mathrm{main}}_{\mathrm{H2O}} = 1\,\mathrm{mbar}$, a resolution of $0.0018\,\mathrm{nm}$, and at 250 laser shots per point.

than the laser bandwidth, the RDT will not be reduced equally for all modes. Consequently, the RDT appears too long and the absorbance too small. Improvements were made to the laser bandwidth with the adoption of laser system II however this was outside the timescale of the measurements made in this chapter. This has influenced the choice of water lines chosen to monitor pressures by limiting the accessible cross-sections. Figures 5.5b and c show scans of lines chosen to have a strength $< 2 \cdot 10^{-24}\,\mathrm{cm}^2$ and well isolated from nearby peaks. These lines, which have been scanned at the highest resolution, now replicate data obtained from HITRAN. Therefore in following experiments $583.563\,\mathrm{nm}$ was used to monitor the pressure range $1 \rightarrow 10\,\mathrm{mbar}$, and $589.514\,\mathrm{nm}$ the range $0 \rightarrow 1\,\mathrm{mbar}$. For the pressure range $0 \rightarrow 1\,\mathrm{mbar}$ it would have been preferable to use stronger cross-sections at temperatures of ice around $220 \rightarrow 230\,\mathrm{K}$ and thus this was a limitation on the experiment at the time of the measurements.

5.3 Ice Surface Thickness Prediction

In preparation for testing and characterisation of ice film growth it is necessary to predict ice thicknesses for a given amount of water vapour put into the cavity. A calculation was formulated, shown in equations 5.1 and 5.2, derived from ideal gas law and the density relation for water. Thicknesses are shown for ice on the nano to micrometre scale which is appropriate for techniques such as EWCRDS which we plan to use for the study of surface processes in the future. V_{ice} (m^3) and d_{ice} (m) are the volume and thickness of ice respectively and can be estimated using,

$$V_{\mathrm{ice}} = \frac{(P_{\mathrm{in}} - P_{\mathrm{ice}}) * V_{\mathrm{main}}}{RT} \cdot \frac{\rho_{\mathrm{ice}}(T_{\mathrm{ice}})}{0.001 * M_{\mathrm{H_2O}}} \tag{5.1}$$

$$d_{\mathrm{ice}} = \frac{V_{\mathrm{ice}}}{A_{\mathrm{ice}}} \tag{5.2}$$

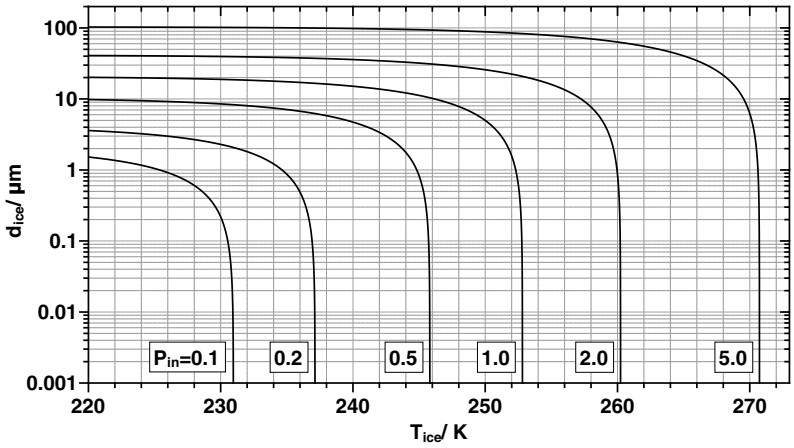

Figure 5.6: Ice surface thicknesses based on changing ice temperature, T_{ice} and an upper surface area of $3\,\mathrm{cm}^2$. Each curve represents a different P_{in} in mbar.

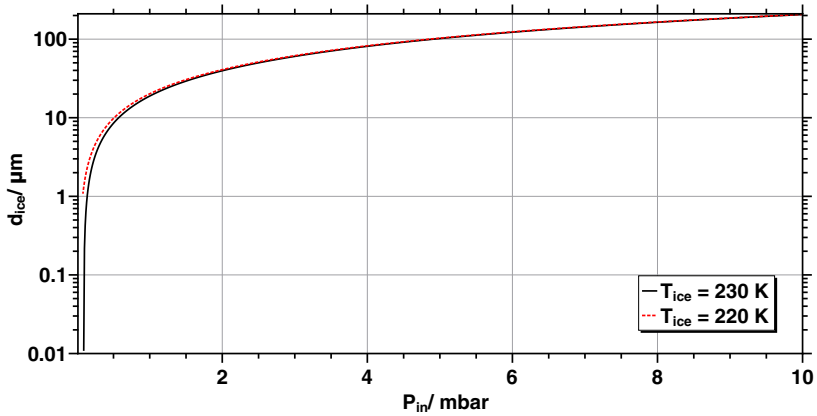

Figure 5.7: Predicted ice surface thicknesses based on changing input pressures of water at $220\,\mathrm{K}$ and $230\,\mathrm{K}$ and an upper surface area of $3\,\mathrm{cm}^2$. Temperatures are relevant to further measurements in this chapter.

V_{main} (m^3) is the volume inside the cavity of the surface set-up. This has been calculated as $7.8 \pm 0.1 \cdot 10^{-3}\,\text{m}^3$ using controlled expansions from a known volume into the main chamber derived from measurements made in appendix A.6. P_{in} (Pa) is the total pressure of water vapour in the cavity before freezing onto the surface. P_{ice} (Pa) is the vapour pressure above ice, formulated by the Wagner-Pruss equation.[186] ρ_{ice} ($\text{kg}\,\text{m}^{-3}$) is the ice density dependent on its temperature, T_{ice} (K), calculated from Feistel and Wagner.[74] R ($\text{J}\,\text{K}^{-1}\,\text{mol}^{-1}$) is the gas constant, T (K) is the ambient temperature and M_{H2O} ($\text{g}\,\text{mol}^{-1}$) the molecular mass of water. Lastly A_{ice} (m^2) is the area over which ice is to be grown. In our set-up this is the upper surface of the SS block, $3 \cdot 10^{-4}\,\text{m}^2$ ($3\,\text{cm}^2$) in size.*

Several assumptions have been made in this calculation. Firstly it is assumed that ice forms a layer of equal density throughout ignoring any structural inconsistencies that might arise during formation. Secondly it is assumed that all vapour goes into the ice surface of area, A_{ice}, and not to any other surface in the cavity; if the reductions are quantifiable this can be adjusted for in P_{in}. Figures 5.6 and 5.7 have been composed using equation 5.2. Figure 5.6 shows the variation of d_{ice} with T_{ice} for a number of different P_{in}. Figure 5.7 shows the variation of d_{ice} with pressures of P_{in} up to $10\,\text{mbar}$ at $T_{\text{ice}} = 230\,\text{K}$ and $220\,\text{K}$ which is relevant for experiments performed in this chapter.

5.4 Preliminary Ice Surface Testing

Ice is to be grown on the upper surface of an SS test block to prepare for growth on a similarly sized prism. Ideally it should range from nanometres to micrometres in thickness and be uniform and structurally consistent across its area, A_{ice}. In order to characterise the layer growth using a surface interference measurement a slow methodical build up is preferable. A_{ice} should also be as close to the maximum, $3\,\text{cm}^2$, of the SS surface as possible in order to provide the largest area for studying dynamics at the interface. It is also desirable that any ice formed remains either constant or can be monitored across a measurement.

To this end several different deposition methods were investigated in order to find the best available for this set-up and test the system. Starting with the simplest possible ideas various methods were investigated. Three of the most pertinent results are shown to put the optimal ice layering method used in context. The three examples are,

1. Surface temperature drop in the presence of water vapour - Section 5.4.1
2. Slow directed water leak in the presence of a pre-cooled surface - Section 5.4.2
3. Low temperature, directed ice growth - Section 5.4.3

The experiments varied from the final build, discussed in chapter 4, as they evolved over time however the broad set-up is similar. Any pertinent differences are discussed within each section.

* See appendix A.1 for further details.

5.4.1 Surface Temperature Drop in Presence of Excess Water Vapour

The initial response of the surface to the presence of water vapour was probed using an amount in excess of that desired. $7\,\mathrm{mbar}$ of water vapour was put into the chamber producing $\sim 140\,\mu\mathrm{m}$ of ice at $T_{\mathrm{ice}} = 230\,\mathrm{K}$ from the idealised curve shown in figure 5.7. The experiment was performed on an SS block with area $30\,\mathrm{mm}$ by $10\,\mathrm{mm}$, and height $12\,\mathrm{mm}$ which had been cleaned with HPLC acetone before use. H_2O admission was at the bottom of the chamber, far from the surface, and it was allowed to equilibrate for $\sim 15\,\mathrm{min}$ before the surface was cooled. The set point of the peltier started at $303\,\mathrm{K}$ at $t = 0\,\mathrm{s}$, then was dropped to $243\,\mathrm{K}$ at $t = 26\,\mathrm{s}$. After $500\,\mathrm{s}$ it was raised back to $303\,\mathrm{K}$. T_{PT1000} was recorded and T_{ice} calculated from vapour pressures monitored in the cavity; T_{ice} is therefore unavailable for surface temperatures higher than those where the vapour pressure of water is $7\,\mathrm{mbar}$. The results were monitored using a camera positioned along the z-axis in place of the CELIF optics. Complete details of the results are displayed in figures 5.8 and 5.9.

The recorded data demonstrates many characteristics of the set-up. Firstly a simple drive down of the surface temperature in the presence of water vapour does not produce a regular ice surface covering the full surface area. Figure 5.9 shows a localised build up of water at the start, condensing in the centre. This likely indicates the presence of a central region colder than the outer regions of the surface and therefore a temperature gradient across the surface as reported in other experiments such as Caloz *et al.*[92] This is backed up by T_{PT1000} and T_{ice} data which do not match across the measurement. Evidence supporting the validity of the T_{ice} measurement is seen at the melting point which derived from the vapour pressure records a temperature $T_{\mathrm{ice}} = 273.16\,\mathrm{K}$ as opposed to the PT1000 probe which records $T_{\mathrm{PT1000}} = 281.6\,\mathrm{K}$. A useful detail of the data occurs at the point of freezing in 5.9c and d. Since the process of freezing water is exothermic a temperature rise and fall is recorded, reflected in the T_{ice} data as well. Indication of the water purity, surface cleanliness and quality is shown by the freezing point occurring well below $273.15\,\mathrm{K}$ at $T_{\mathrm{PT1000}} = 256.7$ and $T_{\mathrm{ice}} = 255.2\,\mathrm{K}$.

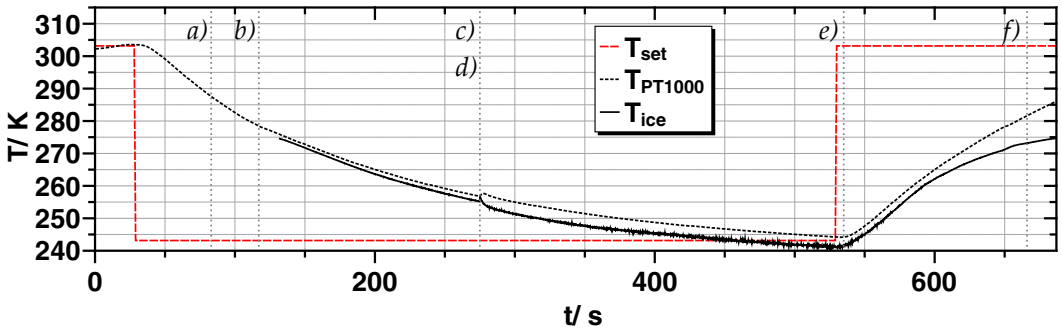

Figure 5.8: The temperature of the surface is shown varied over time. T_{set}, the set point of the peltier, is shown as a red, dashed line. The response of the PT1000 probe on the surface, T_{PT1000}, is shown as a black, dotted line. T_{ice}, derived from vapour pressures in the cavity, is shown as a black solid line. The times of the photos in figure 5.9 are marked. Note that T_{ice} relates the vapour pressure to ice not the supercooled water observed between *b)* and *c)/d)*.

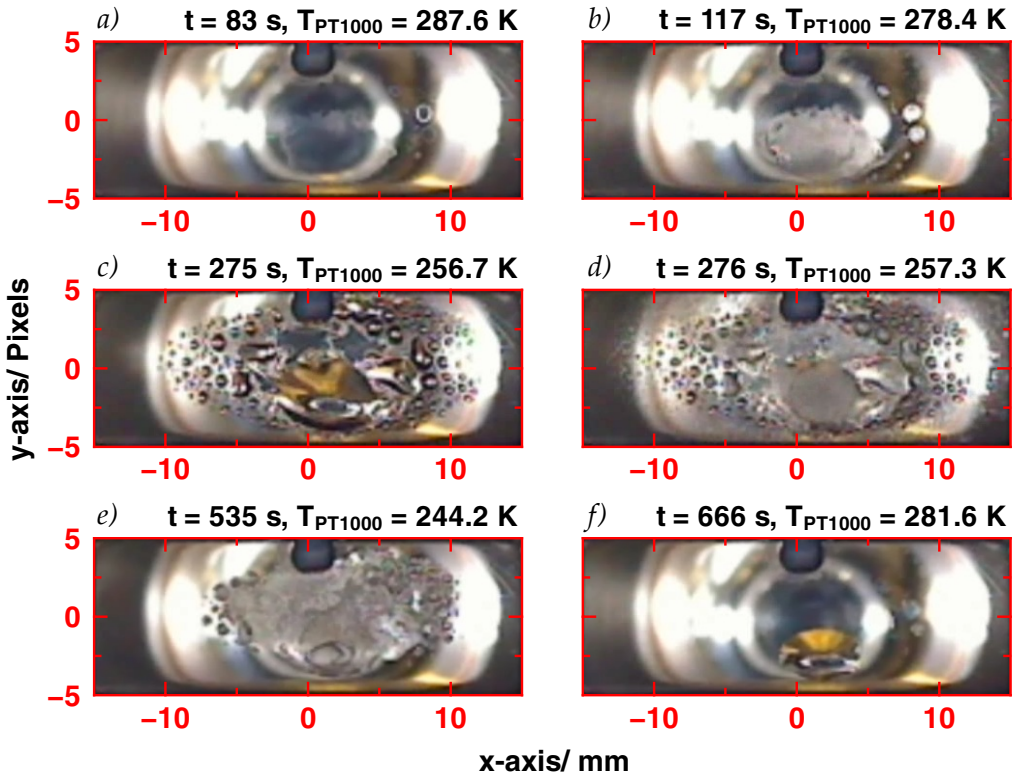

Figure 5.9: Figure displaying pictures of the ice surface during a temperature drop from $T_{\mathrm{set}} = 303 \rightarrow 243\,\mathrm{K}$ with $7\,\mathrm{mbar}$ H_2O inside the chamber. Recorded times are based on the video.
a) shows the surface immediately prior to the condensation event where a clouding of the surface becomes visible in the centre.
b) is the beginning of the main condensation event which results in c.
c) is the surface in the milliseconds before the freezing event in d.
d) Freezing takes place rapidly in fractions of a second, outside the resolution of the data rate of the temperature probe.
e) shows migration to the centre occurring.
f) is the recorded melting point of the ice.

5.4.2 Slow water vapour leak directed onto cold surface

Further testing investigated potential methods to combat the migration and the layering issues raised in the initial test. For this a slow leak in at the lowest temperature of surface was performed under two conditions. Firstly the surface was dosed directly with H_2O and secondly it was dosed into a chamber pre-filled with a background pressure of nitrogen. This was to slow and disperse the application of the water vapour to the surface.

$1\,\mathrm{mbar}$ of water vapour, enough to produce $\sim 20\,\mu\mathrm{m}$ of ice at $230\,\mathrm{K}$, was leaked into the chamber controlled by the high precision needle valve (Hamlet HXF1300) and admitted to the surface through the dispersion nozzle described in section 4.7. Leak rates of the needle valve had been characterised and it was used on a low setting producing a leak rate of $\sim 45 \pm 1\,\mathrm{mbar\,cm^3\,s^{-1}}$.* The temperature of the surface was set to $T_{\mathrm{PT1000}} = 230\,\mathrm{K}$ and vapour was leaked in after it was cooled and stable through the nitrogen background gas. Six tests were run with the cavity in each filled at a different backing pressure of nitrogen, $P_{\mathrm{N2}}^{\mathrm{backing}} = 0$, 0.5, 1, 2, 5, and $10\ \mathrm{mbar}$. Results were monitored using a camera on the CELIF axis trained at the surface. The needle valve was not altered in between measurements therefore the overall leak in time changed from $\sim 3 \rightarrow 4\,\mathrm{min}$ across the different runs depending on the backing pressure in the chamber.

Pictures are shown for $P_{\mathrm{N2}}^{\mathrm{backing}}$ at 0, 0.5 and $5\,\mathrm{mbar}$ in figure 5.10 which typify the complete range of tests performed. 1a and b show that a slow leak rate with no N_2 grows ice in the centre of the surface where the coldest region is believed to exist. This is despite water being directed across its length. However the surface is improved in comparison to figure 5.8 as it is more uniform. 2 and 3 show the effect of N_2 backing the surface. Ice now builds up over a larger area but forms isolated islands. In 3a/b all presence of a flat ice surface in the centre has disappeared at t_{in}. In 2b, $30\,\mathrm{min}$ after t_{in} ice has shown some migration toward the central $10\,\mathrm{mm}$ looking more similar to 1a/b. 3a, which has a higher backing pressure of nitrogen, also shows migration but much less in comparison and the structure remains similar to that at the start even after $30\,\mathrm{min}$. One contribution to these two effects is the increased difficulty of a water molecule diffusing through the backing pressure of nitrogen. The mean free path between collisions for N_2 at 0.5 and $5\,\mathrm{mbar}$ and $293\,\mathrm{K}$, assuming a sphere of roughly $\varnothing 1\,\mathrm{\AA}$, is 1.4 and $0.14\,\mathrm{mm}$.† From this the slower migration speeds and larger area of dispersement in figure 3a/b relative to 2a/b can be somewhat rationalised.

* Needle valve set on gauge marking 1.00. Leak rates based on a volume of $7.8 \pm 0.1\,\mathrm{L}$ calculated for the CRDS system with surface mount installed. † Using the standard equation for the mean free path in a single molecular species derived from kinetic theory, $\lambda = K_{\mathrm{B}}T/(\sqrt{2}\pi d^2 P)$, K_{B} is the Boltzmann constant, T is the temperature, d is the diameter of the gas and P its pressure.

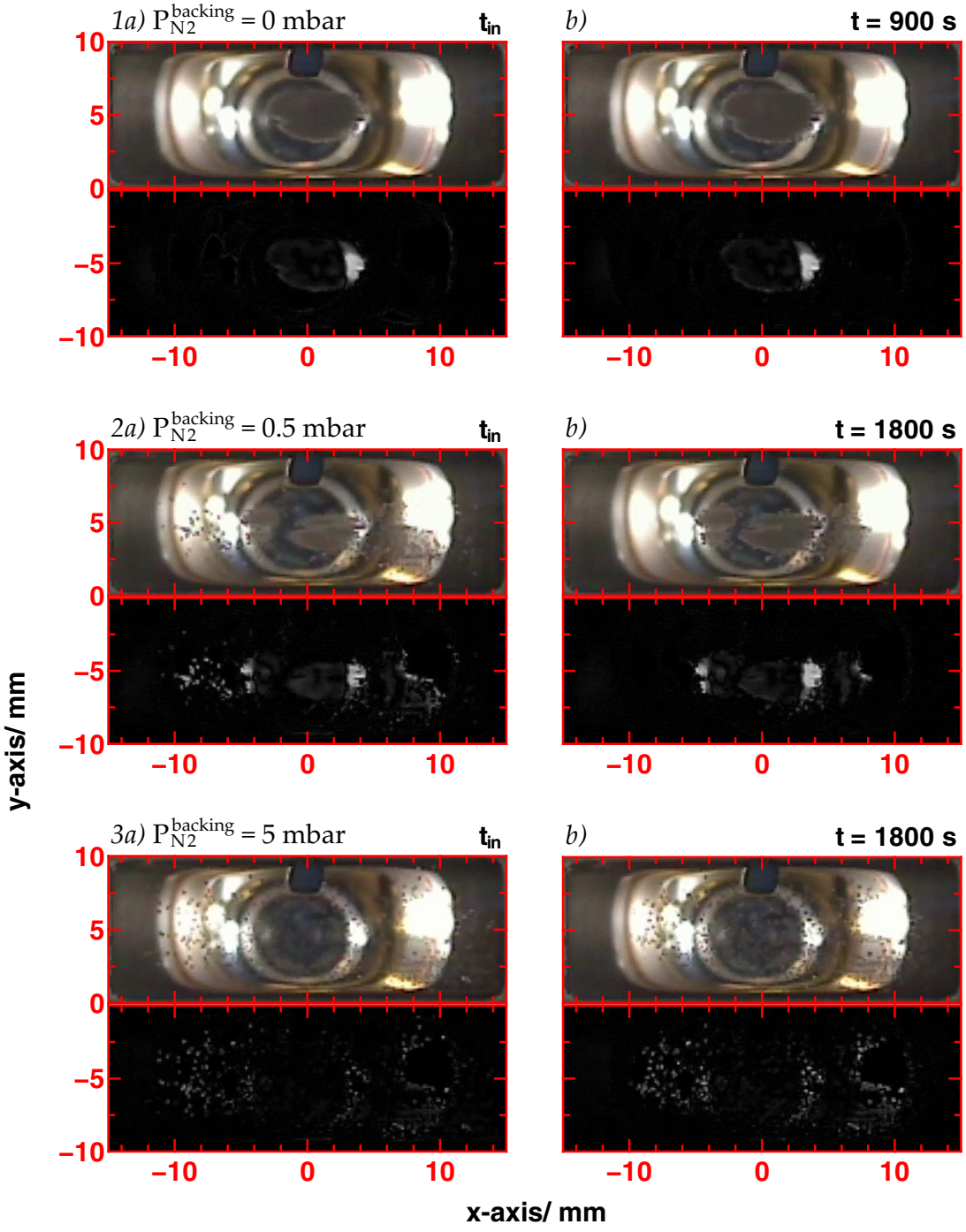

Figure 5.10: Each set of figures is taken at $T_{\mathrm{PT1000}} = 230\,\mathrm{K}$. The upper figure is a still of the surface and the lower a background subtracted image to aid visual location of ice build up. The PT1000 probe can be seen in each shot at $\sim[x, y] = [0, 10]\,\mathrm{mm}$. Figure 1a, 2a and 3a are at time, t_{in} immediately after $1\,\mathrm{mbar}$ water vapour has finished being leaked into the chamber. 1b, 2b and 3b are then at some arbitrary time after t_{in} noted on the diagram.

5.4.3 Low temperature, directed ice growth

One test performed noticeably better in comparison to the others. For this the SS block configuration was used, the same as in section 5.4.1, but with an open $\varnothing 6\,\mathrm{mm}$ pipe directing H_2O vapour towards the surface from one side. In this test the surface was pushed hard towards its lowest temperature. The copper cooling block was held at $T_{\mathrm{Cu}} = 278\,\mathrm{K}$, lower than usual, by setting the cooling unit for the copper heat-sink to a sub-zero temperature. Measurements of T_{ice} recorded a water vapour pressure based temperature of $215 \pm 3\,\mathrm{K}$, where the error is the standard error in 2000 points. Once the surface was set-up, $0.5\,\mathrm{mbar}$ water, $\sim 10\,\mu\mathrm{m}$ in ice thickness, was leaked in using the needle valve at the rate used in section 5.4.2.

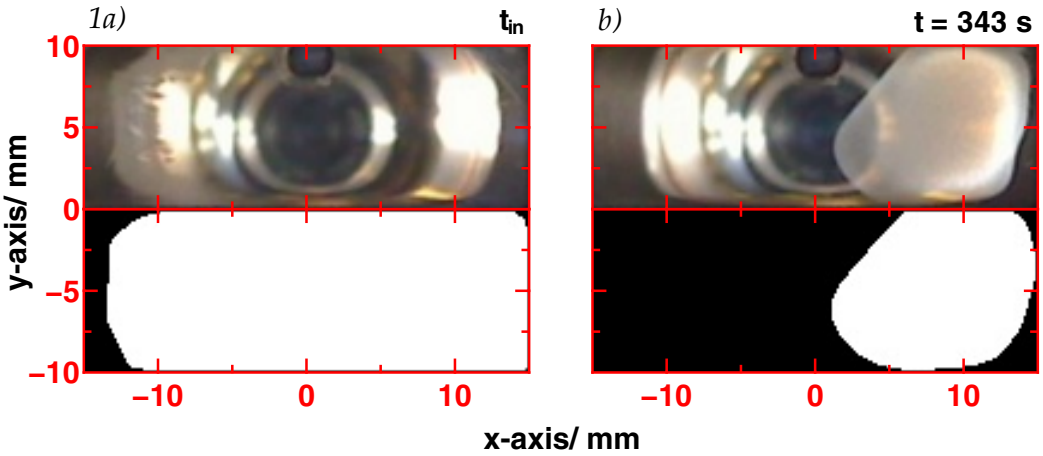

Figure 5.11: Set of figures taken at $T_{\mathrm{PT1000}} = 223\,\mathrm{K}$ with $0.5\,\mathrm{mbar}$ water vapour. Upper figures show the actual surface and lower figures show results of a morphological analysis, described in further detail in section 5.7. *1a)* shows the surface at time, t_{in}, immediately after water has finished being admitted to the chamber. Although difficult to see ice covers the entire surface marked by the filter. *1b)* shows the surface later at $t = 343\,\mathrm{s}$.

Figure 5.11 shows results which are significantly better than those seen previously. In 1a ice is initially layered across most of the surface and is uniform in appearance with a glassy, transparent look expected from the low UV-visible absorption constants in ice. Following deposition, the ice then migrates to a smaller region on the right-hand side, seen in 1b. Despite using the same leak rate as tests in 5.4.2 the ice produced was the best quality seen. The surface temperature reached, $T_{\mathrm{ice}} = 215 \pm 3\,\mathrm{K}$, was colder than was able to be reproduced after this measurement; after a set-up alteration this temperature was not reached again. This test at a lower temperature indicates a significant improvement in the behaviour of ice when grown at colder temperatures.

The biasing to one side of the surface which is seen was caused by a fluid guide initially used in the cooling block. The fluid guide channelled coolant around the cylindrical reservoir inside the cooling block. This caused the cold spot of the surface to sit above the inlet of the fluid circulator. Further measurements have been made without the fluid

guide creating a central reserve of coolant in the cooling block shifting the cold spot to a more central position. This shows that the temperature on the upper surface in some way reflects the efficiency of the cooling on the peltier's hot junction.

5.5 Optimised Ice Surface Production

Preliminary testing of the surface showed that water vapour cannot be in the cavity while the surface cools as ice formed directly onto the coldest parts reducing the area covered from the start. A water leak directed onto the surface at $230\,\mathrm{K}$ produced a similar result. However under similar dosing conditions at $220\,\mathrm{K}$ ice layered uniformly across a large part of the surface before migrating to the centre. Water was also leaked into the chamber through a background gas in order to inhibit migration and slow the dosing rate. Under these conditions although these goals were met ice formed into small nucleated sites. In summary the two major issues which were brought up by the preliminary tests were the low surface area coverages and the migration of ice to smaller areas over time.

These problems were partially solved in a few different ways. Good surface coverage was obtained with a rapid and directed application of water to the surface leaving it little time to migrate. Migration could also be slowed by saturating the surface with a thick, $> 100\,\mu\mathrm{m}$, layer of ice so that it then took longer from the increased volume of ice on the surface. However this formed ice which was much thicker than the nanometre and micrometre layers desired. For controlling migration the most robust method found was to use N_2 (or some other suitably inert gas) above the surface. This forced the ice vapour to diffuse through higher gas levels. Usefully this did not decrease the peltier performance by an appreciable amount, as shown in section 4.9. Background gas levels were only limited by the seal on the join between the partition plate and SS surface; So as long as a maximum pressure difference of $\sim 10 \rightarrow 50\,\mathrm{mbar}$ was not exceeded between the main chamber, P^{main}, and partition, $P^{\mathrm{partition}}$, almost any pressure could be used. The final method, which helps solve migration and coverage, was to drive the surface to the coldest temperatures possible where vapour pressures of ice are lower and sticking coefficients of water vapour to SS and ice increase. This temperature is ultimately decided by the heat load, Q_L, and operating efficiency of the peltier and its build.

From this information the best method for ice deposition with the current set-up was developed. Ice must be deposited at the lowest temperature which for this set-up is $T_{\mathrm{PT1000}} \sim 230\,\mathrm{K}$. After deposition, temperature changes can be made but at the cost of increased migration at the higher temperatures. The best method to layer the ice is by directing it in a fast expansion at the surface. Continuing to use a needle valve was problematic for controlling small dosages of water vapour at a high leak rates into the cavity across the surface. While the ultimate outlook of this method indicates use of a molecular beam or controlled flow system, these are a significant expense to the machine and were neither to hand nor integrated into the experiment at the time.

A simpler method was designed using materials that were available at the time shown

in figure 4.9. A separate chamber, called the reservoir,* was installed between the water source and dispersion delivery system, described in section 4.7. It was isolated from the main chamber using pneumatic diaphragm valves and a capacitance manometer (Leybold CTR100, range $0 \rightarrow 14\,\mathrm{mbar}$) was connected to the chamber so that pressures inside could be measured. The maximum pressure range was restricted by the availability of spare pressure gauges, but it was sufficient water vapour to layer ice surfaces up to $\sim 14\,\mu\mathrm{m}^{\dagger}$ in thickness over the full area of the prism surface, $3\,\mathrm{cm}^2$. Thusly water vapour could be rapidly expanded into the main chamber, initially held at vacuum, across the surface of the prism via the dispersive delivery system. This method produced the best ice surface found so far with this system.

Going forwards the pressures inside the reservoir are termed P^{res}, where water inside the reservoir is $P^{\mathrm{res}}_{\mathrm{H2O}}$ and nitrogen, $P^{\mathrm{res}}_{\mathrm{N2}}$. Partial pressures, after expansion into the main chamber are either $P^{\mathrm{main}}_{\mathrm{H2O}}$ for water or $P^{\mathrm{backing}}_{\mathrm{N2}}$ for nitrogen. Generally experiments are referred to in terms of the reservoir pressures used. For the purpose of calculating the expected pressure inside the main chamber from a specific reservoir pressure the main chamber has been characterised. This is shown by a conversion equation derived from the data in appendix A.6.

$$P^{\mathrm{main}} = 5.639 \pm 0.004 \cdot 10^{-2} * P^{\mathrm{res}} - 1.26 \pm 0.27 \cdot 10^{-2} \tag{5.3}$$

5.6 Temperature Characterisation of the Peltier Setup

Initial testing of the SS ice surface setup indicated that the pressures recorded did not match expected values based on temperatures recorded by the PT1000 sensor. The dominant factor was believed to be the temperature gradient existing across the surface. This was investigated further comparing pressures recorded by CRDS running near to the surface with capacitance manometers far from the surface to characterise the performance of the peltier.

5.6.1 Experimental Setup

The experiment consists of the standard CRD gas cell as set-up in section 4.3 with window, camera and light installed on the CELIF axis for surface monitoring. Pulsed dye laser system Ib (see section 3.3) was used and set-up as explained in section 5.2.1. Water lines, $589.514\,\mathrm{nm}$ and $583.563\,\mathrm{nm}$, were used to monitor water vapour pressures, $P^{\mathrm{main}}_{\mathrm{H2O}}$, at $1 \rightarrow 10$ and $0 \rightarrow 1\,\mathrm{mbar}$ respectively using CRDS. Concurrently with CRD measurements, $P^{\mathrm{main}}_{\mathrm{H2O}}$ is also monitored using C2 from the pressure gauge array discussed in section 4.6. High purity water was degassed and admitted into the chamber by the method from section 4.7.

* Made from a CF40 cross. † See figure 5.7.

The SS replica prism surface was prepared in the following manner in addition to the standard cleaning and set-up described in section 4.11. The surface was pulled back in accordance with the surface diffraction data while monitoring the CRD signal. T_{PT1000} was dropped to 230 K. Once stable with no hysteresis in the temperature, a controlled leak from the high precision needle valve (Hamlet HXF1300) was performed. The needle valve was used on its highest setting with a leak rate into the chamber of $\sim 2590 \pm 30\,\mathrm{mbar\,cm^3\,s^{-1}}$* and H_2O was admitted using the dispersive delivery system.

Temperatures and pressures were recorded at 1000 laser shots per measurement, in the range $T_{\mathrm{PT1000}} = 230 \rightarrow 276\,\mathrm{K}$ in steps of 2 K. During the measurements the copper block ranged from $T_{\mathrm{Cu}} = 287\,\mathrm{K}$ at $T_{\mathrm{PT1000}} = 273\,\mathrm{K}$ to $T_{\mathrm{Cu}} = 299\,\mathrm{K}$ at $T_{\mathrm{PT1000}} = 230\,\mathrm{K}$. Two different experiments were performed. In method one 10 mbar water was admitted. After ice was formed and the system had equilibrated, the temperature of the surface was driven to $T_{\mathrm{PT1000}} = 250\,\mathrm{K}$ rapidly promoting ice to the cold spot in the centre. Measurements were then taken from $250 \rightarrow 230\,\mathrm{K}$, and then from $250 \rightarrow 276\,\mathrm{K}$. In method two, a significant amount of water, $> 10\,\mathrm{mbar}$, was admitted covering a large portion of the surface area with ice. The temperature was then ramped up from $230 \rightarrow 276\,\mathrm{K}$ and the ice allowed to evolve naturally. From this a comparison between both methods, the first which covered a small defined area and the second which covered a larger and more variable area, could be compared.

5.6.2 Results

Photos of the ice surface from both methods were taken during the measurements at different temperatures. A selection of these is shown in figure 5.12. The pictures provide the difference in the ice surface coverage between the two measurements across the main temperatures of interest. Figure 5.13 shows the surface characterisation, T_{PT1000} measured against $P^{\mathrm{main}}_{\mathrm{H2O}}$ as calculated by the CM and CRD. The difference in temperature, ΔT, is described in equation 5.5 where T_{ice} is the temperature derived by $P^{\mathrm{main}}_{\mathrm{H2O}}$ from the CM or RDT measurements. Temperatures were obtained using a solver function in MATLAB[187] on the Wagner-Pruss[75] form of the ice vapour pressure equation.

Qualitative fits have been used to describe the temperature vs pressure trend of the ice surface using an average of both sets of CM data. Figure 5.13a uses an extended form of the Antoine equation, which is derived from the Clausius-Clapeyron equation. It is shown in equation 5.4 with the extended parameters in braces. ΔT has been fit to a second order polynomial, equation 5.6. The fitting parameters are provided so that T_{ice} can be predicted from a measurement of T_{PT1000}.

$$\log_{10} P^{\mathrm{main}}_{\mathrm{H_2O}} = A + \frac{B}{C + T_{\mathrm{PT1000}}} + \left\{ D \log_{10} T_{\mathrm{PT1000}} + E \cdot {T_{\mathrm{PT1000}}}^{F} \right\} \tag{5.4}$$

* Needle valve set on gauge marking 3.00. Leak rates based on a volume of 7.8 ± 0.1 L calculated for the CRDS system with surface mount installed.

$$\Delta T = T_{\mathrm{PT1000}} - T_{\mathrm{ice}} \tag{5.5}$$

$$\Delta T = A' + B' \cdot T_{\mathrm{PT1000}} + C' \cdot {T_{\mathrm{PT1000}}}^2 \tag{5.6}$$

where,

$$A' = -13.7, \qquad B' = 0.2, \qquad C' = -5 \cdot 10^{-4}$$

$$SSE = 0.1,\, RMSE = 0.07,\, R\text{–Square} = 0.9923,\, \text{Adjusted}\, R\text{–Square} = 0.9915$$

$$\text{Valid for range, } T_{\mathrm{PT1000}} = 230 \rightarrow 274\,\mathrm{K}$$

5.6.3 Analysis

Data shown in figure 5.13 displays the trend expected from laboratory observations. The centre of the SS surface is consistently colder than the PT1000 probe reports based on pressures expected from the Wagner-Pruss relationship. Although the exact nature of the temperature gradient across the surface cannot be characterised at this point, a key result from figure 5.13 is that both layering methods employed produce similar results despite a significant difference in ice surface area and volume. Near-surface CRD data correlates well with CM data indicating that localised vapour pressures are not too different to those measured far from the surface. Generally however the CRD data, as it moves towards $230\,\mathrm{K}$, seems to measure lower pressures than the CM data. This may indicate that the CM data is measuring an average of the surface temperature where the CRD, which cuts across the centre of the surface is measures colder temperatures from observing a different, more central section of the surface. The CRD data is well within a standard deviation of the CM data but only just within a standard error at low T_{PT1000}. It would have been more informative if stronger water lines were able to be used. However these were outside the ability of the laser system used at the time.

ΔT peaks at $\sim 5\,\mathrm{K}$ in difference when T_{PT1000} is at $230\,\mathrm{K}$. It is non-linear across the measured range showing that its behaviour does not match the Wagner-Pruss curve simply shifted on the x-axis. As T_{PT1000} is driven to lower temperatures the difference between the probe and the temperature derived from the pressure measurements becomes larger. This shows that the observed temperature gradient on the surface changes as the peltier drives the surface temperature down. Two causes could be behind this, either the centre cools more efficiently as the surface temperature drops or the outside cools less efficiently. In the first case one might expect T_{PT1000} to also cool more efficiently. Therefore it is likely the second case.

Changing thermal conductivities should not be the main effect of the trend observed. This property only relates to the rate at which heat can be removed from the surface. Moreover the thermal conductivities in the bulk materials used in the set-up do not change much over the range of the experiment, displayed in A.4. Linear expansion co-

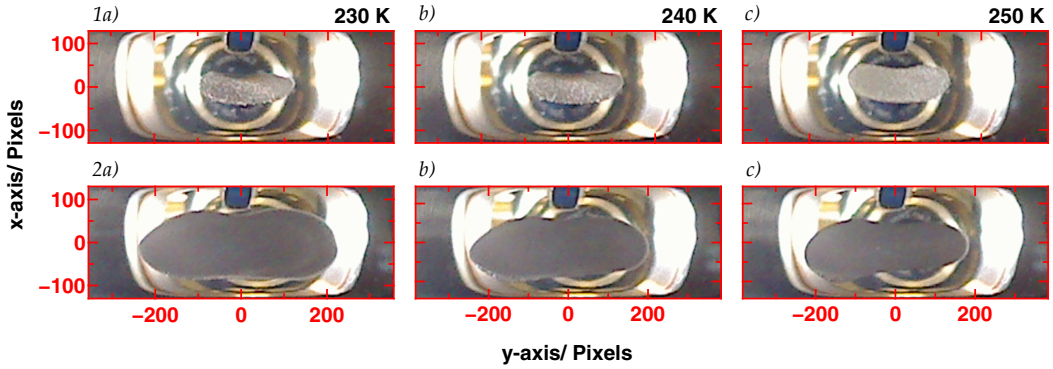

Figure 5.12: Photographs of the ice in the two different runs are shown. *1a), b)* and *c)* is method one, where ice is driven to the coldest part of the surface. *2a), b)* and *c)* is method two where a large amount of ice is left to evolve naturally. Shown in each picture is the PT1000 gauge, a blue square, top centre, roughly at pixel position [0,100]. T_{PT1000} in *1a), b)*, and *c)* is dropped from $250 \rightarrow 230$ (then increased from $252 \rightarrow 276\,\mathrm{K}$). In *2a), b)*, and *c)*, T_{PT1000} increases from $230 \rightarrow 276\,\mathrm{K}$

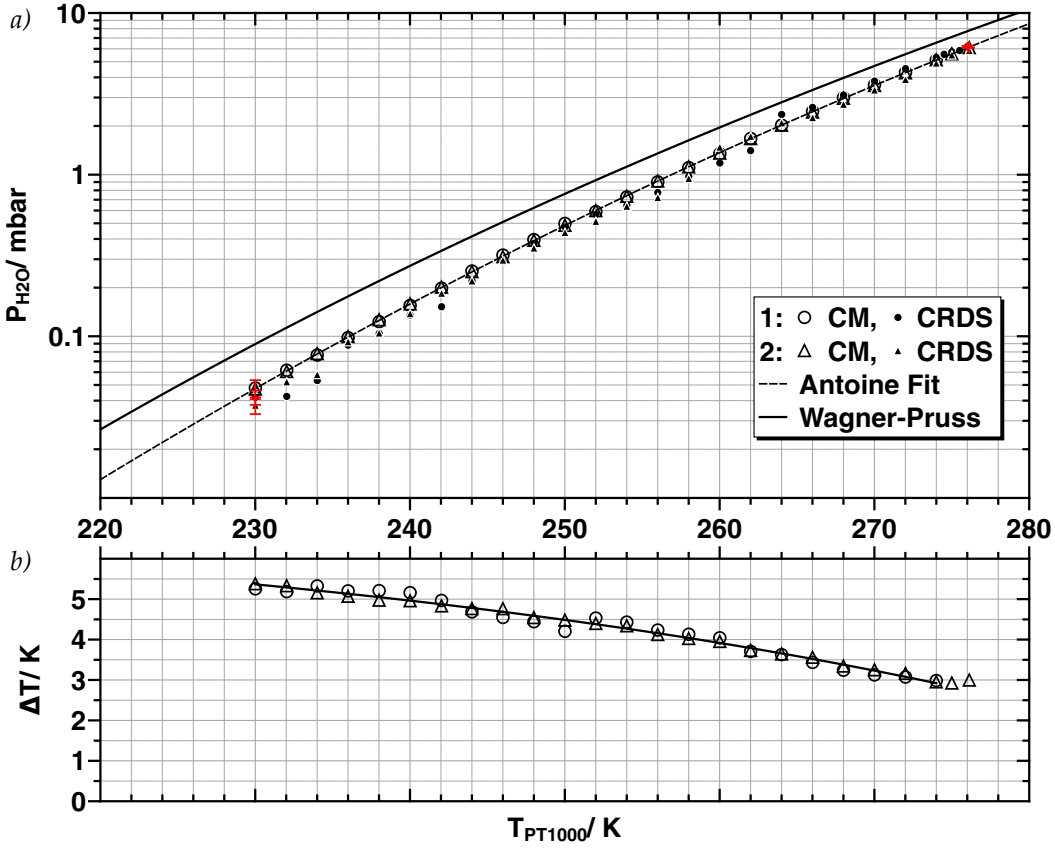

Figure 5.13: *a)* displays $P_{\mathrm{H2O}}^{\mathrm{main}}$ versus T_{PT1000}. Data taken using method 1 is shown in circles and method 2 in triangles. Capacitance manometer data is shown by large open shapes (○,△) and CRD data by small filled shapes (●,▲). The solid line shows the ice vapour pressure according to Wagner-Pruss and dashed line is a qualitative fit using the Antoine equation to an average of the CM data. *b)* displays the ΔT between T_{PT1000} and that derived from $P_{\mathrm{H2O}}^{\mathrm{main}}$. A simple polynomial of order 2 is used to fit the trend. Errors shown on method 2 represent the spread of the data on CM data and the standard error in CRD data. Errors shown are the largest in the set and are similarly sized for method 1.

efficients will have a greater impact on the surface temperature. Assuming a perfect sandwich of layers above the peltier, as they cool they should compact. As well as this the edge bond between the surface and the partition should thin out decreasing the cross-sectional area. Thus with lower residual pressures above the surface the peltier should find the environment less demanding to cool at lower temperatures. However the reality of the set-up is that structurally the sandwich is imperfect and the hard layers rather than being perfectly flat have a varying amount of convex nature. Therefore as the system reacts to the temperature drop it will warp. This will cause the cold face of the peltier to cool less well on the outside while remaining more efficient in the centre where the convex surfaces are closest. Similarly on the peltier hot face the ability of the cooling block to pump heat in the centre will remain more efficient relative to the outside. Therefore the structural changes in the set-up caused by thermal contraction must cause the peltier to drive harder to cool the outside to the set temperature which is then reflected by ΔT increasing in the centre.

5.7 Morphological Analysis of Ice Migration

The SS test prism has been characterised in terms of its temperature and the best method to produce ice so far has been found. Work proceeded to investigate techniques to characterise the ice in terms of thickness and area. This was done in two ways morphologically with video analysis and using an optical interference technique. Using these migration rates to the cold central region on the surface were investigated and the effect of a nitrogen background gas was characterised in order to slow the rate at which the area of ice decreased over time with a view to the application in a surface dynamics experiment.

5.7.1 Experimental Setup

The set-up going forward was the final, most advanced iteration of the peltier based system. It is described in detail in chapter 4. Included here is a brief overview and the details of any major differences from the previous experiments. The set-up consisted of the standard CRD gas cell with window, camera (Logitech C905) and light installed on the CELIF axis for surface monitoring and morphological analysis (MA). Pulsed dye laser system Ib (see section 3.3) was used and set-up as previously explained in section 5.2.1. Water line, $583.563\,\mathrm{nm}$, was used to monitor ice vapour pressures, P_{ice}, using CRDS. As in the surface temperature characterisation these measurements were broadly in line with data provided more readily from the capacitance manometer array discussed in section 4.6. T_{PT1000} was set to $230\,\mathrm{K}$, where it remained for all experiments. P_{ice} averaged across the experiments performed was $0.051 \pm 0.001\,\mathrm{mbar}$ giving $T_{\mathrm{ice}} = 225.2 \pm 0.2\,\mathrm{K}$. T_{Cu} was held at $303\,\mathrm{K}$ and T_{peltier} was recorded at $220\,\mathrm{K}$.

Experiments were performed in three ways, each looking to characterise the ice in terms of its area, thickness and migration towards the centre. Runs were first made by using

different reservoir pressures of water, $P^{\text{res}}_{\text{H2O}}$, thus altering the expansion across the surface and thickness. Secondly they were made by inhibiting migration using nitrogen. The SS replica prism ice surface was prepared in accordance with the standard set-up in section 4.11 and the surface pulled back from the CRD waist as in 5.1. High purity water was degassed per section 4.7 and vapour amounts of $4 \rightarrow 12\,\text{mbar}$ held in the reservoir chamber. Time for equilibration was allowed during which $\sim 2\,\%$ was lost to adsorption to the walls. At the start of an experiment a pneumatic valve connected to the main chamber was opened and the vapour expanded into vacuum via the dispersion nozzle across the surface forming ice. Measurements were simultaneously recorded using the camera and CRD set-up. In measurements using a background, nitrogen was admitted to the main chamber via a separate line, in the seconds following water admission.

Image data has been acquired from camera footage of the ice surface as it evolves with time and then processed to find the surface coverage. It has been analysed using the image processing toolbox package included in MATLAB[187] through a process of cropping, background subtraction and edge analysis using a Canny algorithm.* Post edge analysis a convex hull was applied to the image to obtain an overall ice area. This is discussed in further detail in section 5.7.3. Video data of the PT1000 probe indicated no visual existence of ice covering it. Therefore its area was convoluted with the image data to remove it from the resulting convex hull.

5.7.2 Results

Figures 5.14 and 5.15 show the surface area, A_{ice}, and thickness, d_{ice}, for pure water expansions of $P^{\text{res}}_{\text{H2O}} = 4$, 6, 8, 10 and $12\,\text{mbar}$, equivalent to 2.5, 4.8, 7.3, 9.35, $11.8\,\mu\text{m}$ of ice over $3\,\text{cm}^2$. In theory ice should form for any value of $P^{\text{res}}_{\text{H2O}} \gtrsim 1.1\,\text{mbar}$ as this value, after expansion into the main cavity, exceeds P_{ice} at $225.2\,\text{K}$. In practice however the lowest pressure which produces visible ice is $\sim 2.5\,\text{mbar}$. However this does not expand across the surface well instead migrating rapidly to a small ill defined spot. Therefore $4\,\text{mbar}$ was used as the lowest $P^{\text{res}}_{\text{H2O}}$. Figures 5.16 and 5.17 show ice formed from an $8\,\text{mbar}$ expansion with different nitrogen background levels, $P^{\text{backing}}_{\text{N2}} = 1$, 2, 5 and $10\,\text{mbar}$. Due to the presence of slow leaks across the partition surface seal, $0.7\,\text{mbar}\,\text{cm}^3\,\text{s}^{-1}$ at 5 mbar, and $13\,\text{mbar}\,\text{cm}^3\,\text{s}^{-1}$ at 10 mbar, small top ups were made to the nitrogen above $5\,\text{mbar}$ during the runs.

Surface areas, A_{ice}, have been normalised against the maximum area of the SS prism without the PT1000 probe, $2.92\,\text{cm}^2$. It is assumed that no ice is formed anywhere other than on the target SS surface and that for estimations in the surface thickness, d_{ice}, it forms a regular thickness across the area covered. Since area alone is used to derive d_{ice} this method is unable to detect layers still depositing while the gas phase is equilibrating with the surface. Therefore during early times the thickness is overestimated. For the

* Other algorithms such as Roberts, Prewitt and Sobel were tested but the Canny method was found to be the most effective.

calculation of surface thickness the temperature dependent density of crystalline water is used as per appendix A.1. Measurements from Keyser[99] place a value for the bulk density of ice accounting for porosity at $0.64 \pm 0.03\,\mathrm{g\,cm^{-3}}$. Therefore to account for this a factor of 1.56 can be applied to the values of d_{ice} recorded. Errors shown in the surface thickness data include an estimate for the maximum error in the surface area measurements of 5%. The precise error in many of the processed images is smaller than this becoming smaller at later times. Errors in the image analysis are discussed in further detail in next section.

5.7.3 Systematic Errors in the Morphological Analysis

To understand the systematic error in the MA deeper knowledge of the method is required. For each image first it was cropped down to the area of the surface and then background subtracted leaving ice on a noisy background. The Canny algorithm was then used to define the edges against the noise in the subtracted ice image. This process resulted in a simplified binary image of white ice edges on a black background. Convex hulling then calculated the minimum area able to encompass all edges creating a measurable estimate of A_{ice}. The PT1000, which was assumed to be ice free, was subsequently removed. If left in, it overstated the area during the early stages of migration, but not by more than 3%.

Systematic errors in the MA are caused by the both the Canny algorithm and convex hull methods. The convex hull approach simply encircles all edge pixels, which have been located by the Canny algorithm. Therefore any noise or erroneously located edge ends up included inside the convex hull. This can lead to a systematic overestimation if pixels outside the ice area are included as shown in figure 5.18a. An underestimate in the area can occur from a failed edge detection depicted in 5.18b which in the ice data it occurred for two reasons, undetectable edges and blind spots.

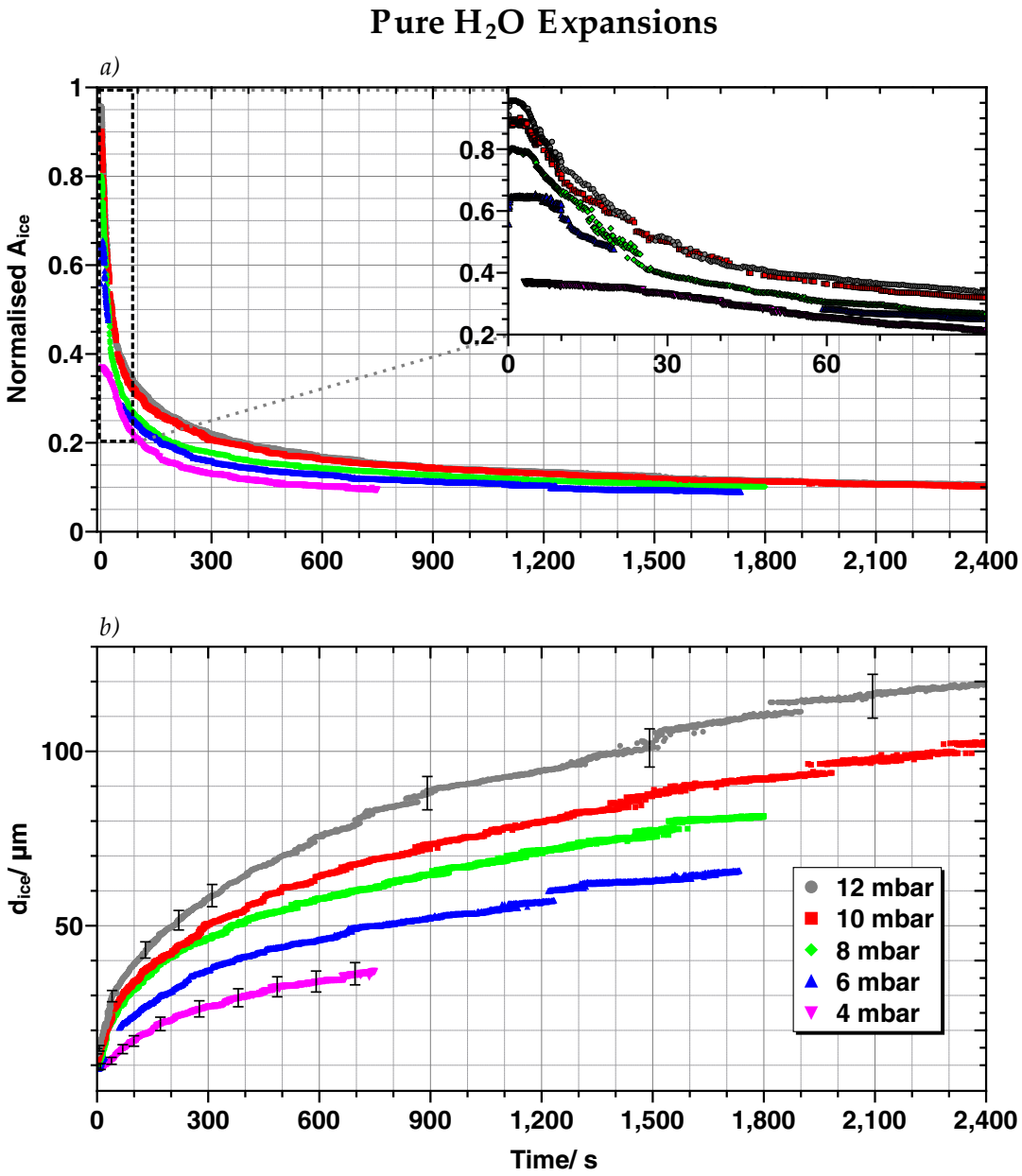

Figure 5.14: Morphological analysis showing *a)* A_{ice} and *b)* d_{ice} versus time plots for $P^{\mathrm{res}}_{\mathrm{H2O}} =$ 12, 10, 8, 6 and 4 mbar. Thicknesses are derived from equation 5.2. The errors shown are the standard deviation, including an estimate for the error in *a)* of $\sim 5\,\%$. Data has been clipped where it clearly deviates from observed ice surface areas. Areas are normalised relative to the area of the SS surface excluding the area occupied by the PT1000 temperature probe.

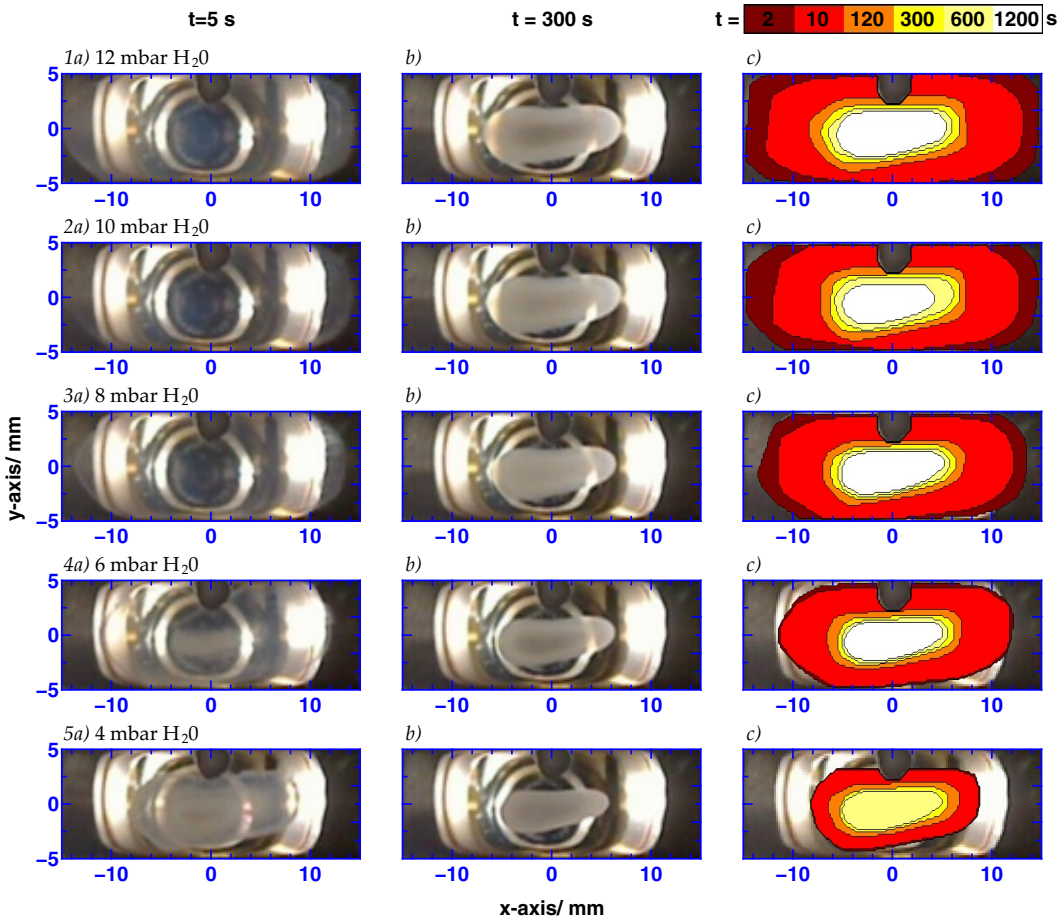

Figure 5.15: Comparison of the ice layers from figure 5.14 taken at two different times, *a)* at $t = 5\,\mathrm{s}$ and *b)* $300\,\mathrm{s}$. Times have been chosen arbitrarily to best represent different stages in the analysis and migration. *c)* shows contour plots of the time varying ice areas as indicated by the colour scheme above the column.

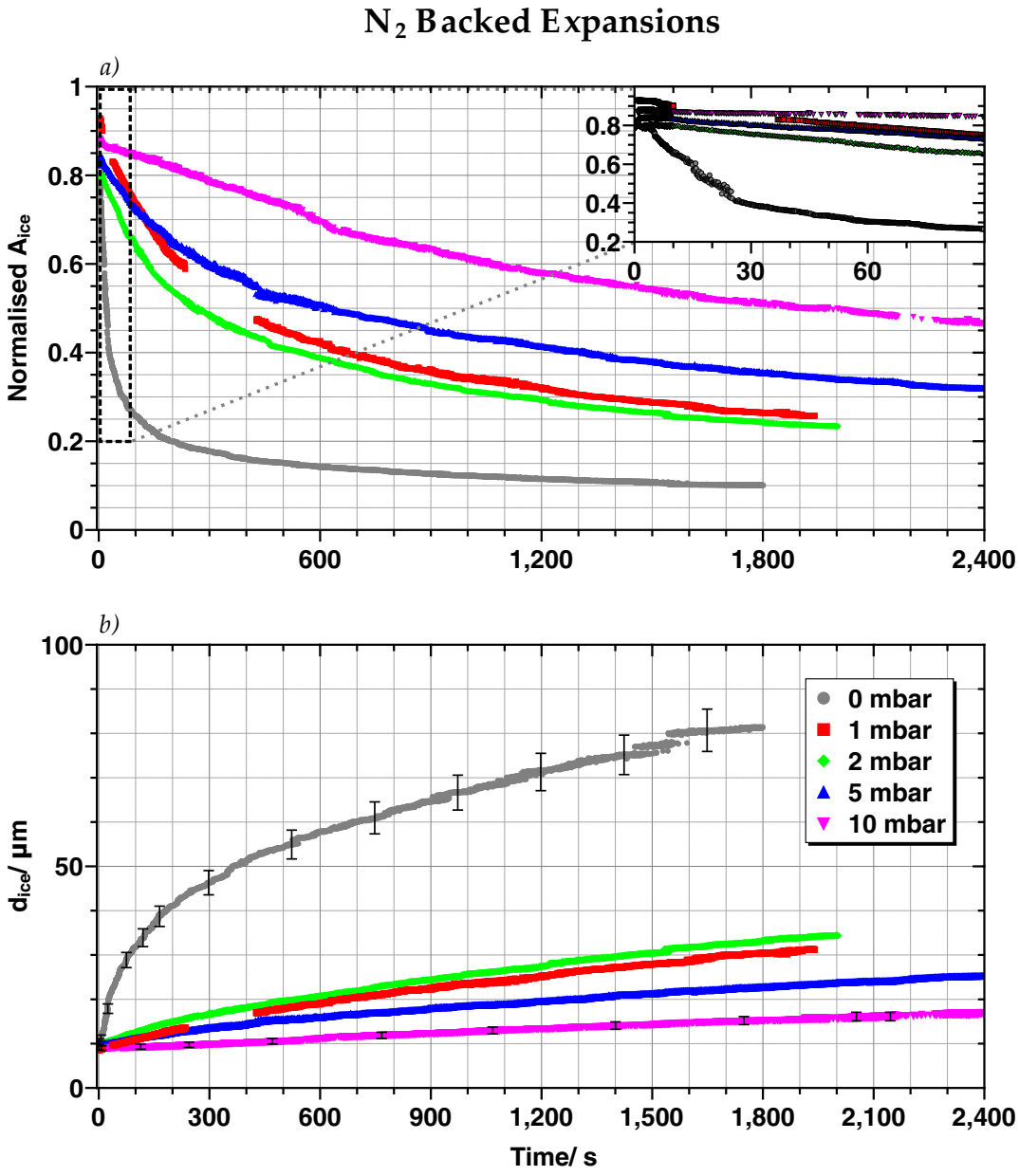

Figure 5.16: Morphological analysis showing *a)* area and *b)* thickness versus time plots for $P_{\mathrm{H2O}}^{\mathrm{res}} = 8\,\mathrm{mbar}$ followed by a background fill to $P_{\mathrm{N2}}^{\mathrm{backing}} = 1, 2, 5$ and $10\,\mathrm{mbar}$ N_2. Thicknesses are derived from equation 5.2 and the errors shown are the standard deviation in the calculation, including an estimate for the error in *a)* of $\sim 5\,\%$. Data has been clipped where it clearly deviates from observed ice surface areas. Areas are normalised relative to the area of the SS surface excluding the area occupied by the PT1000 temperature probe.

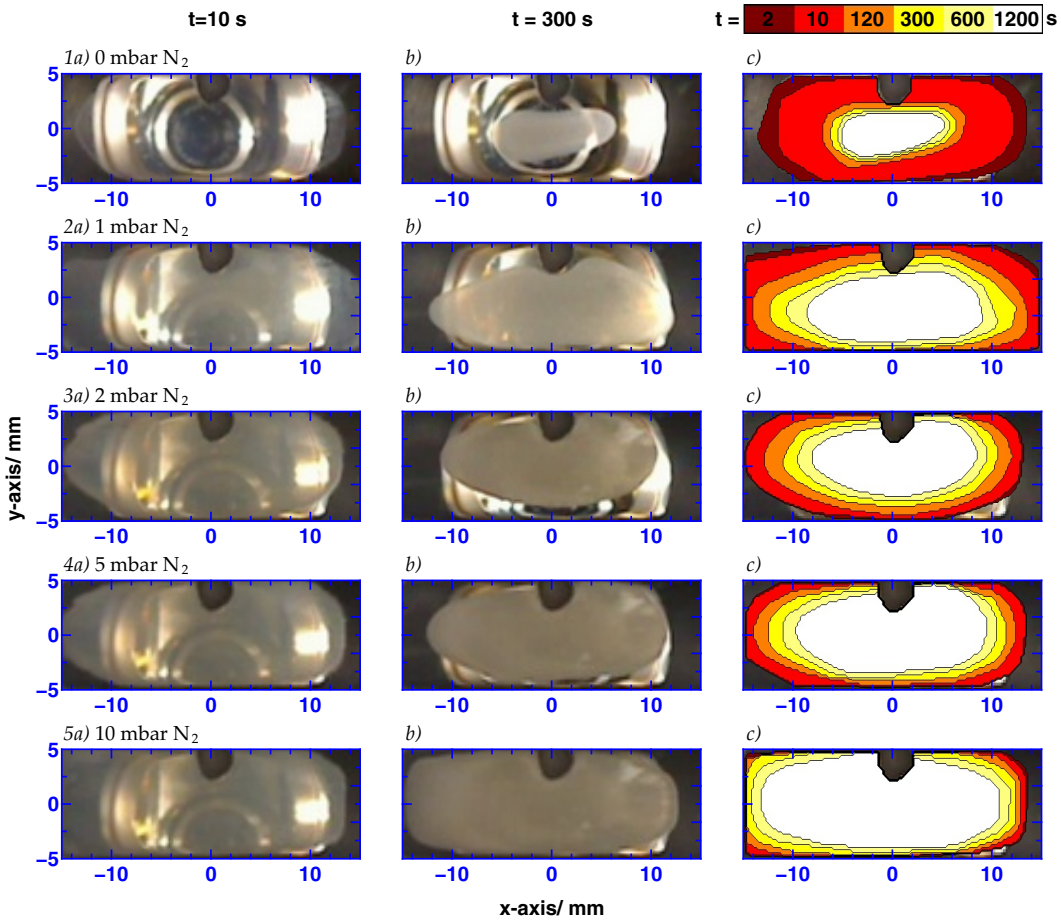

Figure 5.17: Comparison of the ice layers from figure 5.16 taken at two different times, *a)* at $t = 10\,\mathrm{s}$ and *b)* $300\,\mathrm{s}$. Times have been chosen arbitrarily to best represent different stages in the analysis and migration. *c)* shows contour plots of the time varying ice areas as indicated by the colour scheme above the column.

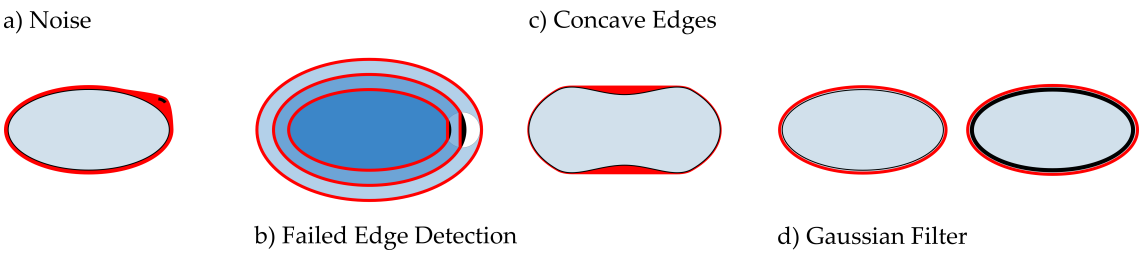

Figure 5.18: Depiction of systematic errors from the MA. Ice is shown in blue with the convex hull area represented as a red outline.
a) shows the effect of a fake edge being detected outside the real edge of the ice. An overestimate in the area is created.
b) shows the underestimate while ice migrates to a decreasing area through a blind spot marked in white. Unable to detect the edge in this region the black area shows the area from missing the convex hull.
c) shows the effect an area of ice with concave edges. The red segments show the overestimate in the area.
d) shows the effect of thickening in the edge analysis. An exaggerated broken line represents the type of edge which results from image analysis. This would also cause an underestimate of the area in a similar manner to *a)*

In the first reason, the edge could not be detected as the changes in intensity in the image which mark the edge were not large or distinct enough for effective detection without the inclusion of noise or undesired edges. The Canny algorithm uses operating parameters to isolate the correct intensity bands for edge location combined with a Gaussian filter for noise removal. The parameters and the filter level were be chosen to maximise edge detection whilst ensuring that noise and erroneous edges were not detected. In the second reason there were regions on the surface with blind spots. Figures 5.15 and 5.17 indicate a bright spot caused by the light reflecting from the surface into the camera (centered at $\sim[x, y] = [9.5, 1]\,\mathrm{mm}$ in most runs). After background subtraction this produced a blind spot for edge analysis and while ice retreated through this section edges were undetectable. Overall this caused a small understatement noticeable on the right hand side of the contour plot in 5.15 for 1c and 2c at $t = 120\,\mathrm{s}$. Errors derived from this were calculated to be no greater than $\sim 2 \rightarrow 3\%$.

Another systematic error appeared when the ice area deviated from being convex in shape and had concave sections in the perimeter. The convex hull approach is not able to detect convex edges and from this an overestimation was obtained as shown in figure 5.18c. Errors from this were usually no bigger than $\sim 2 \rightarrow 4\%$ dependant on the severity of the concave nature in the ice. A fourth and final error originated from the thickness of the lines used to indicate the location of the detected edge. Shown in figure 5.18d this is derived from the strength of the Gaussian filter used. This error, however, was marginal in comparison to the previous sources mentioned. All of these errors decrease in size with the area of ice. As the ice thickens, the edge becomes less glassy, more defined and easier to detect, it tends towards a convex shape and migrates past the blind spot. Mostly any large deviations caused by poor analysis were easily confirmed by comparing processed convex hull images to unprocessed images. The comparison would then display a clear

deviation from the overall migration trend.

Area estimations were also limited by the resolution of the camera. At early times the ice area is more accurate than at later ones when it covers a smaller number of pixels. During area calculations at late times an abrupt change in A_{ice} can be caused. It was most clearly visible in the surface thickness measurements, such as in figure 5.14b. Resolution on the ice images is dependant upon the distance the camera was from the surface. This changed between measurements ranging from $3.5 \rightarrow 5.8 \cdot 10^{-4}\,\text{cm}^2$, the area represented by a pixel. Overall an estimate of 5% was chosen as an appropriate error in the area calculations to account for the potential errors from multiple sources. It is understood however that for the majority of images, especially at the mid to late times, $> 60 - 120\,\text{s}$, the systematic error was usually no worse than $\sim 1 \rightarrow 2\%$.

5.7.4 Analysis

Morphological analysis of the area has been shown to be effective in characterising the migration of ice towards the colder central region of the SS surface. Table 5.1 above displays key data derived from the figures and accompanying graphs showing the overall trends can be found in appendix A.7. Together with figures 5.14 to 5.17 a clear enhancement in slowing ice migration through the use of an N_2 background gas is seen. For a pure water expansion with no background gas, ice rapidly migrated towards the centre reaching roughly a third of its initial area after only a few minutes. In comparison this increased by a factor of $14 \rightarrow 64$ with the application of just $1 \rightarrow 10\,\text{mbar}$ nitrogen. Overall the trend shows the rate decreasing over time, initially sharply during the first minute before levelling off, where it indicates ice was migrating to a small defined area.

An attempt has been made to describe the observed data using a number of different fits. Looking at the pure data, after ice has finished building up, it exhibits a fast early, $0 \rightarrow 60\,\text{s}$ drop in area followed by the much slower late time rate which may propagate to a non-zero equilibrium area. The data has the quality of a multi-exponential fit, a summed series of first order components. While a single exponential shows a strong deviation to the data, additional terms create a stronger fit where the best is a triple exponential.

$$A(t) = A\exp\left(\frac{-t}{B}\right) + C\exp\left(\frac{-t}{D}\right) + E\exp\left(\frac{-t}{F}\right) + A_\infty \tag{5.7}$$

$A(t)$ is the ice area changing with time, t, and A_∞ is a non-zero equilibrium ice area. Qualitative fits to the pure water data showed the presence of a fast exponential decay with a time constant in the order of the first $20 \rightarrow 40\,\text{s}$ and two progressively slower ones in the order $100\,\text{s}$ and $1000\,\text{s}$. Beyond this rationalisation of the different components in terms of specific processes is difficult. There are several different ones occurring inside the cavity that might be tied into this description. These will be highlighted and discussed in the following two sections. For a quantitative fitting further data and a simulation of the surface and its environment is required. The result of a full investigation

Table 5.1: Data derived from ice migration figures 5.14 and 5.16. Errors in values specified represent the standard deviation. The settings for each run are shown in the columns under P. A_0 is the peak initial area covered by ice and $t_{\frac{1}{3}A_0}$ is the time taken to migrate to a third. dA/dt shows migration rates taken at t_0, immediately after stabilisation of A_0 and two later points. Rates are derived using linear regression across a limited time range with errors from the fit. The highlighted rows display N_2 inhibited data set, which includes the $8\,\mathrm{mbar}$ pure run. Figures of the data are provided in appendix A.7.

$\mathbf{P}$ (mbar)		$\mathbf{A_0}^a$	$\mathbf{t_{\frac{1}{3}A_0}}^{a,b}$ (s)	$-\frac{\mathbf{dA}}{\mathbf{dt}}{}^b$ ($\cdot 10^{-2}\,\mathbf{cm^2\,s^{-1}}$)	($\cdot 10^{-4}\,\mathbf{cm^2\,s^{-1}}$)	
$\mathbf{P^{res}_{H2O}}$	$\mathbf{P^{backing}_{N2}}$			$\mathbf{t_0}$	$\mathbf{t_{600}}$	$\mathbf{t_{1200}}$
12	-	0.96	101	5.40 ± 0.05	3.21 ± 0.07	0.90 ± 0.01
10	-	0.89	114	5.24 ± 0.10	2.79 ± 0.05	1.10 ± 0.01
8	-	0.80	91(1 x)	4.82 ± 0.04	2.01 ± 0.02	0.94 ± 0.01
6	-	0.65	139	4.05 ± 0.06	2.00 ± 0.03	1.11 ± 0.01
4	-	0.34	359	$0.34/0.75 \pm 0.01^c$	1.48 ± 0.02	-
8	1	0.93	1,270(14 x)	0.60 ± 0.03	8.17 ± 0.06	4.44 ± 0.05
8	2	0.80	1,460(16 x)	0.54 ± 0.01	6.55 ± 0.03	3.75 ± 0.05
8	5	0.84	3,950(38 x)^d	0.32 ± 0.01	6.20 ± 0.09	3.89 ± 0.04
8	10	0.88	9,600(64 x)^d	0.10 ± 0.01	8.37 ± 0.14	3.75 ± 0.04

[a] Error $= \pm 5\%$. [b] Bracketed values in the column show number of times longer for that background level of N_2 relative to the pure $8\,\mathrm{mbar}$ run. [c] Two distinct initial rates observed with both quoted. First rate is from $6 - 20\,\mathrm{s}$, the same time frame as the other rates. The second one is from $20 - 50\,\mathrm{s}$. [d] Although values are not available from the data directly, a qualitative fit to equation 5.7 has been made and values derived.

of the different processes involved might ultimately require a different more mathematically complicated fit. In the short term this qualitative fit serves mainly to extract some of the features from the data.

5.7.5 Pure Water Expansions

For pure water expansions the ice layer is set in size in the initial $500\,\mathrm{ms}$ of growth while expansion out of the reservoir occurs. Water vapour however continues to freeze out onto the surface indicated by visual changes in its colour and quality; initially ice is clear and glassy then, while the area remains the same size, it becomes more opaque. Opacity changes are displayed in the pictures in figure 5.15, and evidence of migration to the centre is seen from the appearance of a differently coloured core over time. The initial area of ice, A_0, is strongly dependant on the pressure inside the reservoir; as $P^{\mathrm{res}}_{\mathrm{H2O}}$ increases A_0 also increases. In figure 5.14, there is a flat region with little to no change in area ranging from $\sim 2\,\mathrm{s}$ at $P^{\mathrm{res}}_{\mathrm{H2O}} = 12\,\mathrm{mbar}$ to $\sim 8\,\mathrm{s}$ at $6\,\mathrm{mbar}$. At the lowest pressure measured its length is less clear but it is longer still. Upon opening the valve between the reservoir and main chamber, water vapour expands out into the chamber via the holes in the dispersive nozzle. Freezing out onto the surface is not immediate leading to a period of continued ice growth where equilibration of the pressures in the reservoir and cavity occurs. During this time vapour must be depositing onto the ice at rate that is equal to the equilibration

effects occurring.

Subsequently migration begins as it outpaces any residual water vapour still to freeze out onto the surface. Initial rates are fast relative to all other times and decrease with lower $P^{\text{res}}_{\text{H2O}}$. Two factors may effect this rate, surface temperature and ice volume. Although its specific size is contested, the sticking coefficient of H_2O(g)-ice is temperature dependent becoming higher at lower temperatures.[89,91] Based on the migration, it is assumed that it is much greater than that of H_2O(g)-SS. Therefore freezing out onto the surface should be more probable in the centre where it is colder than the outside. Working in conjunction with this a higher localised vapour pressure on the outside will promote a general net transfer of molecules to the colder part of the surface. The volume of ice should affect the migration rate purely because there are more layers to migrate before the area can decrease in size.

At the beginning, despite A_0 decreasing in size with $P^{\text{res}}_{\text{H2O}}$, ice is thinner with decreasing $P^{\text{res}}_{\text{H2O}}$. If ice volume were to play a significant role then the higher $P^{\text{res}}_{\text{H2O}}$ runs should have a slower rates than lower ones. This is not seen and is evidence supporting that the surface temperature has a greater effect. At higher A_0, rates are faster due to ice existing further away from the centre where it is coldest. Therefore despite a larger thickness, i.e. more ice to shift, the initial migration rate is faster at larger $P^{\text{res}}_{\text{H2O}}$ due to a combination of lower sticking coefficients and higher localised vapour pressures both of which are dependent on surface temperature. Rates at $t = 600\,\text{s}$ for $P^{\text{res}}_{\text{H2O}} = 12 \rightarrow 6\,\text{mbar}$ are $100 \rightarrow 200$ times slower than the initial rates but still show a decreasing trend. However $P^{\text{res}}_{\text{H2O}} = 4\,\text{mbar}$ only shows a factor 22 decrease again due to its much smaller starting area. By $t = 1200\,\text{s}$ rates no longer clearly display a decreasing trend instead they are all at $\sim 1 \cdot 10^{-4}\,\text{cm}^2\,\text{s}^{-1}$.

The final area of ice, potentially mapping out the central cold region, is difficult to determine. It was unrealistic to run the experiment for long times, therefore the data is inconclusive as to the final area the ice is migrating to. The pure data does show an end area which gets smaller with lower $P^{\text{res}}_{\text{H2O}}$ but it is unknown if each run would eventually end up with the same area; qualitative triple exponential fits indicate this may not be the case. The smallest area displayed by the data ranges from ~ 0.1 at $12\,\text{mbar}$ to ~ 0.09 at $4\,\text{mbar}$, $10\,\%$ of the maximum surface area of $2.96\,\text{cm}^2$.*

5.7.6 Expansions with Nitrogen

In contrast, runs performed with nitrogen display much slower rates of migration. The application of just $1\,\text{mbar}$ increases the time taken for migration to a third of A_0 by a factor of 10 rising to 64 at $10\,\text{mbar}$. Initial rates also fall by a factor of 10 and become slower with increasing $P^{\text{backing}}_{\text{N2}}$. Similarly to the pure runs at late times these rates become less distinguishable. Since a bigger initial area of the surface is covered with ice, rates are

* Excluding the area of the PT1000 temperature probe.

larger than those for the pure runs at the same point but of a similar order of magnitude. The final rate after $t = 1200\,\mathrm{s}$ is approximately $4 \cdot 10^{-4}\,\mathrm{cm^2\,s^{-1}}$. This is four times larger than the pure runs after the same amount of time but crucially for a surface dynamics experiment the area of ice remains significantly larger over a longer time frame.

Increasing the gas concentration above the surface however has also changed the quality of the ice in figure 5.17. In the pure pictures clear glassy ice is seen which becomes more opaque as time passes, particularly in the centre where a central core of ice, different in colour to the surround, is seen. In the presence of nitrogen the colour is more evenly spread and the appearance of a core less obvious. Shortly after introducing nitrogen, much of the glassy quality is not observed instead a grey, frosty appearance is taken on. This has several ramifications. Since the ice is more opaque previous systematic errors from blind spots are reduced, particularly in higher $P_{\mathrm{N2}}^{\mathrm{backing}}$. However the data becomes more susceptible to errors from concave sections in the perimeter caused by the slower migration rates. This is seen in the data in the 5 and $10\,\mathrm{mbar}$ runs at 400 and $550\,\mathrm{s}$ respectively.

5.7.7 Experimental Error

Experimental error is mostly attributed to systematic errors involved with the MA. Aside from the assumptions made during the evaluation of the surface area and thickness described in section 5.7.2, another error derives from assuming the surface remains at a constant temperature. At late times this is true. However the peltier system is driven by a PID controller which makes changes to the cooling rate based on feedback from the PT1000 surface temperature gauge. Appropriate parameters are set up on the control unit which can maintain the temperature set point with an error of approximately $\pm 0.05\,\mathrm{K}$, the shot-to-shot error in the PT1000 measurement. However during the water vapour freezing out and with the initial exposure to increased gas levels above the surface, an increased heat load on the peltier is caused. The peltier driver therefore shifts to accommodate this change and a small amount of hysteresis is seen by the PT1000 gauge shown in figure 5.19 for the two worst cases. The hysteresis causes ripples in the temperature of the surface up to $1.3\,\mathrm{K}$ in size lasting up to a minute into the experiment.

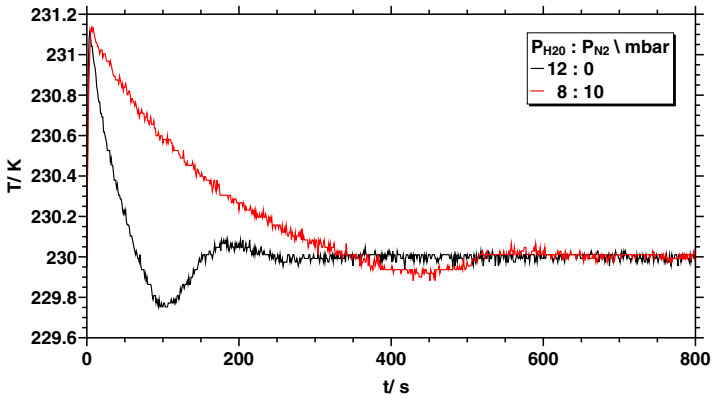

Figure 5.19: Figure of the PT1000 temperature response immediately after gas is let into the main chamber from the reservoir for the $P^{\mathrm{res}}_{\mathrm{H2O}} = 12$ (black), and $P^{\mathrm{res}}_{\mathrm{H2O}} = 8$ with $P^{\mathrm{backing}}_{\mathrm{N2}} = 10\,\mathrm{mbar}$ (red).

5.8 Optical Monitoring of Ice Thickness during Migration

Discussed in section 1.15 and laid out in the various literature sources,[89,108] a simple CW diode laser may monitor changing d_{ice} using patterns derived from constructive and destructive interference between reflections from the H_2O(g)-ice and SS-ice boundaries. Using the previously ascertained method for ice layering the HeNe was integrated into the set-up and tested. Success would allow this to be combined with the MA to calculate and compare ice thicknesses measured from both methods.

5.8.1 Experimental Setup

The experimental set-up and conditions are laid out previously in 5.7.1. The primary difference was on the CELIF axis, where in place of the camera and light, a HeNe Laser (JDSU Model 1125/P, CW, $5\,\mathrm{mW}$, Beam $\varnothing 0.81\,\mathrm{mm}$) was directed to pass through a window in a CF40 flange along the z-axis. This reflected from the ice surface at an angle of $\sim 2 \pm 0.5\,^{\circ}$. Reflected light was detected using an amplified photodiode (Thorlabs PDA36A). The power of the HeNe laser was reduced by $\sim 50\%$ using a neutral density (ND) filter and the peak voltage detected was $0.025\,\mathrm{V}$ with noise in the recorded voltages of $1 \rightarrow 2\,\%$. Figure 5.20 shows a schematic of the experimental set-up used. Signal from the photodiode was recorded using the PC integrated scope and LabVIEW at a rate of $100\,\mathrm{Hz}$* concurrently with pressures from the capacitance manometer array. As the layers of ice built up, a sinusoidal interference pattern was received and recorded on the photodiode.

* Unfortunately limited by the LabVIEW program being used to concurrently measure across several devices. Modifications for a faster sampling rate were outside the timescale of the experiments being performed.

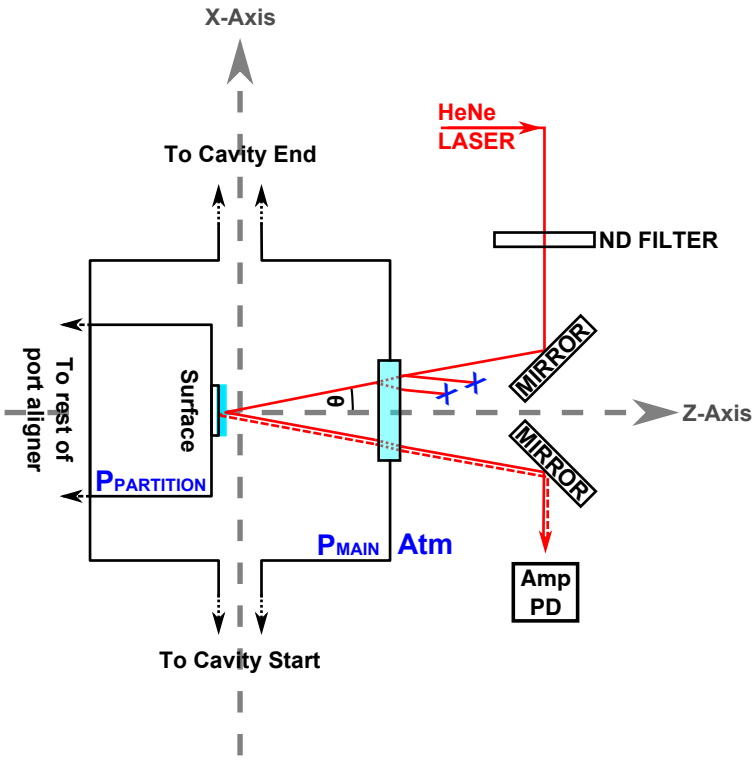

Figure 5.20: The set-up of the HeNe laser relative to the CELIF axis (z-axis) is shown. Light from the HeNe travels in from the right after passing through a ND filter. It is angled, through a window, into the main chamber reflecting from the centre of the ice-prism boundary, at $\Theta \sim 2 \pm 0.5\,^{\circ}$from the z-axis. The interference signal is output onto an amplified photodiode and recorded over time.

5.8.2 Results

Experiments were run varying $P^{\text{res}}_{\text{H2O}}$ with and without a nitrogen background gas. Pure water vapour expansions replicated experiments performed in the MA, however those with nitrogen were performed differently. During preliminary testing HeNe interference patterns were found only during the first $0 \rightarrow 6\,\text{s}$ after which attenuation in the signal caused them to disappear. In the MA nitrogen was filled directly into the main cavity, immediately after the surface had been exposed to water vapour. This coincided with the time frame over which interference measurements were made. Therefore to avoid disruption nitrogen was filled into the expansion reservoir along with the vapour for ice formation.

Due to the availability of pressure gauges, the total reserve pressure, $P^{\text{res}}_{\text{H2O}} + P^{\text{res}}_{\text{N2}}$, could not exceed $\sim 14\,\text{mbar}$. Therefore the maximum pressure that could be put into the main chamber was $\sim 0.8\,\text{mbar}$.* Combinations of $P^{\text{res}}_{\text{H2O}}$ and $P^{\text{res}}_{\text{N2}}$ were kept at $12\,\text{mbar}$ whilst varying the ratio of gases to keep the expansion pressure across the SS surface equal in each run. Sufficient time was allowed for good mixing in the reservoir before admission

* See appendix A.6

to the chamber. Experiments were run twice filling the reservoir first with N_2 and then H_2O and also vice-versa to ensure that the order in which the gases were filled did not affect the results. Both runs were nearly identical therefore only one set of the measurements is shown.

The signal from the HeNe is shown in figures 5.21 and 5.22 and the derived surface thicknesses in figure 5.23. Pure water ice expansions were used at $P^{\mathrm{res}}_{\mathrm{H2O}} = 12$, 10, 8, 6 and $4\,\mathrm{mbar}$. Mixed expansions were used in the ratio of $P^{\mathrm{res}}_{\mathrm{H2O}} : P^{\mathrm{res}}_{\mathrm{N2}} = 12:0$, $10:2$, $8:4$, $6:6$, $4:8$ and $2.5:9.5\,\mathrm{mbar}$. Surface thicknesses have been calculated analysing the spacing between concurrent interference peaks and valleys in combination with equation 1.7. Peak spacing has been measured to an accuracy of $\pm 0.01\,\mathrm{s}$, the resolution of the data where peak widths occupy only several data points. This increases to $\pm 0.03\,\mathrm{s}$ for broadest peaks.

5.8.3 The Shape of the Signal

Figures 5.21 and 5.22 display clear interference patterns during the early seconds of ice formation. After expansion across the surface ice builds up slowing as the system reaches equilibrium with its vapour pressure around $T_{\mathrm{ice}} = 225\,\mathrm{K}$. This is reflected in the period decreasing over time. A strong overall attenuation in the signal is seen and along with this the interference fringes attenuate into the noise of the measurement after only a few seconds of the measurement.

Pure bubble free ice has an absorption coefficient of $0.002\,\mathrm{cm}^{-1}$ at $632.8\,\mathrm{nm}$.[76] This is widely believed to be accurate and not superseded by other sources for the wavelength range $600 \rightarrow 1400\,\mathrm{nm}$[78] but has been shown to be potentially overestimated at lower wavelengths.[79] For an absorption of this strength a signal drop to only $\sim 99.9999\,\%$ travelling through the thickest of ice formed in this experiment, $\sim 100\,\mu\mathrm{m}$, would be expected. Here reductions in the signal are measured several orders of magnitude greater than this. Experimental observation showed that surface diffraction was largely negligible; visually the beam shape was unchanged during the ice growth and only the intensity altered. Light, upon interaction with a molecule may either be scattered or absorbed. There should be no other absorbers at this wavelength range present in the cavity so the absorption coefficient should be negligible. Therefore this only leaves a large scattering coefficient as the dominant role in reducing laser intensity.

It has been shown in the work of previous groups that ice at this temperature forms a polycrystalline structure made from micrometre sized grains, and creates a porous network both internally within the grains and externally between the grains.[99,188] Grains monitored from a slower ice growth by Keyser *et al.* averaged $5 \rightarrow 10\,\mu\mathrm{m}$ in size between $200 \rightarrow 230\,\mathrm{K}$. Assuming a similar grain size the large signal loss can be explained with Mie scattering. This process should occur strongly as the incident wavelength, $0.6328\,\mu\mathrm{m}$, is a similar size to the grains observed by other groups in this temperature range. Assuming the ice surface is constructed of roughly spherical grains this produces a size parameter

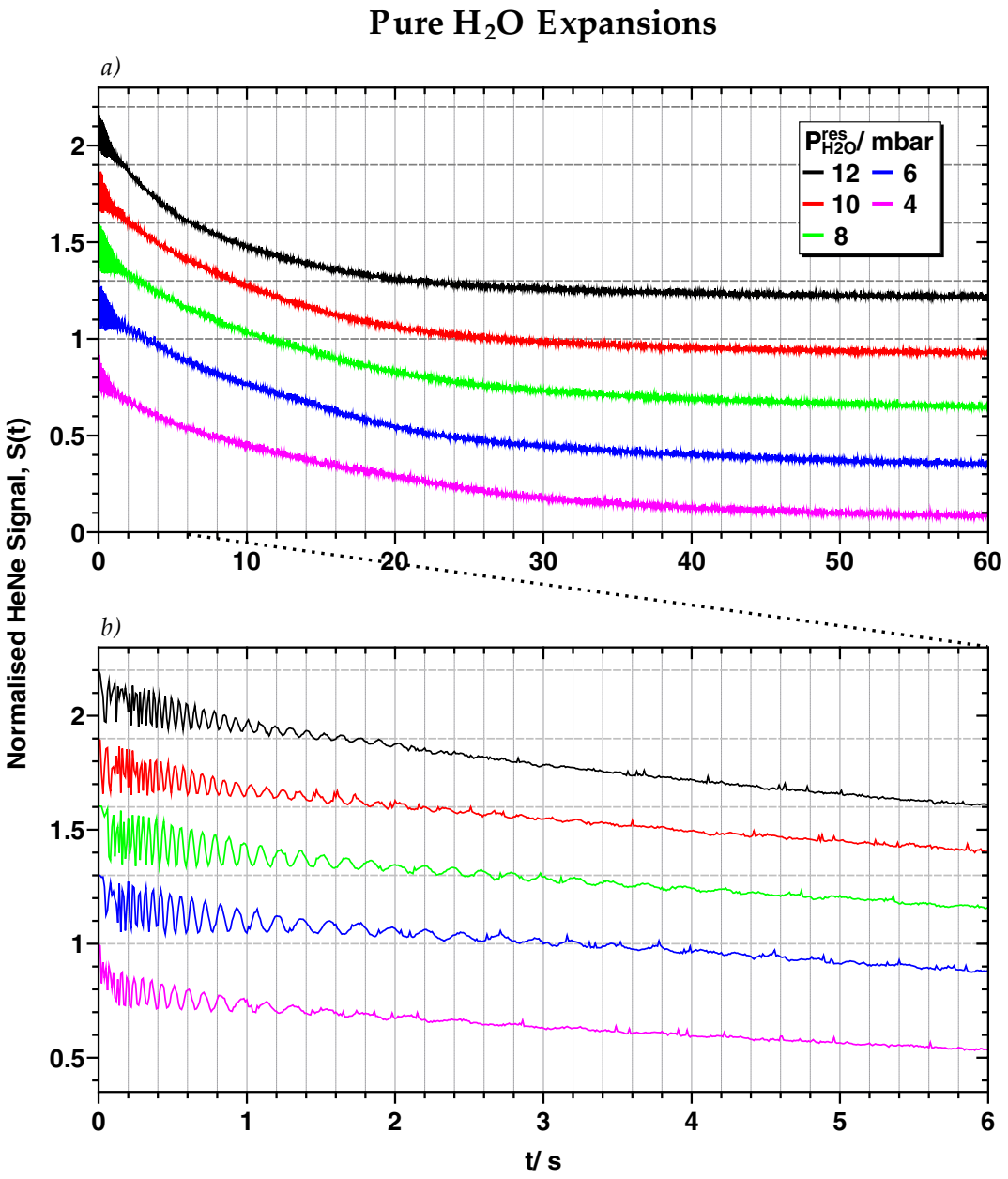

Figure 5.21: HeNe signal is plotted against time and normalised against peak voltage for pure water ice surfaces. *a)* shows plots at each $P^{\mathrm{res}}_{\mathrm{H2O}}$ staggered by 0.3 for ease of comparison; the horizontal dashed lines represent 1 for each measurement. *b)* expands upon the interference signal focusing on the first $6\,\mathrm{s}$.

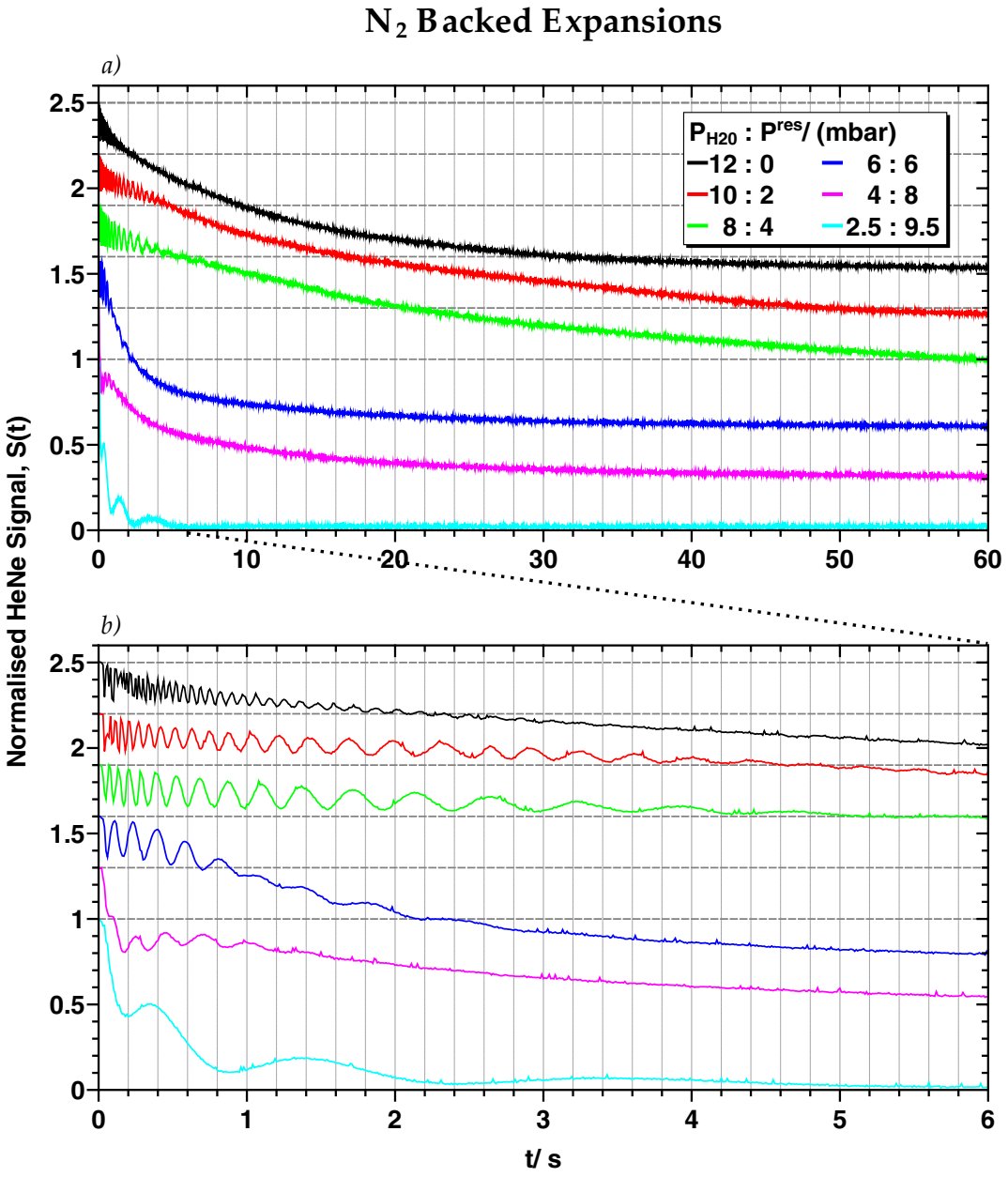

Figure 5.22: HeNe signal is plotted against time and normalised against peak voltage for ice surfaces with an N_2 background. *a)* shows plots at each $P^{res}_{H2O} : P^{res}_{N2}$ staggered by 0.3 for ease of comparison; the horizontal dashed lines represent 1 for each measurement. *b)* expands upon the interference signal focusing on the first $6\,s$.

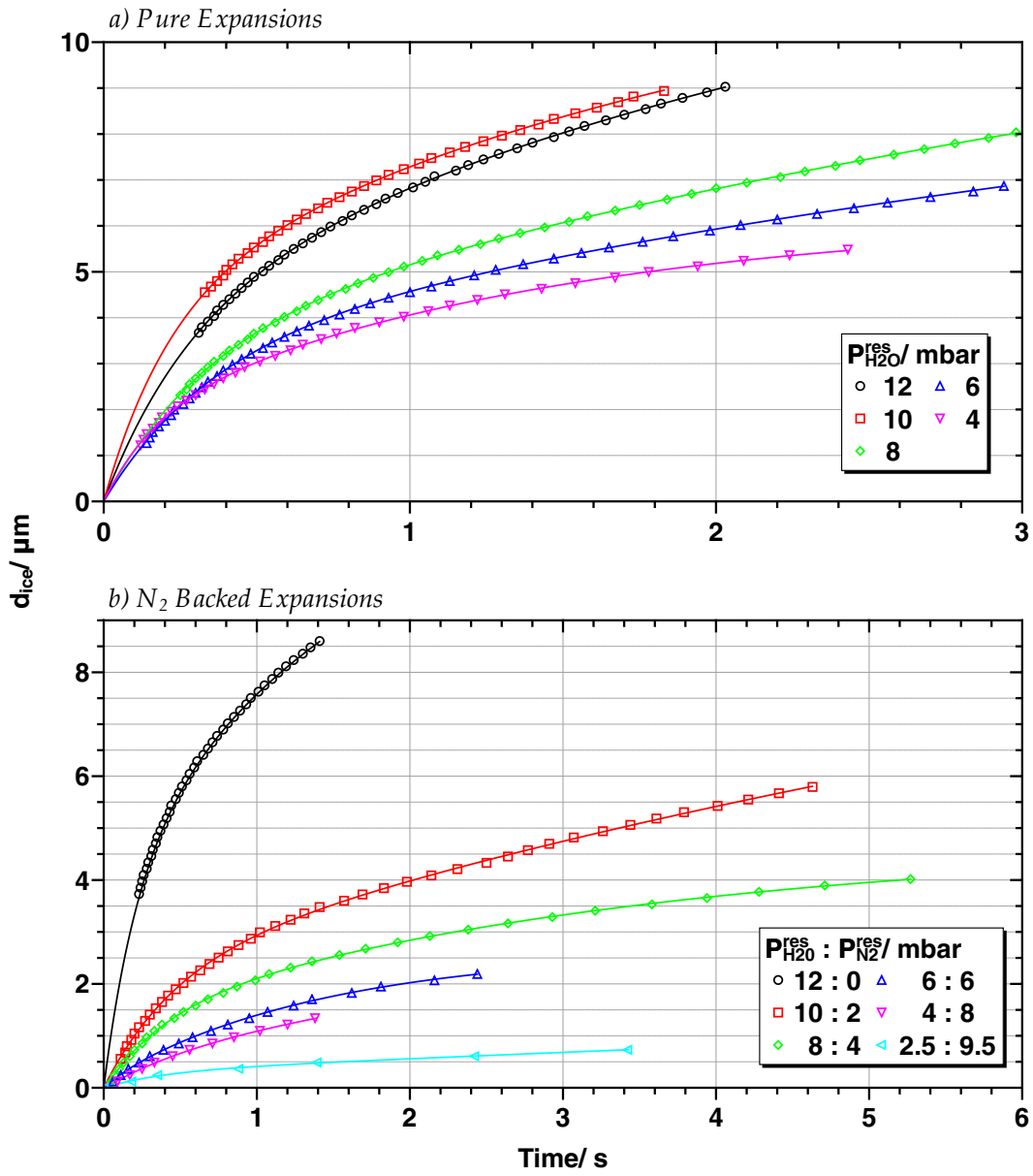

Figure 5.23: Surface thickness variation over time derived from the interference fringes observed in the HeNe data. *a)* is the data derived from the pure measurements shown in 5.21. *b)* is derived from the mixed measurements shown in 5.22. Data has been fit using a double exponential and moved on the y-axis for *a)* and $12:0$ in *b)* see the analysis for further details.

(equation 2.20) of $X = 25 \rightarrow 50$ well within range for strong mie scattering. The effect of this is that the HeNe signal disappears after only a minute of ice build up and migration, and the amplitude of the interference fringes disappear into the noise after only a few seconds, halting continued detection of ice layering.

The overall trend in the signal from the photodiode varying with time, $S(t)$ (V), has a form that can be represented qualitatively by equation 5.8.

$$S(t) = A(t) + B(t) \cdot \cos\{\omega(t) \cdot t + \phi(t)\} \tag{5.8}$$

$$w(t) = \frac{d}{dt}\phi(t) \tag{5.9}$$

$A(t)$ (V) is a fit to the overall absorption trend of the depositing ice and $B(t)$ (V) is a fit to the decreasing amplitude of the interference fringes. $\omega(t)$ ($\mathrm{rad\,s^{-1}}$) is the angular frequency of the interference fringes and $\phi(t)$ (rad) is the instantaneous phase. For frequency varying functions, $\phi(t)$ is time dependent and related to the frequency by equation 5.9.

Early fitting of the data showed promising results, where equation 5.8 was successfully applied to the broad overall absorption and parts of the interference pattern. Qualitative fits were obtained for $A(t)$ similar to the MA data using a summed series of first order processes. The best fit to $A(t)$ found was a double exponential. The additional term in a triple exponential as used in the MA data offered little improvement in the overall fit. $B(t)$ was adequately fit to a single or double exponential, while $\omega(t)$ did not fit well to an exponential. Both of these would benefit from higher resolution data at the early times to more accurately see the data trend. The phase dependency as a derivative of a fit did not allow for a complete fit to the overall signal only a partial one. This might indicate a more complex phase behaviour or simply represents a need for higher resolution data for fits to $\omega(t)$.

5.8.4 Thickness Measurements

Ice thicknesses calculated are displayed in figure 5.23. For mixed water/nitrogen expansions (5.22/5.23b), interference fringes occur slow enough that the data shows them all until attenuation stops it. In pure expansions (5.21/5.23a) early measurements up to $0.1 \rightarrow 0.2\,\mathrm{s}$ are not sampled fast enough to isolate peaks reliably. Therefore to produce thicknesses the data has been fit to a double exponential, regarded to be the best fit as demonstrated in appendix A.8, and moved up on the y-axis to estimate the missing contribution. Table 5.2 compiles data from the MA and HeNe measurements for comparison.

Derived surface thicknesses in the pure data correlate well with the expected values given data from the MA. This indicates strongly that they result from surface layering and not a different phenomenon. After $2\,\mathrm{s}$, d_{ice} measured by the HeNe is approximately $60-70\,\%$

Table 5.2: Table of thickness data derived from figure 5.23. Pressures are reported in the reservoir before expansion, $P^{\text{res}}_{\text{H2O}}$and $P^{\text{res}}_{\text{N2}}$. N_2 is also shown in terms of its final backing pressure, $P^{\text{backing}}_{\text{N2}}$. A_0, is the maximum fraction of surface area covered by ice as derived from the MA data under equivalent expansion pressures. d_{ice} is shown for a theoretical minimum, d_{A_0}, based on A_0, and as derived from the MA and HeNe data at the times stated.

P (mbar)[a]			A_0[b]	d_{ice} (μm)			
P^{res}_{H2O}	P^{res}_{N2}	$P^{backing}_{N2}$		d_{A_0}[b]	$t_{MA}=2$ s[b]	$t_{HeNe}=2$ s[d]	$t_{HeNe}=4$ s[d]
12	···	···	0.96	13.6	13.4	9.0	11.4
10	···	···	0.89	11.9	11.8	9.2	11.2
8	···	···	0.80	10.3	10.4	6.8	9.1
6	···	···	0.65	9.0	9.1	5.9	7.7
4	···	···	0.34	10.1	9.5	5.2	6.0
12	0	···	0.96	13.6	13.4	9.7[c]	11.5[c]
10	2	0.10 ± 0.01	0.96	11.1	···	4.0	5.4
8	4	0.21 ± 0.01	0.96	8.6	···	2.8	3.7
6	6	0.33 ± 0.02	0.96	6.1	···	2.0	2.5[c]
4	8	0.43 ± 0.02	0.96	3.6	···	1.7[c]	2.6[c]
2.5	9.5	0.52 ± 0.03	0.96	1.7	···	0.6	0.8[c]

[a] Main chamber pressures can be derived from the reserve pressures using appendix A.6 [b] Error $= \pm 5\%$. [c] Marked values have been derived from outside data range, from the double exponential fit to the data shown in figure
[d] RMSE~ 0.02 derived from double exponential fits to the data in figure 5.23

of that measured by the MA and d_{A_0}. By $4\,\text{s}$ this has increased to $80\,\%$. This falls in line with the equilibration of water vapour, a first order process, inside the cavity most of which happens across the first $30\,\text{s}$ after admission. The increase in d_{ice} over time will also include a net migration from the warmer region of the surface to the cold centre. Also in comparison to the MA data, which idealises the surface thickness across this time period, the HeNe data is able to detect thickness changes during the very early stages of layering.

For the mixed measurements the addition of nitrogen slows the rate at which water freezes out onto the surface and migrates across the temperature gradient of the surface by diffusion. Here d_{ice} reaches approximately $30\,\%$ of the theoretical value, d_{A_0}, after $2\,\text{s}$ for expansions of $P^{\text{main}}_{\text{H2O}}$. The higher reserve pressures used to expand water across a wider initial area on the surface mean that comparison to MA measurements is not possible as equivalent experiments were not run.

Several different assumptions have been made to compare the two sets of data. First both the MA and HeNe data are independent measurements and were not made observing the same ice surface. Therefore A_0 derived from the MA measurement may not match the equivalent HeNe one exactly. An indication of this can be seen for the $10\,\text{mbar}$ pure water expansion in 5.23a where d_{ice} rises faster than expected relative to the $12\,\text{mbar}$ measurement. This is a further indication again that reproducibility and predictability

between different pressure expansions across the surface is not always obtained. As well as this the value used for A_0, derived from the MA data, may be especially problematic in the mixed measurements where there is no equivalent video footage of A_0 for comparison. Therefore, in the absence of equivalent MA data, A_0 was set to the MA pure water expansion at $12\,\mathrm{mbar}$.

This problem is a because the HeNe itself only observes thickness changes, the exact opposite of the MA which looks at the area. Moreover it only observes a small region in the centre the size of the beam diameter, therefore any thickness measurements may not apply to the whole surface. This may be particularly relevant given how water is deposited to the surface. The nozzle is not able to deposit directly onto the surface and instead is laying slightly beneath it as seen in figure 4.7. This might not create a level thickness across the surface. Lastly although the temperature of the surround is significantly higher in temperature than the surface it is still sub-zero, $T_{\mathrm{partition}} = 271 \rightarrow 267\,\mathrm{K}$. An unknown loss of water vapour to the surrounding surfaces cannot therefore be ruled out and this might affect the comparison between the MA and HeNe data. Overall the data displayed here strongly indicates that the interference patterns are resulting from layering ice. However to provide the best data future measurements are encouraged to combine both video monitoring and MA, with interference measurements to provide a complete characterisation of the ice surface.

5.9 Outlook of the Experimental Build

The aim of this experimental build is to study photodesorption and photodissociation on ice surfaces grown on a glass substrate. A glass substrate is desired in order to induce these photo-processes with an evanescent wave. In contrast to irradiating the surface from above, this avoids unwanted gas-phase photo-processes. An ice film grown onto a glass substrate can thus be analysed using an evanescent wave similarly to an ATR experiment. This way an experiment can be performed simultaneously studying surface reactants and products as well as products released to the gas phase by CRDS and CELIF. While this goal has nearly been reached continuation of the build in several areas is required in order to rectify a few outstanding issues. Firstly the temperature gradient across the surface at low temperatures could be looked at to see if it could be improved. Decreasing the temperature gradient across the upper surface will allow cooling and ice formation over consistently larger surface areas. Although the presence of a temperature gradient will be an innate part of the every cooling system there are two key areas that could be improved. The increase in temperature gradient at low temperatures is believed to be caused by the surfaces within the cooling stack under the substrate being non-flat combined with shrinking of these layers as the system cools. Since the system is fixed at the edge of the substrate surface and at the base of the cooling platform, as the layers shrink, the different layers are pulled apart. Therefore the first way to improve the system at low temperatures is to introduce some method of compensation or suspension,

such as using springs, designed so that the layers can stay together better.

The second way, which could be done with or without introducing the aforementioned method, would be to improve the cooling power of the cooling method. One way to do this is to migrate from a peltier based method to a more conventional liquid cooling (solvent or liquid nitrogen/helium) and resistive heating based technique. Although the advantages of using a peltier would be removed by utilising these methods the system should be able access to higher cooling powers, and thus lower temperatures across a larger surface area. As well as this reducing the number of layers in the cooling stack might reduce the warping which may be the main cause of the temperature gradient. Another advantage with this is that it would be able to move a surface to even lower temperatures such as to where ice has lower vapour pressures and higher sticking coefficients. It would therefore migrate less readily and produce even better quality ice films, as was indicated in section 5.4.3.

A final issue will also need to be dealt with relating to the silicone resin used to seal the edge of the SS prism to the partition in the experiments. Ideally the resin should be cured at high temperatures, above $373 \rightarrow 500\,\mathrm{K}$, over the course of $15 \rightarrow 60\,\mathrm{min}$ depending on the exact temperature used. Instead air curing over several days was used mainly because of time constraints in that an appropriate method with which to both cure it and put the build together while protecting the components was not readily found. During a trial experiment, a significant absorption in the CRD signal (in the UV around $313 \rightarrow 318\,\mathrm{nm}$) was noticed when a $266\,\mathrm{nm}$ laser was dispersed across the glue. It is believed that the $266\,\mathrm{nm}$ laser was ejecting a molecule or some derivative resulting from residual solvent, toluene or a similar derivative, which was still remaining in the glue that should have been fully removed during the curing process. Therefore ideally an alternative to the silicone leak sealant should be found or a method should be devised which would enable a higher temperature curing process to be used on the seal. Suitable alternatives should include alternatives that can be cured at low temperature or without the application of heat at all. Such sealants could include two part epoxy resins or perhaps most suitably a UV curable epoxy. Epoxy resins come in a variety of forms and speciality applications demonstrated by the two-part cryogenic one used in this thesis for cementing the SS prism to the plate which fixes it to the peltier. Another epoxy of note, or a similar one, that would be very useful in place of the leak sealant is the resin, SU-8 (Microchem Corp.), this has good mechanical and thermal stability with low outgassing properties but can be cured simply by applying UV light.

In addition to the continuation of the build there are several experimental enhancements that are recommended. Video monitoring of the ice combined with HeNe monitoring of its thickness has shown that together they are an effective tool for characterising ice during an experiment. Currently the techniques operate individually and it is recommended that for the set-up is modified such that they can operate concurrently. As well as this the dispersion nozzle used for ice layering indicates that a system able to deliver water

directly to the surface might prove useful in the setting up a precise surface thickness. For this a pulsed molecular beam, perhaps utilising a slit nozzle,[189] could provide a layer by layer approach to ice growth. It would be able to constantly refresh the ice layer before it had a chance to migrate away from the prism surface. However this would come with complications from need to characterise the surface thickness as a continually increasing during an experiment however appropriate monitoring from the MA and HeNe should be able to characterise this.

5.10 Future Experimentation on Ice

The chemistry of ice-water films can be separated into three rough temperature ranges. Firstly at temperatures below $\sim 110\,\mathrm{K}$, ice is amorphous; this is the regime most relevant to astrochemistry. Here it has a very low vapour pressure and classical mass-spectrometric techniques can be used. Secondly above this temperature between $\sim 110 \rightarrow 273\,\mathrm{K}$, ice is crystalline, either in the metastable Ic form or Ih. At these temperatures the vapour pressure is too high to use mass-spectrometric methods unless a very challenging differential pumping set-up is used. Above $190\,\mathrm{K}$, the presence of the QLL is expected which increases in thickness towards higher temperatures and effects the nature of the chemistry occurring on the ice surface. The third regime is at temperatures above $273\,\mathrm{K}$, where thin water films exist which have most relevance to precipitation processes occurring in the troposphere.

Of the different regimes mentioned the second is arguably hardest to control. Regime one has the experimental advantage of dealing with low vapour pressures and regime three has higher temperatures, closer to room temperature, which are easier to design experiments around. Thus regime two warrants the use of novel experimental procedures such as this one. The future of this experiment currently lies in two areas. First there are the experiments that can be achieved using the system as it currently is with only minor improvements to it. Secondly there are those which can be performed after correcting the outstanding build issues bringing it in line with the original build specifications, as discussed in section 5.9, in order to perform the heterogeneous water-ice chemistry it was designed to study.

In the current set-up the data obtained of ice deposition onto the SS surface and its subsequent migration to smaller areas down the temperature gradient could be modelled using a simulation. Further information on the exact processes being observed could be extracted by varying the nature of the substrate from SS to alternative materials such as Aluminum and Copper. As well as this additional surface temperature data characterising the gradient in alternative dimensions than that previously measured may prove necessary in putting together an effective simulation of the gas dynamics involved. From a good simulation condensation and evaporation coefficients for ice around $225 \rightarrow 230\,\mathrm{K}$ should be obtained. These values have significance in cloud formation and growth mechanisms of ice in the atmosphere. Previous data has provided an array of widely dif-

fering values with condensation coefficients being measured at both $\sim 0.03 \rightarrow 0.06$ at $190 \rightarrow 220\,\mathrm{K}$ and unity over $210 \rightarrow 230\,\mathrm{K}$.[89] Thus additional data and continued refinement is very important to ensure that atmospheric models remain as accurate as possible.

Using the set-up as it stands in the current 3-stage peltier configuration and using a steel prism it may be more suited to higher temperature surface/thin film experiments in the third regime mentioned, above $230\,\mathrm{K}$ where the temperature gradient should have less effect as indicated in figure 5.13b. However by focussing on a different higher temperature regime, nearer to the freezing point of water, a higher power single or double stage peltier could be used which might reduce the effect of the temperature gradient observed allowing film or ice deposition across a wider area. At higher temperatures towards $273\,\mathrm{K}$ warping of the layers in the system will be less and the glass prism might also be able to be used. This will make the setup ideal for investigating supercooled water films (or any other depositable film) near the freezing point of water up to room temperature. Thin film water on the surface of ice was first proposed by Faraday in 1850 and now has meteorological interest in several different areas including the electrification of clouds, frost heave, soil freezing, perma-frost. Furthermore it is of interest to any other area where ice and interfacial films of water may be involved, such as PSC formations and snowpack chemistry.[86,98]

This system has been designed to look at ice chemistry in the second temperature regime mentioned above. For this the initial system should investigate a well characterised molecule with a wealth of supporting literature and atmospheric relevance but still requiring understanding and research. The ideal molecule for this is that of nitric acid (HNO_3) and its close relatives the nitrate radical (NO_3), anion (NO_3^-), $NO_x = NO + NO_2$, N_2O_5 and nitrous acid (HONO). Systems involving these molecules are well studied due to their presence in a rich variety of complicated tropospheric and stratospheric chemistry. Each plays a role within the nitrogen cycle which controls photochemistry and oxidant levels in the atmosphere.

NO_3 radicals and N_2O_5 are known to interact efficiently with surfaces such as soot, dust, liquids, frozen organics and water-ice. Adsorbed NO_3 and N_2O_5 are thus involved in a number of different atmospheric surface reactions. One of the most important roles of tropospheric and stratospheric NO_3 is its involvement in ozone chemistry where the largest source of NO_3 radicals comes from the reaction of NO_x with ozone. Thus it is directly involved with its regulation. Meanwhile N_2O_5 reacts to form nitric acid with water on liquid or ice surfaces. N_2O_5 itself is formed because the formation of NO_3 requires NO_2 which together sit in equilibrium with N_2O_5. Related to this process and discussed in section 1.5, stratospheric nitric acid is now known to be an important factor of PSC formation and is involved in the heterogenous ozone depletion chemistry that occurs there.

During the day NO_3 levels are regulated through an efficient photolysis process. Ni-

tric acid in comparison is removed from the troposphere by wet and dry deposition to earth bound sinks either directly or via transportation on air-borne particulates. Nitric acid which has been deposited onto buildings and vegetation in this way had previously been thought to be a permanent process. The photolysis rate for gas phase nitric acid, $HNO_3 + h\nu \rightarrow HONO + NO_x$, in the troposphere is known to be slow and thus by extension it was assumed that the photolysis rate for adsorbed nitric acid was also slow. However recent field studies have shown that the photolysis rate for adsorbed nitric acid is $1 \rightarrow 2$ orders of magnitude faster than in the gas phase. Looking at this further Zhu *et al.*[88] recently measured HNO_3 photolysis in the gas phase and on aluminium and ice surfaces monitoring NO_2 using CRDS. They demonstrated that its adsorption cross-sections in the UV were $1 \rightarrow 2$ orders of magnitude higher when nitric acid was adsorbed relative to in the gas phase and that also its quantum yield was increased as compared to the aqueous phase.[190,191]

Further chemistry involving nitric acid occurs with the photolysis of NO_3^- anions on the surface of snowpacks which is believed to produce gaseous HONO via a mechanism similar to the production of NO_x. It is known that the favourable conditions for HONO production by this mechanism includes acidic snow surfaces (where alkaline snow surfaces inhibit HONO emission), NO_3^- abundance in the ice surface and strong UV light levels. However in 2006 Beine *et al.* demonstrated that measured nitrous acid fluxes at Browning Pass, Antarctica were unusually low, despite the presence of favourable conditions. From this investigation they speculatively suggested some of the best chemical and physical pathways for HONO formation which addressed the missing HONO fluxes. These are shown below in figure 5.24. It was clear that HONO production depended strongly on both physical and chemical makeup of the surface environment and that there is a need for well designed laboratory experiments which can vary the nature and chemistry of an ice substrate in order to elucidate the complete picture.[192,193]

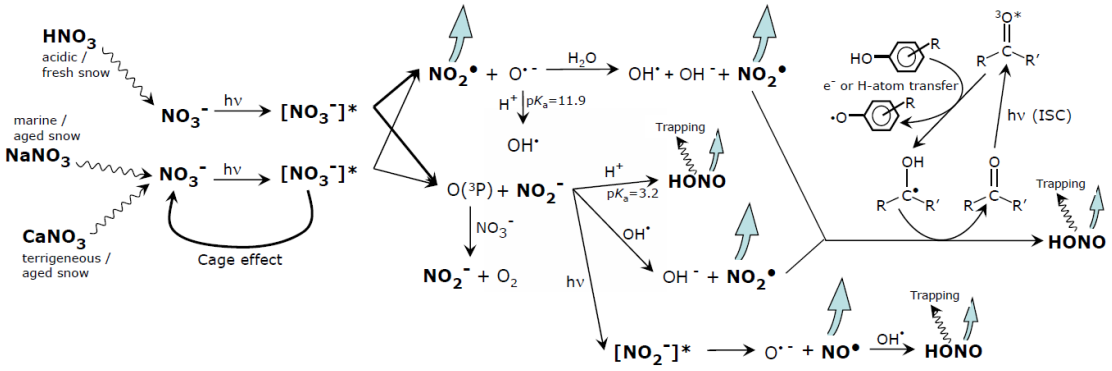

Figure 5.24: A series of potential reaction mechanisms for HONO formation via NO_3^-. Blue arrows are gaseous emissions and curvy arrows transport mechanisms. The pathways shown mainly relate to reactions in aqueous solution however several have been shown to occur in ice surfaces and snow. Figure taken from Beine *et al.*[193]

CRDS has already been proven capable of measuring concentrations of gas phase nitric acid by observing NO_2 resulting from its photolysis at $308\,\mathrm{nm}$ and also related species

such as nitrous acid in the UV, $\sim 350\,\mathrm{nm}$, by Wang *et al.* Furthermore the demonstration of EWCRDS as a spectroscopic probe of surfaces has been shown in groups such as Aarts *et al.* and importantly in studying the formation of the nitric acid radical by Pipino *et al.*[176,177,194] Thus this work lays a strong groundwork which supports the design of this setup to study the photolysis processes involved with nitric acid at the snow/ice interface at temperatures towards $230\,\mathrm{K}$ and higher ones nearer to the melting point. Across this range the QLL of water is known to vary in thickness where at the higher temperatures it will likely approximate more similarly to experiments using nitric acid in aqueous solutions.

The designed system, with changes introduced from section 5.9, is thusly well posed to study the reaction dynamics of nitric acid on snow and ice surfaces. A snow/ice surface can be prepared onto the surface of a cooled glass prism sealed into the partition plate such that only the upper surface is exposed to the main CRD chamber. Inside the partition a UV photolysis laser can be directed internally around the prism to create an evanescent wave that will penetrate into a surface film out to $\approx 1\,\mu\mathrm{m}$ in thickness (see appendix A.5). CRDS can then be used to detect the chemistry occurring above the ice surface, monitoring NO_2 and HONO. In addition CELIF can be used to extend the dynamic range of CRDS where feasible. Beyond this further reactions can then be studied by extending this experiment to cover other acids and moreover the small trace volatile organics found in the atmosphere, such as acetone that has previously been characterised using CELIF in this thesis, and which are of keen interest to GTPMs and other models of the heterogenous chemistry occurring in the atmosphere.

5.11 Conclusion

This study has investigated a novel peltier based set-up for the purpose of cooling a prism to grow thin, nanometre to micrometre thick, ice films isolated to its uppermost surface in the range $210 \rightarrow 273\,\mathrm{K}$. The objective is to use CRD, CELIF, and ultimately EWCRD, spectroscopies to monitor the interaction and surface dynamics of atmospherically relevant molecules such as acetone and other trace compounds at this ice-air interface. A setup has been built using a three stage commercially available peltier to cool a SS test prism. It was found that to restrict ice growth to the upper surface of a prism alone that the cooling apparatus and parts of the prism below the surface had to be confined to a partition. A set-up was designed and built based around a CF100 port aligner allowing a full range of motion of the surface plane relative to the CRD and CELIF axis. Near-surface reductions to the RDT were caused by the combination of the upper surface of the prism sealed into the top of the port aligner. It was found that a minimum of $12.6w_0$ ($3.8\,\mathrm{mm}$) from the cavity axis at $583.4\,\mathrm{nm}$ was required for zero reduction in τ_0 and that the criteria of a maximum $10\,\%$ loss occurred at $10.4w_0$ ($3.1\,\mathrm{mm}$) .

Temperatures of the system are set using a PID with a PT1000 feedback probe attached to the surface. Under the conditions of near maximum cooling the temperature $T_{\mathrm{PT1000}} =$

230 K was reached. It was kept extremely stable with fluctuations only varying by ± 0.05 K, the error margin on the PT1000 probe. This stability was maintained over any temperature within range of the peltier, tested between $T_{\mathrm{PT1000}} = 230 \rightarrow 303$ K. The set-up can be used across a pressure range of $0 \rightarrow 50$ mbar in the main cavity while maintaining the partition under vacuum; pressures greater than this cause the silicone resin sealing the surface into top of the port aligner to fail. However as long as there is a pressure differential no greater than this between P^{main} and $P^{\mathrm{partition}}$ any pressure can be reached and maintained with only minimal cost to the cooling efficiency allowing any atmospherically relevant pressure to measured.

In order to provide a full characterisation of the surface environment T_{peltier}, T_{ice}, and $T_{\mathrm{partition}}$ in the set-up were measured. At maximum ΔT, the peltier cold junction was $T_{\mathrm{peltier}} \approx 221$ K, in line with predictions from measurements of the heat load, Q_L, from a simpler test set-up of 2.8 ± 0.5 W. After ice growth, T_{ice} was derived from CRD and CM measurements which correlated with each other within error. It was found that for ice formed on the surface at 230 K a measured temperature of 225 ± 0.2 K was recorded independent of the ice surface coverage and volume. Thus the temperature from the peltier to centre of the surface was found to increase from ~ 221 K to 225 ± 0.2 K vertically across the SS prism and horizontally across the short side of the surface from 225 ± 0.2 K near the centre to 230 K on the outside. Finally measurements of $T_{\mathrm{partition}} \sim 273 \rightarrow 268$ K showed that cooling had managed to be successfully restricted to the prism by thinning out its boundary with it to 0.5 mm in thickness. By this method the cold surface was well restricted to the upper area of the prism in the cavity.

The formation of the temperature gradient across the surface was shown to strongly effect the process of ice formation. Except at the lowest temperatures ice demonstrated a rapid process of migration towards a small area in the centre. The best method found for forming micrometre thick ice films, that were visually even and covered most of the surface, was a controlled, rapid, expansion of water vapour out of a directed nozzle while the surface was held at the coldest possible temperature. Ice film formation was explored by expanding a reserve volume of water vapour, at $P^{\mathrm{res}}_{\mathrm{H2O}} = 4 \rightarrow 12$ mbar into vacuum across the surface. This would produce ice film thicknesses of $2.5 \rightarrow 11.8\,\mu$m fully covering a $2.92\,\mathrm{cm}^2$ surface area. For monitoring surface areas and thicknesses two techniques were employed. First video monitoring combined with a morphological analysis was used to automatically derive areas. Secondly a HeNe laser was installed to monitor thicknesses from interference patterns as several groups have done previously[89,91].

Using the MA initial surface coverages, A_0, of up to 96 % at $P^{\mathrm{res}}_{\mathrm{H2O}} = 12$ mbar were obtained and a non-linear trend of decreasing A_0 with decreasing $P^{\mathrm{res}}_{\mathrm{H2O}}$ was observed. The temperature gradient across the ice surface was found to promote a decrease in A_0 towards a central region, $0.028 \pm 0.002\,\mathrm{cm}^2$ in size. As $P^{\mathrm{res}}_{\mathrm{H2O}}$ decreased from $12 \rightarrow 6$ mbar the initial migration rate of ice was found to decrease from $5.40 \rightarrow 4.05 \pm 0.05 \cdot 10^{-2}\,\mathrm{cm}^2\,\mathrm{s}^{-1}$. Thus the initial rate was shown to be caused by the temperature gradient relative to the A_0 of

ice at the start of migration. In the longer time frame, after $20\,\mathrm{min}$, when ice had mostly moved to the centre, migration stabilised at $\sim 1 \cdot 10^{-4}\,\mathrm{cm^2\,s^{-1}}$ across all measurements. A nitrogen background gas was tested as a simple method to increase surface area coverage for longer periods. Initial migration rates were found to decrease by a factor of $10 \rightarrow 50$ for $P_{\mathrm{N2}}^{\mathrm{backing}} = 1 \rightarrow 10\,\mathrm{mbar}$. The HeNe was successfully used to monitor ice thicknesses producing data that was in line with measurements made by the MA. A strong scattering coefficient in the ice surface measurements was observed and so measurements were not possible beyond the first $2 \rightarrow 6$ seconds of ice growth. This demonstrates the production of a polycrystalline ice surface likely comprised of granules $1 \rightarrow 10\,\mu\mathrm{m}$ in diameter as observed by other groups.[99]

A peltier based system for depositing thin films onto the surface of a prism has been built. Overall the advantages of this set-up over conventional methods of ice film formation are clear. The peltier provides a dial up method to both cool and heat. It is able to rapidly, over the course of minutes, obtain stable and accurate temperatures with an indefinite lifetime so long as the peltier functions. In principle peltier cooling has been implemented here successfully to cool a surface to nearly the full range of temperatures desired, $210 \rightarrow 273\,\mathrm{K}$. After continued work on the build, this experiment shows promise to look at heterogeneous chemistry on ice, first with nitric acid and then subsequently on acetone and other trace atmospheric organics such as acetone, at temperatures relevant to the troposphere and stratosphere. Here atmospheric dynamics experiments on ice films can be performed to provide important data on the processes occurring within it where the new spectroscopic tool, CELIF, can be used where available to enhance standard CRD measurements by extending the detection sensitivity towards lower concentrations, potentially up 3 orders in magnitude.

APPENDIX A

A.1 Physical Properties of Ice

Vapour Pressure

Vapour pressure formulations are provided for ice, P_{ice}, and water, P_{water}, in pascals at the temperature ranges stated. They have been obtained from the review Murphy and Koop *et al.*[70] but the specific papers for each equation are cited below. Murphy and Koop have a large amount of additional details and analysis on the specifics of each formulation and also include additional less prominent ones for ice and water, and those for supercooled water (liquid water below the freezing point). If required the reader is referred there.

Goff-Gratch (1965)[71–73]

Range, $180 < T < 273.16\,\text{K}$

$$\log_{10} P_{\text{ice}} = \log_{10}(611.11) - 9.096936\left(\frac{Tt}{T-1}\right) - 3.56654 \cdot \log_{10}\left(\frac{Tt}{T}\right) + 0.876817\left(1 - \frac{T}{Tt}\right)$$

Range, $273.15 < T < 373.15\,\text{K}$

$$\log_{10} P_{\text{water}} = \log_{10}(611.11) + 10.79586\left(1 - \frac{Tt}{T}\right) - 5.02808 \cdot \log_{10}\left(\frac{T}{Tt}\right) + 1.50474 \cdot 10^{-4}(1 - 10^{-8.29692\left(\frac{T}{Tt}-1\right)}) + 0.42873 \cdot 10^{-3}\left(10^{4.76955\left(1-\frac{Tt}{T}\right)} - 1\right)$$

Hyland and Wexler (1983)[195]

Range, $173.16 < T < 273.16$

$$\ln P_{\text{ice}} = \frac{-5674.5359}{T} + 6.3925247 - 0.96778430 \cdot 10^{-2}\, T + 0.62215701 \cdot 10^{-6}\, T^2 + 0.20747825 \cdot 10^{-8}\, T^3 - 0.94840240 \cdot 10^{-12}\, T^4 + 4.1635019 \cdot \ln T$$

Range, $273.15 < T < 473.15$

$$\ln P_{\text{water}} = \frac{-5800.2206}{T} + 1.3914993 - 0.48640239 \cdot 10^{-1}\, T + 0.41764768 \cdot 10^{-4}\, T^2 - 0.14452093 \cdot 10^{-7}\, T^3 + 6.5459673 \cdot \ln T)$$

Wagner and Pruss (1993/1994)[75,186]

Range, $273.16 < T < 647\,\text{K}$ with $Tc = 647.096\,\text{K}$ and $\tau = 1 - (T/Tc)$,

$$\frac{\ln P_{\text{water}}}{(2.2064 \cdot 10^7)} = \left(\frac{Tc}{T}\right)\Big(- 7.85951783\tau + 1.84408259\tau^{1.5} - 11.7866497\tau^3 + 22.6807411\tau^{3.5} - 15.9618719\tau^4 + 1.80122502\tau^{7.5}\Big)$$

Range $190 < T < 273.16\,\text{K}$,

$$\ln P_{\text{ice}} = \ln 611.657 - 13.9281690\left(1 - \left(\frac{Tt}{T}\right)^{1.5}\right) + 34.7078238\left(1 - \left(\frac{Tt}{T}\right)^{1.25}\right)$$

Density of Ice

The following equations provide the temperature dependent density ($\text{Kg}\,\text{m}^{-3}$) of ice taken from Feistel and Wagner.[74] Constants are provided in table A.1, only real parts are quoted where g_{0k} constants have no imaginary part.

$$\rho(T, P) = g_P^{-1} \tag{A.1}$$

$$g_P = g_{0,P} + T_t \cdot \mathrm{Re}\left(r_{2,P}(t_2 - \tau) \cdot \ln(t_2 - \tau) + (t_2 - \tau) \right.$$
$$\left. + (t_2 + \tau) \cdot \ln(t_2 + \tau) - 2t_2 \cdot \ln(t_2) - \frac{\tau^2}{t_2} \right) \qquad \text{(A.2)}$$

$$r_{2,P} = \sum_{k=1}^{2} r_{2k} \frac{k}{P_t} (\pi - \pi_0)^{k-1} \qquad g_{0,P} = \sum_{k=0}^{4} g_{0k} (\pi - \pi_0)^k \qquad \text{(A.3)}$$

Table A.1: Table of constants for use in temperature dependent density of ice calculation. Taken from Feistel and Wagner[74]

Coefficient[a]	**Real Part** **(J Kg^{-1})**	**Coefficient**	**Real Part** **(J Kg^{-1} K^{-1})**
g_{00}	-632 020.233 449 497	t_2	0.337 315 741 065 416
g_{01}	0.655 022 213 658 955	r_{20}	-72.597 457 432 922
g_{02}	-1.893 699 293 261 31·10^{8}	r_{21}	-5.571 076 980 301 23·10^{-5}
g_{03}	3.397 461 232 710 53·10^{15}	r_{22}	2.348 014 092 159 13·10^{-11}
g_{04}	-5.564 648 690 589 91·10^{-22}		

[a] No imaginary parts for $g_{0,P}$ coefficients

A.2 Thermal Conduction Testing

Ice, ideally, should be grown only on the upper surface of the block and in no other region. Therefore a thermal contact boundary with the partition plate was foreseen as a potential issue as during the cooling process the partition would also be cooled. In order to better confine cooling to the upper surface of the prism or block the partition plate edge was thinned from 2 to $0.5\,\mathrm{mm}$ in thickness at the boundary to the surface to reduce conductivity across the it.

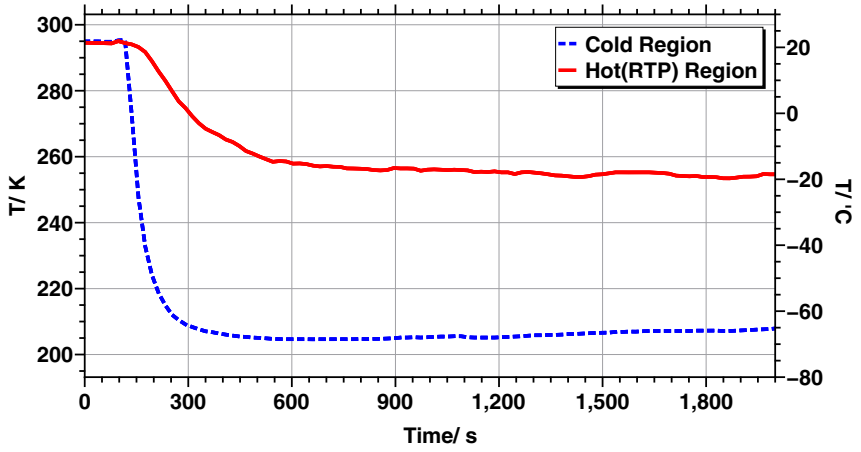

Figure A.1: Time varying temperature of a $\varnothing 100\,\mathrm{mm}$ Al plate split into two zones connected by a circular $0.5\,\mathrm{mm}$ thick groove. The central region was cooled using a CO_2/MeOH slush bath while the hot region was left at rtp. Cooling begins around $100\,\mathrm{s}$.

Prior to this a short test was performed demonstrating that, by reducing the cross-section thermal conduction is occurring through, a significant ΔT can be maintained over a long time frame across two different regions on a metal plate with high thermal conductivity. A circular Al plate, mimicking the partition plate, $\varnothing 100\,\mathrm{mm}$ and thickness $2\,\mathrm{mm}$, had a groove, $0.5\,\mathrm{mm}$ thick and $3\,\mathrm{mm}$ wide cut into it leaving a central reserve of $\varnothing 60\,\mathrm{mm}$. A copper block was used to support the plate in the centre with thermal grease spread in between. The copper block was then put into a tray containing a CO_2/MeOH slush bath. Two k-type TCs recorded the temperature variation over time of the central cold reserve and the outer hot reserve. The measurements were performed at rtp.

Figure A.1 shows the result of this test. $\Delta T = 50\,\mathrm{K}$ was maintained between the two regions for well over $30\,\mathrm{min}$ although this is not shown in the data above. Repeated with the peltier cooled surface for a silicone resin seal between the partition plate and the prism surface this process achieved a $T_{\mathrm{partition}}$ varying between $273 \rightarrow 268\,\mathrm{K}$ for an experiment run at $T_{\mathrm{PT1000}} = 230\,\mathrm{K}$. Although this meant that the partition was below the freezing point of water this was the best that could be achieved with the current set-up.

A.3 Peltier Performance Data

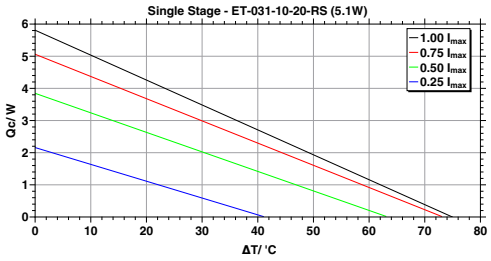

(a) ET-031-10-20-RS, Single Stage, 5.1 W, Peltier

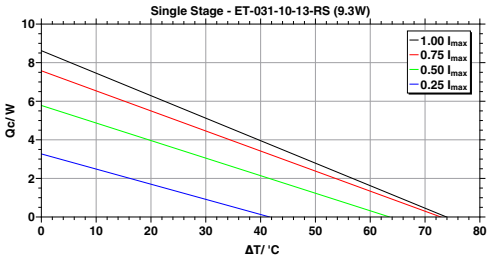

(b) ET-031-10-13-RS, Single Stage, 9.3 W, Peltier

Figure A.2: Figures of the performance data for the two single stage peltiers used to calculate the heat load on the set-up in section 4.9.

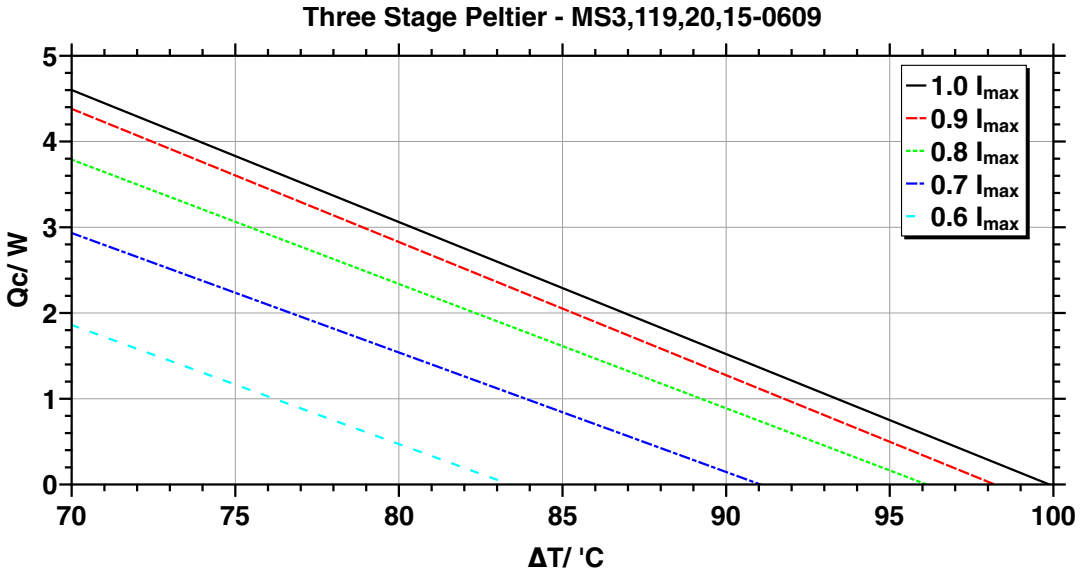

Figure A.3: Figure of the performance data for the main three stage peltier (Lairdtech - MS3,119,20,15-0609) used in the peltier surface experiment.

A.4 Selected Material Properties

Thermal conductivity, k, and the linear coefficient of thermal expansion, α, is shown for several materials used in the main experimental build and the prototyping phase. Data has been obtained from the CRC Chemistry and Physics Handbook[196] and data sheets supplied with the compound where relevant.

Table A.2: Table of properties of materials used in different surface builds where T_k and T_α are the temperatures for the measured k and α respectively

Material	$\boldsymbol{T_k}$ **(K)**	$\boldsymbol{k}$ **(W m^{-1} K^{-1})**	$\boldsymbol{T_\alpha}$ **(K)**	$\boldsymbol{\alpha}$ **($\cdot 10^{-6}$ m m^{-1} K^{-1})**
Aluminium Pure	300	237	298	23.1
Aluminium 1100	194	220		
	273	220		
Copper ETP	194	400	273-298	16.5
	273	390		
Cryogenic Epoxy (Oxford Instruments, C5-102)[b]	[a]	0.17-0.19	[a]	125-135
Ice	173	3.5		
	223	2.8		
	273	2.2		
Stainless Steel 310	200	15.75	194	13
	250	16.56	273	14
	300	17.31		
Stainless Steel 304	273-298	150	273-298	17.3
Teflon (PTFE, Polytetrafluoroethylene)	80	0.16	[a]	100
	298	0.26		

[a] Temperature not provided by text. [b] Measurement provided by datasheet not CRC handbook.

A.5 Surface Laser

Included in the design was the option for a surface laser to be guided through a glass prism when it is used as a substrate. Parts needed to fit around the surface set-up which had been designed with this in mind. Two custom, adjustable miniature mirror mounts are displayed in figure 4.4b. Fitting a mirror of $\varnothing 16\,\mathrm{mm}$, and thickness $3\,\mathrm{mm}$, they were designed to minimise their thickness in order to fit around the peltier and heatsink. Commercially available miniature mounts were found to be too big for such a tight space. Two mirrors are shown, one receiving a laser and the other reflecting it out through windows in the feedthrough flange (5c in figure 4.4b).

A fused silica prism was designed with the angled faces such that a laser laying perpendicular to them will reflect $65\,^\circ$ from the normal of the surface. This value was chosen so that for visible light the penetration depth, d_{pen}, of an evanescent wave reflecting from a glass-ice boundary would range from $\sim 200 \rightarrow 800\,\mathrm{nm}$. When light totally internally reflects at the boundary between two interfaces of refractive index, $n1$ (the prism) and $n2$ (ice), energy is able to penetrate from one medium into the other. This penetrating energy is called the evanescent wave, the amplitude of which decreases with distance from the boundary and is dependent on the angle of incidence, θ_i, at which light reflects. d_{pen} measures the amplitude drop with distance of the evanescent wave given by,

$$d_{\mathrm{pen}} = \frac{\lambda}{2\pi\sqrt{n_1^2 \sin^2 \Theta_i - n_2^2}} \tag{A.4}$$

Data has been compiled into figure A.4 showing the variation of d_{pen} with wavelength using the Sellmeier equation for the variation of refractive indices in a transparent medium combined with ice refractive indices using Warren[78] and Iwabuchi.[182] The data used for the refractive index of ice was from Warren, valid at $266\,\mathrm{K}$, and Iwabuchi indicates this to be relatively unchanged at lower temperatures down to $160\,\mathrm{K}$.

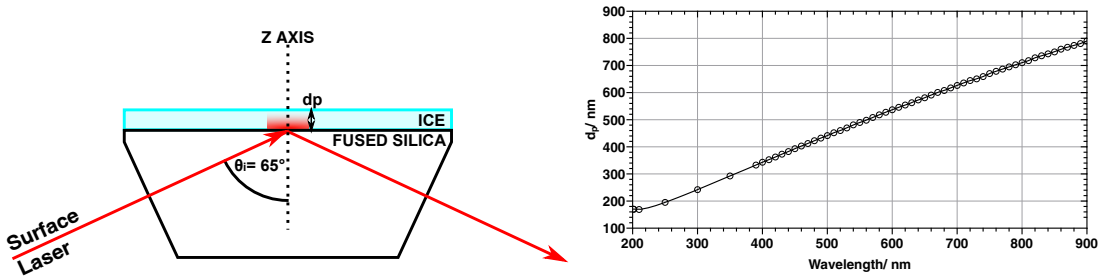

(a) Prism design for evanescent waves

(b) Variation of penetration depth with wavelength

Figure A.4: Details of the prism set-up and penetration depth are shown for the design specifications of the build.

A.6 Characterisation of Pressure Expansions from the Reservoir into the Main Chamber

A characterisation of the pressure in the main chamber, P^{main}, after releasing pressure stored in the reservoir, P^{res}, is shown in figure A.5. Pressures were measured using the capacitance manometers detailed in section 4.6. The resulting linear fit was performed using a scaled Levenberg-Marquardt algorithm. The equation formulated is used throughout chapter 5 when deriving the expected pressures inside the main chamber after expansion of a known amount of water from the reservoir.

$$P^{\text{main}} = 5.639 \pm 0.004 \cdot 10^{-2} * P^{\text{res}} - 1.26 \pm 0.27 \cdot 10^{-2} \tag{A.5}$$

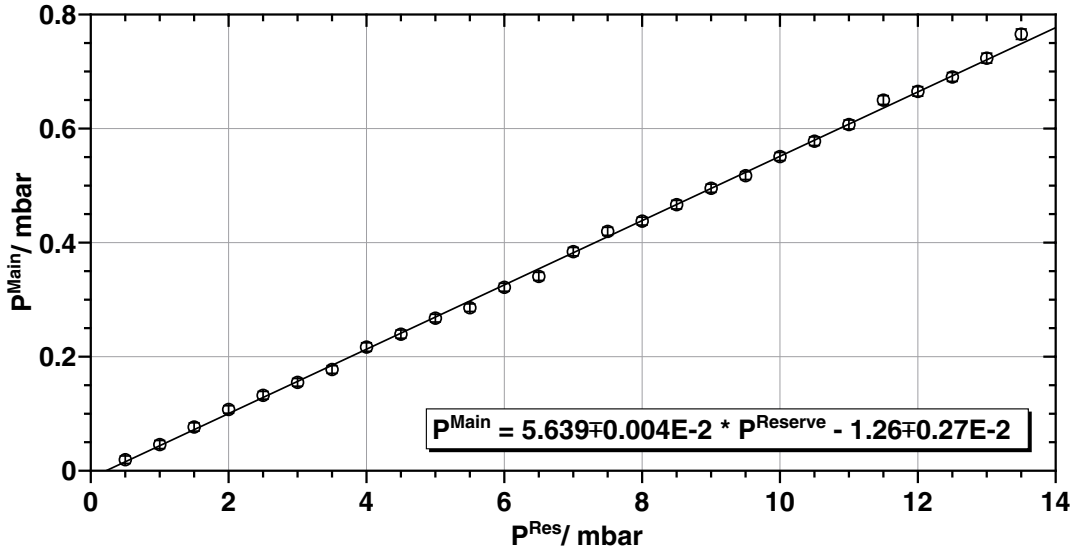

Figure A.5: Pressure of nitrogen gas held within the reservoir relative to the pressure obtained after expansion to fill the main chamber

A.7 Graphs of Data from Table 5.1

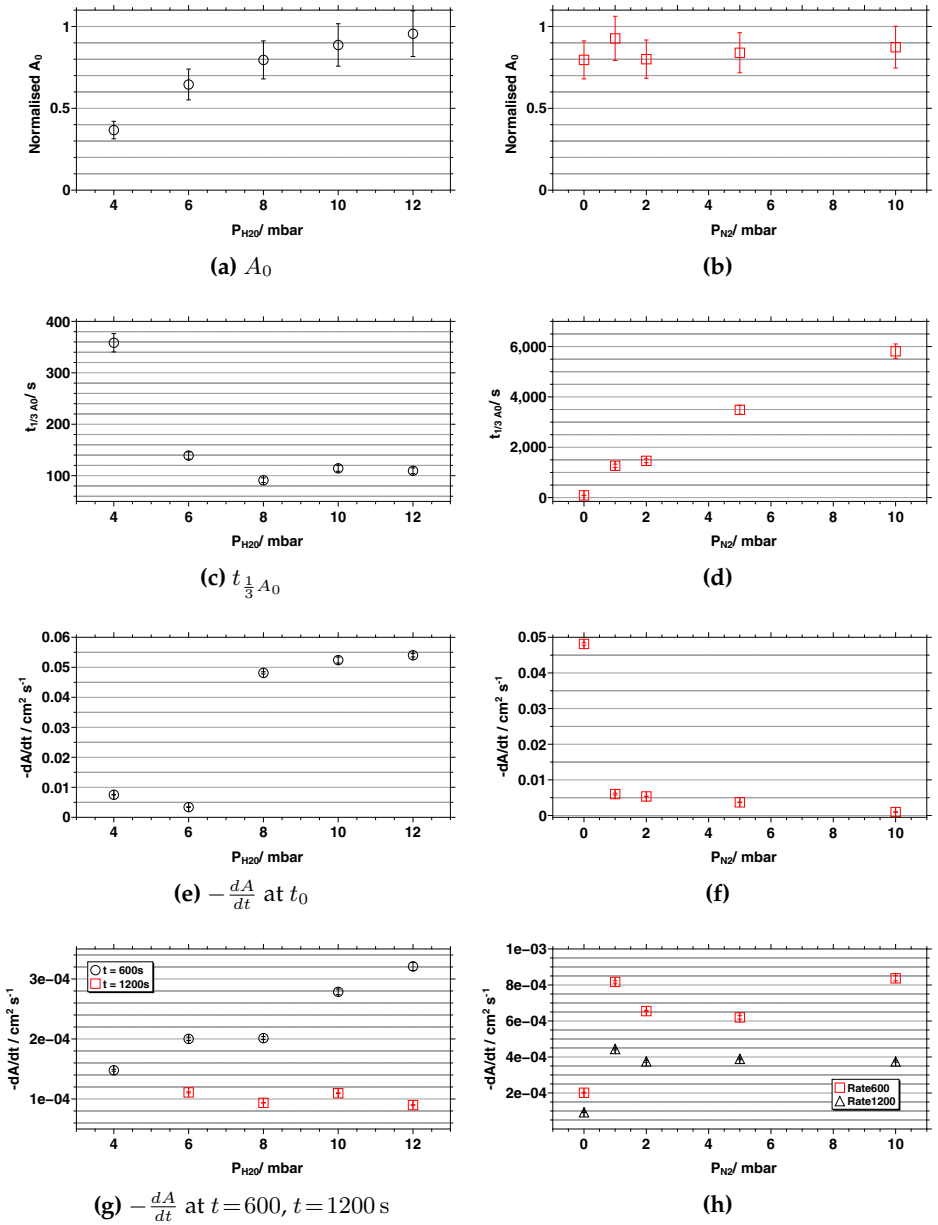

(a) A_0 **(b)**

(c) $t_{\frac{1}{3}A_0}$ **(d)**

(e) $-\frac{dA}{dt}$ at t_0 **(f)**

(g) $-\frac{dA}{dt}$ at $t = 600$, $t = 1200\,\mathrm{s}$ **(h)**

Figure A.6: Figures produced from the data in table 5.1. Two sets are shown the left hand column (a, c, e and g) show data from the expansion of a reservoir filled with water vapour to pressure, $P^{\mathrm{res}}_{\mathrm{H2O}}$ across an SS surface at $T_{\mathrm{sur}} = 225.2\,\mathrm{K}$. The right hand column (b, d, f and h) shows the $P^{\mathrm{res}}_{\mathrm{H2O}} = 8\,\mathrm{mbar}$ with different backing pressures of N_2, $P^{\mathrm{backing}}_{\mathrm{N2}}$ inhibiting migration.
a)/b) show peak ice areas, A_0. These are normalised against the full area of the stainless steel surface less the area of the PT1000 probe, $2.92\,\mathrm{cm}^2$.
c)/d) display the time taken to migrate to $\frac{1}{3}A_0$.
e)/f) show initial migration rates immediately after the peak area is reached.
g)/h) show late migration rates 10 and 20 minutes after the initial expansion event.

A.8 HeNe Data Fitting in Figure 5.8

Several different test fits were trialled in order to qualitatively describe the changing thickness over time of the ice surface monitored in the first $2-6\,\mathrm{s}$. The motivation for this was to be able to account for ice growth occurring in the first $0.5\,\mathrm{s}$ during pure water expansions across the cold stainless steel surface. During this time frame, data was not recorded fast enough to properly recognise interference maxima and minima from the HeNe measurements, therefore to accommodate this missing data a qualitative fit was used to calculate the missing thicknesses where the fit crosses the time axis at $t=0\,\mathrm{s}$. Fits used were variants of an exponential fit consistent with a first order process or combination thereof. Fits were performed using Matlab using a Trust-Region algorithm.

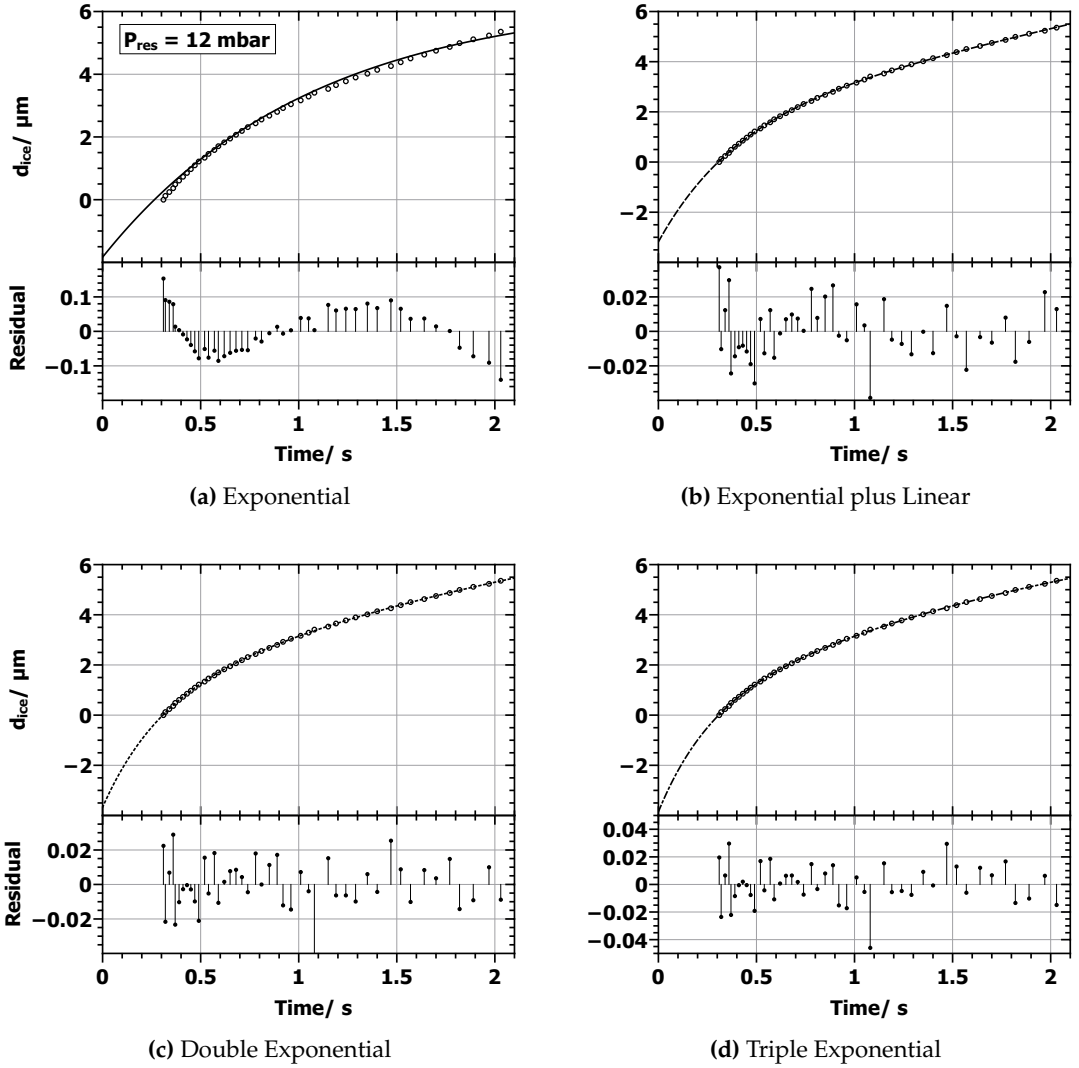

(a) Exponential

(b) Exponential plus Linear

(c) Double Exponential

(d) Triple Exponential

Figure A.7: Comparison between several different qualitative fits to the HeNe thickness data for $P_{\mathrm{H2O}}^{\mathrm{res}}=12\,\mathrm{mbar}$ across the cold surface.
a) shows an exponential fit
b) shows an exponential plus linear fit
c) shows a double exponential fit
d) shows a triple exponential fit

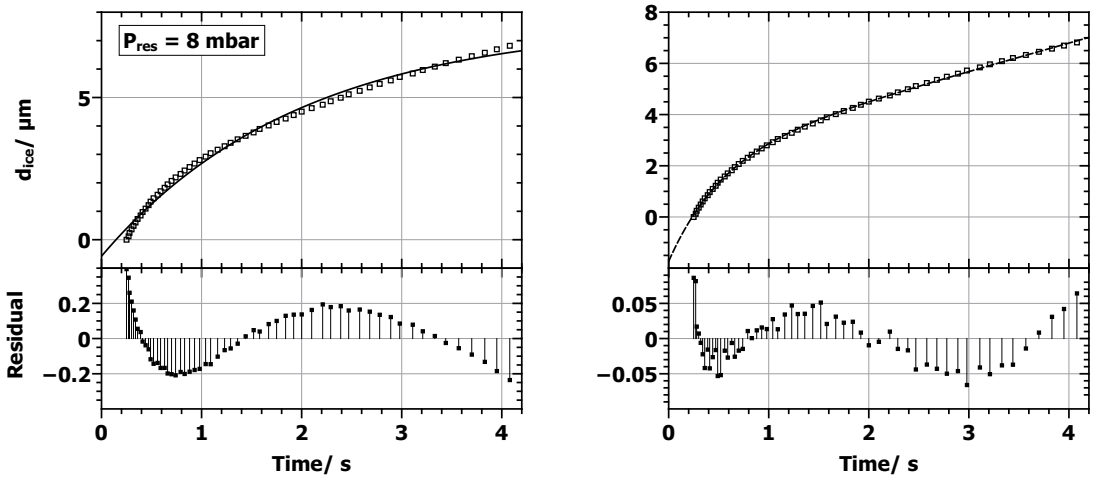

(a) Exponential

(b) Exponential plus Linear

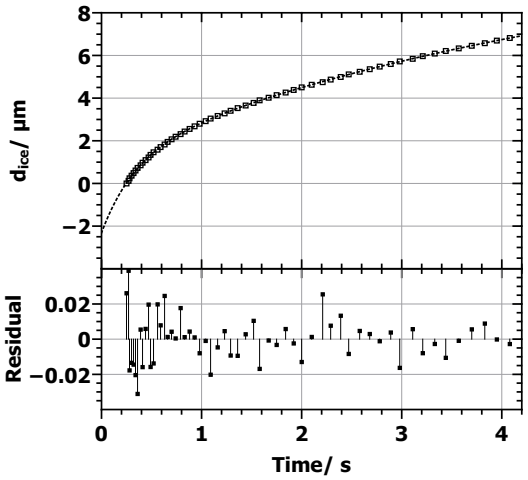

(c) Double Exponential

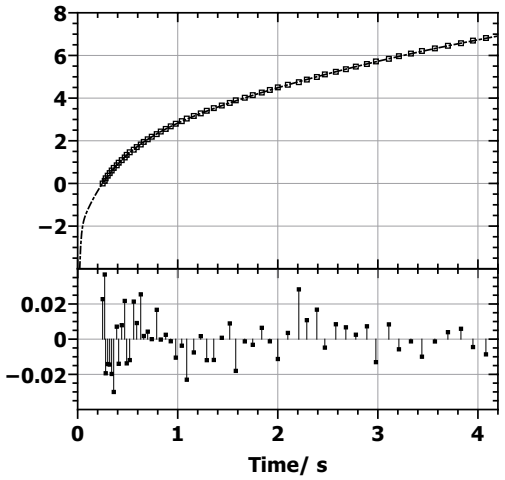

(d) Triple Exponential

Figure A.8: Comparison between several different qualitative fits to the HeNe thickness data for $P_{\mathrm{H2O}}^{\mathrm{res}} = 8\,\mathrm{mbar}$ across the cold surface.
a) shows an exponential fit
b) shows an exponential plus linear fit
c) shows a double exponential fit
d) shows a triple exponential fit

REFERENCES

[1] J. Seinfeld, *Atmospheric chemistry and physics from air pollution to climate change*. New York: Wiley, 1998.

[2] J. C. Farman, B. G. Gardiner, and J. D. Shanklin, "Large losses of total ozone in Antarctica reveal seasonal ClOx/NOx interaction," *Nature*, vol. 315, pp. 207–210, May 1985.

[3] S. Solomon, "Stratospheric ozone depletion: A review of concepts and history," *Reviews of Geophysics*, vol. 37, no. 3, p. 275, 1999.

[4] M. R. Schoeberl and D. L. Hartmann, "The dynamics of the stratospheric polar vortex and its relation to springtime ozone depletions.," *Science (New York, N.Y.)*, vol. 251, pp. 46–52, Jan. 1991.

[5] J. Kuttippurath, F. Lefèvre, J.-P. Pommereau, H. K. Roscoe, F. Goutail, a. Pazmiño, and J. D. Shanklin, "Antarctic ozone loss in 19792010: first sign of ozone recovery," *Atmospheric Chemistry and Physics*, vol. 13, pp. 1625–1635, Feb. 2013.

[6] NASA, "Ozone Hole Watch, ozonewatch.gsfc.nasa.gov/."

[7] G. L. Manney *et al.*, "Unprecedented Arctic ozone loss in 2011.," *Nature*, vol. 478, pp. 469–75, Oct. 2011.

[8] M. G. Lawrence and P. J. Crutzen, "The impact of cloud particle gravitational settling on soluble trace gas distributions," *Tellus Series B-Chemical and Physical Meteorology*, vol. 50, pp. 263–289, 1998.

[9] M. A. Zondlo, P. K. Hudson, A. J. Prenni, and M. A. Tolbert, "Chemistry and microphysics of polar stratospheric clouds and cirrus clouds," *Annual review of physical chemistry*, vol. 51, pp. 473–99, Jan. 2000.

[10] J. P. D. Abbatt, "Interactions of atmospheric trace gases with ice surfaces: Adsorption and reaction," *Chemical Reviews*, vol. 103, pp. 4783–4800, 2003.

[11] J. M. Picone, "NRLMSISE-00 empirical model of the atmosphere: Statistical comparisons and scientific issues," *Journal of Geophysical Research*, vol. 107, no. A12, p. 1468, 2002.

[12] NASA, *US Standard Atmosphere*. US Government Printing Office, Washington D.C., 1976.

[13] R. Wayne, *Chemistry of atmospheres : an introduction to the chemistry of the atmospheres of earth, the planets, and their satellites*. Oxford England New York: Oxford University Press, 2000.

[14] C. Fabry and H. Buisson, "L'absorption de l'ultra-violet par l'ozone et la limite du spectre solaire," *Journal de Physique Théorique et Appliquée*, vol. 3, no. 1, pp. 196–206, 1913.

[15] C. Fabry and H. Buisson, "The absorption of the ultraviolet ray by ozone and the extremity of the solar spectrum," *Comptes rendus hebdomadaires des seances de l'acadaemie des sciences*, vol. 156, pp. 782–785.

[16] G. M. B. Dobson, "Forty Years Research on Atmospheric Ozone at Oxford: a His-

tory," *Applied Optics*, vol. 7, p. 387, Mar. 1968.

[17] S. Chapman, "A theory of upper atmospheric ozone," *Memoirs of the Royal Meteorological Society*, vol. 3, pp. 103–125, 1928.

[18] M. R. S. McCoustra and A. B. Horn, "Towards a laboratory strategy for the study of heterogeneous catalysis in stratospheric ozone depletion," *Chemical Society Reviews*, vol. 23, no. 3, p. 195, 1994.

[19] J. Hampson, *Photochemical Behaviour of the Ozone Layer*. Canadian Arm. Research and Develop. Establishment, Quebec., 1964.

[20] M. Nicolet, "Ozone and Hydrogen Reactions," *Annales de Geophysique*, vol. 26, no. 2, p. 531, 1970.

[21] P. J. Crutzen, "The influence of nitrogen oxides on the atmospheric ozone content," *Quarterly Journal of the Royal Meteorological Society*, vol. 96, pp. 320–325, Apr. 1970.

[22] P. J. Crutzen, "The Role of NO and NO2 in the Chemistry of the Troposphere and Stratosphere," *Annual Review of Earth and Planetary Sciences*, vol. 7, pp. 443–472, May 1979.

[23] M. J. Molina and F. S. Rowland, "Stratospheric sink for chlorofluoromethanes: chlorine atomc-atalysed destruction of ozone," *Nature*, vol. 249, pp. 810–812, June 1974.

[24] R. S. Stolarski and R. J. Cicerone, "Stratospheric Chlorine: a Possible Sink for Ozone," *Canadian Journal of Chemistry*, vol. 52, pp. 1610–1615, Apr. 1974.

[25] M. J. Molina, T. L. Tso, L. T. Molina, and F. C. Wang, "Antarctic stratospheric chemistry of chlorine nitrate, hydrogen chloride, and ice: release of active chlorine.," *Science (New York, N.Y.)*, vol. 238, pp. 1253–7, Nov. 1987.

[26] M. B. McElroy, R. J. Salawitch, S. C. Wofsy, and J. A. Logan, "Reductions of Antarctic ozone due to synergistic interactions of chlorine and bromine," *Nature*, vol. 321, pp. 759–762, June 1986.

[27] M. Norval, R. M. Lucas, A. P. Cullen, F. R. de Gruijl, J. Longstreth, Y. Takizawa, and J. C. van der Leun, "The human health effects of ozone depletion and interactions with climate change.," *Photochemical & photobiological sciences : Official journal of the European Photochemistry Association and the European Society for Photobiology*, vol. 10, pp. 199–225, Feb. 2011.

[28] A. Andrady *et al.*, "Environmental effects of ozone depletion and its interactions with climate change: progress report, 2009," *Photochemical & Photobiological Sciences*, vol. 9, no. 3, p. 275, 2010.

[29] M. Hervig, R. E. Thompson, M. Mchugh, L. L. Gordley, J. M. R. Iii, and E. Summers, "First confirmation that water ice is the primary component of polar mesospheric clouds," vol. 28, no. 6, pp. 971–974, 2001.

[30] R. Atkinson, "Atmospheric chemistry of VOCs and NOx," *Atmospheric Environment*, vol. 34, no. 12-14, pp. 2063–2101, 2000.

[31] C. E. Kolb *et al.*, "An overview of current issues in the uptake of atmospheric trace gases by aerosols and clouds," *Atmospheric Chemistry and Physics*, vol. 10, pp. 10561–10605, 2010.

[32] V. F. McNeill *et al.*, "Organics in environmental ices: sources, chemistry, and impacts," *Atmospheric Chemistry and Physics*, vol. 12, pp. 9653–9678, Oct. 2012.

[33] T. Bartels-Rausch *et al.*, "A review of airice chemical and physical interactions (AICI): liquids, quasi-liquids, and solids in snow," *Atmospheric Chemistry and Physics*, vol. 14, pp. 1587–1633, Feb. 2014.

[34] P. J. Crutzen and F. Arnold, "Nitric acid cloud formation in the cold Antarctic stratosphere: a major cause for the springtime ozone hole," *Nature*, vol. 324, pp. 651–655, Dec. 1986.

[35] O. B. Toon, P. Hamill, R. P. Turco, and J. Pinto, "Condensation of HNO 3 and HCl in the winter polar stratospheres," *Geophysical Research Letters*, vol. 13, pp. 1284–1287, Nov. 1986.

[36] D. M. Murphy, "In Situ Measurements of Organics, Meteoritic Material, Mercury, and Other Elements in Aerosols at 5 to 19 Km," *Science*, vol. 282, pp. 1664–1669, Nov. 1998.

[37] T. Koop, U. M. Biermann, W. Raber, B. P. Luo, P. J. Crutzen, and T. Peter, "Do stratospheric aerosol droplets freeze above the ice frost point?," *Geophysical Research Letters*, vol. 22, pp. 917–920, Apr. 1995.

[38] C. R. Hoyle, I. Engel, B. P. Luo, M. C. Pitts, L. R. Poole, J.-U. Grooß, and T. Peter, "Heterogeneous formation of polar stratospheric clouds Part 1: Nucleation of nitric acid trihydrate (NAT)," *Atmospheric Chemistry and Physics*, vol. 13, pp. 9577–9595, Sept. 2013.

[39] S. Solomon, R. R. Garcia, F. S. Rowland, and D. J. Wuebbles, "On the depletion of Antarctic ozone," *Nature*, vol. 321, pp. 755–758, June 1986.

[40] Y. Matsumi, M. Kawasaki, T. Sato, T. Kinugawa, and T. Arikawa, "Photodissociation of chlorine molecule in the UV region," *Chemical Physics Letters*, vol. 155, pp. 486–490, Mar. 1989.

[41] J. P. D. Abbatt, "Interaction of HNO 3 with water-ice surfaces at temperatures of the free troposphere," *Geophysical Research Letters*, vol. 24, pp. 1479–1482, June 1997.

[42] W. L. Chang, P. V. Bhave, S. S. Brown, N. Riemer, J. Stutz, and D. Dabdub, "Heterogeneous Atmospheric Chemistry, Ambient Measurements, and Model Calculations of N2O5 : A Review," *Aerosol Science and Technology*, vol. 45, pp. 665–695, Apr. 2011.

[43] P. J. Crutzen and P. H. Zimmerman, "The changing photochemistry of the troposphere," *Tellus A*, vol. 43, pp. 136–151, Aug. 1991.

[44] Y. Wang, D. J. Jacob, and J. A. Logan, "Global simulation of tropospheric O 3 -NO x -hydrocarbon chemistry: 1. Model formulation," *Journal of Geophysical Research*, vol. 103, p. 10713, May 1998.

[45] Y. Wang, J. a. Logan, and D. J. Jacob, "Global simulation of tropospheric O 3 -NO x -hydrocarbon chemistry: 2. Model evaluation and global ozone budget," *Journal of Geophysical Research*, vol. 103, p. 10727, May 1998.

[46] Y. Wang, D. J. Jacob, and J. a. Logan, "Global simulation of tropospheric O 3 -NO x -hydrocarbon chemistry: 3. Origin of tropospheric ozone and effects of nonmethane

hydrocarbons," *Journal of Geophysical Research*, vol. 103, p. 10757, May 1998.

[47] P. J. Crutzen and L. T. Gidel, "A two-dimensional photochemical model of the atmosphere: 2. The tropospheric budgets of the anthropogenic chlorocarbons CO, CH 4 , CH 3 Cl and the effect of various NO x sources on tropospheric ozone," *Journal of Geophysical Research*, vol. 88, no. C11, p. 6641, 1983.

[48] D. W. Fahey, K. K. Kelly, S. R. Kawa, A. F. Tuck, M. Loewenstein, K. R. Chan, and L. E. Heidt, "Observations of denitrification and dehydration in the winter polar stratospheres," *Nature*, vol. 344, pp. 321–324, Mar. 1990.

[49] J. N. Crowley, M. Ammann, R. A. Cox, R. G. Hynes, M. E. Jenkin, A. Mellouki, M. J. Rossi, J. Troe, and T. J. Wallington, "Evaluated kinetic and photochemical data for atmospheric chemistry: Volume V heterogeneous reactions on solid substrates," *Atmospheric Chemistry and Physics*, vol. 10, pp. 9059–9223, Sept. 2010.

[50] A. Symington, L. M. Leow, P. T. Griffiths, and R. A. Cox, "Adsorption and Hydrolysis of Alcohols and Carbonyls on Ice at Temperatures of the Upper Troposphere," *Journal of Physical Chemistry A*, vol. 116, 2012.

[51] A. B. Horn, M. A. Chesters, M. R. S. McCoustra, and J. R. Sodeau, "Adsorption of stratospherically important molecules on thin D2O ice films using reflection absorption infrared spectroscopy," *Journal of the Chemical Society, Faraday Transactions*, vol. 88, no. 7, p. 1077, 1992.

[52] A. B. Horn, T. Koch, M. A. Chesters, M. R. S. McCoustra, and J. R. Sodeau, "A low-temperature infrared study of the reactions of the stratospheric NOy reservoir species dinitrogen pentoxide with water ice, 80-160 K," *The Journal of Physical Chemistry*, vol. 98, pp. 946–951, Jan. 1994.

[53] K. I. Öberg, R. T. Garrod, E. F. van Dishoeck, and H. Linnartz, "Formation rates of complex organics in UV irradiated CH 3 OH-rich ices," *Astronomy and Astrophysics*, vol. 504, pp. 891–913, Sept. 2009.

[54] J. Bouwman, H. M. Cuppen, M. Steglich, L. J. Allamandola, and H. Linnartz, "Photochemistry of polycyclic aromatic hydrocarbons in cosmic water ice," *Astronomy & Astrophysics*, vol. 529, p. A46, Mar. 2011.

[55] J. D. Thrower, D. J. Burke, M. P. Collings, A. Dawes, P. D. Holtom, F. Jamme, P. Kendall, W. A. Brown, I. P. Clark, H. J. Fraser, M. R. S. McCoustra, N. J. Mason, and A. W. Parker, "Desorption of Hot Molecules from Photon Irradiated Interstellar Ices," *The Astrophysical Journal*, vol. 673, pp. 1233–1239, Feb. 2008.

[56] V. F. Petrenko and R. W. Whitworth, *Physics of Ice*. Oxford New York: Oxford University Press, 1999.

[57] A. D. Walsh, "The electronic orbitals, shapes, and spectra of polyatomic molecules. 1 AH2 Molecules," *Journal of the Chemical Society*, pp. 2260–2266, 1953.

[58] F. Franks, *Water a matrix of life*. Royal Society of Chemistry, 2000.

[59] F. Franks, ed., *Water A Comprehensive Treatise: Volume 1 The Physics and Physical Chemistry of Water*. Plenum Press, 1972.

[60] N. Bjerrum, "Structure and Properties of Ice," *Science*, vol. 115, pp. 385–390, 1952.

[61] J. L. Finney, "The water molecule and its interactions: the interaction between theory, modelling, and experiment," *Journal of Molecular Liquids*, vol. 90, pp. 303–312, 2001.

[62] F. H. Stillinger, "Water Revisited," *Science*, vol. 209, pp. 451–457, 1980.

[63] C. G. Salzmann, P. G. Radaelli, E. Mayer, and J. L. Finney, "Ice XV: A New Thermodynamically Stable Phase of Ice," *Physical Review Letters*, vol. 103, 2009.

[64] P. Jenniskens and D. F. Blake, "Structural transitions in amorphous water ice and astrophysical implications," *Science*, vol. 265, pp. 753–756, 1994.

[65] C. G. Salzmann, P. G. Radaelli, A. Hallbrucker, E. Mayer, and J. L. Finney, "The preparation and structures of hydrogen ordered phases of ice," *Science*, vol. 311, pp. 1758–1761, 2006.

[66] B. J. Murray, D. A. Knopf, and A. K. Bertram, "The formation of cubic ice under conditions relevant to Earth's atmosphere," *Nature*, vol. 434, pp. 202–205, 2005.

[67] L. F. Keyser and M. T. Leu, "Morphology of nitric acid and water ice films.," *Microscopy research and technique*, vol. 25, pp. 434–8, Aug. 1993.

[68] K. Rottger, A. Endriss, J. Ihringer, S. Doyle, and W. F. Kuhs, "Lattice-Constants and Thermal-Expansion of H_2O and D_2O Ice Ih between 10 and 265 K," *Acta Crystallographica Section B-Structural Science*, vol. 50, pp. 644–648, 1994.

[69] P. V. Hobbs, *Ice Physics*. Oxford University Press, 1974.

[70] D. M. Murphy and T. Koop, "Review of the vapour pressures of ice and supercooled water for atmospheric applications," *Quarterly Journal of the Royal Meteorological Society*, vol. 131, pp. 1539–1565, Apr. 2005.

[71] J. A. Goff and S. Gratch, "Low-pressure properties of water from -160 to 212 F," *Trans. Am. Soc. Heating Air-Cond. Eng.*, vol. 52, pp. 95–122, 1946.

[72] J. Goff, "Saturation pressure of water on the new Kelvin scale," *Trans. Am. Soc. Heating Air-Cond. Eng.*, vol. 63, pp. 347–354, 1957.

[73] J. Goff, "Saturation pressure of water on the new Kelvin scale," in *In Humidity and moisture: Measurement and control in science and industry* (A. Wexler, ed.), vol. 3, Publishing, New York, USA, 1965.

[74] R. Feistel, "A New Equation of State for H2O Ice, Ih," *Journal of Physical and Chemical Reference Data*, vol. 35, no. 2, p. 1021, 2006.

[75] W. Wagner and A. Pruss, "The IAPWS formulation 1995 for the thermodynamic properties of ordinary water substance for general and scientific use," *Journal of Physical and Chemical Reference Data*, vol. 31, pp. 387–535, 2002.

[76] T. C. Grenfell and D. K. Perovich, "Radiation absorption-coefficients of polycrystalline ice from 400-1400 nm," *Journal of Geophysical Research-Oceans and Atmospheres*, vol. 86, pp. 7447–7450, 1981.

[77] D. K. Perovich and J. W. Govoni, "Absorption coefficients of ice from 250 to 400 nm," *Geophysical Research Letters*, vol. 18, pp. 1233–1235, July 1991.

[78] S. G. Warren and R. E. Brandt, "Optical constants of ice from the ultraviolet to the microwave: A revised compilation," *Journal of Geophysical Research-Atmospheres*,

vol. 113, 2008.

[79] M. Ackermann *et al.*, "Optical properties of deep glacial ice at the South Pole," *Journal of Geophysical Research*, vol. 111, no. D13, p. D13203, 2006.

[80] N. Materer, U. Starke, A. Barbieri, M. A. Vanhove, G. A. Somorjai, G. J. Kroes, and C. Minot, "Molecular surface structure of a low temperature ice Ih(0001) crystal," *Journal of Physical Chemistry*, vol. 99, pp. 6267–6269, 1995.

[81] M. Morgenstern, J. Muller, T. Michely, and G. Comsa, "The ice bilayer on Pt(111): Nucleation, structure and melting," *Zeitschrift Fur Physikalische Chemie-International Journal of Research in Physical Chemistry & Chemical Physics*, vol. 198, pp. 43–72, 1997.

[82] K. Morgenstern and K. H. Rieder, "Formation of the cyclic ice hexamer via excitation of vibrational molecular modes by the scanning tunneling microscope," *Journal of Chemical Physics*, vol. 116, pp. 5746–5752, 2002.

[83] R. Rosenberg, "Why is ice slippery?," *Physics Today*, vol. 58, pp. 50–55, 2005.

[84] C. Girardet and C. Toubin, "Molecular atmospheric pollutant adsorption on ice: a theoretical survey," *Surface Science Reports*, vol. 44, pp. 159–238, Dec. 2001.

[85] T. F. Kahan, J. P. Reid, and D. J. Donaldson, "Spectroscopic probes of the quasi-liquid layer on ice.," *The journal of physical chemistry. A*, vol. 111, pp. 11006–12, Nov. 2007.

[86] Y. Li and G. A. Somorjai, "Surface premelting of ice," *Journal of Physical Chemistry C*, vol. 111, pp. 9631–9637, 2007.

[87] A. Symington, "The Heterogeneous Interaction of Organic Acids with Ice Surfaces at Temperatures of the Upper Troposphere," tech. rep., Newham College, University of Cambridge, 2006.

[88] C. Z. Zhu, B. Xiang, L. T. Chu, and L. Zhu, "308 nm Photolysis of Nitric Acid in the Gas Phase, on Aluminum Surfaces, and on Ice Films," *Journal of Physical Chemistry A*, vol. 114, pp. 2561–2568, 2010.

[89] D. R. Haynes, N. J. Tro, and S. M. George, "Condensation and evaporation of water on ice surfaces," *Journal of Physical Chemistry*, vol. 96, no. 21, pp. 8502–8509, 1992.

[90] P. Marchand, S. Riou, and P. Ayotte, "Diffusion kinetics for methanol in polycrystalline ice.," *The journal of physical chemistry. A*, vol. 110, pp. 11654–64, Oct. 2006.

[91] D. E. Brown, S. M. George, C. Huang, E. K. L. Wong, K. B. Rider, R. S. Smith, and B. D. Kay, "H2O condensation coefficient and refractive index for vapor-deposited ice from molecular beam and optical interference measurements," *Journal of Physical Chemistry*, vol. 100, pp. 4988–4995, 1996.

[92] F. Caloz, F. F. Fenter, K. D. Tabor, and M. J. Rossi, "Paper I: Design and construction of a Knudsen-cell reactor for the study of heterogeneous reactions over the temperature range 130750 K: Performances and limitations," *Review of Scientific Instruments*, vol. 68, no. 8, p. 3172, 1997.

[93] N. Peybernes, C. Marchand, S. Le Calve, and P. Mirabel, "Adsorption studies of acetone and 2,3-butanedione on ice surfaces between 193 and 223 K," *Physical Chemistry Chemical Physics*, vol. 6, no. 6, p. 1277, 2004.

[94] E. R. Lovejoy, L. G. Huey, and D. R. Hanson, "Atmospheric fate of CF 3 OH 2: Heterogeneous reaction," *Journal of Geophysical Research*, vol. 100, no. D9, p. 18775, 1995.

[95] M. A. Zondlo, T. B. Onasch, M. S. Warshawsky, M. A. Tolbert, G. Mallick, P. Arentz, and M. S. Robinson, "Experimental studies of vapor-deposited water-ice firms using grazing-angle FTIR-reflection absorption spectroscopy," *J. Phys. Chem. B*, vol. 101, pp. 10887–10895, Dec. 1997.

[96] D. M. Golden, G. N. Spokes, and S. W. Benson, "Very Low-Pressure Pyrolysis (VLPP); A Versatile Kinetic Tool," *Angewandte Chemie International Edition in English*, vol. 12, pp. 534–546, July 1973.

[97] P. Davidovits, C. E. Kolb, L. R. Williams, J. T. Jayne, and D. R. Worsnop, "Mass accommodation and chemical reactions at gas-liquid interfaces.," *Chemical reviews*, vol. 106, pp. 1323–54, Apr. 2006.

[98] V. Sadtchenko and G. E. Ewing, "Interfacial melting of thin ice films: An infrared study," *The Journal of Chemical Physics*, vol. 116, no. 11, p. 4686, 2002.

[99] L. F. Keyser and M.-T. Leu, "Surface Areas and Porosities of Ices Used to Simulate Stratospheric Clouds," *Journal of Colloid and Interface Science*, vol. 155, pp. 137–145, Jan. 1993.

[100] M. T. Leu, L. F. Keyser, and R. S. Timonen, "Morphology and surface areas of thin ice films," *J. Phys. Chem. B*, vol. 101, pp. 6259–6262, Aug. 1997.

[101] M.-T. T. Leu and L. F. Keyser, "Vapor-deposited water and nitric acid ices: Physical and chemical properties," *International Reviews in Physical Chemistry*, vol. 28, pp. 53–109, Jan. 2009.

[102] J.-B. Bossa, K. Isokoski, M. S. de Valois, and H. Linnartz, "Thermal collapse of porous interstellar ice," *Astronomy & Astrophysics*, vol. 545, p. A82, Sept. 2012.

[103] J. Bossa, K. Isokoski, D. M. Paardekooper, M. Bonnin, E. P. V. D. Linden, T. Triemstra, and S. Cazaux, "Porosity measurements of interstellar ice mixtures using optical laser interference and extended effective medium approximations," no. 201311204, pp. 1–9, 2013.

[104] K. Isokoski, J.-B. Bossa, T. Triemstra, and H. Linnartz, "Porosity and thermal collapse measurements of H2O, CH3OH, CO2, and H2O:CO2 ices.," *Physical chemistry chemical physics : PCCP*, vol. 16, pp. 3456–65, Feb. 2014.

[105] S. Gregg and K. Sing, *Adsorption, Surface Area and Porosity*. New York: Academic Press, 1982.

[106] J. L. Hollenberg and D. a. Dows, "Measurement of Absolute Infrared Absorption Intensities in Crystals," *The Journal of Chemical Physics*, vol. 34, no. 3, p. 1061, 1961.

[107] S. Mitlin and K. T. Leung, "Film growth of ice by vapor deposition at 128-185 K studied by Fourier transform infrared reflection-absorption spectroscopy: Evolution of the OH stretch and the dangling bond with film thickness," *J. Phys. Chem. B*, vol. 106, pp. 6234–6247, June 2002.

[108] B. Maté, A. Medialdea, M. a. Moreno, R. Escribano, and V. J. Herrero, "Experi-

mental Studies of Amorphous and Polycrystalline Ice Films Using FT-RAIRS," *The Journal of Physical Chemistry B*, vol. 107, pp. 11098–11108, Oct. 2003.

[109] G. Berden, R. Peeters, and G. Meijer, "Cavity ring-down spectroscopy: Experimental schemes and applications," *International Reviews in Physical Chemistry*, vol. 19, pp. 565–607, 2000.

[110] J. L. Kinsey, "Laser-Induced Fluorescence," *Annual Review of Physical Chemistry*, vol. 28, pp. 349–372, Oct. 1977.

[111] P. M. Johnson and C. E. Otis, "Molecular multi-photon spectroscopy with ionization detection," *Annual Review of Physical Chemistry*, vol. 32, pp. 139–157, 1981.

[112] D. R. Herriott and H. J. Schulte, "Folded Optical Delay Lines," *Applied Optics*, vol. 4, p. 883, Aug. 1965.

[113] J. U. White, "Long Optical Paths of Large Aperture," *Journal of the Optical Society of America*, vol. 32, p. 285, May 1942.

[114] A. O'Keefe, D. A. G. Deacon, and A. Okeefe, "Cavity Ring-Down Optical Spectrometer for Absorption measurements using pulsed laser sources," *Review of Scientific Instruments*, vol. 59, no. 12, pp. 2544–2551, 1988.

[115] J. M. Herbelin, J. A. McKay, M. A. Kwok, R. H. Ueunten, D. S. Urevig, D. J. Spencer, and D. J. Benard, "Sensitive measurement of photon lifetime and true reflectances in an optical cavity by a phase-shift method," *Applied Optics*, vol. 19, pp. 144–147, 1980.

[116] D. Z. Anderson, J. C. Frisch, and C. S. Masser, "Mirror reflectometer based on optical cavity decay time," *Applied Optics*, vol. 23, p. 1238, Apr. 1984.

[117] R. T. Jongma, M. G. H. Boogaarts, I. Holleman, and G. Meijer, "Trace gas detection with cavity ring down spectroscopy," *Review of Scientific Instruments*, vol. 66, pp. 2821–2828, 1995.

[118] G. Berden and R. Engeln, eds., *Cavity Ring-Down Spectroscopy: Techniques and Applications*. Wiley-Blackwell, 2009.

[119] P. Zalicki and R. N. Zare, "Cavity ring-down spectroscopy for quantitative absorption measurements," *The Journal of Chemical Physics*, vol. 102, no. 7, p. 2708, 1995.

[120] J. T. Hodges, J. P. Looney, and R. D. van Zee, "Response of a ring-down cavity to an arbitrary excitation," *The Journal of Chemical Physics*, vol. 105, no. 23, p. 10278, 1996.

[121] K. K. Lehmann and D. Romanini, "The superposition principle and cavity ring-down spectroscopy," *Journal of Chemical Physics*, vol. 105, no. 23, pp. 10263–10277, 1996.

[122] S. S. Brown, H. Stark, T. B. Ryerson, E. J. Williams, D. K. Nicks, M. Trainer, F. C. Fehsenfeld, and A. R. Ravishankara, "Nitrogen oxides in the nocturnal boundary layer: Simultaneous in situ measurements of NO3, N2O5, NO2, NO, and O-3," *Journal of Geophysical Research-Atmospheres*, vol. 108, p. 11, 2003.

[123] S. M. Ball and R. L. Jones, "Broad-band cavity ring-down spectroscopy," *Chemical Reviews*, vol. 103, pp. 5239–5262, 2003.

[124] M. S. Zhao, E. H. Wahl, T. G. Owano, C. C. Largent, R. N. Zare, and C. H. Kruger,

"Near-surface reduction of cavity ring-down spectroscopy detection sensitivity," *Chemical Physics Letters*, vol. 318, pp. 555–560, 2000.

[125] W. T. Silfvast, *Laser Fundamentals*. Cambridge University Press, 2004.

[126] J. Strutt, "On the light from the sky, its polarization and colour," *Philosophical Magazine*, vol. 41, pp. 107–120, 274–279, 1871.

[127] J. W. Strutt, "On the transmission of light through an atmosphere containing small particles in suspension, and on the origin of the blue of the sky," *Philosophical Magazine*, vol. 47, pp. 375–384, 1899.

[128] R. B. Miles, W. R. Lempert, and J. N. Forkey, "Laser Rayleigh scattering," *Measurement Science and Technology*, vol. 12, pp. R33–R51, May 2001.

[129] C. M. Penney, "Light Scattering in Terms of Oscillator Strengths and Refractive Indices," *Journal of the Optical Society of America*, vol. 59, p. 34, Jan. 1969.

[130] G. Mie, "Beiträge zur Optik trüber Medien, speziell kolloidaler Metallösungen," *Annalen der Physik*, vol. 330, no. 3, pp. 377–445, 1908.

[131] H. Naus and W. Ubachs, "Experimental verification of Rayleigh scattering cross sections," *Optics Letters*, vol. 25, pp. 347–349, 2000.

[132] M. Sneep and W. Ubachs, "Direct measurement of the Rayleigh scattering cross section in various gases," *Journal of Quantitative Spectroscopy & Radiative Transfer*, vol. 92, pp. 293–310, 2005.

[133] D. Ityaksov, H. Linnartz, and W. Ubachs, "Deep-UV Rayleigh scattering of N2, CH4 and SF6," *Molecular Physics*, vol. 106, pp. 2471–2479, Nov. 2008.

[134] P. M. Teillet, "Rayleigh optical depth comparisons from various sources.," *Applied optics*, vol. 29, pp. 1897–900, May 1990.

[135] E. J. McCartney, *Optics of the Atmosphere*. John Wiley & Sons, Inc., 1976.

[136] M. Born and E. Wolf, *Principles of Optics*. Cambridge University Press, 7th (expan ed., 1999.

[137] W. J. Tango, "Spectroscopy of K2 Using Laser-Induced Fluorescence," *The Journal of Chemical Physics*, vol. 49, no. 10, p. 4264, 1968.

[138] R. N. Zare, "My life with LIF: a personal account of developing laser-induced fluorescence.," *Annual review of analytical chemistry (Palo Alto, Calif.)*, vol. 5, pp. 1–14, Jan. 2012.

[139] D. A. McQuarrie and J. D. Simon, *Physical Chemistry: A Molecular Approach*. University Science Books, Sausalito, California., 1997.

[140] V. Henri and W. R, "Absorbed Energy in Photochemical Reactions," *Comptes rendus hebdomadaires des seances de l'acadaemie des sciences*, vol. 156, pp. 1012–1015, 1913.

[141] G. H. Damon and F. Daniels, "The Photolysis of Gaseous Acetone and the Influence of Water," *Journal of the American Chemical Society*, vol. 55, no. 6, pp. 2363–2375, 1933.

[142] A. Lozano, *Laser-Excited Lumuinescent Tracers for Planar Concentration Measurements in Gas Jets*. PhD thesis, 1992.

[143] M. C. Thurber, F. Grisch, B. J. Kirby, M. Votsmeier, and R. K. Hanson, "Measurements and Modeling of Acetone Laser-Induced Fluorescence with Implications

for Temperature-Imaging Diagnostics," *Applied Optics*, vol. 37, pp. 4963–4978, July 1998.

[144] A. Lozano, B. Yip, and R. K. Hanson, "Experiments in Fluids, Acetone: a tracer for concentration measurements in gaseous flows by planar laser-induced fluorescence," vol. 376, pp. 369–376, 1992.

[145] G. M. Breuer and E. K. C. Lee, "Fluorescence decay times of cyclic ketones, acetone, and butanal in the gas phase," *The Journal of Physical Chemistry*, vol. 75, pp. 989–990, Apr. 1971.

[146] A. M. Halpern, "Excited Singlet State Radiative and Nonradiative Transition Probabilities for Acetone, Acetone-d6, and Hexafluoroacetone in the Gas Phase, in Solution, and in the Neat Liquid," *The Journal of Chemical Physics*, vol. 54, no. 3, p. 1271, 1971.

[147] M. A. Blitz, D. E. Heard, and M. J. Pilling, "Study of acetone photodissociation over the wavelength range 248-330 nm: evidence of a mechanism involving both the singlet and triplet excited states.," *The journal of physical chemistry. A*, vol. 110, pp. 6742–56, June 2006.

[148] H. J. Groh, G. W. Luckey, and W. A. Noyes, "The Mechanism of Acetone Vapor Fluorescence," *The Journal of Chemical Physics*, vol. 21, no. 1, p. 115, 1953.

[149] H. Hu and M. Koochesfahani, "A novel method for instantaneous, quantitative measurement of molecular mixing in gaseous flows," *Experiments in Fluids*, vol. 33, pp. 202–209, July 2002.

[150] A. Charogiannis and F. Beyrau, "Laser induced phosphorescence imaging for the investigation of evaporating liquid flows," *Experiments in Fluids*, vol. 54, p. 1518, May 2013.

[151] J. J. L. Spaanjaars, J. J. ter Meulen, and G. Meijer, "Relative predissociation rates of OH (A 2Σ+, v=3) from combined cavity ring downLaser-induced fluorescence measurements," *The Journal of Chemical Physics*, vol. 107, no. 7, p. 2242, 1997.

[152] C. B. Dreyer, S. M. Spuler, and M. Linne, "Calibration of laser induced fluorescence of the OH radical by cavity ringdown spectroscopy in premixed atmospheric pressure flames," *Combustion Science and Technology*, vol. 171, pp. 163–190, Jan. 2001.

[153] J. Luque, P. Berg, J. Jeffries, G. Smith, D. Crosley, and J. Scherer, "Cavity ring-down absorption and laser-induced fluorescence for quantitative measurements of CH radicals in low-pressure flames," *Applied Physics B: Lasers and Optics*, vol. 78, pp. 93–102, Jan. 2004.

[154] C. Bahrini, S. Douin, J. Rostas, and G. Taieb, "CRD and LIF spectra of the CaBr and CaI radicals," *Chemical Physics Letters*, vol. 432, pp. 1–5, Dec. 2006.

[155] N. Lamoureux, P. Desgroux, A. El Bakali, and J. Pauwels, "Experimental and numerical study of the role of NCN in prompt-NO formation in low-pressure CH4O2N2 and C2H2O2N2 flames," *Combustion and Flame*, vol. 157, pp. 1929–1941, Oct. 2010.

[156] D. Tokaryk, A. Adam, and M. Slaney, "Cavity ring down laser spectroscopy of the

transition of CaCCH," *Chemical Physics Letters*, vol. 433, pp. 264–267, Jan. 2007.

[157] B. A. Richman, A. A. Kachanov, B. A. Paldus, and A. W. Strawa, "Novel detection of aerosols: combined cavity ring-down and fluorescence spectroscopy," *Optics Express*, vol. 13, no. 9, p. 3376, 2005.

[158] S. E. Sanders, *Laser spectroscopy of wire-like molecules*. PhD thesis, 2012.

[159] S. E. Sanders, O. R. Willis, N. H. Nahler, and E. Wrede, "Absolute absorption and fluorescence measurements over a dynamic range of 10^6 with cavity-enhanced laser-induced fluorescence." Aug. 2013.

[160] S. J. Greaves, E. L. Flynn, E. L. Futcher, E. Wrede, D. P. Lydon, P. J. Low, S. R. Rutter, and A. Beeby, "Cavity ring-down spectroscopy of the torsional motions of 1,4-bis(phenylethynyl)benzene.," *The journal of physical chemistry. A*, vol. 110, pp. 2114–21, Feb. 2006.

[161] F. Hagemeister, C. Arrington, B. Giles, B. Quimpo, L. Zhang, and T. Zwier, "Cavity-Ringdown Methods for Studying Intramolecular and Intermodular Dynamics," in *Cavity-Ringdown Spectroscopy*, ch. 14, pp. 210–232, American Chemical Society, 1999.

[162] J. D. Koch, R. K. Hanson, W. Koban, and C. Schulz, "Rayleigh-Calibrated Fluorescence Quantum Yield Measurements of Acetone and 3-Pentanone," *Applied Optics*, vol. 43, no. 31, p. 5901, 2004.

[163] Q. Chu and Y. Pang, "Vibronic structures in the electronic spectra of oligo(phenylene ethynylene): effect of m-phenylene to the optical properties of poly(m-phenylene ethynylene).," *Spectrochimica acta. Part A, Molecular and biomolecular spectroscopy*, vol. 60, pp. 1459–67, June 2004.

[164] Q. Wu and I. Hodgkinson, "Materials for Birefringent Coatings," *Applied Optics*, vol. 33, pp. 8109–8110, Dec. 1994.

[165] Layertech, "Private Communications," 2013.

[166] A. C. Vandaele, "High-resolution Fourier transform measurement of the NO 2 visible and near-infrared absorption cross sections: Temperature and pressure effects," *Journal of Geophysical Research*, vol. 107, no. D18, p. 4348, 2002.

[167] K. O. Patten and H. S. Johnston, "Internal energy distributions from nitrogen dioxide fluorescence. 2. Collisional energy transfer from excited nitrogen dioxide," *The Journal of Physical Chemistry*, vol. 97, pp. 9904–9915, Sept. 1993.

[168] V. M. Donnelly and F. Kaufman, "Fluorescence lifetime studies of NO2. I. Excitation of the perturbed 2B2 state near 600 nm," *The Journal of Chemical Physics*, vol. 66, no. 9, p. 4100, 1977.

[169] V. M. Donnelly, D. G. Keil, and F. Kaufman, "Fluorescence lifetime studies of NO2. III. Mechanism of fluorescence quenching," *The Journal of Chemical Physics*, vol. 71, no. 2, p. 659, 1979.

[170] D. G. Keil, V. M. Donnelly, and F. Kaufman, "Fluorescence lifetime studies of NO2. IV. Temperature dependence of fluorescence spectra and of collisional quenching of fluorescence," *The Journal of Chemical Physics*, vol. 73, no. 4, pp. 1514–1520, 1980.

[171] T. Gierczak, J. B. Burkholder, S. Bauerle, and A. Ravishankara, "Photochemistry of acetone under tropospheric conditions," *Chemical Physics*, vol. 231, pp. 229–244, June 1998.

[172] M. Wollenhaupt, S. A. Carl, A. Horowitz, and J. N. Crowley, "Rate Coefficients for Reaction of OH with Acetone between 202 and 395 K," *The Journal of Physical Chemistry A*, vol. 104, pp. 2695–2705, Mar. 2000.

[173] J. D. Koch, J. Gronki, and R. K. Hanson, "Measurements of near-UV absorption spectra of acetone and 3-pentanone at high temperatures," *Journal of Quantitative Spectroscopy and Radiative Transfer*, vol. 109, pp. 2037–2044, July 2008.

[174] J. Heicklen, "The Fluorescence and Phosphorescence of Biacetyl Vapor and Acetone Vapor," *Journal of the American Chemical Society*, vol. 81, pp. 3863–3866, Aug. 1959.

[175] T. Fujiwara, M. Z. Zgierski, and E. C. Lim, "Spectroscopy and photophysics of 1,4-bis(phenylethynyl)benzene: effects of ring torsion and dark pi sigma* state.," *The journal of physical chemistry. A*, vol. 112, pp. 4736–41, May 2008.

[176] A. C. R. Pipino, J. W. Hudgens, and R. E. Huie, "Evanescent wave cavity ring-down spectroscopy with a total-internal-reflection minicavity," *Review of Scientific Instruments*, vol. 68, pp. 2978–2989, 1997.

[177] I. M. P. Aarts, A. C. R. Pipino, J. P. M. Hoefnagels, W. M. M. Kessels, and M. C. M. van de Sanden, "Quasi-ice monolayer on atomically smooth amorphous SiO2 at room temperature observed with a high-finesse optical resonator," *Physical Review Letters*, vol. 95, 2005.

[178] L. van der Sneppen, F. Ariese, C. Gooijer, and W. Ubachs, "Liquid-phase and evanescent-wave cavity ring-down spectroscopy in analytical chemistry.," *Annual review of analytical chemistry (Palo Alto, Calif.)*, vol. 2, pp. 13–35, Jan. 2009.

[179] M. Schnippering, S. R. T. Neil, S. R. Mackenzie, and P. R. Unwin, "Evanescent wave cavity-based spectroscopic techniques as probes of interfacial processes.," *Chemical Society reviews*, vol. 40, pp. 207–20, Jan. 2011.

[180] E. Wrede, "LIF Probe Region and Lens Setup Simulation Program."

[181] Y. X. Tang, L. Zhu, L. T. Chu, and B. Xiang, "Cavity ring-down spectroscopic study of acetaldehyde photolysis in the gas phase, on aluminum surfaces, and on ice films," *Chemical Physics*, vol. 330, pp. 155–165, 2006.

[182] H. Iwabuchi and P. Yang, "Temperature dependence of ice optical constants: Implications for simulating the single-scattering properties of cold ice clouds," *Journal of Quantitative Spectroscopy and Radiative Transfer*, vol. 112, pp. 2520–2525, Oct. 2011.

[183] P. Marchand, G. Marcotte, and P. Ayotte, "Spectroscopic study of HNO3 dissociation on ice.," *The journal of physical chemistry. A*, vol. 116, pp. 12112–22, Dec. 2012.

[184] *Thermoelectric handbook*. 1040 Spruce Street, Trenton, NJ 08648 USA: Melcor, Laird Technologies.

[185] L. Rothman *et al.*, "The HITRAN 2012 molecular spectroscopic database," *Journal of Quantitative Spectroscopy and Radiative Transfer*, July 2013.

[186] W. Wagner, "International equations for the pressure along the melting and along

the sublimation curve of ordinary water substance," *J. Phys. Chem. Ref. Data*, vol. 23, no. 3, pp. 515–525, 1994.

[187] MATLAB, *version 8.1.0.604 (R2013a)*. Natick, Massachusetts: The MathWorks, Inc., 2013.

[188] W. C. Pfalzgraff, R. M. Hulscher, and S. P. Neshyba, "Scanning electron microscopy and molecular dynamics of surfaces of growing and ablating hexagonal ice crystals," *Atmospheric Chemistry and Physics*, vol. 10, pp. 2927–2935, Mar. 2010.

[189] H. Linnartz, T. Motylewski, F. Maiwald, D. Roth, F. Lewen, I. Pak, and G. Winnewisser, "Millimeter wave spectroscopy in a pulsed supersonic slit nozzle discharge," *Chemical Physics Letters*, vol. 292, pp. 188–192, July 1998.

[190] S. S. Brown and J. Stutz, "Nighttime radical observations and chemistry.," *Chemical Society reviews*, vol. 41, pp. 6405–47, Oct. 2012.

[191] C. Meusinger, T. a. Berhanu, J. Erbland, J. Savarino, and M. S. Johnson, "Laboratory study of nitrate photolysis in Antarctic snow. I. Observed quantum yield, domain of photolysis, and secondary chemistry.," *The Journal of chemical physics*, vol. 140, p. 244305, June 2014.

[192] L. Wang and J. Zhang, "Detection of Nitrous Acid by Cavity Ring-Down Spectroscopy," *Environmental Science & Technology*, vol. 34, pp. 4221–4227, Oct. 2000.

[193] H. J. Beine, A. Amoroso, F. Dominé, M. D. King, M. Nardino, A. Ianniello, and J. L. France, "Surprisingly small HONO emissions from snow surfaces at Browning Pass, Antarctica," *Atmospheric Chemistry and Physics*, vol. 6, pp. 2569–2580, July 2006.

[194] I. M. P. Aarts, A. C. R. Pipino, M. de Sanden, and W. M. M. Kessels, "Absolute in situ measurement of surface dangling bonds during a-Si : H growth," *Applied Physics Letters*, vol. 90, 2007.

[195] R. Hyland and A. Wexler, "Formulations for the thermodynamic properties of the saturated phases of H2O (from 173.15 K to 473.15 K)," *Ashrae Journal-American Society of heating refrigerating and air-conditioning engieers*, vol. 25, no. 5, p. 64, 1983.

[196] W. M. Haynes, ed., *CRC Handbook of Chemistry and Physics*. CRC Press, 92nd ed.